Chitosan-based Scaffolds for Tissue Engineering and Cancer Research Applications

Ariane Elizabeth Erickson

A dissertation
submitted in partial fulfillment of the
requirements for the degree of

Doctor of Philosophy

University of Washington
2018

Reading Committee:
Miqin Zhang, Chair
Guozhong Cao
Fumio Ohuchi

Program Authorized to Offer Degree:
Materials Science and Engineering

University of Washington

Abstract

Chitosan-based Scaffolds for Tissue Engineering and Cancer Research Applications

Ariane Elizabeth Erickson

Chair of Supervisory Committee:
Professor Miqin Zhang
Department of Materials Science and Engineering

Biomaterial scaffolds are an essential element in tissue engineering (TE), providing an extracellular matrix (ECM) substitute for cell attachment, proliferation, and differentiation at the site of a tissue defect. Designed to support a variety of tissues, biomaterial scaffolds, once used exclusively for TE, have now emerged as a promising tool for disease modeling. Scaffolds recapitulate ECM structural cues and more accurately represent native cell behavior relative to monolayer culture. In cancer research applications, mimicking native cell behavior could result in a better understanding of mechanisms underlying tumor progression leading to development of more effective and targeted anti-metastatic therapeutics.

This dissertation presents novel two-dimensional (2D) and three-dimensional (3D) chitosan-based biomaterial scaffolds for osteochondral tissue engineering and glioblastoma cancer research. Chitosan is a biocompatible, biodegradable, and non-toxic natural polymer with a proxy glycosaminoglycan structure. However, chitosan is prone to swelling and mechanical weakness.

When combined with anionic polymers, cationic chitosan can form a polyelectrolyte complex (PEC) to improve mechanical stability while preserving biocompatibility. This dissertation will explore electrospinning and thermally induced phase separation (TIPS) techniques for chitosan-based scaffold fabrication, highlighting the opportunities and challenges of 2D and 3D scaffolds in mimicking native ECM.

First, the development of pseudo-2D nanofiber substrates is explored using a high-throughput centrifugal electrospinning (HTP-CES) system. The HTP-CES is a high-yield production method resulting in a large number of highly aligned nanofiber samples. Compared to conventional electrospinning techniques, nanofibers produced with the HTP-CES exhibited both superior alignment and enhanced diameter uniformity. Further, the research explored nanofiber diameter tunability by varying the spinneret needle diameter, establishing a concave correlation between the needle diameter and resultant nanofiber diameter. The HTP-CES system shows potential for scaled up production of highly aligned nanofibers with tunable diameters to meet the needs of various engineering and biomedical applications.

Next, highly aligned chitosan-polycaprolactone (C-PCL) nanofibers fabricated with the HTP-CES were employed to study the influence of topography and biochemistry on human glioblastoma multiforme (GBM) cell motility. GBM is a highly invasive form of brain cancer. GBM tumor recurrence and lethality are attributed to diffuse cancer cell invasion into adjacent healthy brain tissue and influenced by topographical cues associated with the brain parenchyma. In this research, we fabricated highly reproducible C-PCL nanofibers coated with hyaluronic acid (HA), a glycosaminoglycan commonly found in the brain, to mimic the structure and biochemistry of native brain tissue. We cultured human GBM-derived cells (U-87 MG) on uncoated and HA-coated C-PCL nanofibers. Elongated cell morphologies occurred along the nanofiber length on all nanofiber substrates. Regardless of coating, cells on nanofibers were more resistant to the therapeutic alkylator temozolomide (TMZ) than cells grown in adherent polystyrene plates. Cell migration captured by time lapse imaging revealed the influence of the HA coating as cells migrated the farthest and the fastest on nanofibers coated with 0.5% HA. These results indicate that HA-coated nanofibers are a promising substrate to characterize GBM migration and investigate novel anti-metastatic therapies.

After evaluation of GBM motility on 2D nanofiber substrates, we investigated the influence of biomechanical cues on GBM tumor sphere progression in 3D porous scaffolds. Tumor matrix stiffness is implicated in the regulation of cell proliferation, drug resistance, and reversion to a more invasive phenotype. Understanding the relationship between stiffness and cell behavior is vital to develop appropriate *in vitro* tumor models. We fabricated chitosan-hyaluronic acid (CHA) polyelectrolyte complex (PEC) scaffolds with varying stiffness, encompassing healthy and tumorous brain tissue to evaluate the effect of scaffold stiffness on human glioblastoma (U-87 MG) cell behavior. After 12 days of culture, we observed larger tumor spheroids and an increased resistance to TMZ-induced cell death in scaffolds with higher stiffness. Moreover, the stiffer 8% CHA scaffolds exhibited an increase in expression of drug resistance and invasion-related genes compared to 2D monolayer culture. These results indicate that CHA scaffolds enhance tumor cell malignancy, providing a valuable *in vitro* microenvironment for studying tumor progression and screening anti-cancer therapies.

Finally, we developed a 3D bilayer porous scaffold for osteochondral tissue regeneration. Osteochondral defects result from damage to the articular cartilage and subchondral bone. When left untreated, osteochondral defects can lead to osteoarthritis and decreased quality of life. Due to the gradient osteochondral tissue, multiphasic scaffolds in which different layers represent

different microenvironments, are a promising treatment approach, yet stable joining between layers remains challenging. We fabricated a bilayer scaffold using thermally induced phase separation (TIPS) where the cartilage region was optimized for HA content and stiffness and the bone region was defined by higher stiffness and osteoconductive hydroxyapatite (HAp) content. The bilayer scaffold displayed seamless interfacial integration and a mechanical stiffness gradient similar to that in the native osteochondral microenvironment. Co-culture with chondrocyte-like (SW-1353 or mesenchymal stem cells) and osteoblast-like cells (MG63) displayed cell proliferation and invasion to the interface, along with increased expression of relevant gene markers indicating the potential of this bilayer scaffold for osteochondral tissue regeneration.

TABLE OF CONTENTS

LIST OF FIGURES

LIST OF TABLES

Acknowledgments

I would like to thank my advisor, Professor Miqin Zhang, for her guidance and support throughout my time in her lab. Her enthusiasm, expertise, creativity, and encouragement has pushed me to think more creatively and shaped me into a better and more independent scientist. I will always be grateful for her inspiration, mentorship, and the opportunities from her lab. Thank you to my committee members – Professor Fumio Ohuchi, Professor Guozhong Cao, and Professor Ying Zheng – for reviewing and advising my graduate research. Additionally, thank you Professor Bruce Hinds and Professor Dwayne Arola for the feedback and advice during my general exam. I would also like to thank Dr. John Silber for the thoughtful critiques, advice, and unlimited science jokes.

Thank you to my colleagues in the Zhang lab, especially Dr. Sheeny Lan Levengood, for the support and friendship. Without your time, patience, mentorship, advice, constructive feedback, and editing (so many reviews!), this would not have been possible. Also, I would like to thank the undergraduate and masters students I have worked with during my PhD, especially Jialu Sun. I am grateful for your consistent reminders and awe at how gratifying and fascinating science can be.

I would like to thank the MSE department staff and lab managers including Tuesday Kuykendall, Karen Wetterhahn, and Bichtien Thach for your support. Additionally, thank you to the lab managers who assisted me in conducting and troubleshooting different analyses, including Glen MacDonald, Wai Pang Chan, Nathaniel Peters, and Scott Braswell.

Thank you to my incredible family and friends who encouraged me throughout this process. I sincerely thank my parents, Dave and Elizabeth, and siblings, Danielle and Zack, for the nonstop cheerleading, financial and emotional support, and the endless encouragement over the last 6 years. I was always just a phone call away from great technical advice and your unwavering love of science inspired me to not give up! I could not have finished without you and it was beyond wonderful to have you all in Seattle at the end to celebrate. Thank you to Jess Hazlett for the encouragement, laughs, endless rides to work, and countless meals. You made Seattle my home away from home and were always able to make the rainiest days the best. I want to thank Ken Laszlo, my fiancé, for your undying support and patience. Thank you for believing in me, building me up, and supporting me. I can’t imagine doing this without you and I am glad I didn’t have to. Even after your graduation, you helped me plan out mine – through the ups and downs, early mornings and late nights. I am excited for our next adventure with our Postdoc. I love you all.

Finally, I would like to acknowledge funding I received in support of this work from the Stoebe Fellowship, National Institutes of Health T-32 Training grant, and the National Science Foundation Graduate Research Fellowship [DGE–1256082]. This work would not have been possible without the sustained support of the NIH [R01CA172455].

Chapter 1: INTRODUCTION

A shift in the United States population to older adults (65+ years old) is largely attributed to longer life spans and the aging baby boomer generation [1]. In the next 20 years, the number of adults 65 and over will double, accounting for an estimated 20% of the population in 2030. Aging coupled with the lack of access to information on risk factors and prevention are key factors in the rise of cancer diagnosis and mortality [2]. Additionally, aging increases the prevalence of organ failure and joint damage, resulting in a decreased quality of life [3-5]. The current clinical gold standard of treatment for organ/tissue damage is transplantation or grafts from a donor, cadaver, or animal model [6]. Transplants and grafts are limited by a greater demand than supply and also by donor site morbidity. To deal with the increasing healthcare challenges of an aging population, innovation is necessary.

Tissue engineering (TE) is a promising treatment approach for tissue disease or damage, bypassing the need for transplants or grafts [7, 8]. TE is an interdisciplinary tactic that couples engineering and life science principles to regenerate or improve tissue function through a combination of biomaterials, cells, and bioactive molecules [8]. The appropriate customization of these factors depends on the patient, and application and may involve both *in vitro* and *in vivo* techniques [9]. Generally, TE involves the implantation of a biomaterial scaffold in a defect site to aid in tissue regeneration. This requires the scaffold to be biocompatible, biodegradable, and tailored to the unique tissue microenvironment. Further, the immune response to the scaffold must allow for functional replacement of the missing or damaged tissue over the lifetime of the patient. In pediatric patients, this means that the biomaterial scaffold must grow and develop with the surrounding tissues and organs [10].

TE scaffolds have been customized to a wide variety of tissue systems enabling complex *in vitro* cultures more representative of those found in the human body. Recently, applications of TE scaffolds have expanded to encompass recapitulation of tissue-specific disease progression, such as 3D modeling of cancer tumors [11]. Using TE scaffolds, the influence of biochemical, topographical, and biomechanical cues on different types of cancer can be investigated to develop a better understanding of malignancy cues. Biologically relevant cancer cell behavior allows for investigation of metastasis and cell-extracellular matrix (ECM) cues for development of more efficient and targeted therapeutics, Further, scaffolds can be used as 3D tumor platforms for enhanced drug screening and drug discovery *in vitro*.

This dissertation details 2D and 3D biomaterial scaffolds for cancer research and osteochondral TE applications. First, a novel electrospinning technique, high throughput centrifugal electrospinning (HTP-CES) is examined, demonstrating increased nanofiber alignment and diameter uniformity. We then used nanofibers fabricated with the HTP-CES technique as a brain parenchyma mimic to study glioblastoma cell motility. Next, the C-PCL nanofibrous substrates were coated in hyaluronic acid (HA), a glycosaminoglycan found in brain tissue, to determine the effect of biochemistry on migratory cell behavior. Cells cultured on nanofibers were more resistant to temozolomide (TMZ)-induced cell death relative to cells cultured on conventional monolayer polystyrene culture plates. Subsequently, we examined the use of 3D porous scaffolds for glioblastoma tumor modeling with a range of scaffold stiffness encompassing healthy brain tissue and brain tumor tissue. Higher stiffness substrates promoted larger tumor sphere formation and greater resistance to TMZ-induced cell death. Finally, this dissertation presents a bilayer scaffold for osteochondral tissue engineering where each layer of the scaffold was tailored to the unique biological cues found in the native osteochondral tissue microenvironment. When the layers were combined, the bilayer scaffold possessed a stiffness gradient and integrated interface between layers that supported increased metabolic activity and cellular infiltration after two weeks of co-culture with osteoblast-like and chondrocyte-like cells.

1.1. ORGANIZATION OF DISSERTATION

Chapter 1 introduces the necessity and benefit of novel therapeutic solutions to tissue/organ damage and metastatic cancer therapies, including an overview of biomaterial scaffolds and the content of this dissertation.

Chapter 2 describes the benefits and challenges of biomaterial scaffolds in TE and highlights considerations for design of successful scaffolds tailored to unique tissue microenvironments, including a discussion of the advantages of chitosan-based scaffolds.

Chapter 3 illustrates the role of scaffolds in the future of cancer research, describing the design considerations and benefit of these materials for drug development and drug screening applications.

Chapter 4 reviews the current state of nanofiber substrates for glioblastoma drug screening and drug delivery applications focusing on nanofiber substrates for investigation of glioblastoma cell motility, metastasis, and invasion, as well as nanofibers as delivery vectors highlighting the delivery of chemotherapeutics, anti-angiogenic, and stem cells.

Chapter 5 details the high throughput centrifugal electrospinning (HTP-CES) system, a novel electrospinning approach for nanofiber fabrication to increase alignment and diameter tunability including an experiment highlighting the concave relationship between spinneret needle diameter and the resultant nanofiber diameter.

Chapter 6 describes the use of chitosan-polycaprolactone (C-PCL) nanofibers with varying hyaluronic acid coating as a brain parenchyma mimic for study of glioblastoma multiforme cell motility, including quantification of cell speed and resistance to temozolomide-induced cell death.

Chapter 7 presents porous chitosan and hyaluronic acid (C-HA) scaffolds with varying stiffness encompassing the range of healthy brain tissue to tumorous tissue with increased tumor size, enhanced drug resistance, and elevated expression of relevant chemoresistant gene markers in scaffolds with increased stiffness.

Chapter 8 examines a chitosan-based composite bilayer scaffold for osteochondral defect repair including co-culture experiments exhibiting cell penetration to the scaffold interface and increased expression of relevant gene markers after two weeks of co-culture.

Chapter 9 summarizes the conclusions presented in this dissertation with comments on the future potential of each scaffold.

Chapter 2: SCAFFOLDS FOR TISSUE ENGINEERING

2.1. TISSUE ENGINEERING BACKGROUND

Tissue engineering (TE) is a multidisciplinary approach aimed at regeneration of damaged, diseased, or deteriorating tissue or organs [8]. TE, also termed regenerative medicine, uses a combination of cells, bioactive factors, and biomaterial scaffolds (**Figure 2.1**) to restore, maintain, or improve tissue function. The current clinical gold standard of treatment for damaged tissue/organs is transplantation or grafting. However, lack of donors remains a challenge with 114,000+ patients currently on the national transplant waiting list and wait times for some organs exceeding 5 years [12]. Tissue autografts (same individual) and allografts (from one individual to another) are limited by lack of viable tissue, potential immune response, and donor-site morbidity. As a result, TE has emerged as a promising approach to the tissue/organ shortage, aiming to regenerate tissue in the defect site, and eventually produce functioning tissue/organs *ex vivo* for transplantation.

The success of TE relies heavily on the design and fabrication of biomaterial scaffolds [8, 10]. During regeneration, cells need a temporary support structure as cell–cell contacts develop, and secretion of a new permanent support structure begins. Thus, scaffolds need to mimic the function and spatial cues of the native tissue. Mimicking the native microenvironment requires optimization of the biochemical, biomechanical, and structural cues of the scaffold in conjunction with integration of bioactive factors to influence cell behavior (i.e., growth factors, peptides, and/or drugs). Generally, TE is conducted using either acellular or cell-seeded scaffolds. An acellular scaffold is designed to be directly implanted into the defect site and recruit cells from the surrounding tissue to populate the scaffold [13, 14]. Additionally, cells can be harvested, expanded *in vitro*, and seeded into the scaffold before implantation into the defect. Both acellular [13-17] and cell-seeded [18-21] approaches have shown promise *in vivo* and in human trials, signifying the importance of scaffold design. The most crucial scaffold design consideration is customizing the scaffold to mimic the inherent tissue structure presented by the native extracellular matrix (ECM).

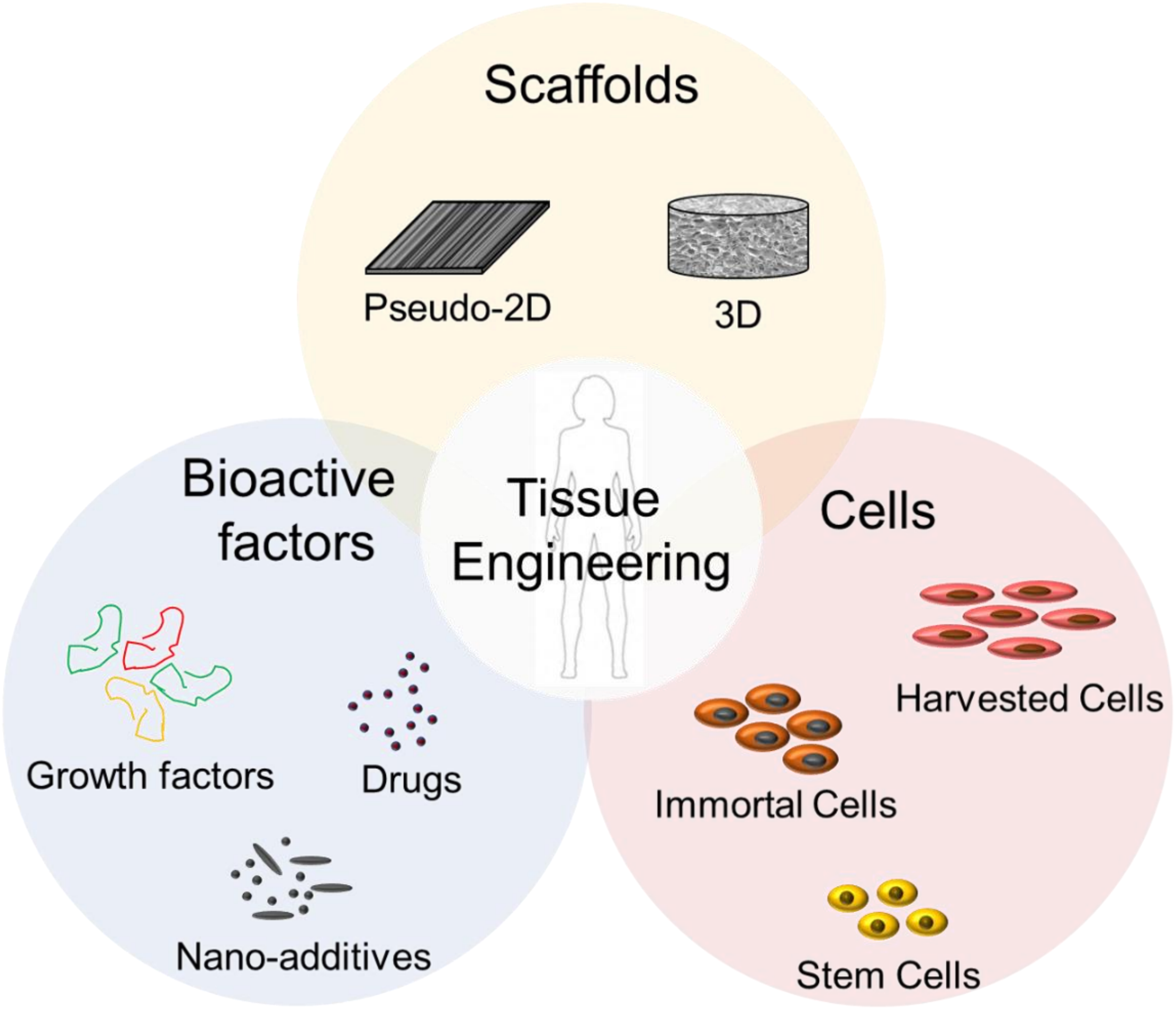

Figure 2.1. A simplified overview of tissue engineering detailing the three components for regeneration – scaffolds, cells, and bioactive factors. The specifics of each component depend on the application and tissue system.

2.2. EXTRACELLULAR MATRIX AND TISSUE STRUCTURE

Tissue functionality is dependent on the spatial organization of the individual cells and the underlying structural matrix [22]. In healthy tissue, the basement membrane or extracellular matrix (ECM) provides support for cell adhesion, directing contact guidance between cells and orienting multilayers of cells. The ECM is fibrous structure composed mainly of collagen. Collagen and other fibrous proteins provide mechanical strength to the tissue, defining the tissue size and shape. The other structural proteins, such as fibronectin and laminin, aid in cell adhesion. Between the collagen fibrils, water-soluble polymers such as polysaccharide-rich proteoglycans and hyaluronan, hydrate and swell, providing compressive strength to the tissue and preventing tissue collapse [22]. Hydrogel-like polymers facilitate the diffusion of nutrients, growth factors, and signaling molecules to the cells, and also the elimination of waste.

The ECM is in a constant state of dynamic reciprocity that influences cell morphology and phenotype. In response to biomechanical cues or oxygen/nutrient gradients, cells modify the secretion of ECM to aid in cell survival and proliferation. The dynamic state is customized to each unique tissue where the demands of the ECM vary, and the ECM of brain has different signaling and structural needs relative to bone ECM [22].

Because of the plethora of spatial cues in native ECM, development of biomaterial TE scaffold is non-trivial. To capture the unique cues of tissue-specific ECM, decellularized tissue has emerged as a popular TE scaffold material. Derived from human, pig, and cow tissues, several decellularized matrix scaffolds are currently commercially available (e.g., AlloDerm, CuffPatch™, MatriStem, Pelvicol, and Dura-Guard®) [23]. Although promising, reproducibility remains a challenge with decellularized matrix materials. Because ECM is tissue-specific, scaffold materials vary between differing tissue types. Additionally, differences in the decellularization process and material preparation can alter the mechanical strength and porosity of the resultant scaffold. Therefore, further advancement is necessary to develop a reproducible TE scaffold capable of customization to the natural, tissue-specific ECM.

2.3. SCAFFOLDS

Tissue engineering continues to change and evolve with advancements in biomaterial fabrication, stem cell biology, and cell culture techniques. Over the last 50 years, scientific advancements have changed the face of medical treatments, including the definition of biomaterials [24]. Researchers chose early biomaterials by pairing the mechanical and materials properties to the tissue defect/damage. If integration of biomaterials resulted in the lack of further tissue damage or harmful host response, the material was considered successful. For example, bone cement and Dacron were extensively used as they were relatively inert, and the foreign body response was tolerable. Second-generation biomaterials such as titanium, poly (lactic-co-glycolic acid) (PLGA), and collagen focused on enhanced and sustained integration into the body, and biodegradation. Third-generation biomaterials were focused on bioinduction and integration into adjacent tissue, displaying a shift from inert and unreactive biomaterials to now designing materials to influence biological properties.

2.4. SCAFFOLD PROPERTIES

No one material is capable of satisfying all TE needs, so the ideal biomaterial scaffold is dependent on the application and must be selected in an application-specific manner [8]. Therefore, a plethora of materials and fabrication techniques have been explored for scaffold fabrication. Nevertheless, regardless of the tissue site, several key considerations affect development of a successful TE scaffold. There are many excellent reviews highlighting scaffold design considerations [8, 10, 25-27]. Here, a subset of those considerations is presented.

2.4.1. Biocompatibility and Host Response

Biocompatibility is defined as the lack of a toxic or injurious response upon transplantation [28]. For TE, scaffolds must exhibit appropriate cell behavior *in vitro* and *in vivo*, supporting cell attachment and infiltration. Additionally, the scaffold must elicit an amenable immune response upon implantation. An inflammatory response can reduce healing and may cause scaffold rejection.

The immune response of scaffolds can be tailored through biomaterial selection. Upon damage to the local tissue, the healing cascade occurs in four phases – hemostasis, inflammation, proliferation, and remodeling [29]. During the inflammation phase, macrophages can adopt different phenotypes ranging from pro-inflammatory (M1) to pro-remodeling (M2), playing a key role in tissue regeneration [29]. Briefly, upon initial tissue damage, M1 macrophages are recruited to the defect site to remove dead cells and destroy potential pathogens. If the transition from M1 to M2 macrophages occurs early in the healing cascade, constructive remodeling will result. If M2 macrophages become predominant later in the healing process, scar tissue formation will occur [30]. By tailoring the composition of the implanted scaffold, the phenotypic response of macrophages can be influenced. Positive macrophage responses have also been documented in ECM-based materials, engineered scaffolds [31, 32], and in highly sulfated hyaluronic acid scaffolds where a transition from the M1 to M2 macrophage phenotype was induced [33]. A more comprehensive characterization of the immune response to different materials may lead to a better material selection process and improved implantation outcomes.

2.4.2. Materials

Scaffolds are generally composed of either synthetic or natural polymers depending on the application [10]. Synthetic polymers have precisely controlled molecular weights, mechanical properties, and degradation rates with less batch-to batch-variability relative to natural polymers. Common synthetic polymers used in TE include polystyrene (PS), poly-l-lactic acid (PLLA), poly (ethylene glycol) (PEG), poly (lactic co-glycolic acid) (PLGA), poly (caprolactone) (PCL), poly (ethylene terephthalate), and polyglycolic acid (PGA). However, synthetic polymers are generally less biocompatible and can have harmful degradation products resulting in necrosis at the defect site. Significant work has been dedicated to increasing the bioactivity of synthetic polymers with ECM-derived adhesive peptide modifications where modification with RGD sequences is the most popular [34, 35].

The mechanism that mediates cell recognition of material cues is not well understood. Nevertheless, natural polymers are advantageous as scaffold materials because they contain naturally occurring amino acid sequences that facilitate cell attachment, migration, differentiation, and immune recognition [36]. Additionally, natural polymers are biodegradable. Common natural polymers used in TE are naturally occurring polymers (e.g., silk, alginate, and chitin), purified ECM proteins (e.g., collagen and elastin), and ECM-derived decellularized tissues (e.g., small intestine submucosa, dermis, and urinary bladder matrix) [24]. However, these biomaterials alone lack the signaling, mechanical, and spatial cues of the native ECM. Scaling up production of these natural polymers also remains a challenge as homogenous and reproducible fabrication is a challenge. Additionally, natural polymers are generally not suitable in load-bearing applications due to the weak mechanical properties, but modifications such as the formation of a polyelectrolyte complex (PEC) can improve the stability of these polymers.

2.4.2.1. Chitosan

Chitosan is a cationic, biocompatible, and biodegradable polymer widely used in TE applications [37]. As the only pseudo-natural cationic polymer, chitosan is unique [38]. Chitosan is a linear polysaccharide composed of random monomeric units with a molar fraction degree of acetylation (DA) of β-(1→4) N-acetyl-D-glucosamine and a fraction (1-DA) of β-(1→4) D-glucosamine [38, 39]. Chitosan is derived from partial deacetylation of chitin (**Figure 2.2**), a naturally occurring polymer derived from shrimp shells. Chitinases are widely found in nature (e.g., bacteria, fungi, plants, and the digestive tracts of animals), and consequently chitosan is biodegradable. Chitin contains a small number of N-deacetylated groups and therefore is less soluble in acidic solvents, whereas chitosan is comprised of less N-acetylated groups and therefore is soluble in acidic solvents [40].

The degree of deacetylation in chitosan determines the number of amino groups along the polymer chain. If the degree of deacetylation is < 60 mol%, the material is considered chitin. At > 60 mol% deacetylation, the material is deemed chitosan and becomes soluble in acidic aqueous solutions [41]. Deacetylation of chitin is accomplished by chemical hydrolysis in alkaline conditions or enzymatic hydrolysis, as with chitin deacetylase [37, 38]. Chitosan is a heteropolysaccharide where the content and sequence of linear β-1,4-linked units determines the physicochemical and biological properties. Solution properties of chitosan depend on the DA, molecular weight, and location of the acetyl groups along the main chain [42]. Further, the distribution of acetyl groups, whether random or block-wise, may influence inter-chain interactions due to H-bonds and hydrophobic character of acetyl groups. Using the functional groups on chitosan, modifications with growth factors like (RGD)-modified UV-cross-linked chitosan [43], platelet-derived growth factors BMP-2 and BMP-7 [44], and heparin functionalization can enhance the bioactivity of chitosan.

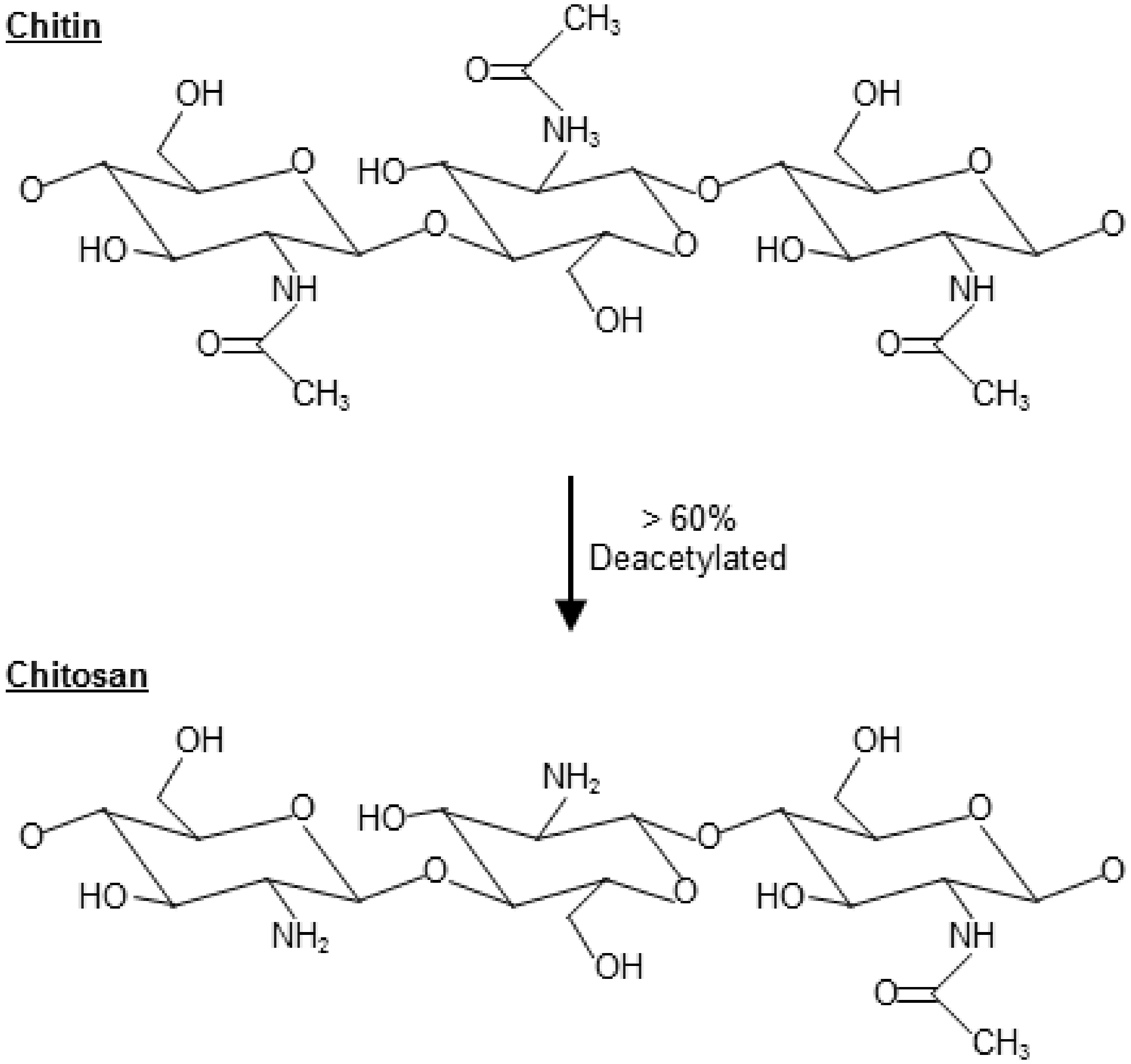

Figure 2.2. Chemical structure of chitin and the partially deacylated (> 60%) form chitosan.

Due to the amino groups, chitosan can be protonated and therefore soluble in dilute acidic solutions (pH < 6). The $-NH_2$ groups also allow chitosan to complex metal ions, making it useful for water filtration, heavy metal recovery, and beverage clarification, as in wine or juices. When protonated, chitosan is a polycation. The net cationicity and the multiple functionalities make chitosan an attractive biomolecule, especially for biomedical applications [45].

Chitosan can form electrostatic complexes and polyelectrolyte complexes (PEC). An electrostatic complex can be formed in low deacetylated chitosan involving the cooperative stacking of surfactant alkyl chains, like with sodium dodecyl sulfate. Chitosan can also form PECs with oppositely charged polymers (e.g., proteins, polyanions, DNA) [45]. With an anionic polymer such as hyaluronan or alginate, the electrostatic reaction is pH dependent and stability depends on ionic strength [46]. PECs add versatility to processing where materials can be built up layer by layer by alternating polyanion and polycation exposure, leading to encapsulation and controlled release applications.

Chitosan-based materials can be processed into a variety of forms including hydrogels [47-49], membranes [18, 50], nanofibers [16, 51, 52], beads [53, 54], microparticles [55, 56], nanoparticles [57-59], and porous scaffolds [60, 61] allowing for a versatile array of applications. Chitosan has been extensively used in tissue engineering for bone [62, 63], cartilage [64, 65], skin [16, 66], liver [67], and nerves [68-70].

2.4.3. Architecture

Generally, TE scaffolds are highly porous 3D materials with an interconnected pore structure. Interconnected pores ensure that cells can invade and infiltrate the full volume of the scaffold. A porous architecture also facilitates the infiltration of nutrients and growth factors and the diffusion of waste similar to the native ECM. The mean pore size of a scaffold is a key factor in cell adhesion and is a function of surface area and ligand availability. Scaffold pores need to be large enough for cells to migrate through the structure and adhere, yet small enough to have a high specific surface area for efficient cell binding [71, 72]. The appropriate pore size is unique to each tissue system and dependent on the vascularization and cell behavior [73, 74]. In general, increased porosity results in increased cell infiltration and subsequent vascularization.

Core degradation is a persistent challenging plaguing TE scaffolds [75]. Core degradation occurs due to the lack of nutrient diffusion in and waste diffusion out of the scaffold creating an inner core of underdeveloped cells [75, 76]. Vascularization and consistent diffusion throughout the entirety of the scaffold volume remains a crucial barrier to advancement in TE [75-77].

2.4.4. Mechanical Properties

Tissue mechanics play a crucial role in tissue morphogenesis where stiffness can influence cell maturation and direct the lineage in cell differentiation [78]. For example, changing the stiffness of the underlying substrate can direct mesenchymal stem cells to a neuronal, myogenic, or osteogenic lineage [78]. Recapitulating the mechanical cues of the tissue microenvironment is one of the grand challenges in TE as the scaffold must be stable enough for handling during implantation and sustain mechanical integrity until remodeling is complete [79].

The complex interplay between biomechanics and porosity in porous materials is highlighted in TE [10]. First-generation biomaterials recognized material stiffness as a crucial design characteristic and aimed to match scaffold stiffness with the anatomical site. However, at the same time the push to move from monolithic materials to more porous materials in support of vascularization resulted in a drastic decrease in scaffold mechanical properties. Ample time and resources were shifted to matching the tissue and porous scaffold mechanical properties with a focus on bone TE. Although important, mechanical properties are not the sole design consideration. Many scaffolds matching the mechanical properties of bone with exhibited potential *in vitro* have failed *in vivo* due to lack of porosity, making vascularization impossible and thereby reducing tissue functionality.

Scaffold stiffness is generally tuned through cross-linking or porosity for 3D porous matrices. The scaffold composition can also vary to provide a tailored stiffness to each unique microenvironment. Mechanical stiffness can alter the immune response of the host to the implant, making it more prone to rejection [80].

2.4.5. Degradation

To facilitate tissue regeneration, scaffold degradation is necessary, to ensure cells secrete a new ECM, filling the space of the temporary scaffold and returning tissue functionality [10]. Determination of an appropriate degradation rate, however, is nontrivial as tissue regeneration rates vary with patient age and differing cell growth rates. Degradation of the support scaffold must be slow enough that cells adhere, migrate, proliferate, and populate the full volume of the scaffold, providing a basis for integration into adjacent tissue. However, degradation must be fast enough that the reconstruction process is not impeded. To control the degradation rate, peptides sensitive to enzymatic cleavage can be integrated into the biomaterial [81].

In addition to optimizing the scaffold degradation rate, consideration of the degradation products is also necessary. After degradation, the implanted scaffold should be able to exit the body without interference or toxicity in the organs. The complexity of degradation rate and the impact of degradation products has created a prominent role for immunology in TE [10, 82].

2.4.6. Bioactive factors

Because cell behavior from attachment to differentiation must be controlled for successful TE, integration of specific bioactive factors is frequent. Bioactive factors can range from growth factors to peptides to integration of specific molecules or compounds found in the native tissue ECM. Bioactive factors are most successful when tailored to the specific tissue. For example, in nerve regeneration, sustained delivery of fibroblast growth factor (FGF-1) improved regeneration

[83]. To enhance osteogenesis, the integration of tricalcium phosphate or hydroxyapatite, a naturally occurring inorganic calcium apatite and a major constituent of bone, increases expression of osteogenic gene markers in osteoblast cultures [84]. In cartilage TE, the integration of hyaluronic acid has improved the proliferation rate and deposition of chondrocytes [85].

Integration of hydroxyapatite and tri-calcium phosphate in bone TE scaffolds is widespread with fabrication of sintered ceramic scaffolds, eliminating the use of a polymer matrix [25]. Ceramic scaffolds have a high stiffness (Young's modulus), but low elasticity, leading to brittle behavior. These ceramic scaffolds are biocompatible with similar chemical and architectural cues to the mineral phase in bone. Further, osteogenic cells display enhanced differentiation and proliferation on ceramic or polymer-ceramic scaffolds [86]. The clinical relevance of ceramic scaffolds has been limited due to the brittleness and difficulty molding the scaffold to the defect site. Additionally, regenerated bone tissue using a ceramic scaffold template was unable to withstand the required mechanical load [87].

While much is left to be studied and understood in TE, the research continues to grow exponentially, resulting in a $240 million industry annually [88]. Therefore, ongoing research into bioactive, bioinstructive, and stimuli-responsive biomaterials is valuable [89]. While challenges remain, the opportunities are abundant.

2.5. MICROENVIRONMENT DIMENSIONALITY

The role of a TE scaffold is to provide support and structure for cell attachment towards the regeneration of functional tissue. The aim is to customize a scaffold to mimic the body's natural support structure, the extracellular matrix (ECM). Scaffolds that accurately represent the ECM could be key to discovering mechanisms behind tissue formation, regeneration, and function, as well as, studying how disease disrupts normal tissue function. Monolayer cell culture has been used to study stimulus response and cell behavior *in vitro*, but mounting evidence indicates that cells in 2D monolayer culture do not accurately represent *in vivo* cell behavior [90, 91]. To overcome this limitation, nanofibrous 2D scaffolds and porous 3D scaffolds can be utilized to better mimic the native tissue ECM.

2.5.1. Pseudo-2D Electrospun Nanofiber Substrates

Nanomaterials have evolved as a useful tool in biomedical research capable of nanoscale manipulation of cell behavior. Nanotopography, including nanofibers or patterned surfaces can direct cell behavior sans biological cues effecting cell function from differentiation [92] to apoptosis [93]. The specific mechanisms behind tissue formation are not well understood, and many nano-scale materials approaches have been employed for study and control of cell behavior.

Electrospinning is a popular, versatile, and inexpensive fabrication technique capable of producing fibers ranging from tens of nanometers to microns. A wide range of materials have been electrospun including polymers, polyblends, composites, semiconductors, and ceramics in a wide range of morphologies (i.e., beaded, ribbon, porous, and core-sheath) [94, 95]. Electrospun nanofiber mats have a wide range of applications varying from water filtration to wound healing [94]. Nanofibers are attractive in biological applications due to the high surface area, ability to be functionalized, and similarities to the native fibrous ECM topography. Fiber alignment has proven key in determination of the appropriate tissue microenvironment. Randomly oriented nanofibrous mats are advantageous in skin wound healing applications [16], whereas aligned nanofibers have shown great potential with anisotropic tissues such as nerve [96] or skeletal muscle [97].

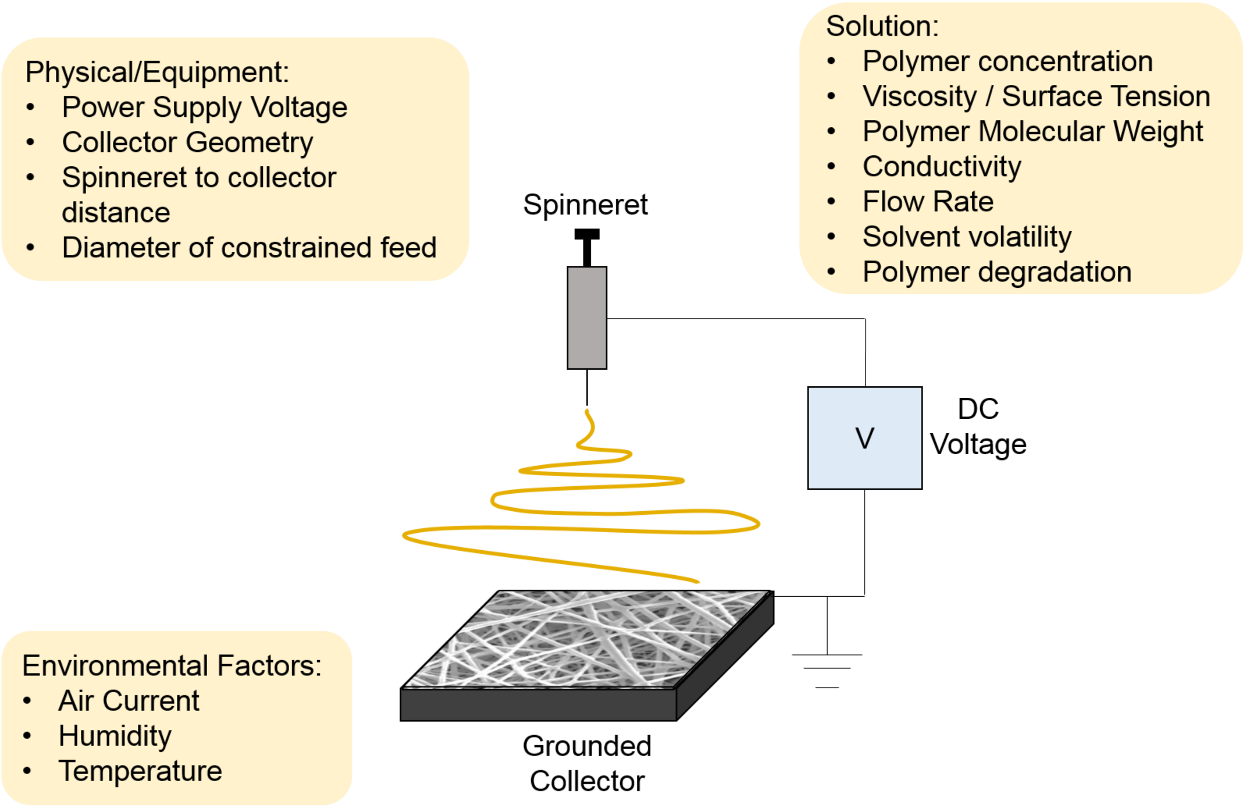

Figure 2.3. Illustration of a simple electrospinning set-up with various processing parameters for consideration, including solution properties, physical and equipment parameters, and environmental factors.

Similar to other nanofiber fabrication techniques (dry spinning, melt-spinning), electrospinning is based on the ability to stretch a viscoelastic solution [95]. Unlike other fiber spinning techniques, however, electrostatic forces stretch the fibers until they solidify. To electrospin, a polymer solution is first fed through a spinneret [94, 95, 98]. A high voltage (usually > 5kV) is applied to the solution until the repulsive force of the charged jet overcomes the surface tension of the polymer solution, and a fiber jet erupts from the spinneret. Near the spinneret tip, the fiber jet is stable, although as it travels to the collector a bending instability stage occurs, further stretching the polymer jet under electrostatic force as the solvent evaporates. The fiber solution is drawn until there is no more feed solution. Although electrospinning is a straightforward process, many processing parameters need to be optimized, ranging from polymer solution properties to environmental parameters. A basic electrospinning set-up is shown in **Figure 2.3**, including necessary processing parameters for consideration.

2.5.2. 3D Porous Scaffolds

Dimensionality of the culture microenvironment has a profound influence on cell–cell interactions and nutrient access [90, 91]. Capturing the 3D morphology and stimuli in the native tissue microenvironment is nontrivial, where cell function is closely related to cell–cell and cell–ECM interactions. In 3D tissue systems, nutrient and oxygen gradients regulate tissue formation. Flat monolayer culture and 2D culture systems cannot accurately recapitulate the complex interplay in 3D cell-cell and cell-ECM interactions and therefore are not truly representative of the 3D tissue microenvironment. Instead, porous polymer scaffolds with large surface areas for cell adhesion can be used

Porous scaffolds are widely used in TE applications and can be manufactured using a variety of different techniques (i.e., particle leaching, emulsion, gas foaming, rapid prototyping) [99]. Despite a variety of fabrication techniques, thermally induced phase separation (TIPS) remains the most common technique for porous scaffold fabrication as it is cost effective, versatile, and tunable. Further, integration of bioactive cues and growth factors can enhance the effectiveness of these scaffolds with applications ranging from cartilage, skeletal muscle, or bone repair to cancer tumor modeling.

2.5.2.1. Thermally Induced Phase Separations (TIPS)

In the 1980s, Aubert and Clough utilized thermally induced phase separations (TIPS) to fabricate a microporous polystyrene foam [100]. Since then, TIPS has emerged as a dominant fabrication technique for TE scaffolds, foams, and membranes due to the resulting highly porous architecture. The mechanism of TIPS is liquid-liquid demixing where removal of thermal energy separates a homogenous solution into a polymer-rich and a polymer-lean phase. Subsequent lyophilization, sublimates the polymer-lean solvent phase, leaving a highly porous architecture. The thermodynamics of the phase separation play a crucial role in determining the final pore structure. Pore characteristics are highly dependent on whether the mode of phase separation is binodal demixing, spinodal decomposition, or a combination of both (**Figure 2.4**) [101, 102]. If the quenching endpoint is in the metastable region between binodal and spinodal curves, binodal demixing will occur resulting in a poorly interconnected bead-like pore structure. Conversely, when quenching occurs in the unstable region below the spinodal curve, spinodal decomposition occurs resulting in highly interconnected spheroidal domains [103, 104]. Spinodal decomposition is generally preferred for TE applications as the interconnected open-porous structure supports cell infiltration and diffusion of nutrients and waste. Varying the polymer concentration, solvent, cooling rate, surfactants, and final temperature can influence the phase separation path and final porous scaffold properties [105]. Further, the addition of an annealing step can enlarge the pore size formed under either mechanism [104].

Briefly, fabrication of a porous material via TIPS first requires dissolution of the polymer in a solvent. Aqueous solvents are preferred for biomedical application to prevent subsequent toxicity that can result from some organic solvents. The polymer solution is then transferred to a mold of the desired shape. A temperature drop is then introduced, freezing the solution. As the solution solidifies, mass transfer and heat transfer occur simultaneously as ice crystals form and separate from the polymer-rich phase. Once frozen, lyophilization occurs, sublimating the ice crystals and yielding a porous polymer foam. Controlling key aspects of the TIPS process such as polymer concentration, freezing temperature, and thermal gradients, makes it possible to fabricate scaffolds with a range of pore sizes, shapes, and morphologies form to suit a variety of tissue systems [101].

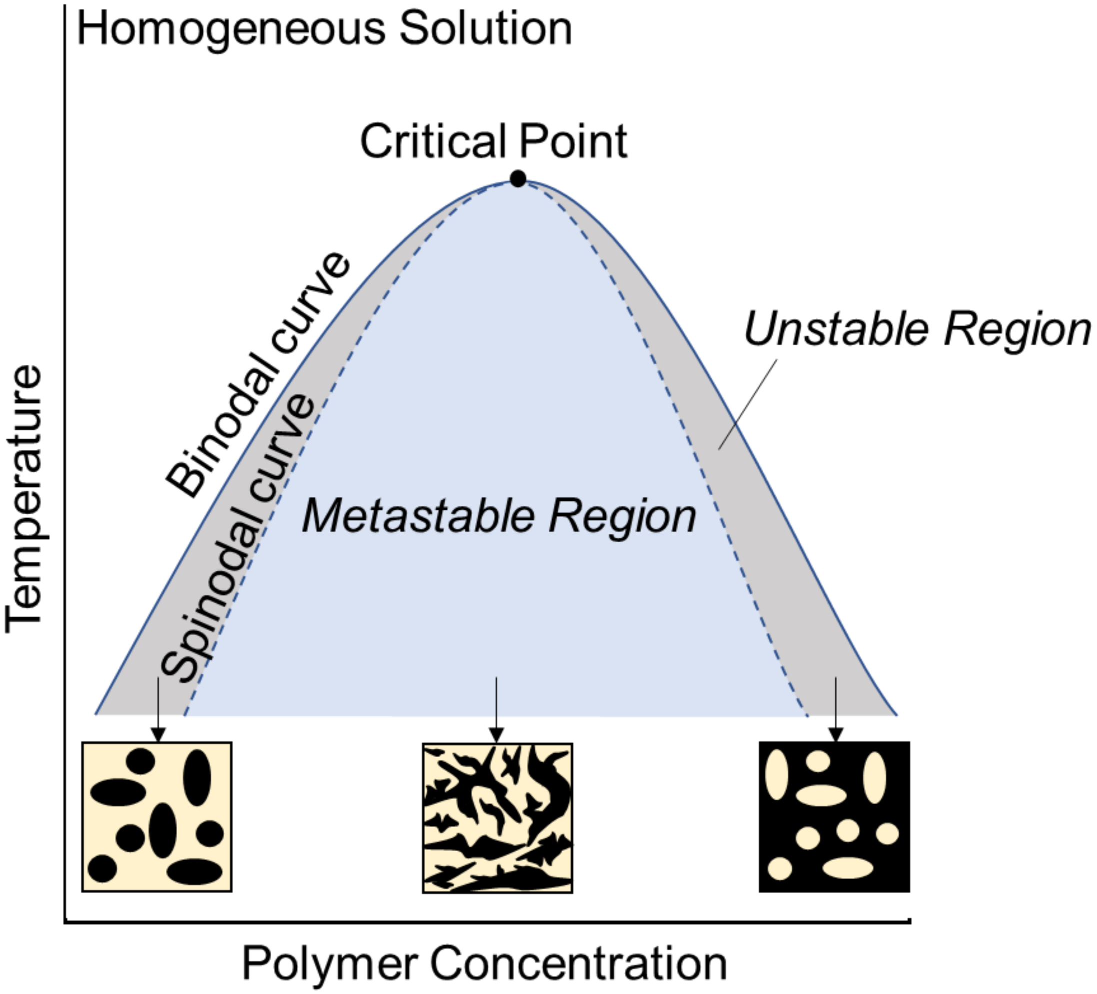

Figure 2.4. Schematic of binary phase diagram of a polymer solution highlighting potential morphologies dependent on quench endpoint resulting from thermally induced phase separations. Figure adapted from [103, 104].

Chapter 3: SCAFFOLDS FOR CANCER RESEARCH

3.1. CANCER BACKGROUND

In the United States, cancer is the second leading cause of death with approximately 38.4% of people experiencing a cancer diagnosis during their lifetime. Nationally, the expenditure for cancer care was $147.3 billion in 2017 with projected increases in healthcare costs due to the adoption of new and more expensive therapies and treatments [106]. The plethora of drug discovery and drug delivery research has resulted in new and innovative treatments leading to earlier diagnosis and more targeted therapies. However, the underlying mechanisms of tumor initiation, proliferation, and metastasis are not well understood resulting, in a high failure rate of targeted therapeutics after costly clinical trials.

Cancer is characterized by the unchecked proliferation and metastasis of cells [107]. Due to activation of oncogenes and deactivation of tumor suppressor genes, the cell cycle progresses uncontrolled with deactivation of apoptosis (highly regulated cell death process). Progression from benign tumors to malignant tumors occur upon metastasis, where cells down regulate tissue-specific adhesion receptors and up-regulate cell motility receptors [108].

While drug development and new therapeutic techniques have aided in early diagnosis and more targeted therapies, the mechanisms of tumor initiation are not well understood. Drugs targeting specific characteristics of tumor progression show promise but are hindered by the lack of a biologically relevant *in vitro* drug screening model. Currently, most of the 175 FDA-approved anti-cancer drugs target DNA replication and repair pathways (e.g., alkylating agents, anti-metabolics, anthracyclines, topoisomerase inhibitors, or mitotic inhibitors) [109]. Several anti-angiogenic targeted drugs are also approved [110]. However, no approved drugs target cell–ECM interaction, despite mounting evidence that the ECM may be key to malignancy [111].

Additionally, the specific pathways for cell–ECM interactions are not fully recognized due to the challenging nature of studying native cell–ECM behavior. Development of a drug screening model that better captures the complex cell–cell and cell–ECM interactions could provide a better model for drug effectiveness *in vivo*. Moreover, a biologically relevant model capable of recapitulating the local tumor microenvironment may help provide insight into the complex tumor stroma, highlighting potential future pathways for targeted interventions. Therefore, a preclinical disease model for both pharmaceutical testing and biological research and assay development is necessary.

3.2. TISSUE ENGINEERING AND CANCER RESEARCH

Communication between cells and the local ECM regulate both tissue homeostasis and tumor progression where the tumor microenvironment has been implicated in regulation of cancer initiation, progression, and patient prognosis [111]. Advancements in our understanding of the tumor microenvironment have added complexity to the tumor stroma. Initial models of tumor microenvironments assumed only one cell type was responsible for cancer progression, yet recent advancements have proven that tumor complexity is the result of a heterogenous cell population. A complex array of cancer cells, cancer stem cells, immune cells, cancer-associated fibroblasts, and others plus a variety of activation sites, and the ECM composition, all play a role in cancer metastasis [111].

For decades, tissue engineers have designed scaffolds to study signaling and cell behavior in a diverse array of tissues by creating a biological template that suits the unique needs of various ECMs [8]. In the context of tissue regeneration, research has been driven by the need for increasingly complex, yet tunable biomaterials that reliably mimic the ECM of specific tissues/organs. These materials require consideration and optimization of the mechanical stiffness, biocompatibility, 3D architecture, structural organization, and cell adhesion characteristics of the scaffold. Through studying the influence of the cell–ECM interaction, the constant state of dynamic reciprocity in tissue became apparent where tissue organization is maintained through a complex array of signaling factors and remodeling between cells and the ECM [111]. Cells respond to and tune the microenvironment to suit their needs, so tissue engineers aim to harness the cells to be their own "tissue engineers" via cell–cell, cell–ECM, and signaling interactions. Recently, the TE approach has been extended to provide a better understanding of the pathophysiology of cancer. In cancer research, the application of scaffolds for tumor modeling and drug screening has proven successful, yet not integrated into a clinical setting.

Recent studies have illuminated the link between the tumor microenvironment and cancer cell behavior, including promotion of drug resistance and tumor recurrence [111]. As the understanding of tissue regeneration and disease progression has expanded, the insufficiency of modeling cell behavior in a 2D monolayer culture has become apparent as not representative of the microenvironment. Much like tissue engineering, the study of cell dynamics and tumor progression in 2D monolayer culture does not supply an accurate model of the progression of cancer and is unable to model the cell–ECM relationship. Using TE strategies to unravel the influence of the microenvironment on cell behavior may provide further insight into the pathology of cancer.

3.3. BIOMATERIALS IN THE TUMOR MICROENVIRONMENT

The tumor microenvironment has been implicated in the formation, metastasis, and progression of cancer [111]. The use of a monolayer culture for cell expansion in TE applications decreased native-like gene expression and cell behavior, even when cultured back into a 3D microenvironment. Additionally, cancer researchers have found 2D monolayer culture to be an insufficient model of the tumor microenvironment. The role of the microenvironment in the regulation of cancer progression is apparent, as each unique cancerous tissue displays unique oncogenic mutations allowing manifestation only in specific tissues/regions of the body [112]. Cancer cells take cues from the microenvironment, adapting and modifying it through secretion of enzymes to facilitate the proliferation and invasion, while the physical characteristics of the ECM (e.g., stiffness, topography, ligand presentation) influence cell behavior [78]. Cancer cells grown in 3D cultures display different morphologies, gene expression profiles, proliferation profiles, and drug resistance compared to cells cultured in 2D monolayer culture. To date, the most promising cancer tumor models involve 3D culture, yet 2D cultures are still advantageous for investigation of some underlying cancer mechanisms. Recapitulating the tumor microenvironment using an *in vitro* scaffold requires consideration of several key factors, with several articles providing a comprehensive review of these factors [111]. Here, a subset of these key factors are summarized.

3.3.1. Stiffness

Cancerous tissues are generally stiffer than healthy tissues [113-115]. Scaffolds capable of encompassing the stiffness range from healthy to cancerous tissue offer an advantage in studying specific mechanosensitive pathways and cell behaviors [61, 116]. ECM stiffness influences cell migration, adhesion, proliferation, and differentiation [117, 118]. Various factors cause the increased stiffness of the tumor microenvironment, including fibrosis [119, 120] and increased interstitial pressure due to a chaotic microvasculature [121].

The influence of stiffness on cancer cell behavior can be studied through tunable biomaterials with a range of stiffness. Porous 3D scaffolds composed of chitosan-hyaluronic acid have been adjusted using polymer content to encompass the stiffness range of healthy and cancerous brain tissue [61]. Higher stiffness scaffolds resulted in larger tumor sphere formation and an increase in drug resistance [61]. The stiffness of collagen gels can be tailored by varying agarose content [122] or collagen fiber content [123]. Many synthetic gels are tunable through adjustment of crosslinker to monomer [124] or curing agent ratios [125]. Synthetic polymers, however, are less biomimetic than natural polymer and thus natural polymers are preferred.

3.3.2. Ligand Accessibility

Nano-scale variation in ligand densities influenced cell adhesion [34, 93]. Protein composition of the tissue-specific ECM regulate a range of cell behaviors from adhesion to viability [126]. ECM composition and upregulation of ECM proteins [127] are closely correlated to tumor grade where cells remodel the ECM to enhance drug resistance [128]. Techniques capable of precise control over ligand composition and spacing provide insight into focal adhesions and chemoresistance [129]. However, we can also infer the influence of ligands on cell behavior through the variation of ECM proteins. Exposure to laminin or fibronectin has resulted in a more invasive cell phenotype [130] and altered cell stiffness, illustrating the role of biochemistry in cell malignancy.

3.3.3. Topography

The local ECM is composed of oriented fibrils and supramolecular structural patterns [131]. These fibrous structures provide guidance for cancer cell migration and metastasis. Aligned or radially oriented nanofibers capture some of the topographical cues cancer cells encounter in the tumor microenvironment. When cultured on aligned versus random nanofibers, cancer cells migrate farther and faster, exhibit a more elongated invasive phenotype, and are more resistant to chemotherapeutic-induced cell death [52]. Another variation of topography includes pore size, whether between nanofibers or in a porous 3D polymer foam. When cancer cells were cultured on a matrix with a pore size smaller than the cell body, upregulation of genes responsible for ECM degradation were triggered to allow cell penetration and migration [132].

3.3.4. Dimensionality

Cancer cells express different phenotypes when cultured in 2D versus 3D microenvironments. In 3D culture, malignant cells can be distinguished due to their propensity to grow rapidly and invade the surrounding microenvironment [133]. Variations in 3D culture have even led to *in vitro* prediction of malignancy potential [134]. Models of 3D tumorigenesis *in vitro* have helped to better characterize early tumor architecture where metastatic events and relevant gene expression profiles can be directly recapitulated, resulting in tumor behavior more akin to in *vivo* and providing a model for screening cell-drug outcomes.

Although 3D tumor models express more biologically relevant cell behavior relative to 2D monolayer culture, most *in vitro* cancer experiments are still conducted on featureless 2D monolayer polystyrene plates. Adding topographical cues to the 2D platform, like seen in electrospun nanofibrous substrates, enhances biological relevance, providing a better model for studying certain cancer cell behaviors like motility and invasion [111]. Cancer cell invasion along the white matter tracts in the brain or collagen fibrous tissue in the breast is closely mimicked by nanofibrous substrates.

The interplay between the tumor microenvironment and cell behavior is not well understood, yet microenvironment characteristics influence malignancy. The immensely complex array of chemical and mechanical cues in tumor ECM make it difficult to evaluate key factors for targeted therapeutics. A biologically relevant tumor model tailored to tissue-specific microenvironments could aid in development of appropriate targets and more effective drugs. Further, a model that truly recapitulates the complexity and heterogeneity in the cancer cell population may provide an enhanced platform for drug screening, decreasing the time and cost of clinical development and personalizing drug cocktails to each unique tumor.

Chapter 4: ELECTROSPUN NANOFIBER-BASED DRUG DELIVERY AND DRUG SCREENING PLATFORMS FOR GLIOBLASTOMA

4.1. ABSTRACT

Glioblastoma multiforme (GBM) is a highly invasive primary brain tumor with a poor patient prognosis and is characterized by aggressive infiltrative growth blurring the boundary between tumorous and healthy brain tissue. The lethality of glioblastoma multiforme (GBM) is largely attributed tumor invasion and recurrence. Metastasis coupled with the physiological challenges of delivering adequate concentrations of chemotherapeutics to the tumor site remain key obstacles to effective GBM treatments. Development of a robust *in vitro* tumor model for investigation of underlying tumor progression mechanisms and advancement of anti-metastatic therapies could drastically improve patient outcomes. Additionally, development of a platform capable of sustained, long-term, and local drug delivery to the tumor site could greatly increase the effectiveness of current treatments. Electrospun nanofibers represent a promising multi-faceted approach for both targeted drug discovery and sustained drug delivery. Nanofibers mimicking the native tumor stroma have led to a deeper understanding of metastatic cell characteristics and cell-extracellular matrix (ECM) interactions. Additionally, the high surface area of the nanofibers provides a valuable tool for sustained, consistent delivery for a range of therapeutics. This review first investigates the utility of nanofibers as a substrate for enrichment of a migratory GBM cell phenotype. Next, the potential of nanofibers as potential delivery vectors is discussed. Finally, the obstacles, as well as, the emerging future applications for nanofiber substrates in GBM therapeutics will be highlighted.

4.2. INTRODUCTION

Glioblastoma multiforme (GBM) is one of the most common and lethal types of brain cancer [135]. GBM tumors aggressively infiltrate healthy brain tissue making differentiation of the tumor margins nontrivial. The contemporary standard of care employs maximal safe tumor resection followed by radiotherapy and adjuvant chemotherapy [135, 136], yet local recurrence within 2 cm of the original tumor site generally occurs 6 - 9 months after primary treatment [137, 138]. The prevalence of tumor recurrence coupled with the restriction of systemic drug delivery by the tight capillary junctions in the blood brain barrier (BBB) [139] render current therapeutic approaches ineffective and largely palliative. A plethora of research into molecular targets and drug delivery approaches has resulted in new and innovative cancer treatments leading to earlier diagnosis and more targeted therapies. However, the underlying mechanisms of tumor initiation, proliferation, and metastasis are not well understood resulting in a lack of clinical translation and high drug failure rates after costly clinical trials.

Over the last several decades, nanomaterials have been critical to the advancement of regenerative medicine by playing a role in controlled drug delivery and drug release, regulation and guidance of cell behavior, and mimicking the local microenvironment for *ex vivo* modeling of complex tissue systems. Recently, nanomaterials have emerged as a promising approach to targeted cancer therapies [140]. providing unprecedented manipulation and control of cell behavior at the nanoscale. Mounting evidence has revealed that nanomaterials not only passively interact with cells, but also actively engage to mediate cellular functions and molecular processes [141]. Specifically, nano-scale fibers with diameter ranging from tens to hundreds of nanometers have become a staple of biomedical research, finding utility ranging from regenerative medicine, to diagnostics, to drug and gene delivery.

The fibrous morphology of nanofibers mimic the native extracellular matrix (ECM) resulting in unique cell-matrix signaling capable of driving cell behaviors including migration, proliferation, and differentiation [142]. The local GBM tumor stroma has been implicated in upregulation of a more migratory and invasive cell phenotype. Mimicking the local nanotopography could provide a platform for investigation of metastatic cues and development of anti-metastatic therapeutics.

Furthermore, due to the high surface area, delivery of a variety of payloads from localized fibrous meshes have proven to aid in tissue regeneration and localized drug delivery [143]. Recently, the benefits exhibited by nanofibers in tissue engineering applications have been applied to cancer research. Tunability of the diameter, composition, length, and surface functionalization have allow drug release rates to be optimized to specific tissue-systems and drug payloads.

In this review, the current applications of electrospun nanofiber substrates are examined as both *in vitro* brain tumor microenvironment mimics and drug delivery vectors for treatment of GBM. Recent advancements in nanofiber substrates for modeling the brain tumor stroma towards enrichment of a more migratory GBM cell phenotype are evaluated for use as a platform for anti-metastatic drug screening and tumor progression monitoring. The integration of therapeutic agents into these fibers for continued therapy is evaluated as a potential local drug delivery tool. Finally, an overview of emerging technologies and barriers to nanofiber translation in a clinical setting are discussed.

4.3. ELECTROSPINNING AND NANOFIBERS

Electrospinning is a highly tunable and facile nanofiber fabrication technique capable of tight control of the fiber morphology and topography [94]. Electrospinning remains dominant over other nanofiber fabrication techniques (e.g. drawing [144], dry spinning [145-147], phase separation [148], vapor phase polymerization [149], self-assembly [150], and template directed synthesis [151]) due to the inexpensive experimental set up and high production rate [94]. The high specific surface area and ability to align nanofibers have proven advantageous in a wide range of applications from energy storage [152, 153] and liquid filtration [154] to drug delivery [155, 156] and tissue engineering [157].

Electrospinning is a simple and straightforward process [94, 158]. First, a polymer solution is passed through a spinneret where a high voltage is applied to charge the solution. At a critical voltage, the electrostatic forces overcome the surface tension of the solution and the Taylor cone is formed ejecting a charged polymer jet from the spinneret tip. The charged jet is then subject to bending instability as the solvent evaporates, and nanofiber morphology solidifies before being deposited layer-by-layer on a grounded collector.

The tunability and versatility of the produced fibers is an advantage of the electrospinning technique [94]. By adjusting solution and processing parameters, fibers ranging from tens of nanometers to microns can be obtained. Additionally, most soluble polymers with high molecular weights can be electrospun resulting in a wide range of possible nanofiber compositions for investigation of tailored surface chemistry (i.e. natural polymers, synthetic polymers, polymer blends, and composites) [94]. Further, a variety of morphologies can also be attained (i.e., core and shell, hollow tube, porous, and beaded) to customize surface area, topography, degradation, or payload release kinetics. Through exploitation of the electric field or mechanical manipulation, fiber alignment as well as woven, interlaced, tubular, radial fiber formation can be achieved. This versatility allows for nanofibers to be integrated in a wide range of diverse applications.

4.4. NANOFIBERS FOR GBM MICROENVIRONMENT MODELING AND DRUG SCREENING

GBM lethality is generally attributed to the diffuse invasion of highly migratory single cells away from the primary tumor along white matter tracts and abluminal blood vessels surfaces [159, 160]. Disperse invasion limits the effectiveness of resection resulting in subsequent secondary tumors formation. Unlike other cancer, gliomas rarely metastasize extracranially, but can move large distances within the brain. Further, despite similar biochemical compositions, tumor cells are generally found in the fibrous white matter versus the gray matter in the brain. These findings imply that the implicate the local white matter topography in upregulation of a more migratory cell phenotype and suggests that the local tumor microenvironment plays a dominant role in GBM progression by regulating cell motility and secondary tumor initiation [161].

Traditional *in vitro* culture studied cancer motility and drug resistance on flat, featureless tissue culture polystyrene (TCPS) surfaces. These 2D adherent monolayer cultures were quantitative and informative, yet did not truly capture structural, chemical, and mechanical cues of the tumor microenvironment resulting in motility, morphology, and gene expression profiles dissimilar from those found in native brain tumors [161, 162]. To enhance biological relevancy, organotypic brain slice assays are also frequently used for migration studies to capture the structural cues in native brain, This culture allows study of cell interactions with real structures found in the brain like neurites and blood vessels to observe cell behavioral changes in different parts of the brain like the cortex, white matter, and basal ganglia [163]. However, this assay is laborious to produce, difficult to reproduce, and tissue necrosis occurs days into culture thereby potentially influencing cell behavior and migratory patterns. These early models have provided insight into the complex tissue microenvironment and have led to a decisive shift away from monolayer and organotypic culture to more biologically relevant, reproducible biomaterial platforms that more accurate mimic the structure of the native 3D tumor niche [164].

Electrospun nanofibers present a significant advantage over conventional 2D monolayer culture as the fibrous topography mimics the native white matter tracts in the brain ECM [165, 166]. Further, Nanofibers also present an improvement over organotypic brain slice assays due to the reproducibility and robustness. Nanofibers can be chemically and physically tuned to study a variety of topographic cues – providing a valuable tool to study motility in neural-like structures with the potential to become the basis for tailored bioassays of tumor biopsies. Nanofibers advance a realistic *in vitro* system for simulating tumor migration while maintaining compatibility with downstream assays like western blotting, immunostaining, live cell imaging, and RT-PCR. Due to the high surface area for cell adherence, highly reproducible fabrication techniques, and high degree of tunability (i.e. diameter, composition, morphology, surface functionalization), nanofibers present a promising alternative to current assays. Electrospun nanofiber substrates resemble the fibrous white matter tracts and could be used to study anti-invasion therapies especially when aligned nanofibers have been shown to mimic the topographical cues encountered by migratory cells in the tumor stroma.

Biomaterial scaffolds mimicking the physicochemical cues within the tumor microenvironment may play a key role in highlighting the cell-intrinsic pathways of disease progression. Limiting the metastatic potential of GBM can then convert it to a focal disease capable of being treated with more effective focal therapies [161]. To do so however, a more detailed understanding of glioma invasion mechanisms is necessary. A platform that truly mimics the tumor stroma may provide a basis a high throughput testing platform for development and screening of potential anti-invasion therapies [167].

Several excellent reviews of the electrospinning fabrication process have been conducted [94, 95, 98], highlighting collector configurations, processing parameters, and a diverse array of nanofiber applications. Variations of nanofiber characteristics like alignment, fiber spacing, diameter, mechanical stiffness, fiber roughness and surface chemistry influence cell behavior. Here, we focus on the influence of those cues on GBM cell behavior with a focus on motility.

4.4.1. Influence of alignment

Nanofiber alignment is a key consideration when developing a brain tumor microenvironment model. White matter tracts and blood vessels run parallel in the human brain, presenting an aligned pathway for cell invasion. Directional topography influences cell polarity inducing a single, leading extension for directional and persistent migration. Conversely, loss of cell polarity results in a broad ruffled leading edge as seen in randomly oriented fibroblast-like cell motion [163]. Mimicking the anisotropy in the fibrous matrix may be key to upregulation of a more migratory GBM phenotype capable of invasion into healthy brain tissue.

Human GBM cells (U251) cultured on polycaprolactone (PCL) nanofibers, exhibit different morphology and motility characteristics aligned nanofibers (**Figure 4.1a and b**) relative to randomly oriented nanofibers (**Figure 4.1c and d**) [165]. Cells cultured on aligned nanofibers displayed an elongated spindle-like morphology (average cell length of 32 µm) and cell motion along the fiber axis. Conversely, on random nanofibers, GBM cells display a rounded, spherical morphology (average cell diameter of 15 µm) with no preferential extension direction and hindered cell motion due to cell oscillations at nanofiber intersections. Persistent and directional motion along the fiber axis resulted in a five-fold increase in displacement on aligned nanofibers relative to random nanofibers [165]. Mitosis and slight defects in alignment had the greatest influence on motility. Small imperfections in alignment, including defects as small as misalignments of 20°, halted cell motion and highlighted the importance of defect-free nanofiber topography. Morphology differences on random versus aligned fibers correlate with cell morphologies seen in noninvasive (rounded) versus infiltrating (elongated) glioma cells *in vivo* [163]. Previous works studying neural progenitor cells in the early postnatal brain have detailed a similar migration pattern to GBM on aligned nanofibers [168-170]. Additionally, in a study conducted by Agudelo-Garcia et al., the enhanced motility and elongated morphology of GBM cells cultured on aligned PCL was also accompanied by a substantial increase in expression of STAT3, a known driver of glioma progression [171].

Despite the lack of specific ECM molecular signals, cell migration on PCL nanofibers closely matched that *in vivo*, suggesting that the topography alone in white matter versus gray matter could direct cell migration [165]. Enhanced motility on aligned nanofibers relative to random nanofibers was mirrored in experiments conducted on chitosan-polycaprolactone (C-PCL) nanofibers with U87 MG human GBM cells [166]. It has been postulated that the topography of the white matter may act as a pathway of least resistance even when lacking the preferred cell adhesion molecules [172].

Neurospheres offer an enhanced biologically relevant view of cell dispersion from the primary tumor due to the presence of gradients potentially leading to cell population heterogeneity like seen in the native tumor microenvironment [173, 174]. Investigating the influence of topography on cell migration away from the primary tumor, 3D neurospheres were cultured on random and aligned nanofibers (**Figure 4.1e and f**) [165]. On aligned nanofibers, GBM cells dispersed and migrated away from the neurosphere (**Figure 4.1e**). Cell dispersion along the nanofibers was 6-fold greater than across the nanofibers, showing the influence of alignment. In **Figure 4.1f**, GBM cells on random nanofibers did not detach from the neurosphere and instead the neurosphere retained size and shape over 20 hours [165]. Since tumor recurrence is frequently attributed to glioma stem cells, studying of tumor initiating cells is crucial. Neurosphere culture elucidates the amenability of aligned nanofibrous platforms for screening and study of patient biopsies or biopsy-derived cells to quantify migratory capacity. Thus, effective drug cocktails combinations could be identified through direct quantificatios.

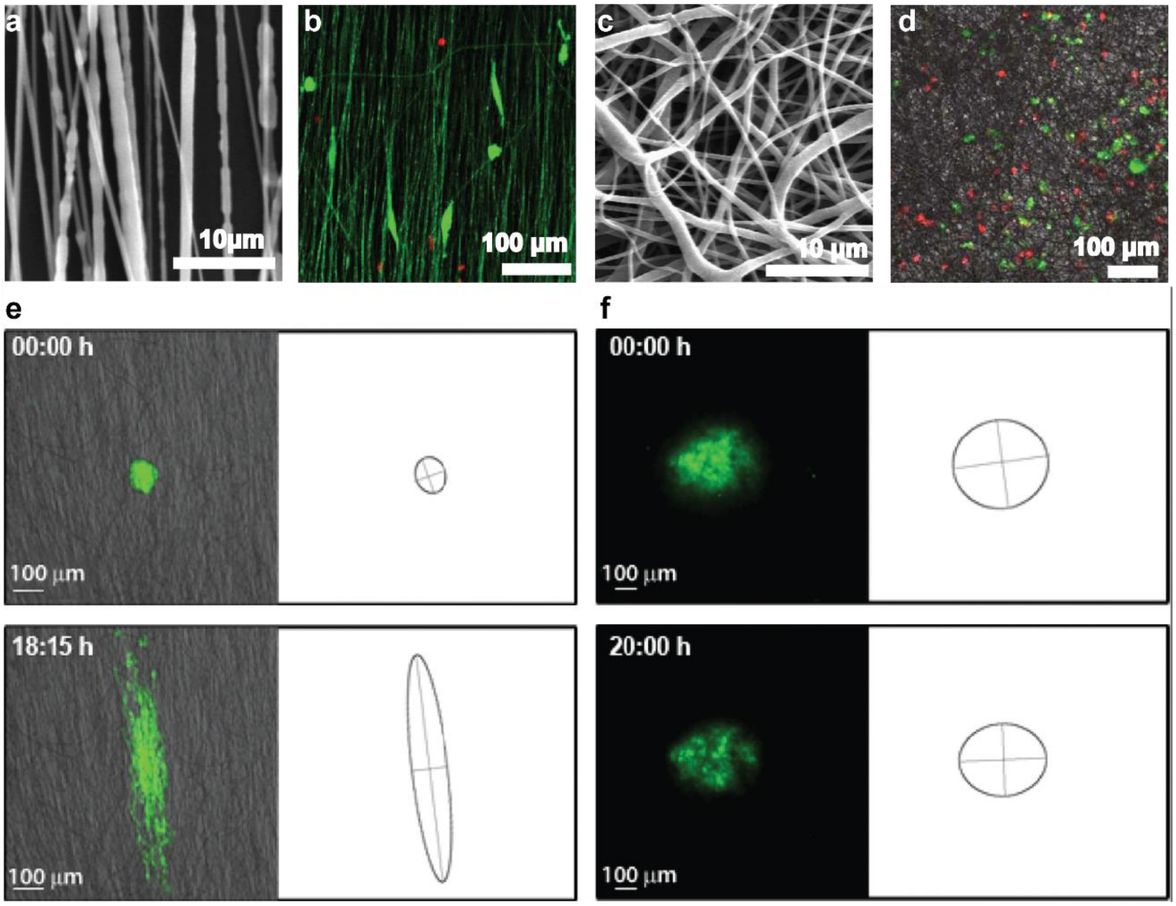

Figure 4.1. Aligned versus random PCL nanofiber morphology and corresponding GBM (U251) cell behavior. PCL nanofiber morphology imaged with a scanning electron microscope (SEM) displaying (**a**) aligned nanofibers and corresponding confocal imaging of glioma cells (U251) cultured on the aligned nanofiber substrates displaying (**b**) spindle-like elongated morphology. Cells detected by nuclear red and cytoplasmic green fluorescence merged with fibers under phase contrast illumination. Aligned nanofibers

autofluoresce and appear green. (**c**) Morphology of randomly oriented nanofibers and (**d**) corresponding confocal imaging of glioma cells (U251) expressing a rounded cell morphology. Representative confocal images of cell dispersion from neurospheres on (**e**) aligned and (**f**) random PCL nanofibers. The change in cell dispersion revealed a six-fold increase along-axis versus across-axis on aligned nanofibers. Reprinted with permission from [165].

Beliveau et al., [175] discovered that the nanofiber alignment not only influences the cell elongation and migration, but also the cytoskeletal stiffness. When comparing GBM cells cultured on aligned fibers relative to random nanofibers and smooth films, the cytoskeletal stiffness was significantly lower than in healthy astrocytes. Decreased cytoskeletal stiffness indicates that tumor cells will have a greater ability to deform the cell body and invade the surrounding ECM [175]. Further GBM cell cytoskeletons cultured on aligned nanofibers were less stiff than when the same cells were cultured on smooth films or random nanofibers. This can be attributed to the increased spatial organization of the actin cytoskeleton of elongated cells and the lack of crosslinking in parallel actin networks. Additionally, an increase in migratory genes SNAI1 and NOTCH1 and a downregulation in CDK20 and CCND1 was seen in cells cultured on aligned fibers indicating the aligned substrate may be influencing the cells into a more migratory phenotype at the arresting of the proliferative processes.

4.4.2. Influence of 1D versus 2D topography

To determine the influence of nanofiber topography on GBM motility, Estabris et al., suspended 400 nm diameter nanofibers as single and parallel fibers and compared this condition with flat 2D culture [145]. Cells moved faster and more persistently in 1D (single nanofiber or parallel nanofibers) relative to flat 2D culture. Additionally, cell migration was faster on parallel suspended nanofibers than on single nanofibers potentially due to the increased adhesion area of two fibers versus one. The influence of cell adhesion on GBM cell speed correlated with CD44-mediated migration where high and low concentrations of CD44 resulted in slower cell speeds and intermediate concentrations resulted in the fastest cell speeds. The increased adhesion area for cells spanning two parallel fibers increased the persistence of the cell motion and reduced the chance of motion in a reversed direction. These experiments indicated that cell motion on fibers can be fully explained in terms of fiber geometry and cell adhesion and does not necessarily require changes in phenotypic or molecular expression.

The influence of fiber curvature on GBM cell protrusion was studied by again using the suspended fiber model [176]. Here, high curvature round fibers were compared against low curvature flat ribbons. Protrusions on low curvature flat ribbons broaden dramatically faster relative to round fibers. Sensitivity to environmental conditions like fiber diameter and ligand concentration were explored where the protrusion dynamics indicated that MDA-MBA-231 (breast adenocarcinoma) was highly sensitivity to changes in fiber diameter whereas DBTRG-05MG (glioblastoma) was less dependent on diameter. Flat TCPS substrates could not be used to show cell-specific and sensitivity to ECM fiber diameter, displaying the utility of a nanofiber-based migration model.

4.4.3. Influence of diameter

The diameter of white matter tracts in the human brain can range from 0.2 – 9 µm and vary between patients and location within the brain, yet the majority of white matter tracts have a diameter below 1 µm [177]. By adjusting processing parameters like electrospinning solution properties, nanofiber diameters can be tuned within a range of tens of nanometers to microns (increased viscosity generally results in larger fiber diameters). Varying nanofiber diameter exposes cells to different fiber curvatures. The influence of nanofiber curvature on GBM adhesion and motility was studied by Kievit et al., on aligned chitosan-polycaprolactone (C-PCL) nanofiber mats with diameters of 200 nm, 400 nm, or 1.1 µm [166]. Regardless of nanofiber diameter, GBM cells (U87 MG) elongated and aligned along the nanofiber length (**Figure 4.2a**). GBM cell elongation appeared to increase with increasing nanofiber diameter, yet values were not statistically significant. GBM cell motility was persistent and directional across all nanofiber diameters, but GBM cells migrated the farthest and the fastest on 400 nm diameter nanofibers. Additionally, after only 24 hours of culture, GBM cells cultures on 200 nm and 400 nm aligned nanofibers overexpressed invasion-related genes b-catenin, Snail, STAT3, TGF-B, and TWIST. Asymmetric endosomal trafficking and cell division was observed suggesting the promotion of a mesenchymal transition with higher curvature nanofibers promoting enhanced migratory behavior (**Figure 4.2b**). This effect at an early timepoint is promising for drug screening applications where a long culture time is not required to enrich for a more migratory cell.

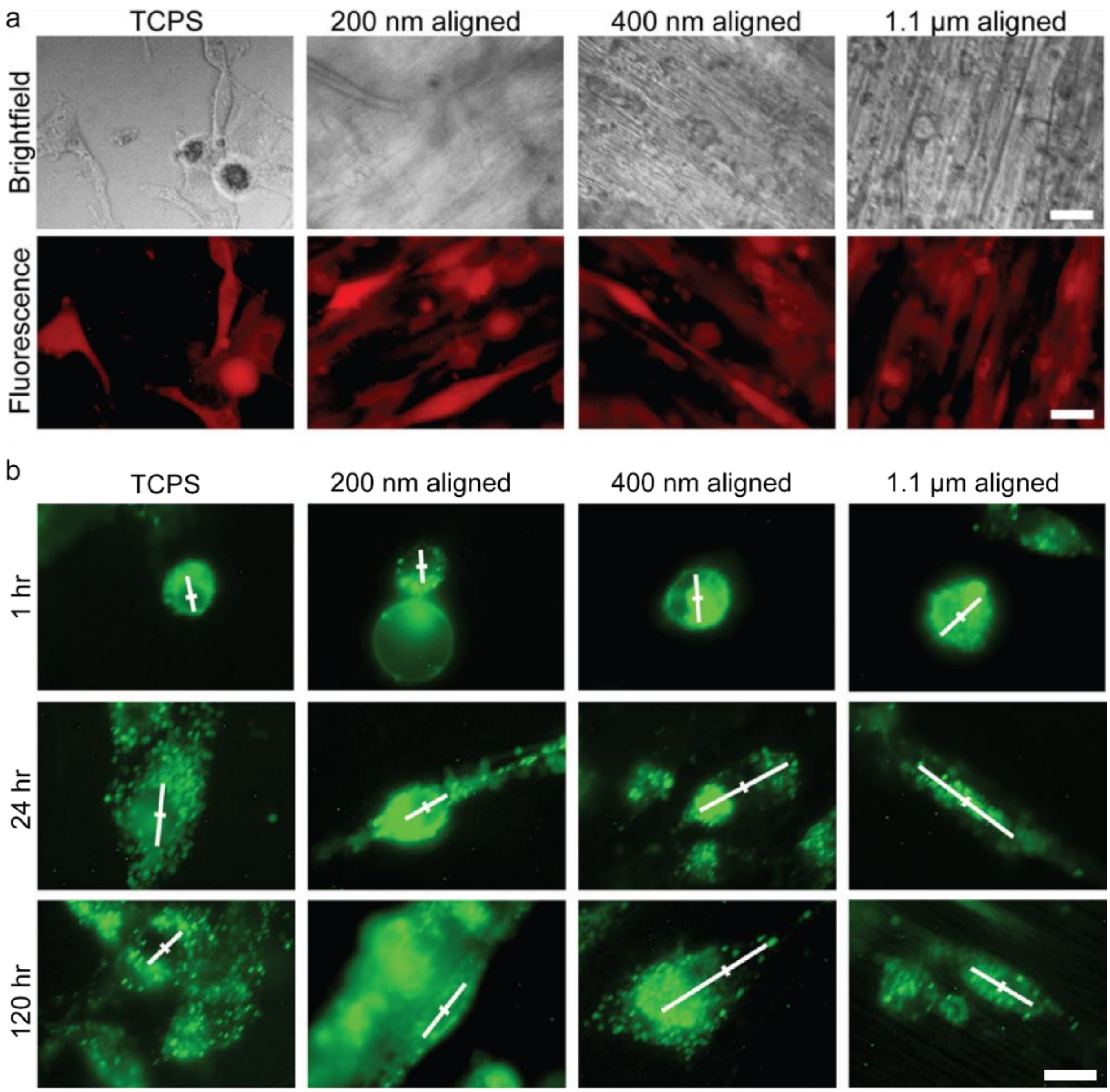

Figure 4.2. GBM cells (U-87 MG) cultured on 2D monolayer TCPS and aligned chitosan-PCL (C-PCL) nanofibers with a range of diameters for 120 hours. (**a**) GBM cells were RFP transfected (red) and viewed under brightfield (top panel) and fluorescence imaging (bottom panel). Cells on TCPS displayed no directionality. On all aligned nanofiber substrates, cells elongated along the length of the fibers. Scale bar represents 20 μm. (**b**) GBM cells with DiO-stained membranes immediately after seeding on TCPS and aligned C-PCL nanofibers with various diameters. White lines indicate endosomal distribution

where the center of the cell is marked with a perpendicular line for reference. Scale bar represents 10 µm. Reprinted with permission from [166].

4.4.4. Influence of stiffness

Stiffness gradients in the tumor microenvironment are key contributing factor in cancer progression and metastasis. To investigate the influence of stiffness on GBM cell motility, Rao et al., utilized core and shell nanofibers where a consistent shell material, in this case PCL, presented a consistent surface chemistry for cell attachment (**Figure 4.3**) [178]. By varying the core material of the nanofiber, the elastic modulus could be varied from low stiffness (2 MPa in PCL-gelatin) to medium (8 MPa in PCL) to high stiffness (29 MPa in poly(ehersulfone) (PES)-PCL and 33 MPa in polydimethylsiloxane (PDMS) -PCL). Peak migration speed was observed on the nanofibers with an intermediate elastic modulus (8 MPa in PCL nanofibers). Cells cultured on nanofibers with a higher and lower modulus displayed slower migration speeds with the softest nanofibers promoting the slowest migration. Slow migration speeds on softer substrates have been reported previously as the result of lowered resistance to cell-generated traction forces. The gene expression was also correlated to elastic modulus with decreased expression of FAK and MCL2 in the softest substrate (PCL-gelatin) [178, 179]. Increased expression of FAK and MLC2 have been implicated in glioma migration [161].

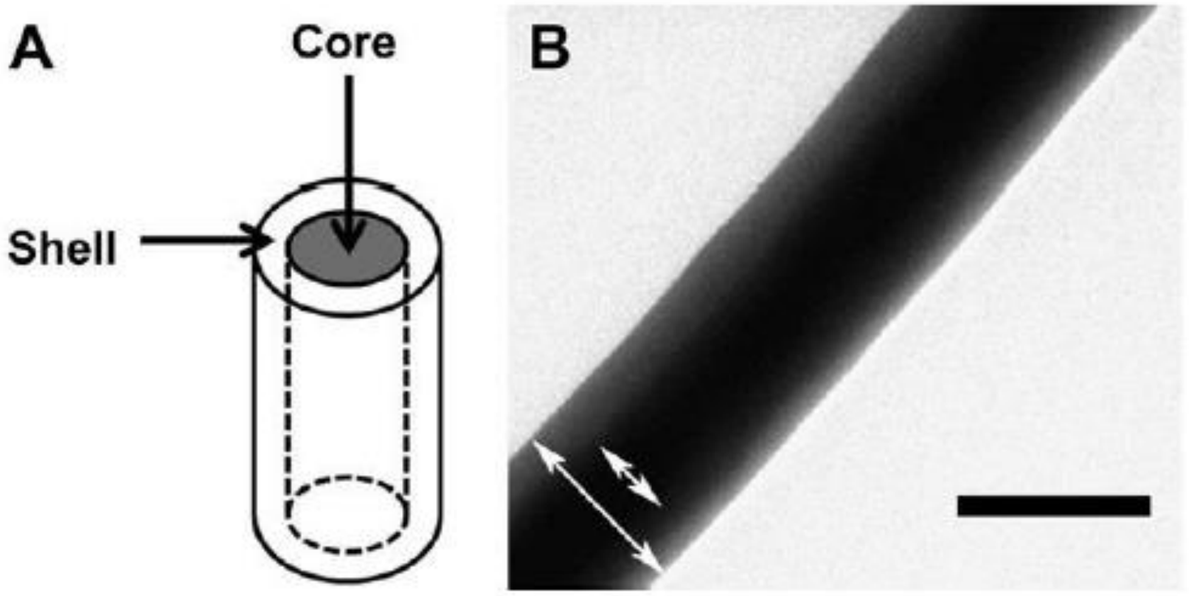

Figure 4.3. Core and shell nanofiber with PDMS core and PCL shell. (**a**) Schematic and (**b**) transmission electron microscopy (TEM) image of core-shell configuration. Scale bar represents 0.2 µm. Reprinted with permission from [178].

4.4.5. Influence of surface chemistry

Surface chemistry influences cell adhesion and is a key factor in cell motility. Using core and shell electrospinning, Rao et al., produced nanofibers with a consistent core material (in this case PCL) to maintain a consistent stiffness. Nanofiber surface chemistry was varied by changing the composition of the nanofiber shell to either collagen, hyaluronic acid (HA), or Matrigel. Cell attachment and migration on all nanofibers was similar, except on HA fibers, where a decreased cell number of adherent cells and slower cell migration was observed. This result contrasts observations where HA was migration-inducing when used as a soluble factor or incorporated with other ECM components [180, 181]. HA, a major component of the brain ECM has been shown to both favorably [182] and adversely[178] impact cell migration. Because the coating during this experiment did not influence the motility of cells despite being known to enhance cell adhesion, Rao et al., postulated that topographical cues alone could be sufficient to support GBM cell migration [178].

4.5. NANOFIBERS FOR LOCALIZED DELIVERY

Achieving therapeutic drug concentrations for a sustained period of time at the site of a brain tumor is a major barrier in GBM treatment [183-185]. Current drug delivery approaches include intraventricular drug diffusion and disruption of the blood brain barrier (BBB). These approaches are highly invasive, restricted by the short drug circulation times and the tight cellular junctions in the BBB and ultimately are inefficacious for improved patient outcomes [186, 187]. Because tumor recurrence happens at the primary tumor margins, sustained and local drug delivery at the resected tumor site is ideal [188, 189]. Further, local drug delivery can decrease systemic toxicity of chemotherapeutics and deliver a more sustained dosage over time bypassing restrictions from the BBB [190].

Current therapeutics for controlled drug delivery include micro/nanoparticles, wafers, and discs [184, 188, 191], yet risk of the expulsion from the tumor site due to the high interstitial pressure remains a challenge. Drug diffusion from wafers/discs is nontrivial due to the low surface area and polymer degradation rates [188]. Further, both technologies struggle with systemic neurotoxicity due to the initial burst release of drugs [184, 192].

Nanofibers have merged as a promising drug delivery system due to the high surface area and extensive tunability [193]. By tailoring the microstructure, composition, encapsulation method, or dimensionality, highly controlled and sustained release is possible [194, 195]. To date, this versatility has been demonstrated through integration of antibiotics, proteins, DNA, RNA, growth factors, and living cells via a variety of incorporation techniques (e.g. blend, emulsion, surface modification, coaxial electrospinning, etc.) (**Figure 4.4**). Several reviews have outlined the full suite of drug loading techniques and payloads [143, 193, 195] but here, we focus on specifically on technologies used for GBM drug delivery.

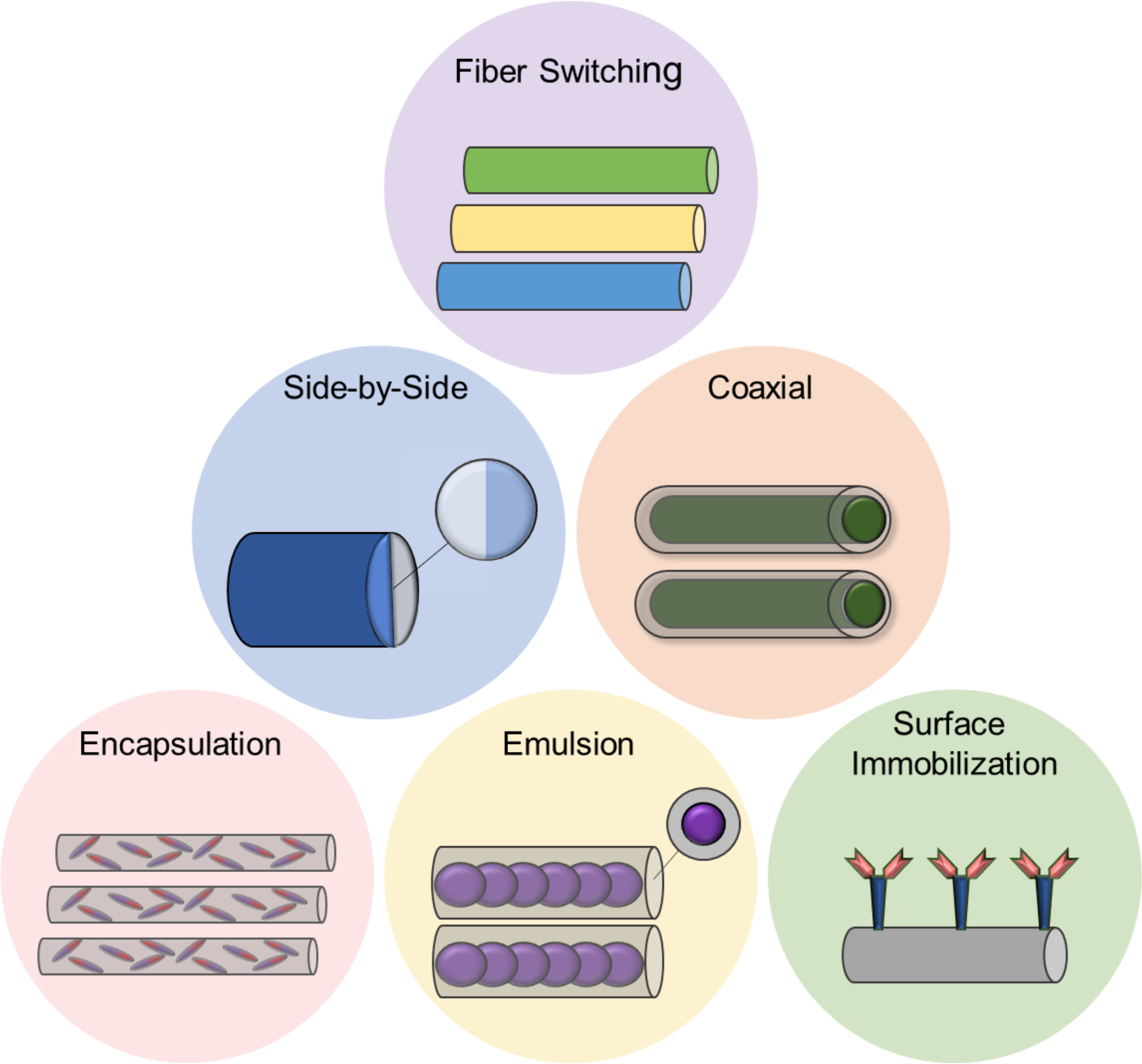

Figure 4.4. Schematic illustrating common integration methods for drug delivery using nanofibers platforms.

4.5.1. Chemotherapeutic delivery

The role of chemotherapeutics in GBM treatment has been limited with only marginal improvements for limited durations. Currently, chemotherapeutics are administered either systemically, into the cerebral spinal fluid (CNS), or locally in the tumor resection cavity. Failure of drugs administered systemically and into the CNS is largely attributed to failure to cross the blood-brain barrier (BBB) [196, 197]. A local delivery system capable of sustained therapeutic release after implantation into the tumor site would increase local exposure to the drug at the site of potential secondary tumor formation and minimize adverse reactions from systemic exposure.

Chemotherapeutics are the most common payload for drug delivery tailored to GBM. Chemotherapeutics block tumor growth and proliferation. Specifically, anti-cancer drugs like paclitaxel, temozolomide, and carmustine are most frequently integrated into nanofibers. Paclitaxel (PTX) is a mitotic inhibitor that enhances the rate of microtubule formation, increases mitotic phase arrest, decreasing cellular motility, and causing apoptosis in dividing cells [198, 199]. Because cells exposed to PTX accumulate in the G2 and M phase of the cell cycle, the drug also enhances cell radiosensitivity [200, 201]. PTX has been used *in vitro* [202, 203] and *in vivo* [199] for GBM applications with some success yet systemic administration of PTX has not resulted in greatly improved patient outcomes [204]. PTX is hydrophobic, clears the plasma quickly, and has poor absorption across the BBB and commercial form Taxol (PTX + an ionic surfactant) has been implicated in side effects including anaphylactic hypersensitivity, and neurotoxicity [188].

Temozolomide (TMZ) is a DNA alkylating agent capable of oral administration [205]. TMZ is associated with a low incidence of adverse reactions. The small molecular weight (194 Da) of the lipophilic TMZ ensures the molecule can cross the BBB. TMZ has a short 1.8 hour plasma half-life with poor stability in solutions above pH 7 [135, 206]. Encapsulation of TMZ and local delivery has been shown to be superior relative to oral administration in rodent GBM models [207].

Finally, carmustine (BCNU) is an alkylating agent that is highly lipid-soluble and capable of BBB penetration [208, 209]. BCNU inhibits DNA synthesis, RNA production, and RNA translation [210]. BCNU delivered intravenously often results in bone marrow suppression, hepatic dysfunction, and pulmonary fibrosis. The short plasma half-life of 20 minutes *in vitro* and less than 15 min *in vivo* limits the systemic application of BCNU and requires the use of a delivery vector [210, 211]. It is clear, better and more controlled delivery methods are required for improved delivery of chemotherapuetics

4.5.1.1. Influence of diameter on release rate

To study the influence of surface area and nanofiber diameter on drug release rate, PTX loaded poly(lactide-co-glycolide) (PLGA) were fabricated with submicron (50/50 PLGA nanofibers: 930 ± 35 nm) and micro-sized diameters (85/15 PLGA microfibers: 3.5 ± 0.32 mm) [188]. Both fibrous platforms exhibited sustained release over 80 days, yet due to the increased degradation rate and higher surface area of the submicron fibers, a higher release rate was observed [188]. Further, in terms of cell apoptosis, the sustained release of PTX from the fibers was superior over systemic Taxol administration. Using the sustained release nanofiber mats subcutaneously in mice with GBM tumors, up to 61% smaller tumors were seen at day 32 post-inoculation relative to Taxol-treated animals [188]. When evaluating the PTX penetration depth in microfibers versus nanofibers, PTX-loaded PLGA nanofibers displayed superior sustained penetration in mouse brain (5 mm after 42 days post-implantation) whereas the lower drug release rate of the microfibers did not penetrate as deep. Intracranially, a 30-fold increase in tumor inhibition and a lower proliferation index was exhibited in the nanofiber treated mouse models relative to placebo controls [190].

4.5.1.2. Influence of biochemistry on release rate

Fiber switching is a drug delivery mechanism where blend fibers are implanted for sustained release of a drug ranging from days to months depending on the specific degradation kinetics of the differing fibers (**Figure 4.5**) [212]. In an orthotopic rat, PLGA-PLA-PCL nanofibers loaded with TMZ were implanted and the drug release was measured at 116.6 ug/day. Compared to the release rate from administration to the peripheral blood, the nanofibers delivery platform displayed an ~1000-fold increase in the drug concentration at the tumor site. Further, after long term implantation (> 4 months), survival of 85.7% of the animals was observed coupled with no signs of tumor recurrence. These promising nanofiber results were contrasted with 1-week drug release nanofibers where tumor recurrence was prevalent in 54.6% of animals with a median survival of only 74 days [212].

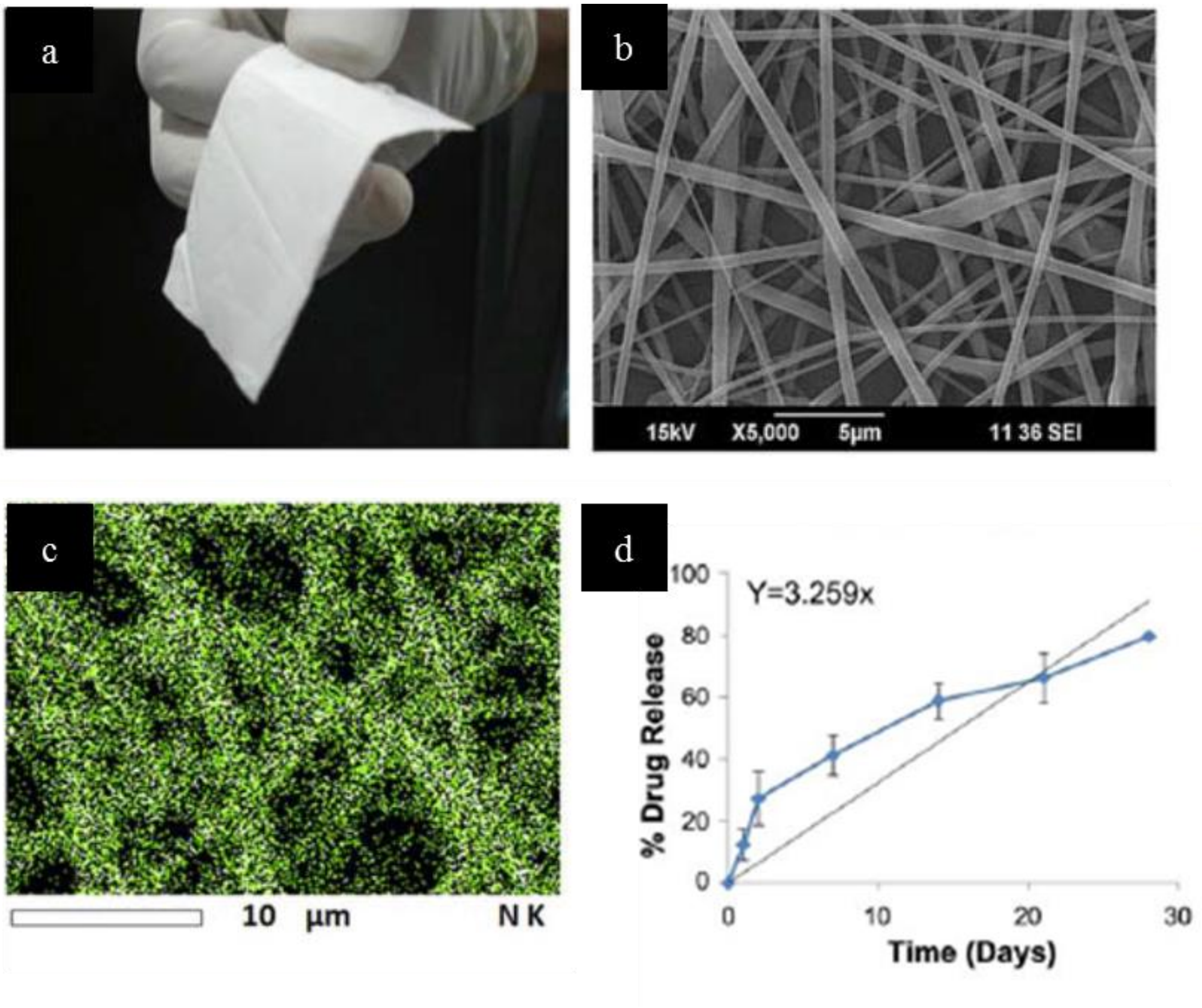

Figure 4.5. Morphology of TMZ-loaded PLGA-PLA-PCL nanofiber implant for GBM treatment. (**a**) Photograph and (**b**) SEM image of 20 wt% TMZ-loaded nanofiber implant displaying flexibility and fibrous morphology. (**c**) EDS map of TMZ integration into nanofibers exhibits uniform distribution of throughout the nanofibers. (**d**) Drug release rate of implant tested in tumor bearing rat brain over 30 days. Reprinted with permission from [212].

4.5.1.3. Influence of mat flexibility on release rate

Gliadel® is a United States Food and Drug Administration approved, commercially available, biodegradable wafer that releases BCNU upon implantation into the tumor cavity post-resection [213, 214]. Clinically, Gliadel® has increased the survival of GBM-diagnosed patients by 2 months relative to those without the treatment [186, 215]. However, rapid release and the rigidity of the wafer are major drawbacks [216]. PLGA nanofibers loaded with BCNU sustained release of high drug concentrations for up to 6 weeks when studied in cerebral cavity [187]. This technology was advantageous over Gliadel® since no immune response was elicited and the nanofibrous membranes were able to conform to the geometry of the brain tissue, resulted in improved drug transport.

4.5.2. Anti-angiogenic delivery

Angiogenesis is essential for tumor growth and invasion [217]. Chemotherapeutics do not target the angiogenetic processes of cancer. Common anti-angiogenic targets include matrix metalloproteinase-2 (MMP2), an essential proteinase for adjusting invasion and angiogenesis and mycophenolic acid (MPA), an FDA-approved immunosuppressant. An RNA plasmid expressing matrix metalloproteinase (MMP-2) was complexed with a gene carrier (PEI) and dual encapsulated with PTX in PLGA nanofibers. Sustained release of both payloads was exhibited. On intracranial xenograft tumor models, significant tumor inhibition was seen in the nanofiber condition relative to commercial PTX treatment indicating the synergistic therapeutic effect of dual gene and chemotherapeutic delivery [217]. Further when three chemotherapeutics (BCNU, irinotecan, and cisplatin) were loaded with combretastatin (an antiangiogenic agent) into PLGA nanofibers, rapid release of the chemotherapeutics was coupled with a slower sustained release of combretastatin over 2 weeks. Compared to the blood, drug concentrations were higher in brain tissue for 8 weeks. Compared to treatments without the anti-angiogenic, C6 GBM-bearing rats benefited from prolonged survival and retardation of tumor growth when treated with the combination chemotherapeutic and anti-angiogenic drugs [218].

4.5.3. Stem cell delivery

Stem cell-based therapies are an emerging approach for GBM therapy [219]. Stem cells (SC) are an ideal drug carrier vectors for active targeting in tumor cells due to the unique honing ability of SC to locate and invade the tumor. However, retention of SCs post-injection at the tumor site is a challenge [219]. PLA fibers loaded with human mesenchymal stem cells (hMSCS) capable of drug release were seeded in the surgical cavity. A 5-fold increase in hMSC retention and a 3-fold increase in prolonged persistence was seen relative to direct inject of SCs. Further, release of the anti-tumor protein TRAIL led to a 3-fold decrease in overall tumor volume, 2.3-fold inhibition of GBM foci regrowth and an increased survival time from 13.5 to 31 days in mice [219].

4.6. CONCLUSIONS AND FUTURE OUTLOOKS

Nanofibers have the potential to play an influential therapeutic role in drug screening and drug delivery application of GBM. The enhanced native-like GBM cell behavior exhibited by cells cultured on aligned fibrous platforms *in vitro* may provide a robust and reproducible platform for enrichment and investigation of a more migratory phenotype. Further, study of gene expression in this more invasion subpopulation may provide insight into potential anti-metastatic therapeutic targets. Additionally, sustained and controlled delivery from nanofiber-based platforms provide a tool for delivery of effective chemotherapeutic concentrations directly to the surgical resection site. Nanofiber-based delivery decreases systemic exposure and toxicity and improves outcomes in rat models. Further, synergistic delivery of chemotherapeutics and other biologics presents a promising approach to target metastatic tumors on multiple fronts.

Chapter 5: HIGH-THROUGHPUT AND HIGH-YIELD FABRICATION OF UNIAXIALLY ALIGNED CHITOSAN-BASED NANOFIBERS BY CENTRIFUGAL ELECTROSPINNING

5.1. ABSTRACT

The inability to produce large quantities of nanofibers has been a primary obstacle in advancement and commercialization of electrospinning technologies, especially when aligned nanofibers are desired. We present a high-throughput centrifugal electrospinning (HTP-CES) system capable of producing a large number of highly-aligned nanofiber samples with high-yield and tunable diameters. The versatility of the design was revealed when bead-less nanofibers were produced from copolymer chitosan/polycaprolactone (C-PCL) solutions despite variations in polymer blend composition or spinneret needle gauge. Compared to conventional electrospinning techniques, fibers spun with the HTP-CES not only exhibited superior alignment, but also better diameter uniformity. We quantified nanofiber alignment by using fast Fourier transform (FFT) analysis. In addition, we identified a concave correlation between the needle diameter and resultant fiber diameter. This system can be easily scaled up for industrial production of highly aligned nanofibers with tunable diameters that can potentially meet the requirements for various engineering and biomedical applications.

5.2. INTRODUCTION

Electrospinning is a versatile fabrication technique used to produce fibers with diameters on the order of tens of nanometers to microns while allowing for unprecedented control over diameter, length, alignment, and morphology. This technique has been successfully applied to produce various nanofibrous structures (i.e., beaded, ribbon, core and shell, hollow tube, and porous) using a wide range of polymers and polymeric composites [94]. Due to the inexpensive experimental set-up and superior versatility in resultant fiber composition, electrospinning remains a dominant area of research over other nanofiber fabrication methods such as drawing [144], thermally induced phase separation [148], vapor phase polymerization [149], self-assembly [150], and template directed synthesis [151]. The high surface-to-volume ratio and anisotropy of electrospun nano-scale fibers have proven advantageous in many applications including liquid filtration [154], energy storage [152, 153], drug delivery [155, 156], piezoelectric devices [220, 221], and biological wound healing [157]. Two nanofiber properties that are especially important for success in these applications are uniform diameters and high degrees of fiber alignment.

Despite significant progress made in this field in the past decade, challenges remain in the widespread commercialization of electrospinning technologies. The main impediment is the limited throughput of nanofiber production using currently established methods. Thus, there is an urgent need for development of new electrospinning systems suitable for the large-scale production of high-quality nanofibers in a controlled manner. The primary barrier to effective system scale-up is largely due to the complex interplay of the operating parameters such as electric field, electrostatic charging of the polymer, and solvent volatilization, which make it difficult to increase the throughput while maintaining optimized and uniform fiber production [222]. In addition, mass production often results in increased sample loss during the collection process. The product of high-throughput electrospinning systems is generally a nanofibrous mat collected on a large plate or substrate [223-227]. Removal of the mat from the substrate without nanofiber loss can present a challenge. Subsequently, handling and cutting the mat into samples of useful size often leads to a compromised nanofiber structure. Overall efficiency of the collection process can be very low due to the number of associated steps.

In conjunction with increased throughput, production of nanofibers with controlled orientation is desirable. For example, aligned nanofibers are particularly useful for tissue engineering applications where they have shown improved cell proliferation [97], migration [228, 229], and differentiation [230]. The most common methods for attaining fiber alignment are exploitation of a rotating drum collector [231, 232] or a parallel-electrode collector [233, 234] where nanofibers selectively align across an insulating gap between two electrodes. Although both of these techniques produce aligned nanofibers, the sample size or fiber length is limited. To overcome both limitations, we introduced a centrifugal electrospinning (CES) system to accommodate the need for production of highly aligned fibers over a large area [221]. Using the CES, we deposited fibers across an insulating gap that could be adjusted to obtain fibers up to tens of centimeters in length. Nevertheless, this system was unable to produce many samples of these highly aligned nanofibers. In addition, cutting a large-size nanofiber mat into smaller samples of useful size can be challenging and often leads to compromised nanofiber alignment. Furthermore, only a small portion (~20%) of ejected polymer was deposited between the electrode gaps as aligned nanofibers while the majority was deposited on the large electrode plates as unaligned nanofibers, thus unusable in designated applications, and thereby significantly reducing the nanofiber yield.

While electrospinning has been extensively investigated, a system capable of fabricating many highly aligned nanofiber samples has not been demonstrated. We present a high-throughput centrifugal-electrospinning (HTP-CES) system that combines the principles of centrifugal spinning and electrospinning using a special configuration of wire electrodes capable of producing highly aligned nanofibers with large sample volume and quantity. Notably, this design allows simultaneous production of aligned nanofibrous mats at 102-collection sites and yet, as a result of the small-wire electrode configuration of the collector, nearly all the ejected polymer was deposited in the electrode gap as collectable, highly aligned nanofibers, with a production yield of nearly 75%. We electrospun natural/synthetic copolymer blend nanofibers across a range of chitosan and polycaprolactone (C-PCL) polymer blend compositions to illustrate the versatility of the HTP-CES. C-PCL blend nanofibers are highly advantageous for tissue engineering applications due to the favorable combination of the mechanical strength of PCL and the biocompatibility of chitosan [235, 236]. We investigated how parameters such as polymer concentration, centrifugal force, and needle gauge affect the morphology and alignment of resultant C-PCL nanofibers. Furthermore, we investigated if changing the needle gauge size can fine tune fiber diameter in highly aligned nanofiber samples.

5.3. MATERIALS AND METHODS

5.3.1. System configuration

The primary components of the high-throughput centrifugal-electrospinning (HTP-CES) system include a syringe-needle spinneret driven by a variable speed DC electric motor (Amtek, Monrovia, CA) and a circular 40.5cm-diameter multiple-pole collector mounted on wooden insulating columns. A 25 kV DC negative high-voltage power supply (HV350REG, Information Unlimited, Amherst, NH**)** was connected to the spinneret placed at the center of the circular collector (**Figure 5.1a**). The needle tip of the spinneret was 10.7cm away from the collector and the collector had 102-grounded wire electrodes spaced 1.27cm apart. Using a high-voltage power supply, we charged and fed the solution to the system using the centrifugal force created by the rotation of the spinneret. As the solution is ejected, the jet experiences both axial and tangential stretching as the solvent evaporates and fibers attach to the wire electrode. The rotational movement of the spinneret induces elongation and minimizes the “whipping region,” allowing deposition of nanofibers perpendiculuar to the wires, and aligment across the wire gap (**Figure 5.1b**). The nanofibers can be harvested directly from the wire gaps onto glass coverslips (**Figure 5.1c**). This system can also operate in a conventional electrospinning (ES) mode, when the spinneret is held stationary.

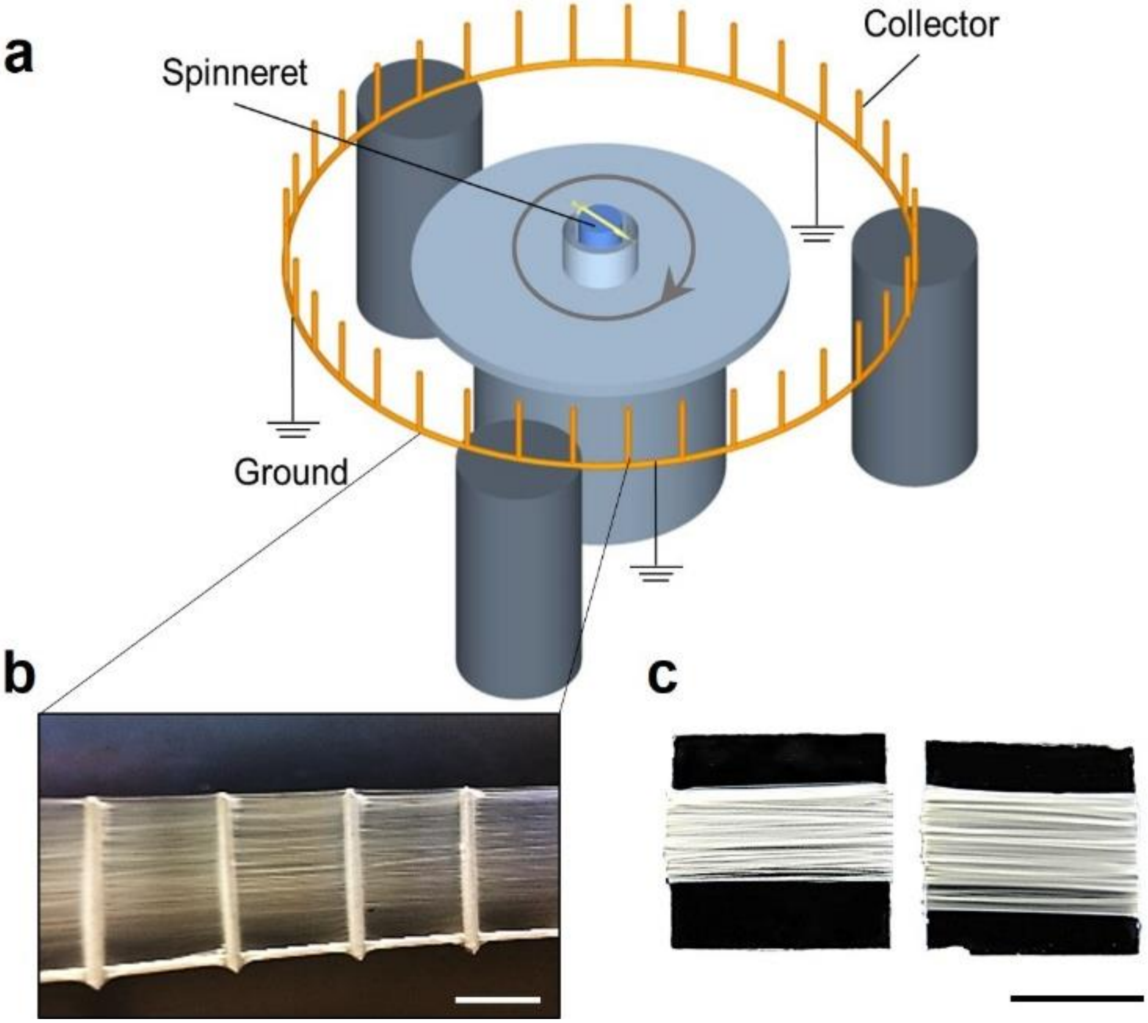

Figure 5.1. HTP-CES configuration for high-throughput production of highly aligned polymer nanofibers. (**a**) Schematic representation of the system configuration depicting a rotating, centrifugally-fed spinneret and grounded 102-metal wire collector atop three wood insulating stands. (**b**) Nanofibers aligned horizontally across four sets of wire electrodes. The scale bar represents 1 cm. (**c**) C/PCL nanofibers collected onto glass

coverslips from the gaps between two wire electrodes on the collector. The scale bar represents 5 mm.

5.3.2. Synthesis of C-PCL nanofibers via HTP-CES

Previously optimized polymer stock solutions were used to electrospin C-PCL copolymer blend nanofibers with some alterations [96]. All chemicals were purchased from Sigma Aldrich (St. Louis, MO) unless otherwise stated. First, the stock solutions of chitosan and PCL were prepared separately and then mixed to create four C-PCL blend solutions of different ratios of chitosan to PCL. Chitosan (75–85% deacetylated, medium molecular weight (200–800cP) in 1 wt% acetic acid at 25ºC) was dissolved in trifluoroacetic acid (TFA) (Fisher, Reagent, $\geq$97%) to yield a 7 wt% solution that was heated and held at 60°C for 12 hours under constant stirring. A 12wt% polycaprolactone (PCL) (Average M_n 80,000) solution was prepared by dissolving PCL in 2,2,2-trifluoroethanol (TFE) (ReagentPlus®, $\geq$99%) overnight under constant stirring at room temperature. The chitosan and PCL stock solutions were combined to form blend solutions that resulted in final nanofiber compositions ranging from 10wt% chitosan and 90wt% PCL (10/90 C-PCL) to 90wt% chitosan and 10wt% PCL (90/10 C-PCL). The chitosan and PCL were mixed immediately prior to electrospinning and refreshed every hour to prevent polymer degradation. Consistent environmental conditions were maintained throughout these experiments by using a humidifier or dehumidifier to maintain the humidity at 40–50% while the room temperature remained at 20–25ºC.

Four copolymer blend electrospinning solutions (10/90 C-PCL, 25/75 C-PCL, 75/25 C-PCL, and 90/10 C-PCL) were used to investigate the relationship between copolymer blend composition and nanofiber morphology. Each solution was centrifugally fed from the spinneret of the HTP-CES using a 24-gauge blunt tip needle. For all solution conditions, a negative DC voltage of 5kV was applied between the spinneret needle and ground. The spinneret rotational speed was held constant at 108 RPM.

We studied the effect of the centrifugal force on nanofiber morphology and alignment by using a 25/75 C-PCL solution. Using the HTP-CES modality, where the centrifugal force was applied, the spinneret was rotated at 108RPM. The spinneret was held stationary for the electrospinning modality (ES) where no centrifugal force was involved. The solution was fed to the system with a voltage of 5 kV and a 24-gauge blunt tip needle for both conditions.

To investigate the effect of needle gauge on fiber diameter and alignment, we centrifugally fed a 25/75 C-PCL solution from the spinneret of the HTP-CES and electrospun it using blunt-tip needles with five different inner diameters (18, 21, 24, 27, and 30-gauge) . All five conditions were subjected to a voltage of 5 kV and spinneret rotation at 108 RPM.

5.3.3. Fiber morphology characterization with scanning electron microscopy (SEM)

Using double-sided carbon tape, nanofibers were gathered from the collector onto a pedestal, sputter-coated with Au/Pd for 40 s at 18 mA and imaged with a FEI Sirion XL30 SEM at an operating voltage of 3 kV.

5.3.4. Chemical characterization using Fourier transform infrared spectroscopy (FTIR)

We performed FTIR spectroscopic analysis of chitosan and PCL as well as polymer blends bu using a Nicolet 5DXB spectrometer (Thermo Scientific, Boston, MA). A few drops of each solution of chitosan in TFA, PCL in TFE, and C-PCL in TFA/TFE were added to one KBr salt plate with a second plate on top and analyzed by averaging 64 scans at a resolution of 2 cm^{-1} over a range of 400 – 4000 cm^{-1}.

5.3.5. Determination of solution viscosity

Rheological studies were conducted using a stress-controlled rheometer (MCR 301, Anton Paart Germany) with a cone and plate configuration of 49.963 mm diameter and 1.008° cone angle. Stock solutions of chitosan-TFA, PCL-TFE, and C-PCL blends (90/10, 75/25, 25/75, and 10/90 chitosan/PCL) were prepared immediately before the measurement. A layer of mineral oil was applied on top of the polymer solution to minimize solution drying. The viscosity was measured as a function of shear rate as shear rate was increased from 10 to 1000 s^{-1} in a dynamic rotatory mode with temperature maintained at 20 °C.

5.3.6. Quantification of fiber alignment

A uniform threshold filter was applied to representative SEM images to eliminate contrast and brightness bias among images. Using ImageJ software (NIH, Bethesda, Maryland, USA), SEM images (in triplicate) were transformed into power spectra using fast Fourier transform (FFT) analysis. A 90º shift was performed on all power spectra to correct for the transformation that is mathematically inherent to FFT. The angle at which the peak appears directly correlates to the principal axis of fiber orientation. Based on the power spectra, we conducted a radial summation of pixel intensity from 0–360º in 1º increments by using the Oval Profile plugin [237]. Given the horizontally symmetric nature of FFTs, we plotted only the data from 0–180º. The pixel intensity values were normalized and plotted against the angle of acquisition. The angle of fiber orientation was determined from the location of the peaks on the intensity plots. The alignment of the sample was determined from the peak characteristics, where the greatest intensity increase over the smallest degree range signified the highest degree of fiber alignment.

5.3.7. Determination of fiber diameter

The diameters of 25 nanofibers were measured from representative 512 × 512 pixel SEM images at 8000× magnification using ImageJ. This procedure was repeated for 6 different images per condition to ensure statistical significance. One-way analysis of variance (ANOVA) was performed and a two-tailed t-test used to determine statistical significance between samples. The significance was determined at $p < 0.05$.

5.3.8. Quantification of nanofiber diameter distribution for HTP-CES versus ES

The diameters of 50 nanofibers were measured from representative 512 × 512 pixel SEM images of fibers spun using the HTP-CES system and the ES system at 8000× magnification using ImageJ. The nanofiber diameters were plotted against the number of nanofibers in the given diameter range to yield histograms showing the diameter distributions.

5.4. RESULTS

5.4.1. Effect of polymer concentration on nanofiber morphology

Scanning electron micrographs of aligned C-PCL nanofibers fabricated by the HTP-CES from four polymer solutions of different ratios of chitosan to PCL are shown in **Figure 5.2a**. Nanofibers fabricated from all four polymer solutions exhibited bead-free morphologies. C-PCL nanofibers composed of 10 wt% chitosan and 90 wt% PCL (10/90 C-PCL) showed the most uniform fibrous structure with no visible branching. Increasing the chitosan concentration (25/75 C-PCL) resulted in less uniform nanofiber morphologies with slight diameter variations. Further increases in chitosan concentration (75/25 C-PCL and 90/10 C-PCL) resulted in the formation of a significant, branched sub-structures, and thus less uniform nanofibers in terms of morphology. Thus, we chose the 25/75 C-PCL solution as the optimal concentration for all subsequent experiments because the resultant nanofibers exhibited the most uniform structure at the highest chitosan concentration, which is important for biological applications.

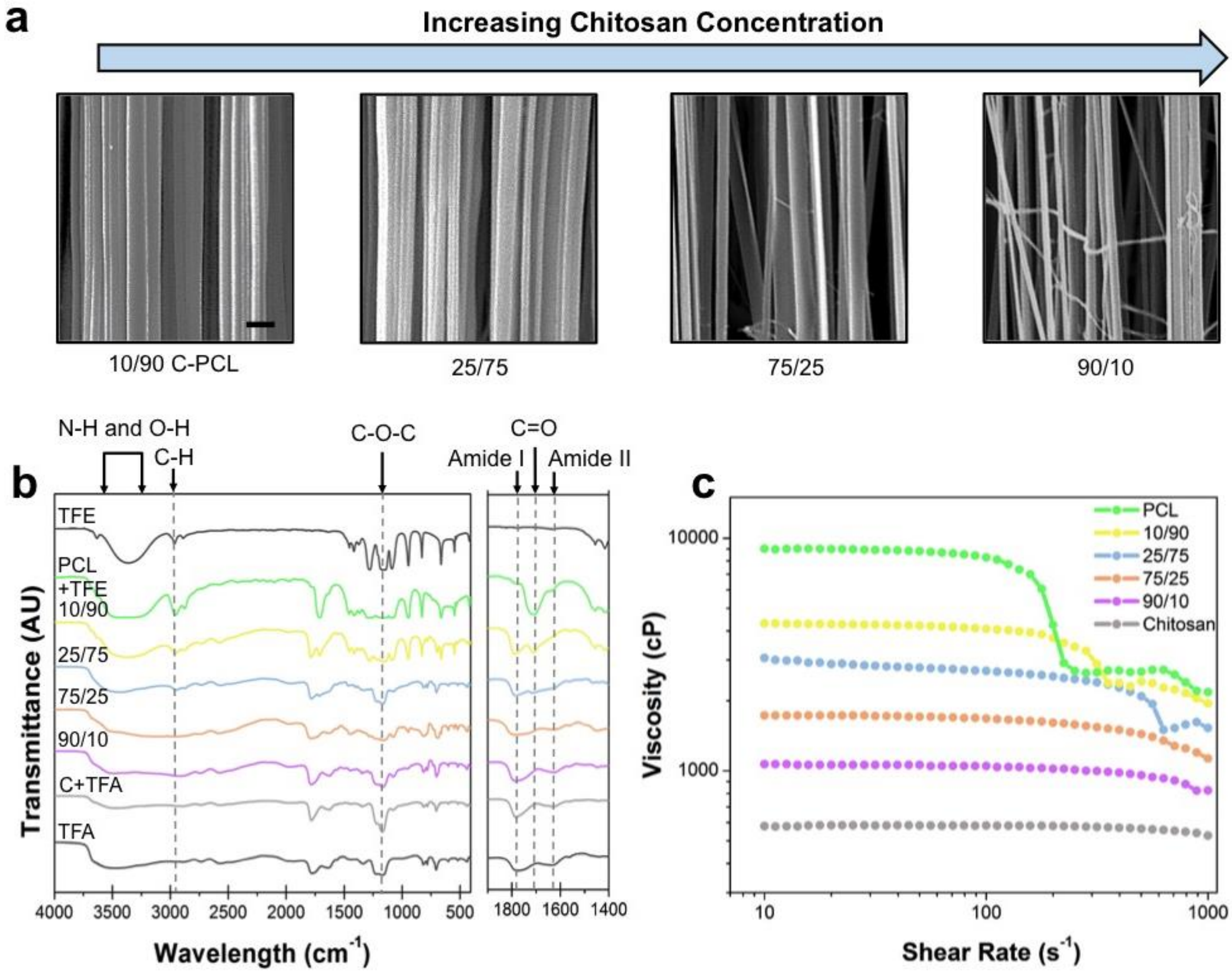

Figure 5.2. Nanofiber morphology and physicochemical properties of C-PCL polymer blend solutions. (**a**) Fiber morphology characterized by SEM. From left to right, the chitosan concentration in the blended copolymer nanofibers was increased. An increase in a branched sub-structure corresponding with less uniform nanofiber morphology was observed with an increase in chitosan concentration. The scale bar represents 750 nm. (**b**) FTIR analysis of solvents, pure polymer stock solutions, and polymer blends. (**c**) Rheological properties of pure polymer stock and polymer blend solutions.

The FTIR spectra for stock chitosan (C + TFA) and PCL (PCL + TFE) solutions as well as blends of the two solutions are shown in **Figure 5.2b**. In the spectrum of C + TFA, the presence of chitosan is confirmed by characteristic peaks of chitosan at 1790 cm^{-1} (C = O, amide I), 1635 cm^{-1} (-CONH, amide II), and at 1080 cm^{-1} (–C-O-C). The presence of TFA is confirmed by three bands due to C - F stretching vibration (815–705 cm^{-1}) [238]. The broad peaks of C + TFA at 3450 cm^{-1} is from the overlapping N – H and O – H stretching vibrations [239]. In the spectra of PCL + TFE, the presence of PCL is confirmed by the peaks at 2960 and 1710 cm^{-1} corresponding to C – H and C = O stretching vibrations, respectively. The broad band around 1200 cm^{-1} is attributed to the overlapping of C – O – C stretching of PCL with C – O stretching of TFE.

As the concentration of chitosan decreases for the blend polymer solutions, the chitosan characteristic peaks at 1790 cm^{-1} (amide I) and 1635cm^{-1} (amide II) decrease and eventually disappear when there is no chitosan, whereas the peak at 1710 cm^{-1} attributed to PCL decreases and becomes dominant. In addition, the chitosan C–O–C peak at 1080 cm^{-1} broadens slightly towards 1200 cm^{-1} where the C–O–C stretching vibration peaks of PCL and C–O stretching peak of TFE are observed on the PCL + TFE spectrum. When chitosan concentration increases, the peak at 2960 cm^{-1} assigned to C – H stretching in PCL diminishes [240]. The characteristic peaks of the pure stock solutions are identifiable, and no additional peaks are present, indicating both the chemical structure of chitosan and PCL remain unchanged with no additional compounds formed when blended to yield the electrospinning solutions.

The viscosity of the polymer solutions plays a significant role in solution spinnability and the resultant nanofiber morphology. **Figure 5.2c** shows the viscosity versus shear rate for the pure polymer stock and blend solutions. The chitosan-TFA stock solution has the lowest viscosity and experiences very little shear thinning as the shear rate is increased. When the chitosan-TFA is blended with 10% PCL-TFE solution, the viscosity increases, and shear thinning occurs as the shear rate increases to 1000 s^{-1}. Further increases in PCL-TFE concentration in the blend increases the viscosity but induces shear thinning at lower shear rates. The stock PCL-TFE solution shows the most drastic shear thinning beginning at 150 s^{-1} and leveling out until further thinning effects are seen at 700 s^{-1}. The viscosities for all C-PCL blend curves fall between the viscosities of the pure polymer stock solutions, indicating the two solutions are miscible and form a single phase upon mixing.

5.4.2. Effect of centrifugal force on nanofiber alignment (HTP-CES versus ES)

We used the HTP-CES system highlighted in **Figure 5.1** as both a centrifugal-electrospinning (HTP-CES) system and a conventional electrospinning (ES) system where centrifugal forces were not applied. SEM micrographs in **Figure 5.3a** depict the morphological differences between nanofibers spun with and without the influence of centrifugal force. Nanofibers produced by HTP-CES are homogeneous in diameter and aligned vertically, whereas substantial branching and fiber diameter non-uniformity is observed in nanofibers produced by ES. We used fast Fourier transform (FFT) analysis to quantify differences in nanofiber alignment; the resultant FFT power spectra are shown in **Figure 5.3b**. A distinct pixel intensity increase along the axis of fiber orientation at 90º confirms nanofiber alignment for both sets of samples. The diameter distributions of nanofibers produced using the two systems were compared by histograms (**Figure 5.3c)**. Nanofibers spun using conventional electrospinning (ES) ranged in diameter from approximately 25 nm to 450 nm, whereas the nanofiber diameter distribution for samples spun in the presence of centrifugal forces (HTP-CES) was narrower and more uniform, ranging from approximately 100 nm to 275 nm. This indicates that the HTP–CES system produces nanofibers with superior uniformity.

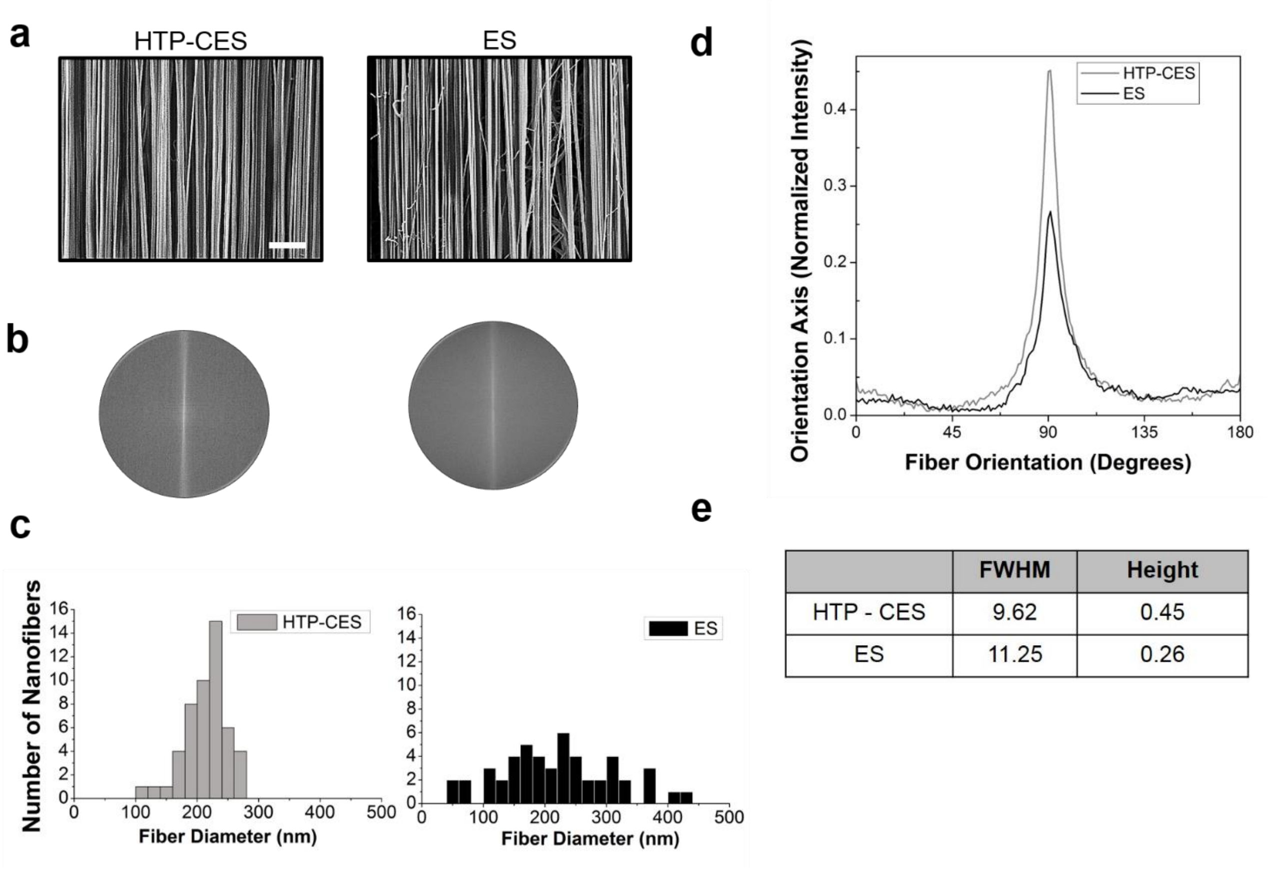

	FWHM	Height
HTP - CES	9.62	0.45
ES	11.25	0.26

Figure 5.3. The effect of centrifugal force on fiber morphology and alignment. (**a**) SEM images of centrifugally electrospun (HTP-CES) versus electrospun (ES) nanofibers showing morphological differences. The scale bar represents 5 μm. (**b**) FFT power spectra based on SEM images of HTP-CES versus ES nanofibers. (**c**) Histograms of nanofiber diameter distributions for HTP-CES versus ES nanofibers. (**d**) The normalized radial summation of pixel intensity versus degree of acquisition of FFT power spectra. (**e**) Quantitative FFT results for HTP-CES versus ES nanofibers including values for the full width half maximum (FWHM) and peak height corresponding to normalized intensity.

The Oval Profile plugin [237] was used to generate a normalized plot from 0–180º (**Figure 5.3d**). We quantified the sample alignment using the peak characteristics, where the greatest increase in normalized intensity over the smallest degree range signifies the highest degree of fiber alignment. The peaks associated with HTP–CES and ES conditions show a similar width, yet the peak height in normalized intensity for the HTP–CES samples (0.45) was greater than that of the ES samples (0.26) (**Figure 5.3e**). The full width half maximum (FWHM) or peak width at half the maximum height was used as a quantitative measure of alignment where a smaller value signifies a narrower peak and thus better alignment. The FWHM is smaller for HTP–CES (9.62) than for ES (11.25), indicating that the HTP–CES system results in better alignment than conventional ES (**Figure 5.3e**).

5.4.3. Effect of needle gauge on nanofiber diameter

We usedSEM images to measure and evaluate the diameters of nanofibers produced using five different needle gauges (18, 21, 24, 27, 30-gauge) with the HTP–CES system. All operating parameters were held constant while the needle guage was varied to determine a correlation between needle diameter and nanofiber diameter. We identified a concave relationship between nanofiber diameter and needle diameter (**Figure 5.4a-b**). The smallest average fiber diameter and the narrowest fiber diameter distribution was achieved using a 24-gauge needle. As the needle gauge was either increased or decreased, a larger fiber diameter and a wider diameter distribution was observed in conjunction with a larger standard deviation.

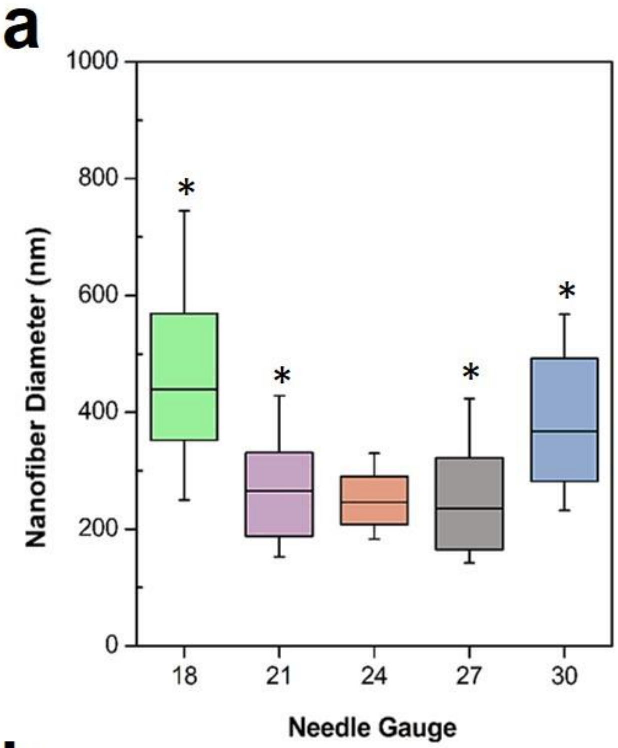

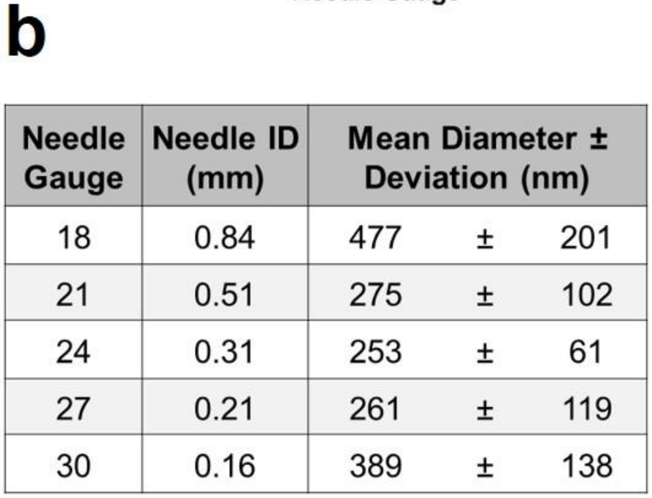

Needle Gauge	Needle ID (mm)	Mean Diameter ± Deviation (nm)
18	0.84	477 ± 201
21	0.51	275 ± 102
24	0.31	253 ± 61
27	0.21	261 ± 119
30	0.16	389 ± 138

Figure 5.4. C-PCL nanofibers produced using various needle gauges. (**a**) Box plot of nanofiber diameter distribution for five needle gauges showing concave relationship between needle gauge and nanofiber diameter. (*$p < 0.05$ as compared with the 24-gauge condition). (**b**) Summary of needle gauge/needle inner diameter versus average nanofiber diameter.

5.4.4. Effect of needle gauge on nanofiber alignment

We investigated the relationship between needle gauge and nanofiber alignment using the three smallest needle gauge conditions (24-, 27- and 30-gauge) due to their superior overall morphology and diameter uniformity of nanofibers produced. Samples associated with all three needle gauges exhibited high degrees of alignment (**Figure 5.5a**). Using the Oval Profile plugin [237], we plotted the power spectra (**Figure 5.5b)** from 0–180º and normalized (**Figure 5.5c**). The FFT power spectra associated with all conditions show a distinct pixel intensity increase in the vertical direction indicating fiber alignment. Further, the normalized intensity versus fiber orientation plot shows three distinct and narrow peaks centered around 90°. To quantify and compare the fiber alignment among samples, the peak heights and the full width half maximum (FWHM) values were calculated (**Figure 5.5d**). As previously mentioned, the best alignment was determined from the peak characteristics, where the greatest increase in normalized intensity over the smallest degree range, as represented by FWHM, signifies the highest degree of fiber alignment. The nanofibers produced using the 24-gauge needle exhibited the highest peak followed by the 30-gauge and 27-gauge fibers. The FWHM value was smallest for the 24-gauge sample (8.60), followed by the 30-gauge sample (12.63), and the 27-gauge sample (13.37). With these quantitative measures, the 24-gauge needle exhibited the highest degree of alignment and the 27-gauge needle exhibited the lowest.

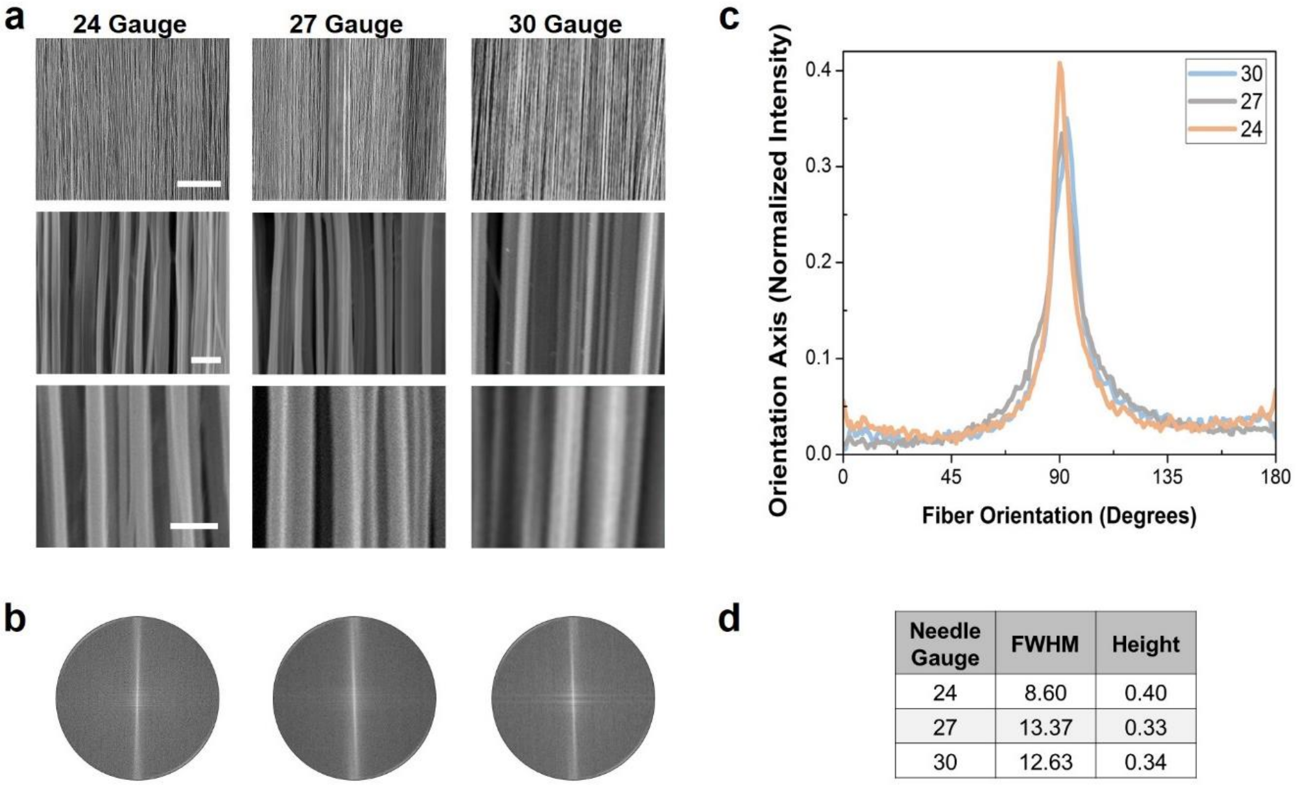

Needle Gauge	FWHM	Height
24	8.60	0.40
27	13.37	0.33
30	12.63	0.34

Figure 5.5. Effect of needle gauge on nanofiber alignment. (**a**) SEM images of nanofibers electrospun using 24, 27, and 30-gauge needles. In the top row of images, the scale bar represents 50 μm. Scale bars for the middle and bottom rows represent 1 μm and 500 nm, respectively. (**b**) The power spectra representing each needle gauge as obtained using FFT (indicates which spectrum is for which needle size from left to right). (**c**) The normalized radial summation of pixel intensity versus degree of acquisition for each FFT for alignment comparisons. (**d**) Full width half maximum (FWHM), and peak height quantification.

5.5. DISCUSSION

Synthetic and natural polymer blend nanofibers are playing an increasingly important role in many engineering applications, but are challenging to fabricate due to poor miscibility between component polymers [235]. Centrifugal spinning has been primarily used to fabricate micron-scale C-PCL fibers [241] and the traditional electrospinning is the dominant technique for fabrication of

C-PCL nanofibers. We present a technology, the HTP-CES system, which allows for production of homogenous, highly-aligned chitosan-polycaprolactone (C-PCL) nanofibers.

Initially, we evaluated various C-PCL blends to determine optimal polymer blend compositions in terms of nanofiber morphology and uniformity, where a higher chitosan concentration yields a more relevant material for biological applications. The effect of natural versus synthetic polymer properties on resultant fibers is evident in **Figure 5.2a** where nanofibers containing a large proportion of PCL (10/90 C-PCL) exhibit the most uniform fibrous structures with no visible branching. This might be due to synthetic polymers generally containing fewer entanglements than do natural polymers such as chitosan, so they are more uniform and easily electrospun. Additionally, PCL dissolved in TFE is highly viscous and exhibits strong non-Newtonian shear thinning properties. The shear thinning of PCL solution allows the polymer chains to interact and align under the centrifugal force so that less branched and more uniform nanofibers are produced. After visual evaluation of the morphology of resultant C-PCL blend nanofibers, we chose 25/75 C-PCL as the optimal composition due to the overall nanofiber uniformity and the need to maximize chitosan content, and thus used it for all subsequent experiments.

The advantage of centrifugal force application on nanofiber alignment was demonstrated by electrospinning C-PCL solution with (1) a stationary spinneret (ES) and (2) a spinneret rotated at 108RPM (CES). All other operating parameters were held constant; however, the polymer solution flow rate was different due to the difference in centrifugal versus gravity feed. Using FFT for quantification of fiber alignment, and SEM imaging for visualization of fiber morphology, clearly showed that the addition of centrifugal force increases nanofiber alignment (**Figure 5.3a**). The high degree of fiber alignment achieved using the HTP-CES occurs via the exploitation of two mechanisms. First, the collector functions as an array of parallel electrodes, where nanofibers selectively align across the insulating gap between two neighboring electrodes (**Figure 5.1a-b**). Second, the centrifugal feed disperses the fibers perpendicular to each wire. Additionally, the centrifugal force imparted by the HTP-CES system on the polymer jet results in additional cohesive forces within the jet that prevent splaying and allows for an increased stretching and elongation region. This leads to a more uniform nanofiber diameter distribution (**Figure 5.3c)**.

In addition to alignment, strict control over nanofiber diameter is highly desirable. The complex interplay among process parameters, fluid dynamics, electrodynamics, and solution rheology associated with electrospinning often means that it is difficult to correlate the effects of specific operating parameters with nanofiber properties. Studies have demonstrated a variety of relationships between the needle diameter and resultant nanofiber diameter, including direct [242-244], inverse [245], concave [246], and convex [247] correlations. These studies indicate that extracting the relationship between needle diameter and nanofiber diameter is difficult, especially because many polymeric electrospinning solutions are non-Newtonian fluids [248-250]. Because the HTP–CES system has an added centrifugal feed component that enhances nanofiber uniformity and alignment, it is possible to spin bead-free fibers over a wider range of needle gauges than is generally possible in an conventional electrospinning system. We identified a concave correlation between needle gauge and fiber diameter for our system (**Figure 5.4a,b**), where other critical parameters such as operating voltage, solution concentration, and spinneret rotational speed are all held constant.

The concave correlation between needle diameter and resultant fiber diameter indicates that two different instability regimes within the polymer jet are present. In the first regime where the polymer solution is centrifugally electrospun through a decreasing needle diameter (18, 21, and 24-gauge), the 25/75 C-PCL solution experiences shear thinning in response to the increased shear force. This aligns the polymer chains, thereby decreasing solution viscosity. In this regime, the fiber diameter decreases as the needle diameter decreases due to the alignment and conformity of the polymer chains.

In the second regime where the centrifugal force becomes more prominent and the needle diameter is further decreased (24, 27, and 30-gauge), the shear thinning behavior of polymer solutions and electrostatic forces are no longer great enough to promote formation of a stable Taylor cone. Upon decreasing the needle diameter, the orifice size becomes too restricted to continuously produce fibers and the increase in the shear force begins to deform the polymer. The viscoelastic properties of the polymer solution result in swelling of the jet upon exiting the restriction. This has also been observed in other studies where polymer solutions are exposed to high shear stresses [251, 252]. The polymer solution jet has a decreased flow rate and a thicker jet is formed resulting in thicker fibers.

Whereas the 24-gauge samples were optimal, samples produced using all needle gauges were composed of fibers on the order of hundreds of nanometers with standard deviations of approximately 200nm or less, demonstrating the versatility of the HTP–CES. It is possible to obtain nanofibers in a defined diameter range by simply changing the needle gauge on the spinneret and leaving all other operating parameters constant.

Nanofibers produced using the three smallest needle gauges (24, 27, and 30-gauge) showed the lowest degree of branching as observed via SEM and were analyzed to characterize the effect of needle gauge on alignment. The greatest degree of alignment occurred in samples produced using the 24-gauge needle (8.60), followed by the 30-gauge (12.63), and finally, the 27-gauge samples (13.37) (**Figure 5.5c-d**). Coupling the diameter and alignment analyses, we conclude that the 24-gauge needle provides the narrowest nanofiber diameter distribution with the best alignment, thereby making it the optimal condition for spinning of 25/75 C-PCL using the HTP-CES.

5.6. CONCLUSION

A nanofiber yield near 75% renders the HTP-CES system convenient for generation and collection of a sizeable number of samples concurrently. Our approach proved to be superior to conventional electrospinning in terms of nanofiber morphology, uniformity, and alignment. The superior morphology of C-PCL nanofibers can be attributed to the addition of the centrifugal force imparted on the polymer solution by the HTP–CES. The unique centrifugal force induces shear thining solution behavior while imparting tangential and axial stretching forces onto the nanofibers, minimizing the “whipping region” and depositing highly uniform fibers under conditions not attainable by conventional electrospinning. The optimal centrifugal-electrospinning condition for producing uniform, highly-aligned 25/75 C-PCL nanofibers was a 24-gauge needle with 5kV operation voltage rotating at 108 RPM. All nanofiber samples analyzed exhibited a narrow diameter distribution with standard deviations of 200nm or less and distinct FFT alignment peaks centered around 90°. The fabrication of aligned nanofibers with specified diameters as demonstrated here is critical in the biomedical and piezoelectric device industries, where uniformity and high degrees of alignment are required.

***This chapter is reprinted with permission from:**

Erickson, A.E., Dennis Edmondson, Fei-Chien Chang, Dave Wood, Alex Gong, Sheeny K. Lan Levengood, and Miqin Zhang. “High-throughput and high-yield fabrication of uniaxially-aligned chitosan-based nanofibers by centrifugal electrospinning.” *Carbohyd Polym* 134, 467-474, doi:10.1016/j.carbpol.2015.07.097 (2015).

Chapter 6: HYALURONIC ACID - COATED ALIGNED NANOFIBERS FOR PROMOTION OF MIGRATORY GLIOBLASTOMA PHENOTYPES

6.1. ABSTRACT

The propensity of GBM cells to migrate along white matter tracts and blood vessels suggests that topographical cues associated with brain parenchyma greatly influence GBM motility and invasion. In vitro cell culture platforms that mimic the physical and biochemical characteristics of brain tissue are needed to develop biologically relevant GBM migration models for advancement of anti-metastatic therapies. Here, we fabricated highly-aligned, highly-reproducible chitosan-polycaprolactone (C-PCL) polyblend nanofibers coated with hyaluronic acid (HA), a glycosaminoglycan commonly found in the brain, to simulate the structure and biochemistry of native brain tissue. The influence of topography on cell behavior was apparent on both HA-coated and uncoated nanofibers where cells aligned axially along nanofibers displaying an elongated morphology associated with migration. Time lapse imaging revealed that migrating cells were less likely to divide on nanofibers, suggesting a shift to a mesenchymal-like phenotype. Further, cells on nanofibers were more resistant to temozolomide than cells grown as adherent cultures on polystyrene plates. Migratory behavior was influenced by HA coating concentration as migratory cells achieved the highest velocity on nanofibers coated with 0.5% HA. These results indicate that HA-coated nanofibers are a promising substrate to characterize GBM migration and investigate novel therapies to counter GBM invasiveness.

6.2. INTRODUCTION

Glioblastoma multiforme (GBM) is a highly invasive and malignant brain cancer with median survival of only 15 months despite aggressive surgical resection and adjuvant treatment with concurrent radiation and chemotherapy [135]. Poor survival is attributed to infiltration of adjacent brain tissue by a subset of tumor cells with a more migratory phenotype and a propensity for locomotion along white matter tracts and blood vessels [253-255]. Despite similar ECM composition for brain tissue white and gray matter, tumor cell infiltration occurs primarily in white matter. This suggests that tissue topography and morphology may influence tumor cell migratory behavior [253]. Importantly, unlike other tumor microenvironments, the brain is composed mainly of hyaluronic acid (HA). Changes in both tissue topography and composition have been implicated in poor patient outcomes, but overall, mechanisms underlying GBM cell migration *in vivo* are not well understood.

Current *in vitro* models for studying cell migration include 2D micro-patterned surfaces and 3D hydrogels. Although micropatterned surfaces provide alignment cues, the walls of micro-grooves do not accurately mimic the surfaces of a blood vessel or white matter tract. Hydrogels, such as Matrigel™, are often used to study the dissemination of tumor spheroids and have been shown to promote an elongated migratory morphology typical of cells *in vivo* [256]. However, hydrogels cannot directly simulate the directional nature of brain white matter and downstream assays like immunostaining are difficult to carry out. Currently, the most utilized model for characterizing GBM invasion is an organotypic slice assay, where cancer cells are cultured on a living brain slice [257, 258]. Although mechanical, chemical, and morphological characteristics of native brain tissue are present, neural cell death within the slice during the culture period may skew results.

Electrospinning provides a unique solution for modeling the GBM microenvironment. The resultant nanofibers, with precisely defined alignment, diameter, and morphology, represent a good *in vivo* model of the HA-rich, nanoscale-diameter fibrous structure through which GBM cells invade [94]. Previously, electrospun nanofibers composed of polycaprolactone (PCL) [165, 171, 178, 259] and polyblend chitosan–PCL (C–PCL) [166] were used to study GBM cell migration. Four hundred nanometer diameter C-PCL nanofibers promoted a migratory GBM phenotype with cell migration profiles similar to those *in vivo* [166]. Polyblend nanofibers are advantageous because the biocompatibility of the natural polymer and the mechanical stability of the synthetic polymer are combined [260]. Defects in aligned nanofiber morphology, which can occur when using traditional electrospinning technology, interrupt cell locomotion and may hinder the characterization of migratory cell behavior. High throughput centrifugal electrospinning (HTP–CES) results in superior nanofiber alignment and diameter uniformity relative to conventional electrospinning [51]. Fabrication of *in vitro* brain parenchyma mimics using the HTP–CES system ensures that cell locomotion is uninterrupted by morphological changes allowing for characterization cell–cell and cell–ECM interactions.

In this work, electrospun polyblend chitosan–polycaprolactone (C–PCL) nanofiber platforms were fabricated to investigate the influence of topography and chemistry on GBM cell migration for development of an appropriate brain tissue model to study GBM migration. By combining chitosan and polycaprolactone (PCL), we fabricated reproducible, biocompatible, mechanically stable, highly aligned nanofiber mats. Because hyaluronic acid (HA), a key proteoglycan found in brain ECM [160], has shown promise as a suitable surface for cell adhesion and proliferation, nanofiber mats were coated with a low, medium, or high concentration of hyaluronic acid (HA). Previously, the aligned nanofiber substrates have been shown to increase cell migration relative to conventional adherent culture on polystyrene plates. While topography has proven a crucial factor for GBM invasion, biochemistry could also play a strong role in migratory cell behavior. We hypothesize that the addition of an optimized HA coating will further improve cell response for attaining a migratory phenotype. We examined the different HA coating conditions to identify an optimal surface chemistry for promoting migratory behavior. The model GBM cell line, U87 MG, was seeded onto nanofiber substrates and imaged after 24, 48, and 96 hours of culture to determine cell morphology and alignment characteristics. We conducted long-term migration assays (> 10 hours) to study the behavior and migration patterns of the cells. Finally, we evaluated resistance to the clinical alkylator temozolomide (TMZ) of nanofiber-seeded cells relative to cells grown on polystyrene culture plates.

6.3. MATERIALS AND METHODS

6.3.1. Materials

All chemicals were purchased from Sigma-Aldrich (St. Louis, MO) unless otherwise specified. Chitosan (75-85% deacetylated, medium molecular weight), polycaprolactone (PCL, average M_n 80,000), and hyaluronic acid sodium salt (from *Streptococcus equi*, molecular weight ~1.5-1.8 x10^6 Da) were used as received.

6.3.2. Nanofiber synthesis and coating

Chitosanpolycaprolactone (C–PCL) polyblend nanofibers were synthesized according to previously published procedures [51, 260]. Briefly, a 7 wt% chitosan stock solution was prepared in trifluoroacetic acid (TFA, Fisher, Reagent grade ≥ 97%) and refluxed at 60°C for 12 hours under constant stirring. A 12 wt% PCL stock solution was prepared in 2,2,2-trifluoroethanol (TFE, ReagentPlus®, >99%) and stirred overnight. The solutions were mixed resulting in a 50 wt% chitosan – 50 wt% PCL polyblend (C–PCL). The polymer solution was electrospun using a 25-

gauge blunt tip needle on the high-throughput centrifugal electrospinning (HTP–CES) system. The collector on the HTP–CES system was composed of 102 parallel electrodes separated by an insulating air gap where the fibers dispersed perpendicularly to the electrodes and aligned 360° around the spinneret [51]. The C–PCL solution was centrifugally fed from a rotating spinneret at 108 RPM and 5 kV applied DC voltage. The chitosan and PCL solutions were combined immediately before electrospinning and refreshed every 2 hours to prevent polymer degradation. Consistent environmental conditions (40–50% humidity and 20–25°C) were maintained throughout the synthesis.

Aligned nanofibers were collected on a 9-mm square cover glass, secured to the cover glass using a medical grade silicone adhesive, neutralized for 15 min in 25 vol% NH_4OH, and thoroughly washed in DI water to remove all residual base. Coating the C-PCL nanofibers with hyaluronic acid (HA) followed procedures described by Maeda et al., [261] and Ahire et al., [262]. Briefly, nanofibers were immersed in 0 wt%, 0.1 wt%, 0.5 wt%, or 1 wt% HA solutions at 37°C for 72 hours. Nanofibers were sterilized for 1 hr in 70% ethanol and washed extensively with Dulbecco's phosphate buffered saline (D-PBS) before cell culture.

6.3.3. Nanofiber characterization

The HA coating ratio was calculated as the difference in weight between individual nanofiber samples before and after coating, using **Equation 6.1**, where W_f represents the weight of the C-PCL nanofibers after the HA coating and W_i is the weight before coating.

$$\text{Coating ratio (\%)} = \left[\frac{W_f - W_i}{W_i}\right] \text{x } 100 \qquad (6.1)$$

We used scanning electron microscopy (SEM) images to characterize the nanofiber morphology and diameter distribution. Nanofibers were collected onto a pedestal coated with double-sided carbon tape, Au/Pd sputter-coated for 30 s at 18 mA, and imaged with a SEM (FEI Sirion XL30) at an operating voltage of 3kV. The nanofiber diameter distribution was determined from ≥ 50 nanofibers in at least 3 representative SEM images and measured using ImageJ. Frequency distributions were generated using Graph Pad Prism 7.

We used a Shimadzu universal tester (AGS-X Series, Kyoto, Japan) for tensile testing uncoated aligned C-PCL nanofibers, which were clamped into pneumatic grips with tape to secure the specimen ends. The strain rate was 0.4 mm/min and tests were conducted until breakage at room temperature. The elastic modulus was measured in the linear elastic region at strains less than 10%.

6.3.4. Cell seeding and imaging

All cell culture reagents were purchased from Life Technologies unless otherwise specified. Minimum essential media (MEM), antibiotic-antimycotic, fetal bovine serum (FBS), and Dulbecco’s phosphate-buffered saline (D-PBS) were purchased from Invitrogen (Carlsbad, CA). The human glioblastoma cell line, U-87 MG, was purchased from American Type Culture Collection (Manassas, VA) and was transfected with pRFP-N2 using Lipofectamine® 2000 reagent according to manufacturer’s instructions [48]. Cells were washed in D-PBS 48 hours after transfection and cultured in fresh media supplemented with G418 (500 mg/mL) for selection of the stably transfected population. Two weeks after transfection, U-87 MG RFP cells were sorted by fluorescence-activated cell sorting (FACS; Vantage SE). Cells were maintained in fully supplemented Minimum Essential Medium (MEM) (Thermo Fisher Scientific, Grand Island, NY) containing 10% FBS and 1% antibiotic–antimycotic at 37°C and 5% CO_2 in a humidified environment.

U87 MG – RFP cells were seeded on sterilized nanofibers in a 24-well plate in 2 mL of fully supplemented MEM at 5,000 cells/mL. Bright field and fluorescence images were obtained 24, 48, and 96 hours after cell seeding to observe alignment and changes in cell morphology. A 4X or 10X objective was used on an upright fluorescence microscope with a Ri1 Color Cooled Camera System and the NIS Elements software package (Nikon Instruments, Melville, NY).

Immunostaining was conducted on 4% paraformaldehyde-fixed samples after 96 hours of culture. The cell membrane was permeabilized with 0.25% Triton X-100 in D-PBS for 20 min at room temperature and then blocked in 1% bovine serum albumin (BSA) in D-PBS for 30 min to block non-specific binding. For Ki-67 staining, samples were incubated in rabbit polyclonal antibody to Ki-67 (Abcam, Cambridge, MA) at 1:200 overnight at 4°C. The samples were then incubated with a goat anti-rabbit FITC secondary antibody (1:400) (Abcam, Cambridge, MA) for 1 hour at room temperature. Samples were rinsed with D-PBS and stained for 5 min with DAPI before imaging.

6.3.5. Quantification of cell number, alignment, and aspect ratio

Cell number, alignment, and aspect ratio were measured using images obtained with a 4X objective on an upright fluorescence microscope with a Ri1 Color Cooled Camera System with the NIS Elements software package (Nikon Instruments, Melville, NY). Images were processed with ImageJ using the “Li” uniform threshold filter. All cell images were converted to binary 8-bit and the “Analyze Particle” plug-in was used to quantify the cell number and morphology. The cell alignment angle was determined using the “best fit ellipse” measurement and recording the angle of alignment of the major axis from the horizontal. At least 350 cells were measured for each condition and converted to a frequency distribution histogram.

6.3.6. Time course migration imaging

U87 MG – RFP cells were seeded on the various substrates and cultured for 24 or 96 hours before imaging using an inverted microscope (Zeiss Axiovert 200M) on an automated stage (Marianas Imaging System, Intelligent Imaging Innovations) operated in a heated chamber at 37°C. Time course images were acquired every 2 min using a 10X objective for ≥ 10 hours. Image sequences were analyzed using ImageJ and at least 7 individual cells were tracked for each condition at 24 or 96 hours using the semi-automated TrackMate plugin.[263] Cell displacement for each 2-minute time interval was measured and plotted for each individual cell. We captured cell speed by measuring total displacement per image time point (2 min). The maximum and effective cell speeds determined for each individual cell were averaged for each condition. Effective cell speed was a measure of the total displacement divided by the total observation time. Only cells visible for > 10 hours were tracked.

6.3.7. Drug response analysis

C-PCL nanofibers were immersed in 0.5 wt% solutions of either HA, chitosan (C), or PCL for 72 hours at 37°C to achieve similar coverage. Coated and uncoated nanofibers were sterilized for 1 hr in 70% ethanol and washed extensively with D-PBS before cell culture. U-87 MG – RFP cells were cultured for 96 hours on 2D TCPS and nanofibers (uncoated C-PCL, HA-coated, C-coated, and PCL-coated). The samples were then treated with either 0 µM (untreated) or 100 µM temozolomide (TMZ) for 48 hours. After 48 hours, 200 µL of an alamarBlue® working solution (10% resazurin and 90% fully supplemented medium) was added to each well and incubated at 37°C for 2 hours. Aliquots of the alamarBlue® solution were transferred to a black-bottom 96-well plate and the fluorescence intensity was measured on a microplate reader. Differences in cell viability (percentage difference in metabolic activity) were reported as a percentage change in fluorescence intensity between TMZ-treated samples relative to untreated controls for each substrate.

6.3.8. Statistical analysis

All data were analyzed to express the mean ± standard deviation of the mean unless stated otherwise. Statistical significance was analyzed by one-sided or two-sided analysis of variance (ANOVA) with post hoc Tukey multiple comparisons testing ($p \leq 0.05$) in GraphPad Prism 7 (Prism version 7.04, Graph Pad Software, San Diego, CA). All frequency distributions were generated using Graph Pad Prism.

6.4. RESULTS AND DISCUSSION

Selective migration of GBM cells down white matter tracts and blood vessels suggest that the physical architecture of the brain may be a key factor in migratory tumor cell behavior [160]. Recapitulating the native brain ECM in an *in vitro* platform may provide insight into the biomechanical and topological cues that initiate phenotypic changes resulting in invasive metastatic cells. Further, materials optimized to mimic brain ECM may provide a reliable substrate for screening anti-metastatic therapeutics.

6.4.1. Characterization and coating of C-PCL nanofibers

Thirty identical, highly aligned C–PCL nanofiber samples were fabricated with the high-throughput centrifugal electrospinning system (HTP–CES) and collected on glass coverslips after 2 hours of centrifugal electrospinning. **Figure 6.1a** shows the typical fiber density of a sample with a high degree of fiber alignment. At higher magnifications (**Figure 6.1b, c**), nanofiber diameter uniformity and a bead-less structure are visible. Aligned nanofiber bundles were tested under tensile load to determine the stress versus strain behavior (**Figure 6.1d**). As expected, the nanofibers exhibited initial linear elastic behavior up to 7% strain with an average compressive modulus of 11.4 ± 4.2 MPa. Previously, the presence of both chitosan and PCL in the resultant nanofibers was confirmed using Fourier transform infrared spectroscopy (FTIR) [51, 166].

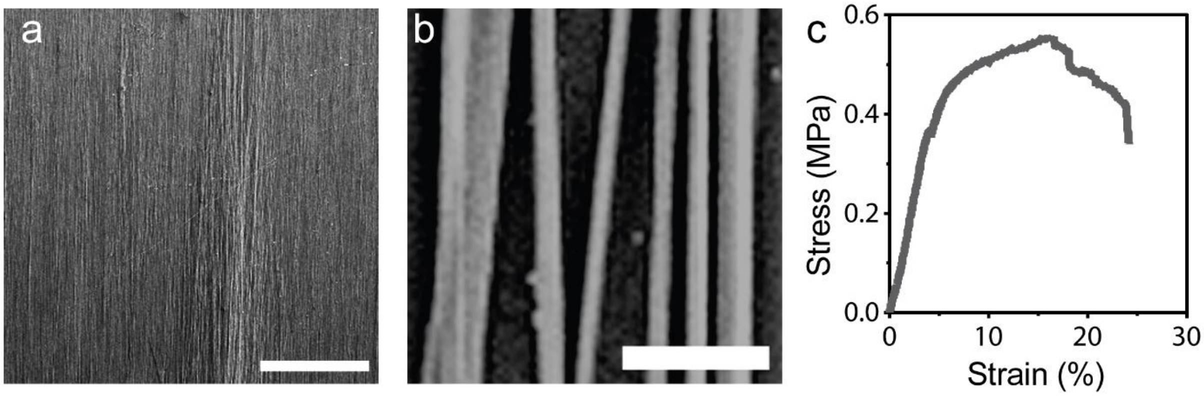

Figure 6.1. Uncoated 50 wt% chitosan – 50 wt% PCL (C-PCL) polyblend nanofiber morphology and mechanical properties. SEM images of nanofiber mat and individual nanofiber morphology. Scale bars are (**a**) 500 µm, (**b**) 2.5 µm. (**c**) Representative stress (MPa) versus strain (%) behavior for uncoated aligned nanofibers.

Biochemical, biomechanical, and topological cues in the ECM play a key role in cell behavior. Importantly, the ECM through which GBM cells invade is rich in hyaluronic acid (HA) and proteoglycans [160]. To mimic this HA-rich, nanoscale-diameter fibrous structure, C-PCL nanofibers were coated with HA. The optimal amount of HA necessary to model the biochemical cues of the brain ECM *in vitro*, was determined by comparing cell behavior on varying HA coatings with an uncoated nanofiber condition. Specifically, the influence of HA surface coating on cell migration and proliferation were characterized. To coat the fibers, C-PCL nanofibers were soaked in a HA solution ranging from 0 wt% – 1 wt% HA and the resultant nanofiber morphologies were characterized (**Figure 6.2**). The 0 – 1 wt% HA solution range was selected based on previous experiments by Maeda [261] and Ahire [262], where the same range resulted in a water-insoluble HA-surface coating due to the polysaccharide ionic complex between chitosan and HA.

The weight change of the nanofiber mats after coating and lyophilization was examined to evaluate the coating ratio, which represents the difference in nanofiber substrate weight before and after coating (**Figure 6.2a**). The uncoated (0% HA) C-PCL nanofibers weighed significantly less than the coated substrates. Although not all conditions were statistically different, the weight of the nanofiber mat increased with increasing HA concentration, signifying successful coating. The diameter distribution of dehydrated, uncoated C-PCL, and HA-coated C-PCL nanofibers was visualized and measured using SEM images (**Figure 6.2b)**. The mean diameter of uncoated and coated nanofibers ranged from 326 nm to 382 nm with no significant difference among the various conditions. This nanofiber diameter range encompasses that of previous nanofibers that were found to promote migratory GBM behavior [166]. We used a light microscope to visually evaluate physical changes in the hydrated coated nanofibers (**Figure 6.2c**). A highly aligned nanofibrous morphology was observed for all conditions over a large field of view with no visible nanofiber agglomeration or macro-scale changes identified due to coating. A nanofibrous morphology was observed for all HA coating conditions (**Figure 6.2d**), although slight agglomeration of nanofibers into multi-nanofiber bundles occurred as HA content increased. This may be an adverse effect of the lyophilization procedure post-hydration to prepare SEM imaging samples, as no multi-nanofiber bundles were identified under the light microscope. Taken together, these results indicate that the overall morphology was preserved, and the physical properties of the nanofibers were not drastically altered by the HA coating.

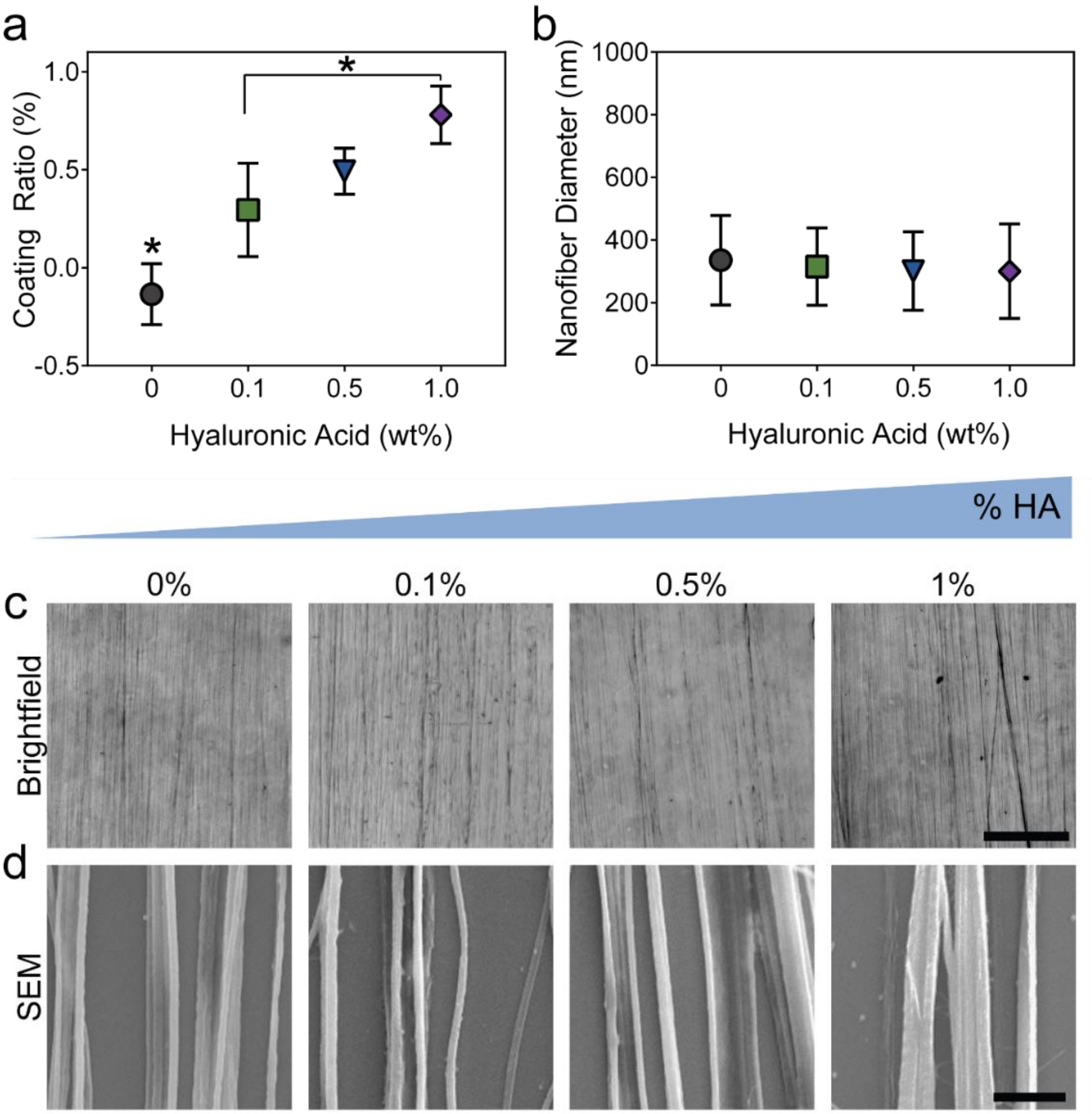

Figure 6.2. Uncoated and HA-coated C–PCL nanofiber characteristics. (**a**) HA coating ratio (wt%) (n = 4) and (**b**) average nanofiber diameter. (n = 50) *Statistically significant from all or specified. ($p \leq 0.05$) Morphological analysis of lyophilized nanofibers using (**c**) brightfield optical imaging for large field-of-view and (**d**) SEM images for morphological changes. The scale bars represent (**c**) 200 µm and (**d**) 5µm.

Previously, HTP-CES demonstrated superior nanofiber alignment and diameter uniformity over conventional electrospinning [51], signifying that fabrication of *in vitro* brain parenchyma mimics using the HTP–CES system may be superior to conventional electrospinning. Uniformity of the nanofiber diameter is critical to ensure subsequent results are a function of the HA coating, and not of morphological differences in the nanofibers. The superior alignment of HTP–CES nanofibers over conventional electrospinning also ensures that cell locomotion is uninterrupted by morphological changes and allows the evaluation of strictly cell–cell and cell–ECM interactions without disruption due to intersections or defects in the alignment of the nanofibers.

6.4.2. Cell behavior on various HA-coated nanofibers

Cell behavior on HA-coated nanofibers was characterized by observing cultures of an RFP-transfected human glioblastoma cell line (U-87 MG RFP) using brightfield and fluorescence microscopy. Due to well-documented migration and invasion characteristics, U87 MG was selected as a representative cell line [166, 175]. U87 MG RFP cells were seeded on 2D tissue culture polystyrene (TCPS), uncoated (0% HA) nanofibers, and HA-coated nanofibers. Cells were cultured for 24, 48, or 96 hours and then imaged to evaluate cell morphology and alignment. Merged brightfield and fluorescence images reveal cell responses to substrates (**Figure 6.3a and b**). After 24 hours, cells on all substrates were sparse, but adherent. After 96 hours (**Figure 6.3b**), cell density increased on all substrates, signifying proliferation. On 2D TCPS, no directionality was observed with cell protrusions visible in all directions under high magnification. The directional influence of the aligned nanofibers, independent of coating, was apparent with cells displaying a highly elongated, spindle morphology with visible protrusions consistently stretching longitudinally along the nanofiber. At high magnification (**Figure 6.3c**), for all nanofiber conditions, aligned and elongated cell morphology was maintained even if cell–

cell interactions were visible, suggesting that cells strongly respond to the physical directionality of the nanofibers. Cell elongation and alignment is common in directional materials, and in GBM the elongated morphology observed on the uncoated and HA-coated nanofibers is similar to native invasive cell morphology.

Using ImageJ, the “Li” automated threshold filter was applied to the fluorescence images in **Figure 6.3** and the cell number was quantified as shown in **Figure 6S.1a, Supplemental Information**. An increase in cell number with culture time was identified for all conditions. Additionally, after 96 hours of contact with the nanofibers, an increase in cell–nanofiber alignment was observed for all nanofiber conditions with a majority of the cell population on the 0.5% HA and uncoated (0% HA) substrates aligned between ± 10° of the horizonal (**Figure S6.1b, Supplemental Information)**. Cell morphology, quantified by aspect ratio measurements, displayed a shift to higher aspect ratios and increased cell elongation with increasing culture time from 24 to 96 hours (**Figure S6.2, Supplemental Information**). In nanofiber cultures, the 0% HA and 0.5% HA exhibited the largest population of cells with an aspect ratio ≥ 3.0, meaning the cell length was three times greater than cell width.

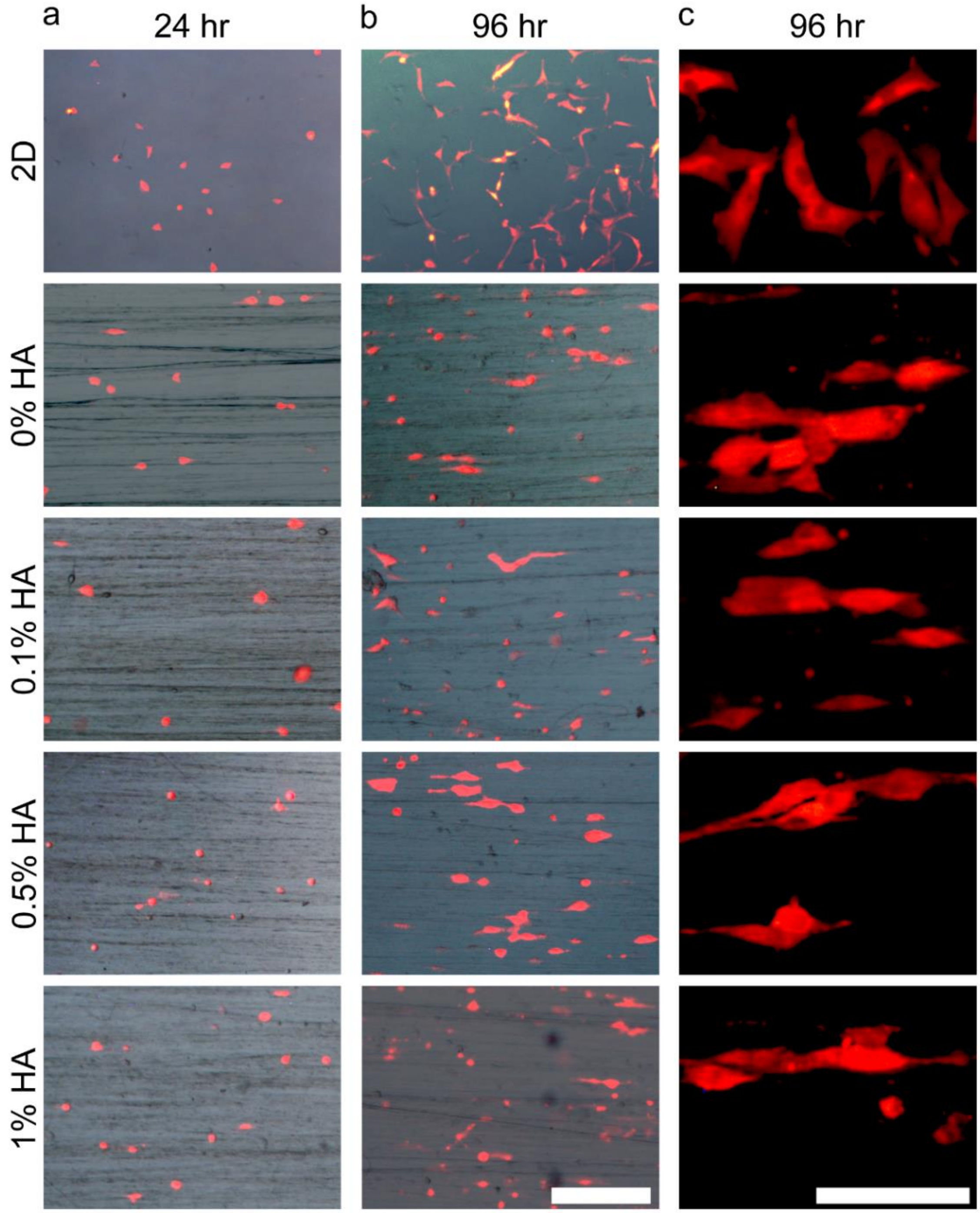

Figure 6.3. U87 MG-RFP cells (red) cultured on 2D TCPS, uncoated C-PCL nanofibers, or HA-coated C-PCL nanofibers. Representative fluorescent and bright field images were merged to show cell alignment and orientation relative to the nanofiber directionality (**a**) 24 hours (arrows indicate and inset magnifies cell protrusions) and (**b**) 96 hours of culture with inset magnifying cell protrusions. On 2D TCPS, cells were randomly oriented. On

nanofiber substrates, cells were aligned and elongated parallel to the aligned nanofibers. Scale bar in (**a**) and (**b**) represents 250 µm. Inset scale bar represents 50 µm. (**c**) A high magnification panel shows further directionality and cell elongation at 96 hours. Scale bar represents 100 µm.

Analysis of cell proliferation, alignment, and aspect ratio indicate that both uncoated and HA-coated nanofibers support attachment and proliferation of U87 MG cells and the nanofiber topography appear to influence cell morphology and alignment. The differences in extent of cell elongation among the HA-coated substrates may indicate differences in the effect of HA coating concentration on cell behavior. Longer cell exposure to the nanofiber topography resulted in an increase in directionality, alignment, and cell elongation for all nanofiber cultures. Cell elongation is an indicator of mesenchymal-like change often indicating a more invasive cell phenotype. Further, the shift to higher aspect ratio cell shapes, signifying a more spindle-like morphology, suggests that the U87 MG cells may be undergoing a mesenchymal change to a more malignant and invasive phenotype. Work by others shows that elongation of cells cultured on C–PCL nanofibers was coupled with an increase in invasion-related genes [166]. At 96 hours the 0% HA and 0.5% HA-coated nanofibers appear most conducive to promotion of cell elongation and therefore were used for further experiments.

6.4.3. Proliferative state of GBM on HA-coated nanofibers

Changes in the proliferative potential of GBM cells have been linked to chemoresistance and invasive behavior. To evaluate proliferative potential, cells associated with all culture conditions were stained with DAPI (blue) and Ki-67 (green) (**Figure 6.4)** and the percentage of Ki-67$^+$ cells quantified (**Figure 6.4a**). Ki-67, a proliferative cell marker [264], has previously been used to predict patient outcomes *in vivo* since diffuse invasion is often the result of single migratory cells that exhibit decreased apoptosis and thus a resistance to cytotoxic insult [160]. To identify possible effects of nanofiber topography on U87 MG proliferative state, nanofiber culture conditions were compared relative to 2D TCPS. Fewer proliferative cells were present on uncoated (0% HA) nanofiber substrates (45 ± 14% Ki-67$^+$ cells) relative to 2D TCPS (74 ± 12%). Further, when comparing 0.5% HA-coated to uncoated nanofibers, similar Ki-67$^+$ cell behavior was observed for both conditions where 40–45% of the cell population expressed Ki-67. When cultured on nanofibers, differences in cell behavior and morphology appeared predictive of the cell proliferative state. Single cells migrating along the nanofibers did not generally express Ki-67 (**Figure 6.4b**), whereas in cell clusters, Ki-67$^+$ expression was predominant (**Figure 6.4c**). Importantly, these types of morphological differences are prevalent in the native tumor microenvironment, where cells are generally either found in proliferative multi-cellular clusters or as single migrating cells [265]. Differences in Ki-67 expression and cell behavior were not mirrored in 2D TCPS culture.

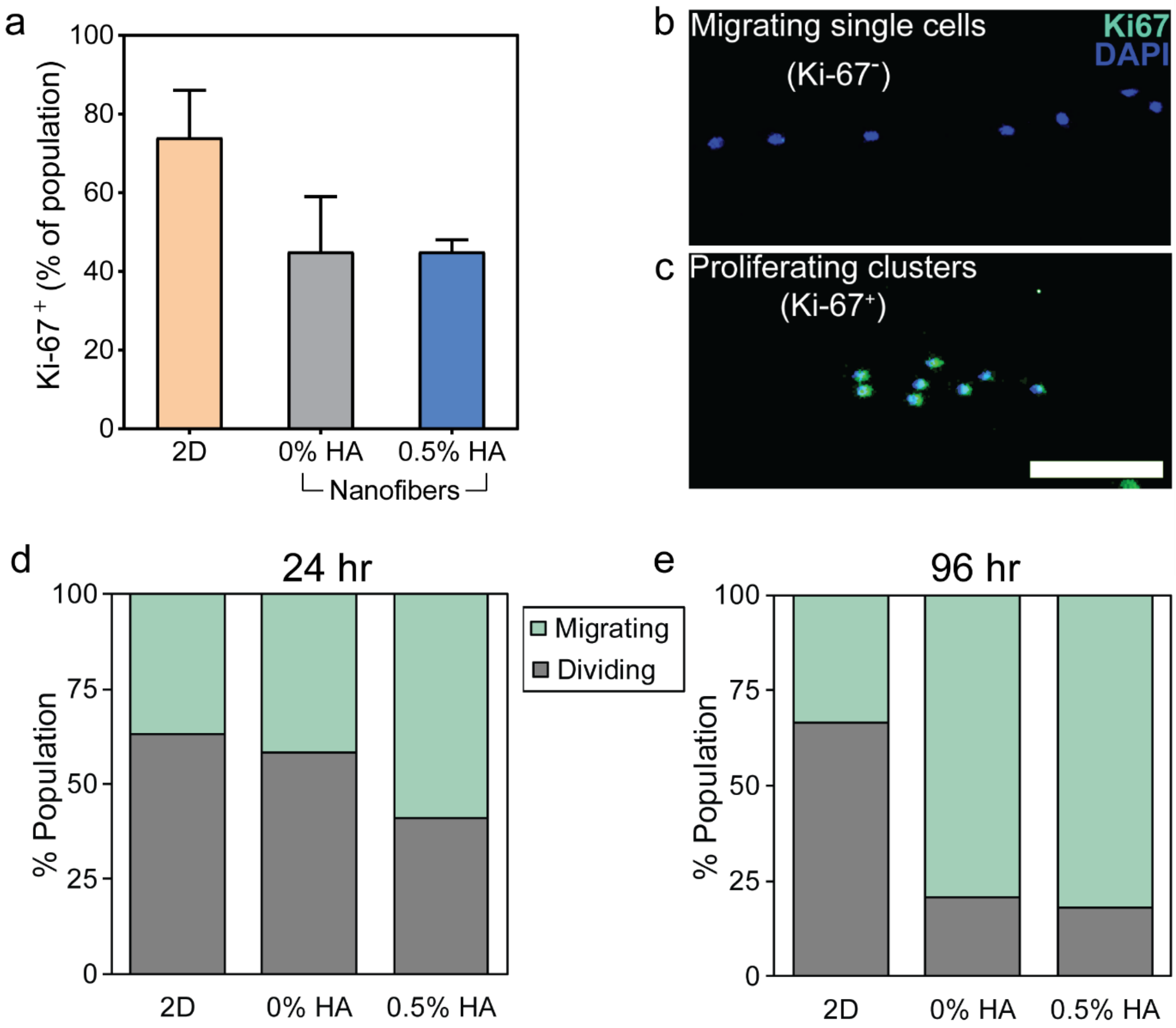

Figure 6.4. Evaluation of cell proliferative state associated with 2D TCPS, uncoated (0% HA) nanofibers, or 0.5% HA-coated nanofibers after 96 hours of culture. (**a**) Ki-67+ cells (green) as a fraction of total cell population on each substrate (n ≥ 150). Ki-67 expression by cells (**b**) aligned along a nanofiber migratory path tended to be Ki-67$^-$ as compared to (**c**) proliferative cell clusters that tended to be Ki-67$^+$. Scale bars represent 100 µm. Proliferative cell behavior over time. Fraction of observed cell population migrating (green) or dividing (gray) over a ≥13-hour time-lapse period following (**d**) 24 and (**e**) 96-hour culture period. (n ≥ 20)

To further summarize the influence of HA-coated nanofibers on GBM cells, the migratory and proliferative behavior was tracked for at least 20 individual cells for > 10 hours using time-course imaging (**Figure 6.4d and e**). At 24 hours, the majority of cells (> 50%) cultured on 2D TCPS and 0% HA nanofibers exhibited at least one division event (**Figure 4d**). These division events were less frequent in cells cultured on 0.5% HA nanofibers. Importantly, at 96 hours, the division events decreased for both nanofiber conditions and a more migratory phenotype was recorded (**Figure 6.4e**).

Previous work by others demonstrated that cells at the leading edge of a tumor have a lower proliferative capacity than cells at the tumor core [266, 267]. Further, a decrease in proliferative capacity is induced in leading edge cells when the cells migrate from the tumor site on aligned nanofiber substrates relative to 2D flat films [259]. Although the mechanisms defining proliferative versus invasive phenotypes are not well understood, the “go versus grow” hypothesis has been experimentally validated where glioma cell proliferation abates and migration is promoted and vice versa [266, 268]. A decline in proliferation of cells cultured on aligned nanofibers demonstrates that the aligned nanotopography mimics the native tumor microenvironment with cells behaving according to the “go versus grow” hypothesis, and potentially enhancing migration at the partial exclusion of proliferation.

6.4.4. Drug resistance on various HA-coated nanofibers

To evaluate the response of U87 MG cells cultured on nanofiber substrates to a therapeutic alkylator agent, we evaluated the relative resistance to temozolomide (TMZ)-induced cell death (**Figure 6.5**). Experimental groups included 2D TCPS, uncoated nanofibers, and 0.5% HA-coated nanofibers. After 96 hours of culture, media was changed for all culture conditions and the replacement media contained either 0 µM (untreated) or 100 µM TMZ. After 48 hours of culture, cell metabolic activity was evaluated by measuring alamarBlue® fluorescence intensity of treated and untreated cultures per condition and calculating the percent reduction in fluorescence intensity for each condition. Higher fluorescence intensity was considered indicative of relatively more viable, metabolically active cells. The 2D TCPS condition exhibited the most significant degree of cell death following TMZ exposure represented by a 42% ± 9% reduction in fluorescence intensity. Both nanofiber conditions treated with TMZ exhibited a slight decrease in fluorescence intensity relative to the corresponding untreated control, ranging from a 1% ± 6% reduction (0.5% HA- coated nanofibers) to an 11% ± 3% reduction (uncoated nanofibers). Direct quantification of the number of viable cells was not possible due to differing interactions of the coatings and alamarblue®, yet it is clear that cells cultured on nanofibers and exposed to 100 μM TMZ were more resistant to cell death relative to the 2D TCPS control.

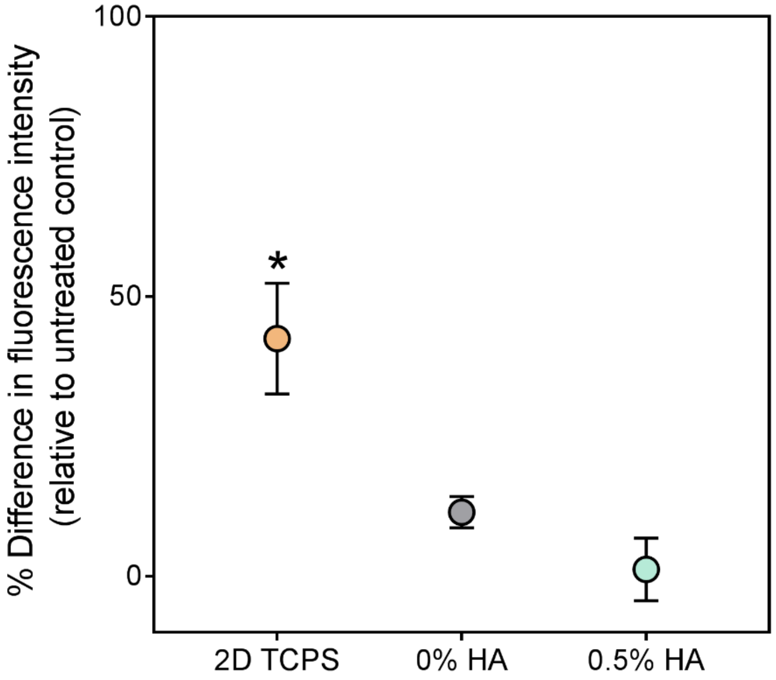

Figure 6.5. Drug resistance of U87 MG RFP to TMZ-induced cell death evaluated using alamarBlue®. All conditions were either untreated or treated with 100 μM TMZ solutions for 48 hours prior to analysis. Percent difference was evaluated by quantifying the fluorescence intensity of the treated sample relative to the untreated controls ($n \geq 3$). *Statistically significant from all conditions ($p \leq 0.05$).

6.4.5. Cell migration, speed, and displacement on various HA-coated nanofibers

To determine the influence of the nanofiber HA coating on U87 MG-RFP cell motility, cell migration on each substrate was tracked using time-course imaging beginning after 24 or 96 hours of culture. Images were acquired every 2 min for > 10 hours and examined with the semi-automated TrackMate plugin for ImageJ.[263] **Figure 6.6a and b** depict representative individual cell migration pathways on 2D TCPS and nanofiber substrates after 96 hours of culture. On 2D TCPS over the course of 246 minutes, no directional preference in cell elongation or migration is observed (**Figure 6.6a**), while cells cultured on nanofibers display an elongated spindle morphology and a consistent linear directional motion (**Figure 6.6b**). Aggregating the migration pathways of several cells cultured on each substrate demonstrates the migration pathways of several cells, where different colors represent unique paths of individual cells (**Figure 6.6c and d**). Overall, cells cultured on 2D TCPS migrated randomly with no directionality (**Figure 6.6c)** whereas cells on nanofiber substrates migrated along a linear path corresponding to fiber alignment (aligned along the horizontal) (**Figure 6.6d)**. GBM cells expressed elongated and directional behavior on both nanofiber substrates regardless of coating, indicating that topographical cues play a key role in cell migration and the nanofiber platforms were effective at directing cell locomotion.

Migratory behavior was quantified to further characterize the influence of HA coatings on cell migration. Individual cell speed over the course of 10 hours was determined by measuring the distance individual cells traveled during consecutive two-minute intervals (images captured every two minutes) for each condition (**Figure 6.6e**). On both 2D TCPS and nanofiber substrates, spikes in cell speed occurred intermittently. Bursts of increased cell speed have also been observed during live imaging of gliomas in mice and correspond to daughter cell migration after cell division.[269] Under these *in vitro* culture conditions, similar bursts of speed were observed during division events, after cell-cell interactions, or in highly migratory cells after extension of lamellipodia. Bursts in cell speed were more frequent and of higher magnitude for cells cultured on nanofibers relative to 2D TCPS. In **Figure 6.6a,** cell elongation and long protrusions result in bursts of cell locomotion similar to that seen between 56 minutes and 58 minutes. Increased cell migration and an elongated spindle morphology have been linked to a highly invasive and drug resistant phenotype. [3]

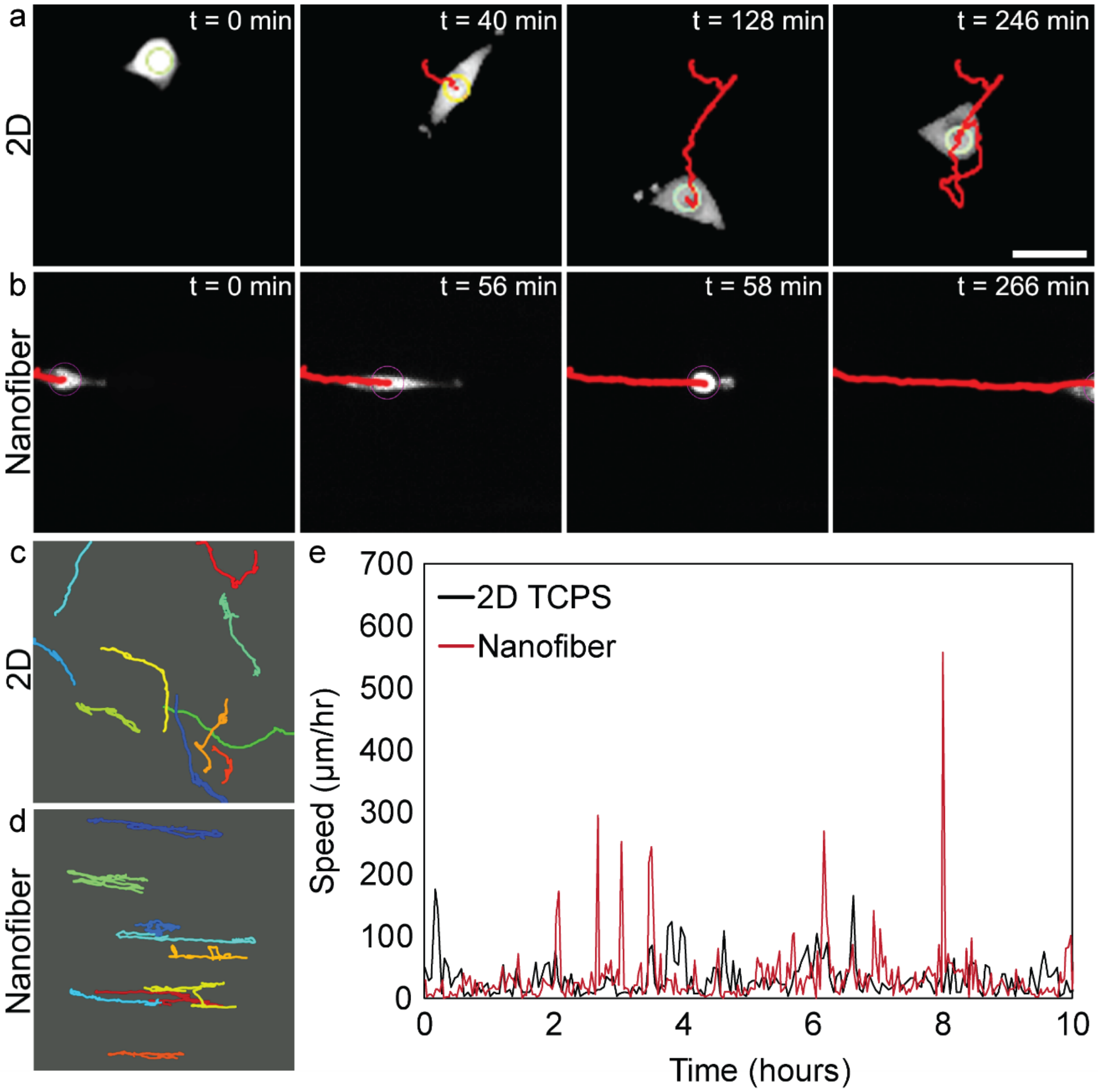

Figure 6.6. Representative cell migration characteristics associated with 2D TCPS, uncoated, and HA-coated nanofibers. Representative migration pathways of an individual cells tracked on (**a**) 2D TCPS or (**b**) nanofibers. Nanofibers were aligned parallel to the horizontal. (**c**) Aggregation of the migration pathways of several cells on 2D TCPS for ≥ 10 hours starting after 96 hours of culture where cell locomotion and elongation does not display directionality. Conversely, (**d**) the migration pathway of cells on a nanofiber substrate showing cell locomotion with clear directionality. Nanofibers were aligned parallel to the horizontal. (e) Representative migration speed versus time measured for an

individual cell on 2D TCPS and a nanofiber substrate. Speed was determined by quantifying cell displacement every 2 min for ≥ 10 hours after 96 hours of cell culture.

By averaging the cell speed from > 7 cells on each substrate, the influence of culture time and substrate on GBM motility can be determined (**Figure 6.7a**). A general increase in average cell speed is demonstrated from 24 to 96 hours, with cells on the 0.5% HA substrate exhibiting the greatest average cell speed at approximately 35 µm/hr. Maximum cell speed for each individual cell tracked was quantified (**Figure 6.7b)** and averaged for each condition. Cells cultured on the 0.5% HA substrate exhibited the highest maximum speeds. This maximum velocity is slightly greater than that seen in brain slice cultures.[265]

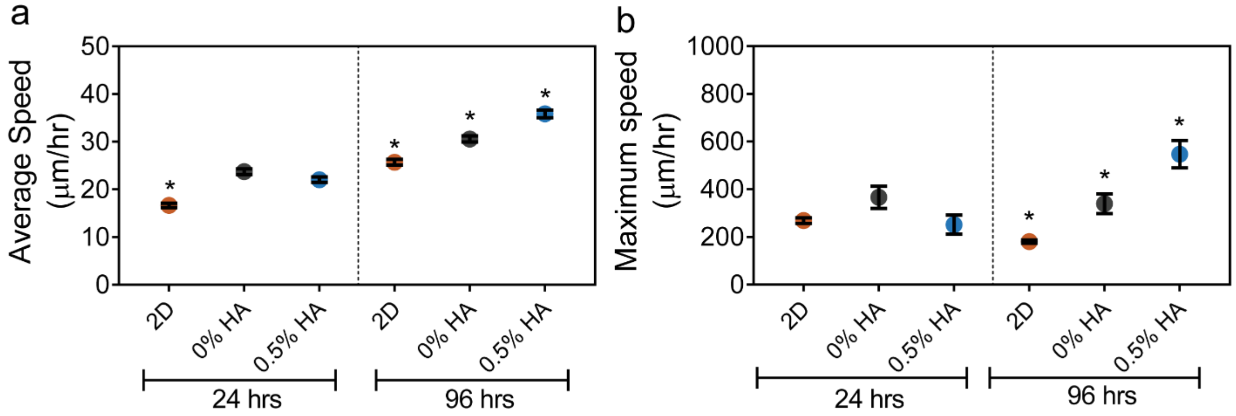

Figure 6.7. Quantification of (**a**) average cell speed ± standard error of mean (SEM) and (**b**) maximum cell speed ± standard error of mean (SEM) for cells cultured on 2D TCPS, 0% HA (uncoated), and 0.5% HA nanofibers. *Statistically significant from all conditions ($p \leq 0.05$).

The migration data shows a difference in behavior of cells cultured in the presence of different HA contents and can be used to determine the optimal HA-coating for *in vitro* brain

ECM mimics. After 96 hours, the most consistent migration, in terms of speed and distance traveled, was observed of cells cultured on 0.5% HA-coated nanofibers. This culture condition resulted in the most consistent cell displacement. Thus, the nanofiber substrates appear to promote migration behavior similar to GBM tumor cells *in vivo* and provide an unhindered migration path allowing for greater speeds *in vitro*.

6.5. CONCLUSION

Polyblend (50-50) chitosan-PCL nanofiber substrates, fabricated using a HTP-CES system are characterized by highly-aligned nanofibers with superior diameter uniformity relative to conventional electrospinning. C-PCL nanofiber substrates with biologically-relevant topography were coated with hyaluronic acid to mimic an important biochemical characteristic of brain ECM. The nanofiber substrates were evaluated as biomimetic *in vitro* substrates for studying U87 MG cell behavior in support of the development of anti-migratory therapeutics. GBM cells cultured on aligned C-PCL nanofibers and nanofibers coated with 0.1% HA - 1% HA displayed a shift at 96 hours to a highly aligned and elongated cell with a spindle morphology. Relative to 2D TCPS, cells cultured on nanofibers were characterized by lower proliferative potential coupled with increased resistance to TMZ induced cell death. Additionally, coating nanofibers with 0.5% HA increased cell displacement and cell speed suggesting a shift of the GBM cell population toward a migratory phenotype. The ability to enrich for migratory cells *in vitro* could simplify phenotypic investigation of these highly invasive cells for development of therapeutics targeted at the metastatic subpopulation. Due to the unique morphology and surface chemistry of the 0.5% HA-coated C-PCL nanofibers reported here, these nanofibers may represent better *in vitro* platforms for studying cell invasion and accelerating the discovery and commercialization of anti-migration therapeutics for control of GBM metastasis.

SUPPLEMENTARY INFORMATION

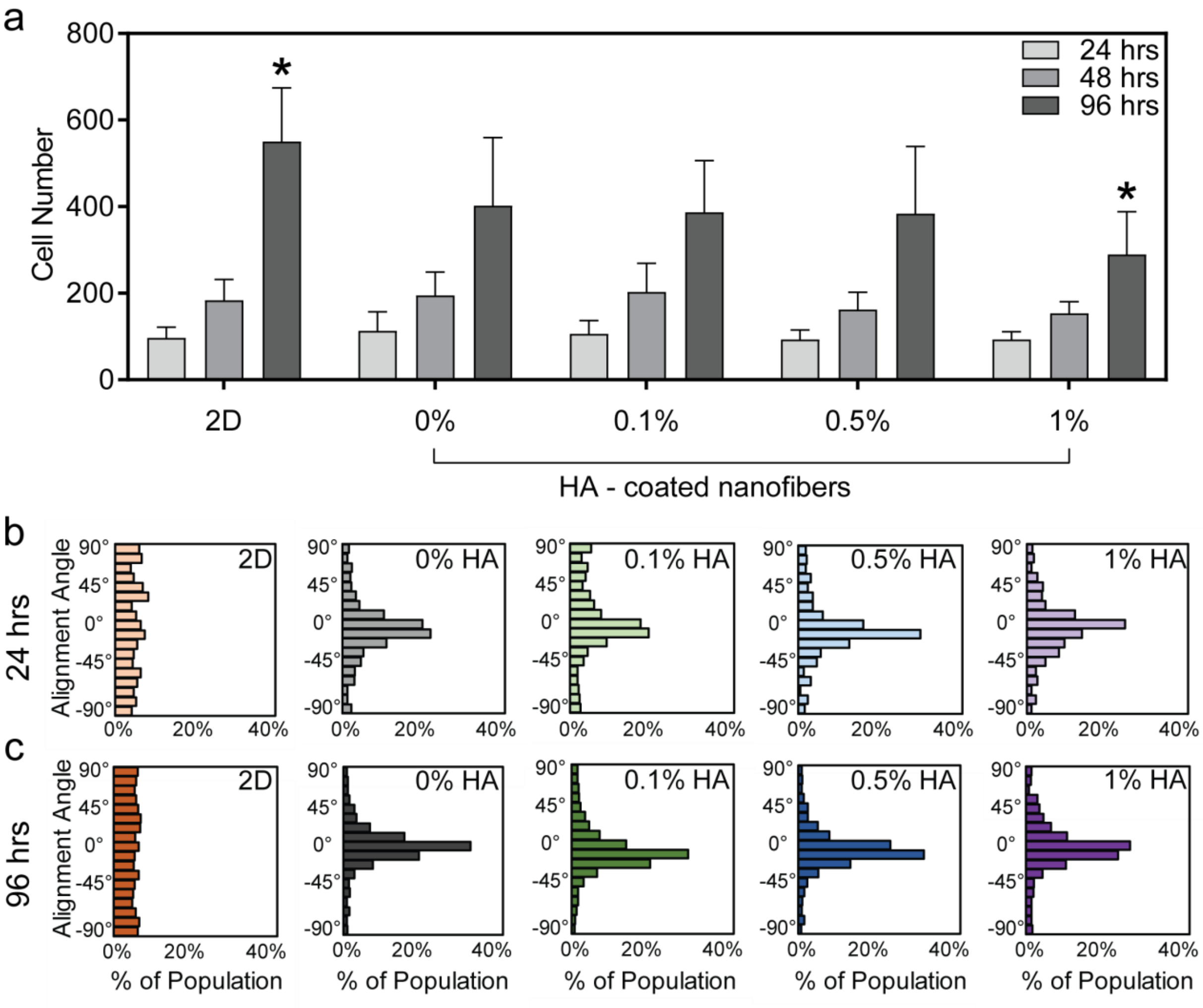

Figure S6.1. Cell proliferation and alignment on 2D TCPS versus nanofibers. (**a**) Quantification of cell number at 24, 48, and 96 hours of culture. (n ≥ 12) *Statistical significance from all other conditions ($p \leq 0.05$). Angle of U87 MG RFP cell alignment after (**b**) 24 and (**c**) 96 hours of culture on nanofibers coated with varying HA. Nanofibers were aligned along the horizontal (0°) (n ≥ 350).

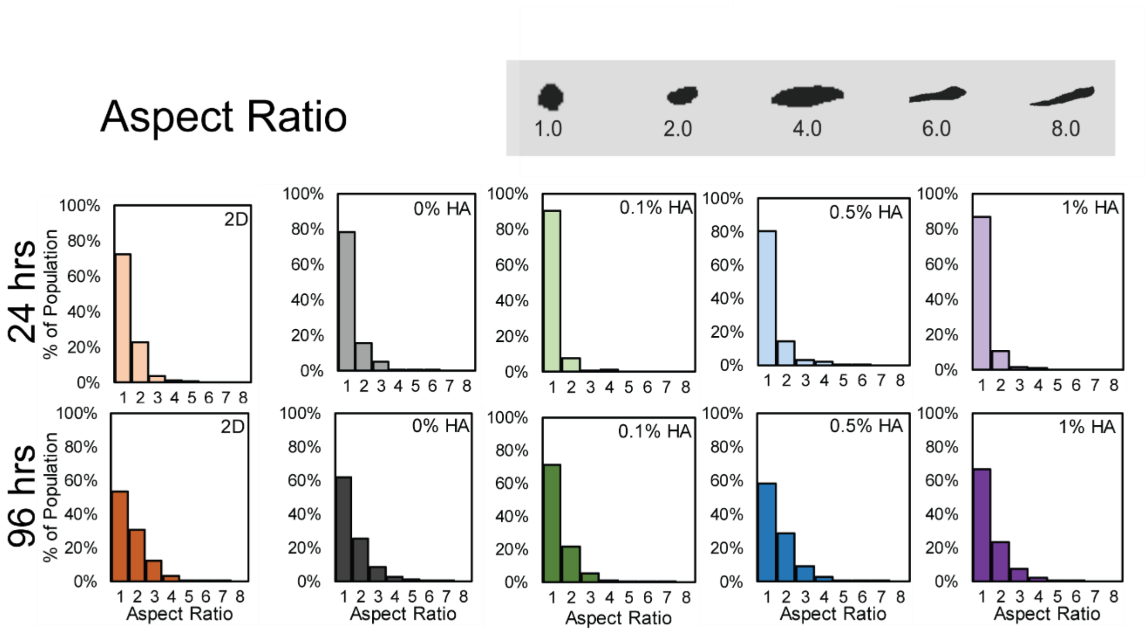

Figure S6.2. Aspect ratio of cells under various culture conditions at 24 and 96 hours. Inset shows example cell shapes for aspect ratio range. At least 350 cells were counted for each condition.

Chapter 7: FABRICATION AND CHARACTERIZATION OF CHITOSAN-HYALURONIC ACID SCAFFOLDS WITH VARYING STIFFNESS FOR GLIOBLASTOMA CELL CULTURE

7.1. ABSTRACT

The invasive and recurrent nature of glioblastoma multiforme (GBM) is linked to a small subpopulation of cancer cells, which are self-renewing, resistant to standard treatment regimens, and induce formation of new tumors. Matrix stiffness is implicated in the regulation of cell proliferation, drug resistance, and reversion to a more invasive phenotype. Therefore, understanding the relationship between matrix stiffness and tumor cell behavior is vital to develop appropriate *in vitro* tumor models. Here, we fabricate chitosan–hyaluronic acid (CHA) polyelectrolyte complex (PEC) scaffolds with statistically significant stiffness variances to characterize the effect of scaffold stiffness on morphology, proliferation, drug resistance, and gene expression in human glioblastoma cells (U-87 MG). All scaffolds supported GBM proliferation over a 12-day culture period, yet larger spheroids were observed in scaffolds with higher stiffness. Additionally, GBM cells cultured in stiffer (8% CHA) scaffolds proved significantly more resistant to the common chemotherapeutic temozolomide. Moreover, the stiffer 8% CHA scaffolds exhibited an increase in expression of drug resistance and invasion related genes compared to 2D culture. CHA scaffolds present a tunable microenvironment for enhanced tumor cell malignancy and may provide a valuable *in vitro* microenvironment for studying tumor progression and screening anticancer therapies.

7.2. INTRODUCTION

Glioblastoma multiforme (GBM) is a highly invasive, primary, malignant brain tumor [270, 271]. Clinical treatment generally utilizes tumor resection followed by chemotherapy and radiation therapy; yet median survival time is approximately 15 months [272, 273]. Unlike other solid tumors, GBMs rarely invade the vasculature to metastasize outside of the brain [274]. Instead, high mortality is attributed to the invasion of therapy-resistant cancer cells located away from the primary tumor that evade resection and initiate tumor recurrence [275]. This behavior suggests that the local brain microenvironment plays a key role in regulation of GBM progression and recurrence [274]. Studies investigating the correlation between matrix stiffness and GBM malignancy yield disparate *in vivo* and *in vitro* results, indicating a critical lack in understanding of GBM progression. Development of novel therapeutics also remains challenging because the response of drug candidates differs among *in vitro* cell lines, animal tumor models, and human tumors. Therefore, to improve our understanding of tumor biology and to develop novel therapeutics for complete GBM eradication, new tools are required to model GBM tumor progression.

Malignant cancer cell behavior is highly influenced by biochemical and biomechanical cues in the surrounding microenvironment. Studies show that tumor microenvironment biomechanics play a significant role in cancer progression including tumor invasion, metastasis, and reversion of tumor cells into cancer stem cells (CSCs) [116, 230, 276, 277]. The tumor extracellular matrix (ECM) is often stiffer than the ECM of surrounding stroma, as is the case for GBM, and studies indicate that increasing matrix stiffness induces the epithelial-to-mesenchymal transition (EMT) [278]. EMT plays a significant role in tumor formation and metastasis [279] and is often linked to a more malignant cell phenotype [230, 276, 280]. Therefore, matrix elasticity of *in vitro* platforms for GBM cell culture should be tunable to encompass both healthy and cancerous tissue in order to study how differences in elasticity affect cell behavior and GBM tumor progression.

Evidence that matrix stiffness regulates multiple characteristics of cancer cells has led to many studies of matrix stiffness and corresponding cell behavior in 2D cultures. Two-dimensional platforms, such as tissue culture polystyrene (TCPS), are effective in promoting GBM cell proliferation when used for monolayer culture, but do not adequately mimic *in vivo* tumor environments. More complex, spherical cancer models such as nonadherent cancer cell line-derived spheroids, or spheroids derived from primary tumor dissociation, promote cell–cell interactions and are frequently used for cancer cell culture. Importantly, nonadherent cultures lack the cell–matrix interactions present in native tumor stroma [281, 282]. Three-dimensional culture platforms, such as hydrogels or scaffolds, promote both cell–cell and cell–matrix interactions and present a diffusion-limited environment not found in 2D cultures. This can result in enrichment of tumor-derived cells with a more malignant, adherent spheroid morphology [182, 283-288]. Many three-dimensional (3D) environments for cancer cell culture are fibrillar protein-based hydrogels [289-291], which do not reflect the glycosaminoglycan (GAG)-based brain ECM. Further, in animal-derived hydrogels, batch-to-batch variability and compositional complexity pose problems [288, 292]. More recently, studies utilizing hyaluronic acid (HA)-based hydrogels have elucidated many important aspects of GBM CSC phenotype, motility, and behavior. Yet HA gels are mechanically weak; thus, control over matrix stiffness and tumor sphere formation is challenging.

Here we present the fabrication and characterization of HA-based, porous scaffolds as potential *in vitro* platforms for modeling the GBM microenvironment. The porous chitosan–hyaluronic acid (CHA) scaffolds of varied stiffness were fabricated using a simple phase separation method with high reproducibility, providing an alternative to hydrogels. HA, an anionic natural polymer, is a major GAG component of the brain ECM [293]. Chitosan, a naturally occurring polysaccharide with a structure similar to GAGs, is cationic and biocompatible [294]. When blended together, chitosan and HA form a stable, polyelectrolyte complex (PEC) enhancing the stability of both natural polymers. Changing the total polymer concentration of CHA scaffolds by varying the chitosan content alters the scaffold microstructure and stiffness in a range encompassing the mechanical properties of normal brain tissue to malignant gliomas. Material properties of CHA scaffolds were characterized including stiffness, density, porosity, polyelectrolyte composition, and swelling behavior. U-87 MG RFP GBM cells were cultured in CHA and on TCPS to compare and evaluate cell morphology, proliferation, dose-dependent drug response, and gene expression.

7.3. EXPERIMENTAL SECTION

7.3.1. Materials

All chemicals were purchased from Sigma-Aldrich (St. Louis, MO) unless otherwise specified. Chitosan (from shrimp shells, practical grade, $\geq$ 75% deacetylated) and hyaluronic acid (hyaluronic acid sodium salt, from *Streptococcus equi*) were used as received.

7.3.2. Preparation of chitosan-hyaluronic acid scaffolds

Chitosan and hyaluronic acid (CHA) blend scaffolds were prepared by first dissolving chitosan (2, 4, or 8 wt%) and hyaluronic acid (1 wt%) separately in 1 wt% acetic acid solution. The solutions were individually mixed for three minutes using a Thinky mixer (ARM-300, Thinky USA, Laguna Hills, CA) at 2000 rpm. Mixing was repeated at least three times to ensure each solution was completely dissolved. The solutions were aged overnight at room temperature to ensure complete dissolution. After aging, the chitosan and hyaluronic acid solutions were mixed again individually for 3 minutes at 2000 rpm. The solutions were combined and mixed three times with the Thinky prior to casting into 24-well tissue culture plates. The plates were refrigerated at 4ºC for 12 hours, frozen at -20°C for 24 hours, and lyophilized for 36 hours with a Labconco Freezone 6 Plus freeze drier (Labconco, Kansas City, MO). The scaffolds were sectioned to obtain 2 mm thick discs, neutralized in 15 vol% ammonium hydroxide for 1 hour under vacuum, washed four times with DI water, and allowed to soak in D-PBS overnight to ensure the removal of any residual base. Neutralized scaffolds were sterilized with 70% ethanol for 1 hour under vacuum, transferred to sterile D-PBS, and placed on an orbital shaker overnight prior to *in vitro* cell culture experiments. Scaffold naming convention and corresponding polymer content (2% CHA, 4% CHA, 8% CHA) are summarized in **Table 7.1**.

Table 7.1. Summary of CHA scaffold naming convention and polymer content. Naming convention is based on chitosan solution content. For all scaffolds the HA content was 1 wt%.

CHA scaffold	Chitosan solution polymer content	HA solution polymer content	Combined CHA solution polymer content
2% CHA	2 wt%	1 wt%	1.5 wt% CHA
4% CHA	4 wt%	1 wt%	2.5 wt% CHA
8% CHA	8 wt%	1 wt%	4.5 wt% CHA

7.3.3. Scanning electron microscopy

Scanning electron microscopy (SEM) was utilized to visualize scaffolds before and after cell culture. Prior to cell culture, dry scaffolds were mounted directly on stubs using carbon tape. After cell culture, samples were fixed with 10% formalin at 4ºC overnight, dehydrated through an ethanol series (0%, 30%, 50% 70%, 90%, 100% ethanol), critical point dried with a Denton DCP-

1 critical point dryer (Denton Vacuum, Moorestown, NJ), sectioned, and mounted on stubs using carbon tape. All samples were sputter coated with Au/Pd for 90 s before imaging with a FEI Sirion XL30 Field Emission SEM (FEI, Hillsboro, OR).

7.3.4. Fourier transform infrared spectroscopy

The interaction between chitosan and hyaluronic acid in forming polyelectrolyte complexes was characterized using Fourier transform infrared spectroscopy (FTIR) and compared to spectra of pure chitosan and pure hyaluronic acid samples. Scaffolds of each blend were sectioned, ground into a powder with KBr and pressed into pellets. Spectra of 64 scans at 2 cm^{-1} resolution were obtained using a Nicolet 5DX spectrometer.

7.3.5. Scaffold density

The apparent bulk density of scaffolds was calculated after measuring individual scaffold mass and volume (n = 8). Scaffold diameters were measured using a micrometer to calculate scaffold volume and mass measured to the ten-thousandth of a gram.

7.3.6. Scaffold porosity

The porosity of CHA scaffolds was measured using a modified liquid displacement method [295, 296]. Isopropanol was utilized as the displacement liquid as it is a nonsolvent and easily penetrates the porous structure with minimal volume change. Briefly, the dry scaffold volume (V_i) and weight (W_i) were recorded. The scaffold was fully immersed in 5 mL of isopropanol of known density (ρ_i) for 15 minutes during which time the scaffold stopped releasing air bubbles and sank to the bottom of the container. The impregnated scaffold was removed from the isopropanol and weighed (W_f). Using **Equation 1**, we calculated porosity as a ratio of volume of solvent within the scaffold pores to the volume of the dry scaffold (n = 12).

$$\boldsymbol{Porosity = \frac{(W_f - W_i)/\rho_i}{V_i} \times 100} \tag{1}$$

7.3.7. Scaffold pore size

Individual pore area was measured from three representative SEM micrographs using ImageJ software. Three separate SEM micrographs were used per scaffold condition to determine median pore area. To ensure consistency in selection of measured pores, two intersecting lines were overlaid on each micrograph. One line was placed from the top left corner to the bottom right corner of the image. A second line was placed extending from the top right corner to the bottom left corner, resulting in an “X”. Pores intersecting the lines were outlined using the freehand selection function in ImageJ and the area measured. At least 90 pores were measured per scaffold condition.

7.3.8. Mechanical testing

The stress versus strain behavior of D-PBS-hydrated scaffolds under compression was measured at room temperature using a Shimadzu universal tester (AGS-X Series, Kyoto, Japan). Scaffolds of 2 mm in height and 17 mm in diameter were compressed at a rate of 0.4 mm/min until at least 40% strain was attained (n = 8). The compressive modulus was calculated as the slope of the linear region of the stress–strain curve (0–10% strain).

7.3.9. Cell culture

The human glioblastoma cell line, U-87 MG, was purchased from American Type Culture Collection (Manassas, VA). Cells were transfected with pRFP-N2 using Lipofectamine 2000 reagent according to manufacturer’s instructions. Forty-eight hours after transfection, the cells were washed with D-PBS and cultured in fresh media containing G418 (500 µg/mL) for selection of the stably transfected population. Two weeks after selection, U-87 MG RFP cells were sorted by fluorescence activated cell sorting (FACS; Vantage SE). Cells were maintained in Minimum Essential Medium (MEM) (Thermo Fisher Scientific, Grand Island, NY) containing 10% FBS and 1% antibiotic–antimycotic at 37°C and 5% CO_2 in a humidified environment. U-87 MG RFP cells (37,500 cells at 1.25×10^6 cells/mL) were seeded onto scaffolds and maintained for 2 hours in an incubator for cell attachment. Following the attachment period, fully supplemented media were added, and cells cultured for 12 days with regular medium changes. Cells were imaged on days 2, 6 and 12 with a Leica SP8X confocal microscopy (Leica, Buffalo Grove, IL).

7.3.10. Proliferation analysis:

Growth kinetics of U-87 MG RFP cells cultured on CHA scaffolds and 2D tissue culture polystyrene (TCPS) were determined using the alamarBlue® metabolic assay and following the manufacturer's protocol (Life Technologies). Briefly, cells (37,500) were cultured on TCPS or CHA scaffolds in a 24-well plate for 3, 6, 9, or 12 days. An alamarBlue® working solution (10% Resazurin and 90% fully supplemented medium) was then added to each well and incubated at 37°C for a predetermined time (2 hrs for 2D and 4 hrs for CHA scaffolds). Then aliquots of the alamarBlue® solution were transferred to a black-bottom 96-well plate and the fluorescence intensity was measured on a microplate reader. The cell number was determined using standard curves. Cells were rinsed with D-PBS to remove residual alamarBlue® solution and the fully supplemented medium was added to each well for further culture.

7.3.11. Drug response analysis

For 3, 6, or 12 days U-87 MG RFP cells were grown in 2D and CHA scaffolds. The scaffolds were then treated with temozolomide (TMZ) for 24 hrs. After 24 hrs, the medium containing the drug was replaced with fresh medium. Cell viability was examined 24, 48, or 72 hrs after treatment using the alamarBlue® assay as described previously. Viability was reported as a percent of viable cells relative to an untreated control.

7.3.12. PCR

Cells were detached from TCPS or the CHA scaffolds using TripLE and RNA was extracted using the Qiagen RNeasy kit (Qiagen, Valencia, CA) following the manufacturer's protocol. An iScript cDNA synthesis kit (Bio-Rad, Hercules, CA) was used for reverse transcription (RT) to prepare cDNA following the manufacturer's instructions. DNA transcripts were probed using SsAdvanced Universal SYBR Green Supermix (Bio-Rad) with the primers listed in **Table 7.2**. Thermocycling was performed in 10 µL solution containing 5 µL SYBR Superrmix, 300 nM primers (Integrated DNA Technologies, Coralville, IA), and cDNA at concentration 4 ng/µL. The thermocycle was performed on BioRad CFX96 System at 95°C for 2 min, 40 cycles at 95°C for 15 s, 58°C for 30 s, and 72°C for 30 s. All qRT-PCR data was analyzed with the CFX Manager software (Bio-Rad) with expression levels normalized to GAPDH and standard error of mean calculated.

Table 7.2. Primers used for PCR to evaluate chemoresistance (ABCG2), hypoxia (HIF-1α), and invasion (CD44, MMP-2, and TWIST1). Expression levels were normalized to GAPDH.

Target	Forward (5'-3')	Reverse (5'-3')
GAPDH	GGT GTG AAC CAT GAG AAG TAT GA	GAG TCC TTC CAC GAT ACC AAA G
ABCG2	GTC GGT GTG CGA GTC AGG GC	CTT GCC TCC GCC TGT GGG TC
CD44	AAC GCT TCA GCC TAC TGC AAA	TCT TCC AAG CCT TCA TGT GAT G
MMP-2	GAG TTG GCA GTG CAA TAC CT	GCC GTC CTT CTC AAA GTT GT
TWIST1	AAT CGA GGT GGA CTG GGA AC	CTT ACG AGG AGC TGC AGA CG

7.3.13. Statistical analysis

Results are presented as mean values ± standard deviation unless otherwise specified. Box plot whiskers represent the 10–90 percentile with the “+” denoting the mean. The drug response profiles were fitted using a nonlinear three-parameter dose response curve in GraphPad Prism 7 (Prism version 7.04, Graph Pad Software, San Diego, CA). Statistical significance was determined using one-way or two-way analysis of variance (ANOVA) followed by post-hoc Tukey’s test for multiple comparisons conducted using GraphPad. Values were considered statistically significant at $p \leq 0.05$.

7.4. RESULTS AND DISCUSSION

7.4.1. CHA scaffold structural and chemical properties

Brain ECM, unlike fibrillar protein-rich ECM of other tissues, is predominantly composed of glycosaminoglycans (GAGs), like hyaluronic acid (HA) [255]. The structure and physical cues of brain ECM are implicated in the induction of highly aggressive cancer cell behavior resulting in metastatic characteristics unlike those of other solid tumors [297]. HA is highly prevalent in glioblastomas where GBM cells overexpress HA receptors, CD44 and RHAMM [293, 298-301]. Moreover, the presence of HA in the tumor stroma is associated with enhanced tumor growth and progression [293]. Therefore, a 3D culture platform that mimics the properties of the GBM microenvironment should contain HA. Pure HA scaffolds are not feasible for this purpose because of their insufficient mechanical properties and failure to promote cell adhesion due to their anionic nature [302]. Chitosan, a naturally occurring polysaccharide with a chemical structure similar to GAGs, is cationic and biocompatible [294]. When blended together, chitosan and HA form a stable, polyelectrolyte complex (PEC) combining the positive attributes of both materials, representing a rational material system to recapitulate brain ECM for *in vitro* GBM cell culture.

Fabrication of chitosan–hyaluronic acid (CHA) PEC scaffolds can be accomplished via thermally induced phase separation (TIPS) of an aqueous phase and polymer-rich phase followed by lyophilization resulting in a highly porous structure amenable to cell culture.

As summarized in **Table 7.1**, the hyaluronic acid content of PEC scaffolds remained constant (1 wt%) whereas the chitosan concentration varied from 2 wt% to 8 wt%. With 1 wt % HA in all scaffolds, the overall scaffold polymer content was 1.5 wt% ("2% CHA" scaffold), 2.5 wt% ("4% CHA" scaffold), or 4.5 wt% ("8% CHA" scaffold).

Figure 7.1a displays hydrated CHA scaffolds where 2% CHA appears most translucent due to low polymer content. **Figure 7.1b-g** depicts the scaffold microstructure as observed using scanning electron microscopy (SEM). CHA scaffolds of all compositions are highly porous with interconnected pores. The formation of a porous structure is attributed to the phase separation of the aqueous solvent and PEC, followed by solvent crystal nucleation and growth during the freezing step. The open porous structure remains following sublimation during lyophilization. The 2% CHA scaffold (**Figure 7.1b, c**) displays a more bimodal pore distribution with small pores embedded in larger pores, forming interconnections between adjacent pores. As the polymer content increased to 8% CHA **(Figure 7.1f, g)**, the presence of these small interconnections decreased due to the increase in solution viscosity. The viscosity of the higher polymer content solution hinders dendritic ice crystal formation, thereby decreasing the interconnections between adjacent walls of the pore structure [46, 303]. **Figure 7.1h** summarizes the apparent density of CHA scaffolds, which increased with increasing polymer concentration and is significantly different among all scaffold compositions ($p \leq 0.05$). By visual examination, hydrated 8% CHA scaffolds were more opaque than 4% and 2% CHA scaffolds (**Figure 7.1a**). This trend of increasing density with increasing polymer concentration was expected as more polymer is present per scaffold volume.

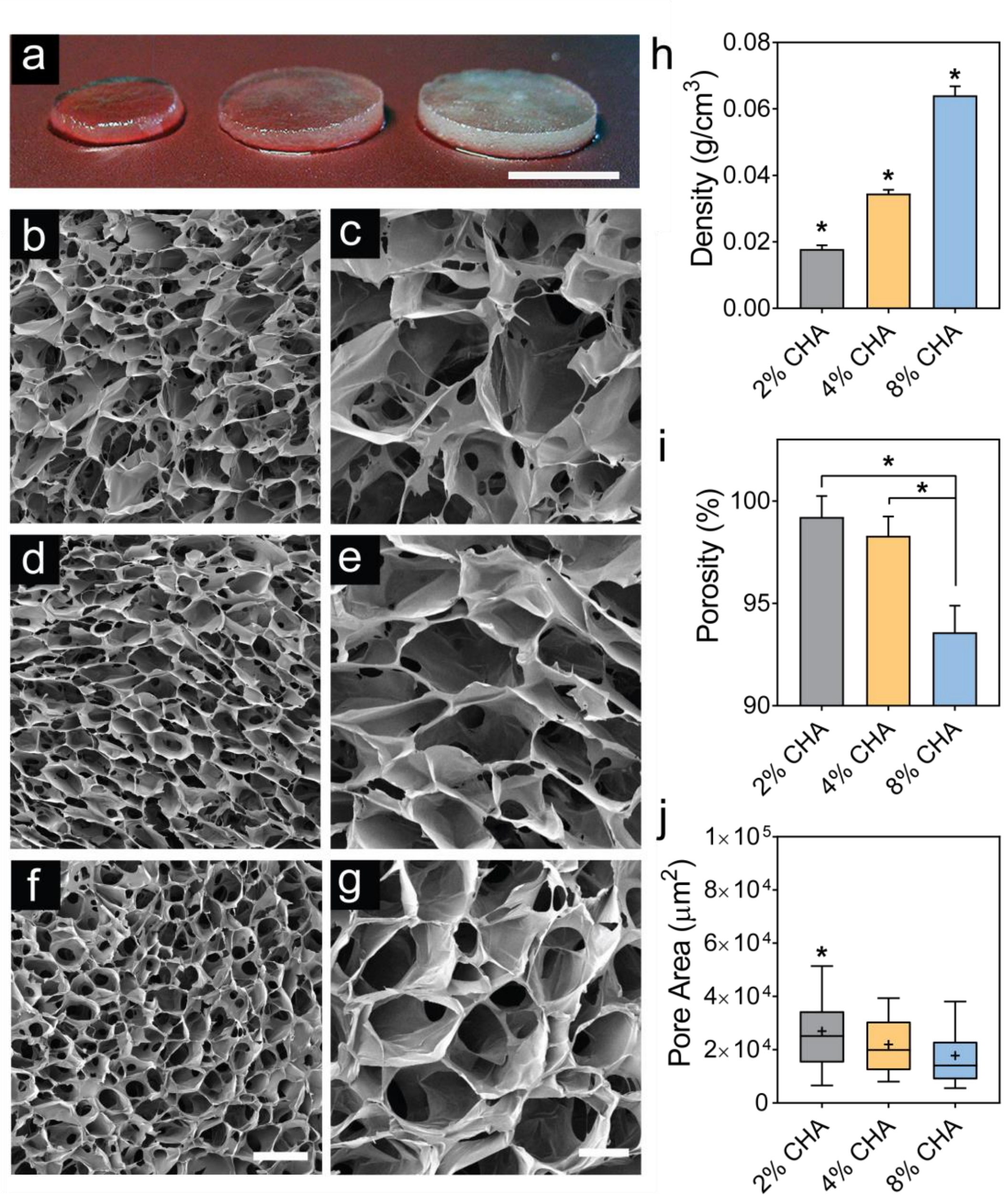

Figure 7.1. Physical properties of CHA scaffolds. (**a**) Macroscale photograph of D-PBS-hydrated CHA scaffolds (left to right: 2% CHA, 4% CHA, 8% CHA). Representative scanning electron micrographs of (**b-c**)_2% CHA, (**d-e**) 4% CHA, and (**f-g**) 8% CHA scaffolds depicting a highly porous scaffold microstructure. Scale bars represent (**a**) 4 mm, (**b, d, f**) 300 µm, and (**c, e, g**) 100 µm. (**h**) Apparent density of CHA scaffolds presented as

mean ± SD (n = 8). **(i)** Total scaffold porosity presented as mean ± SD (n=12) and **(j)** pore area of CHA scaffolds (n = ≥ 90) where "+" denotes mean pore size. P-values were calculated using one-way ANOVA where (*) indicates a significant difference from all other conditions ($p \leq 0.05$).

Liquid displacement was utilized to measure bulk scaffold porosity, which was greater than 90% for all scaffold compositions (**Figure 7.1i**), thereby confirming the presence of interconnected pores. Importantly, an open, interconnected pore structure is critical for maintenance of healthy cells *in vitro* by allowing for diffusion of nutrients, oxygen, and waste. The porosity of 8% CHA scaffolds (94%) is significantly lower than that of 2% CHA (99%) and 4% CHA (98%) scaffolds ($p \leq 0.05$), which corresponds to higher polymer content, thicker pore walls, and decreased interconnections between pores.

The pore diameter associated with the different scaffold compositions was estimated and compared by measuring the area of pore cross-sections from SEM micrographs. **Figure 7.1j** presents the mean (denoted by "+"), median, interquartile range, and 10/90 margin of the pore size distribution for each scaffold composition. The median pore size, in terms of cross-sectional area, was 2.51×10^4 µm^2, 1.99×10^4 µm^2, and 1.41×10^4 µm^2 for the 2%, 4%, and 8% CHA scaffolds, respectively, with the 2% CHA scaffold containing significantly larger pores ($p \leq 0.05$). The CHA scaffold pores were not perfectly spherical. thereby precluding direct measure of pore cross-sectional diameter. For reference, if the average pore areas reported above represented circular pore cross-sections, the corresponding pore diameters would be approximately 179 µm (2% CHA), 159 µm (4% CHA), and 134 µm (8% CHA). These values fall in the range of relevant pore sizes for porous scaffolds useful for *in vitro* cell culture [304-306]. Overall, there was a trend of decreasing pore size associated with increasing polymer content.

7.4.2. FTIR analysis of the CHA polyelectrolyte complex

The CHA scaffolds were analyzed using FTIR to confirm the formation of a CHA polyelectrolyte complex after blending individual polymer solutions (**Figure 7.2**). In the range of 2800–3500 cm^{-1}, two broad absorption bands characteristic of polysaccharide structures are visible for all five spectra. These bands represent the O-H stretching vibration (3000–3700 cm^{-1}) and the C-H stretching vibration (2800–3000 cm^{-1}) [307]. In the fingerprint regions of the spectra (**Figure 7.2**, right panel), amide and carbonyl vibrations result in several distinctive bands between 1500 cm^{-1} and 1700 cm^{-1}. The chitosan spectrum (**Figure 7.2*i***) displays two characteristic bands: a prominent amide I band (C=O vibration) at 1653 cm^{-1} and the overlapping amide II band as well as the N-H bending vibration of the deacetylated amine groups at 1570 cm^{-1} [182]. The carbonyl stretching vibration region of the HA spectra (**Figure 7.2*v***) (1500–1800 cm^{-1}) reveals three absorption bands where the highest intensity peak at 1618 cm^{-1} is derived from the asymmetric stretching vibration of the carbonyl group (COO-) [307]. Additionally, the carbonyl band overlaps an amide I shoulder (-C=O- stretching of carboxylic acid groups) at 1648 cm^{-1} and an amide II band at 1579 cm^{-1}.

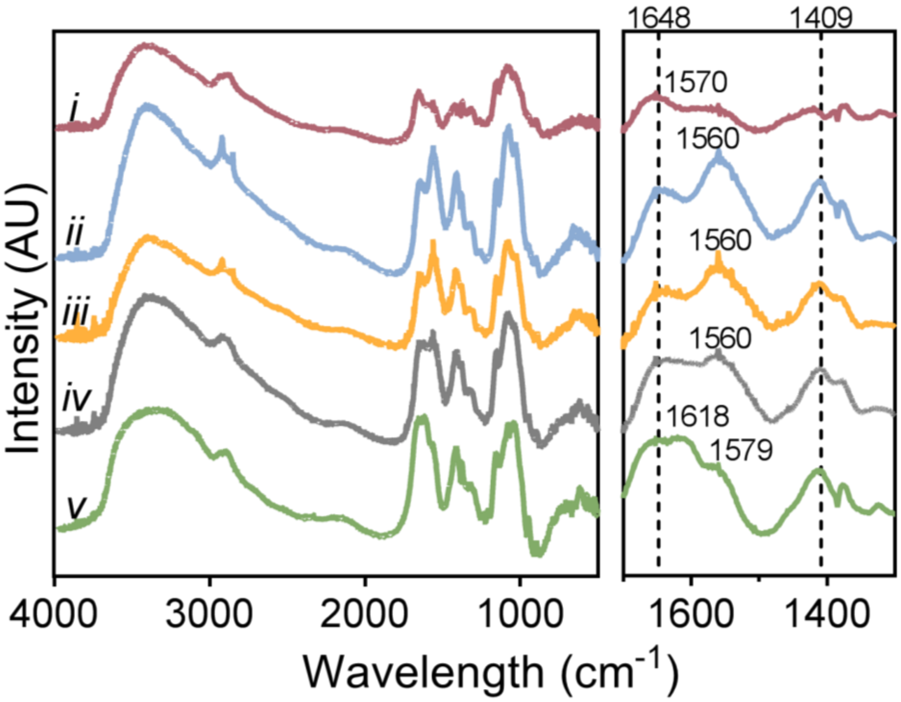

Figure 7.2. Chemical analysis confirming CHA polyelectrolyte complex (PEC) in scaffolds. Fourier transform infrared spectroscopy (FTIR) analysis of (i) pure chitosan, (ii) 8 wt%, (iii) 4 wt%, and (iv) 2 wt% CHA PEC scaffolds, and (v) pure hyaluronic acid.

In the spectra representing CHA blends, **Figure 7.2(*ii*-*iv*)**, the amide II band intensifies and shifts to lower wavelengths (~1560 cm^{-1}) when compared to the pure chitosan or pure HA spectra. The amide I band (~1648 cm^{-1}), prominently displayed in the pure chitosan, is more pronounced in CHA blends, but presents as a small shoulder to the carbonyl stretching vibration band in pure HA. Additionally, a prominent peak in HA at 1409 cm^{-1} is mirrored in all CHA blends with a similar high intensity, but the peak intensity is lower in the pure chitosan. These peak shifts and changes in band intensities suggest the formation of a PEC between the positive amino groups in chitosan and the negative carboxyl groups in HA [182].

7.4.3. Mechanical properties of CHA scaffolds

CHA scaffold stiffness was determined via mechanical testing under compression of hydrated scaffolds. **Figure 7.3a** displays representative compressive stress–strain curves for hydrated CHA scaffolds of varying polymer composition. As the polymer concentration and density of the scaffolds increase, the characteristic regimes for compressing polymer foams are more pronounced and are best depicted by the 8% CHA scaffold. Here, the scaffold initially experiences linear elastic deformation followed by a slight plateau where the stress is less affected by each successive increase in strain, and finally densification, where the pore walls collapse, and the polymer is compressed as a bulk solid [308]. The differing densities among the scaffolds are apparent during the densification phase where stress loading on the scaffold increases with polymer content. **Figure 7.3b** shows that the compressive Young's modulus of fully hydrated CHA scaffolds increases with increasing polymer content from approximately 1.41 kPa for 2% CHA to 27.7 kPa for 8% CHA. The compressive moduli of all scaffolds are significantly different ($p \leq 0.05$), and the moduli range is biologically relevant. Native brain tissue has a compressive modulus in the range of ~0.2–1 kPa [309, 310], and glioma tissue is thought to be stiffer, although conclusive values have not been determined due to the challenges associated with procuring test samples of relevant size [167, 310]. Netti et al., reported a compressive modulus of 26 kPa for tumors generated from human GBM cells using a mouse xenograft model [311].

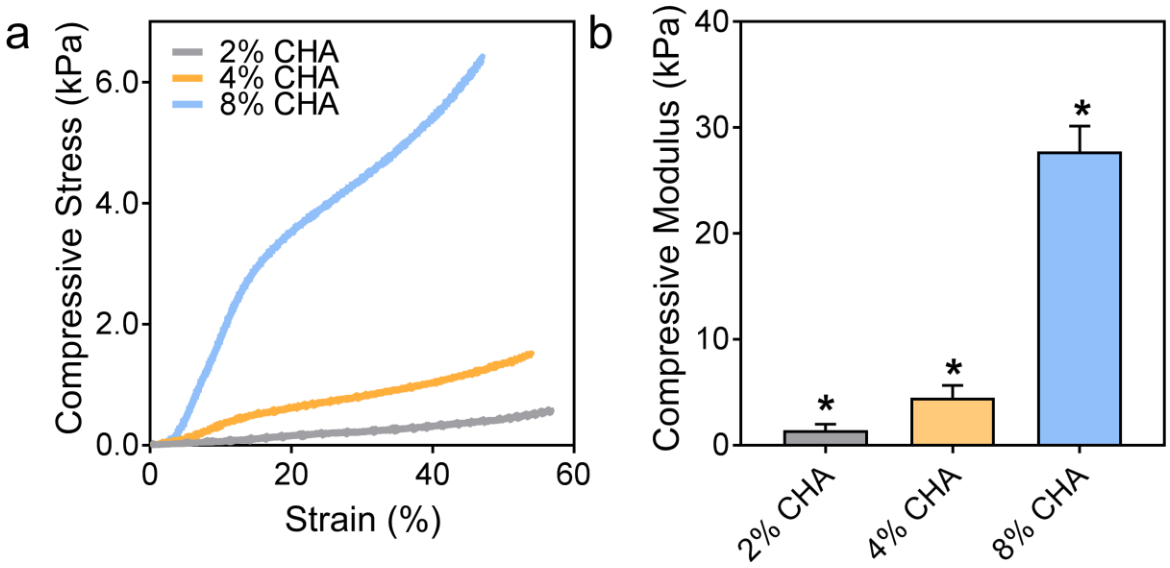

Figure 7.3. Increasing compressive stiffness with increasing polymer content in hydrated CHA scaffolds. (a) Representative compressive stress–strain curves of hydrated CHA scaffolds and (b) mean compressive moduli where the moduli of all scaffolds are significantly different (n = 8). (*) indicates significant difference from all conditions ($p \leq 0.05$).

7.4.4. Proliferation and morphology response of GBM to varied CHA scaffold stiffness

GBM cells were cultured *in vitro* for 12 days to evaluate cell proliferation in response to the CHA scaffold microenvironment at varying polymer contents. The growth kinetics of U-87 MG RFP cells cultured on 2D TCPS and CHA scaffolds were quantified by measuring cell metabolic activity as a function of fluorescence intensity (**Figure 7.4**). The proliferation rate increased significantly ($p \leq 0.05$) for 2D monolayer cells cultured on TCPS, reaching confluence by day 7. The initiation of substantial cell proliferation did not appear until day 3 for all scaffold conditions. Increasing cell number with culture time was observed for all scaffolds, but no statistical difference in cell number among CHA conditions was discerned. Diffusion limitations and the high surface area in 3D systems have been cited as reasons for differences in 2D and 3D culture proliferation rates [312]. Additionally, the growth rates in 3D culture in the presence of increased cell–cell and cell–matrix interactions may be more indicative of native cell behavior [304, 306].

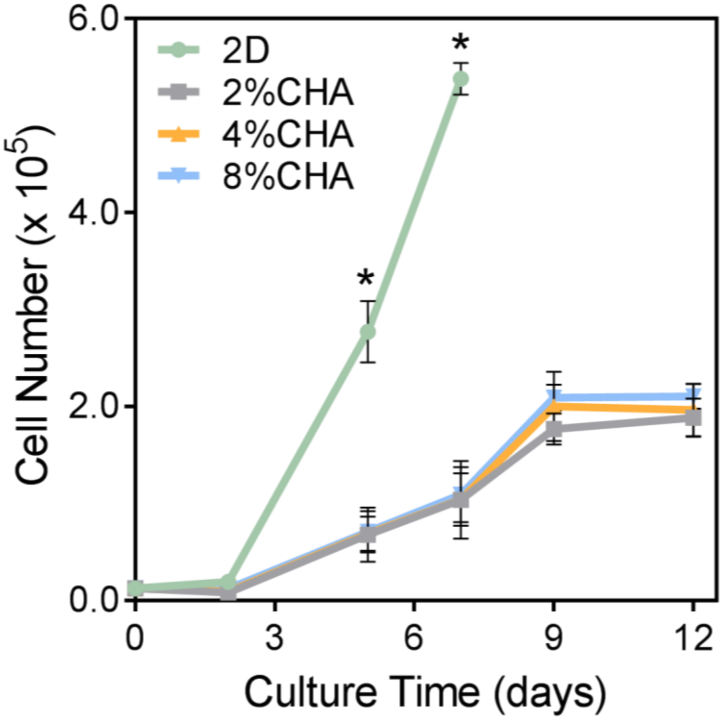

Figure 7.4. Growth kinetics of U-87 MG RFP cells cultured on 2D and CHA scaffolds using the alamarBlue® metabolic assay (n = 4). (*) Proliferation in the 2D culture condition was significantly higher than all 3D conditions ($p \leq 0.05$).

The influence of CHA scaffold stiffness on cell morphology was evaluated using confocal imaging of the red fluorescent protein-expressing U-87 MG cells (U-87 MG RFP) at day 2, 6, and 12 (**Figure 7.5**). At day 2, single cells attached to the pore walls were observed on all scaffolds. On day 6, a higher density of single cells and some small cell aggregates formed within 8% CHA scaffolds. By day 12, tumor spheroids were visible on all scaffolds. Cell aggregates on 2% CHA scaffolds were smaller than the spheroids present on 4% and 8% CHA scaffolds. The highest density of tumor spheroids was seen on the stiffest CHA scaffold (8%). Differences in spheroid size and density were not reflected in the metabolic assay with all CHA scaffolds exhibiting similar growth curves. This may be due to diffusion limitations such that the metabolic activity measured is limited to cells on the outer surface of spheroids. Tumor sphere morphology is linked to a more clinically relevant GBM behavior and often yields tumors with enhanced malignant potential [312], indicating that the 4% and 8% CHA scaffolds may be well suited for use as *in vitro* GBM tumor models.

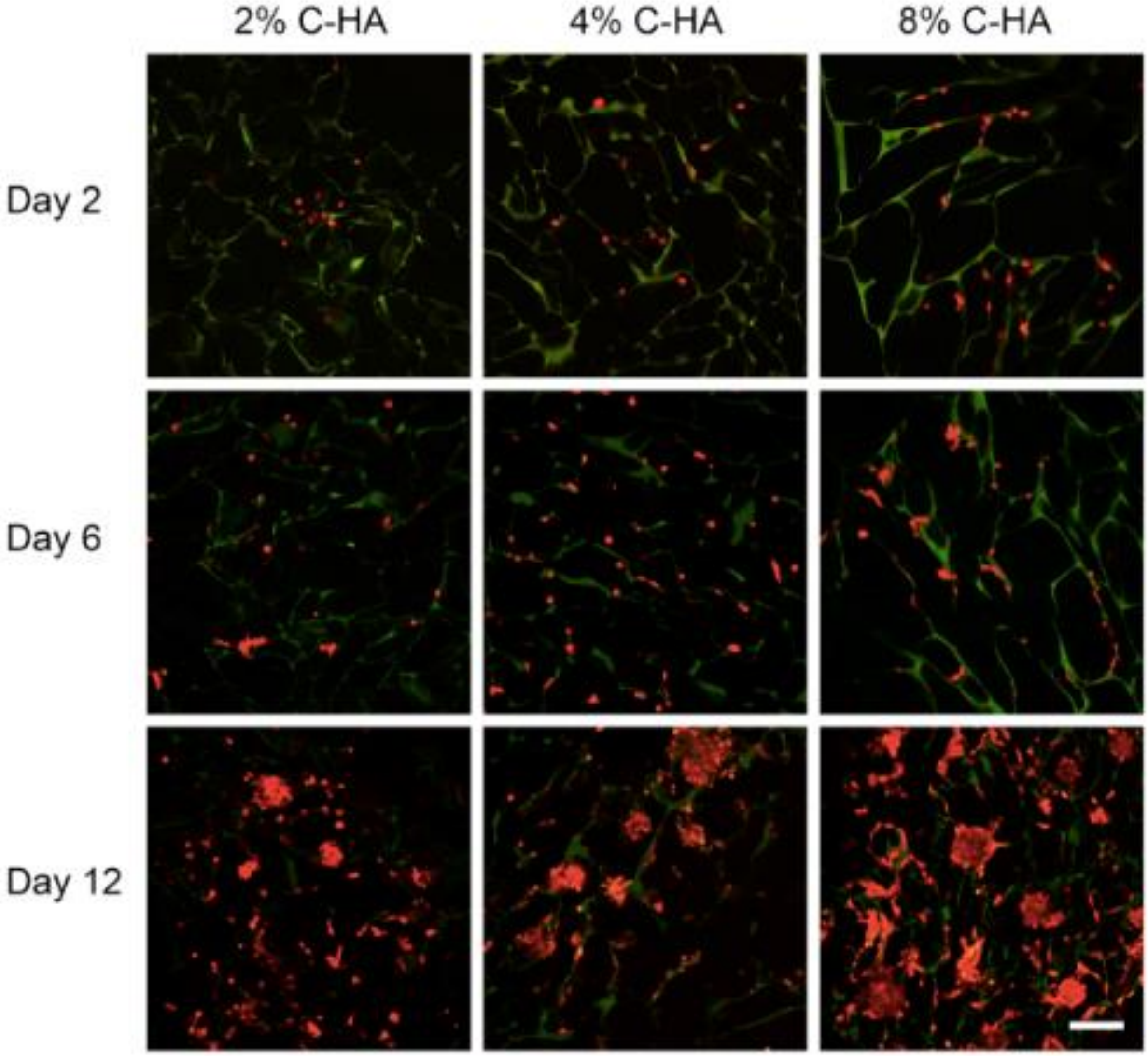

Figure 7.5. Fluorescence imaging of U87-MG RFP cells (red) progressing from single cells to spheroids after 12 days when cultured on 2%, 4%. and 8% CHA scaffolds. CHA scaffolds are visible (green) due to autofluorescence. The scale bar represents 300 µm.

7.4.5. Drug response of GBM cells in CHA scaffolds with varied stiffness

GBM cells cultured on 2D TCPS and CHA scaffolds for 12 days were treated with a common cancer chemotherapeutic, temozolomide (TMZ), and the drug response was assessed. Cells were exposed to doses of TMZ ranging from 0–4000 µM for 72 hours before viability was evaluated with alamarBlue® (**Figure 7.6**). GBM cells in CHA scaffolds displayed increased drug resistance relative to those on 2D for TMZ doses greater than 40 µM. The TMZ ED_{50} for cells cultured in 2D (133 µM) is consistent with similar studies reporting 2D culture of U-87 cells [313]. The highest cell viability and thus greatest resistance to TMZ-induced cell death, was associated with cells cultured in 8% CHA scaffolds. Increased drug resistance of cells cultured in CHA scaffolds may be the result of diffusion gradients, where the TMZ must penetrate the porous scaffold to reach the cells. This is in contrast to 2D culture conditions where all cells are equally exposed. Cells cultured in 8% CHA exhibited a statistically significant increase in resistance to TMZ-induced cell death, as compared with other 3D CHA cultures. This may reflect diffusion gradients within individual tumor spheres, where TMZ was unable to reach cells localized at the core.

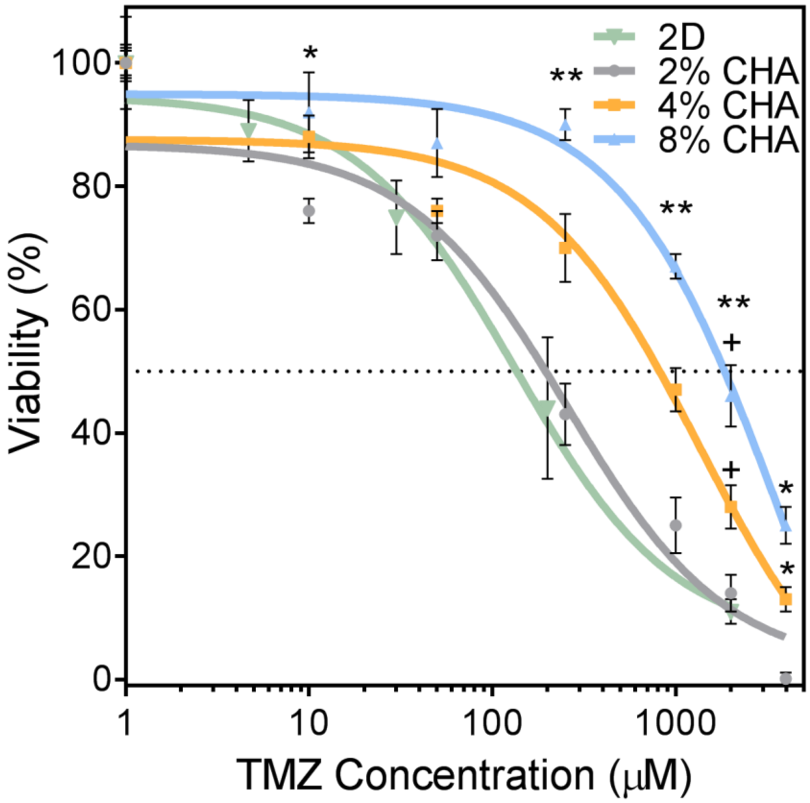

ED_{50} in μM TMZ

2D	2% CHA	4% CHA	8% CHA
133	255	1340	3840

Figure 7.6. Dose-dependent response of U87-MG RFP cells after 12 days of culture and 72 hrs after TMZ exposure. CHA scaffolds containing 3D tumor spheres showed increased ED_{50} relative to 2D culture, signifying increased drug resistance. Viability was determined using the alamarBlue® assay (n = 4). (*) indicates significant difference from 2% CHA condition ($p \leq 0.5$). (**) indicates all scaffolds are significantly different from each other ($p \leq 0.5$). (+) indicates significant difference from 2D ($p \leq 0.05$).

7.4.6. Gene expression of GBM cells in CHA scaffolds with varied stiffness

To better understand the influence of CHA scaffolds on GBM cell characteristics and behavior, the expression profile of a subset of relevant genes was assessed. Markers of chemoresistance (ABCG2), hypoxia (HIF-1α), and invasion (CD44, MMP-2, and TWIST1) were analyzed using quantitative real-time PCR (qRT-PCR) (**Figure 7.7a**) where, in general, upregulation of gene expression was observed for cells cultured on stiffer CHA scaffolds. Here, expression of ABCG2, a member of the ATP-binding cassette (ABC) transporters super family, was upregulated in cells cultured on 4% CHA (3.3 ± 0.23 fold) and 8% CHA (21.0 ± 1.6 fold) scaffolds relative to the 2D and 2% CHA cultures. In glioma, post-treatment tumor recurrence has been linked to a subpopulation of cells that express chemotherapeutic drug resistance. A potential mechanism of this resistance is increased drug efflux, leading to increased cell survival [314]. ABCG2 functions as an efflux pump for chemotherapeutic drugs like TMZ, and its increased expression has been implicated in cell self-renewal and poor patient prognosis [315].

Cellular response to hypoxia, or insufficient tissue oxygenation, is mediated by the hypoxia-inducible factors (HIF) transcription factor family and contributes to aggressive tumor phenotypes, drug resistance, and poor prognosis [316]. The HIF-1α protein is over expressed in a variety of common solid tumors [317]. As expected, in a 3D microenvironment containing diffusion gradients, expression of HIF-1α was upregulated greater than 3-fold for all CHA conditions relative to 2D (**Figure 7.7a**). Expression of genes regulated by HIFs is implicated in influencing many of the cancer "hallmarks" such as unchecked proliferation, apoptosis, invasion, metastasis, and appears to contribute to increased resistance to chemotherapy and radiation [316, 317].

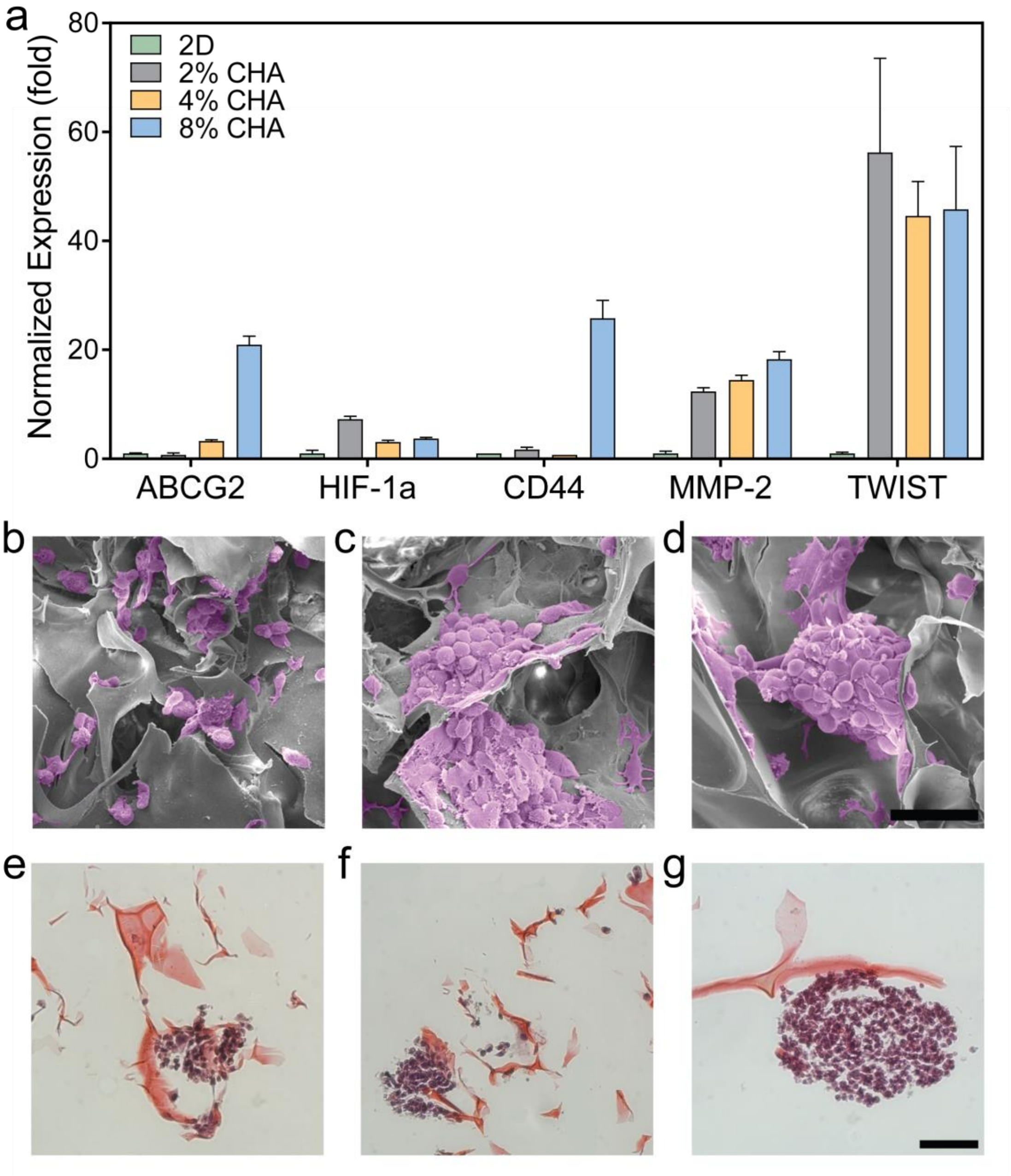

Figure 7.7. Gene expression and morphology of cells cultured on different substrates. (**a**) Relative expression displaying increased drug resistance and invasion specific genes in 3D scaffolds by U87-MG RFP cells after 12 days of culture (n = 3). Error bars represent standard error of mean. Scanning electron micrographs of GBM cells in (**b**) 2% CHA, (**c**) 4% CHA, and (**d**) 8% CHA where tumor sphere morphology increases with increasing stiffness. Histological staining (H&E) of tumor spheroids on (**e**) 2% CHA, (**f**) 4% CHA, and (**g**) 8% CHA scaffolds. Scale bars represent 100 µm (**b-d**) and 50 µm (**e-g**).

Cell invasion in GBM, a key factor in tumor recurrence and poor prognosis, is driven by cell motility, ECM degradation, and the epithelial to mesenchymal transition (EMT). Cell motility in the extracellular matrix is promoted by CD44, a principal cell surface hyaluronic acid receptor that plays a key role in cell adhesion [318]. When cultured for 12 days in 8% CHA scaffolds, GBM cells displayed an increase in CD44 expression (25.8 ± 3.3 fold) relative to those on the 2D control (**Figure 7.7a**). The CD44 signaling cascade in glioma is an important driver of tumor invasion, and upregulation of CD44 here was likely a response to the HA content of the scaffold indicating increased cell motility [319, 320].

Matrix metalloproteinase (MMP) expression is upregulated when invasion occurs via ECM degradation and specifically, expression of MMP-2 is considered a marker of GBM cell invasiveness [321]. MMP-2 expression was upregulated (>12 fold) for all CHA scaffolds relative to the 2D control indicating increased cell-matrix interactions. TWIST1 expression is also frequently upregulated in gliomas with elevated expression of MMP-2 and cell invasion genes. TWIST1 is considered an essential therapeutic target in GBM because the TWIST transcription factors act to repress cell–matrix adhesion, a hallmark of a more invasive cancer cell phenotype [322-324]. Relative to 2D monolayer culture, TWIST1 expression by GBM cells cultured in all CHA scaffolds was upregulated (> 45 fold) (**Figure 7.7a**). TWIST1 expression in the 2% CHA was slightly higher than 4% and 8% CHA scaffolds. This may be attributed to increased cell–matrix interactions in the 2% CHA scaffold due to the presence of single cells and small cell clusters. Importantly, upregulation of markers implicated in increased chemoresistance, invasion, and EMT provides further evidence that the biochemical and biomechanical properties of the 8%

CHA scaffold may be an excellent *in vitro* model for study of GBM pathogenesis and drug interactions.

Further characterization of cell and tumor sphere morphology was completed with SEM and histological staining. Scanning electron micrographs (**Figure 7.7b-d**) show the presence of tumor spheroids within the CHA scaffolds. This confirms the morphology observed using fluorescence microscopy and indicates that formation of GBM cell tumor spheroids is not limited to the scaffold surface. GBM cells present within 2% CHA scaffolds (**Figure 7.7b**) appear to form multicellular aggregates surrounded by disperse single cells that do not resemble the spheroids observed in 4% and 8% CHA scaffolds (**Figure 7.7c** and **7.7d**, respectively). The SEM and confocal microscopy (**Figure 7.5)** results were further confirmed by histological staining (**Figure 7.7e-g**), again showing tumor spheroids with increasing diameter as polymer content and scaffold stiffness increased. Overall, the formation of cell aggregates and tumor spheroids within CHA scaffolds indicates that the 3D scaffolds provide a more biomimetic microenvironment than 2D TCPS, likely by allowing cells to form more cell–cell and cell–ECM contacts. The dramatic difference in GBM cell morphology between monolayer culture and CHA scaffold culture may indicate a more primitive cancer cell phenotype in the latter.

7.5. CONCLUSIONS

Chitosan–hyaluronic acid PEC scaffolds were fabricated with varying chitosan content leading to significant differences in scaffold total density, porosity, microstructure, and compressive modulus. Overall, an increase in polymer content led to a higher apparent density, lower total porosity, smaller pore area, and higher compressive modulus. The scaffolds characterized in this work exhibited >90% total porosity, pores on the order of 100–200 μm in diameter and compressive moduli in a range that encompasses native brain tissue to tumor tissue.

When scaffolds were utilized for culture of U-87 MG RFP cells, cells formed small, irregularly shaped aggregates on 2% CHA scaffolds and tumor spheroids in 4% and 8% CHA scaffolds. Differences in cell morphology and proliferation among the CHA scaffold conditions examined suggest an effect of matrix stiffness on GBM cells *in vitro*. The 8% CHA scaffold formed larger tumor spheres with increased drug resistance, and elevated expression of drug resistance, hypoxia, and invasion-related genes. CHA scaffolds represent a useful tool for *in vitro* culture of GBM cells in a spheroid morphology allowing modeling of the relationship between GBM cells and the surrounding tumor microenvironment. The ability to tune matrix stiffness allows for extended investigation of cancer cell behavior during tumorigenesis, providing a tool to target and study therapy effectiveness at different stages of cancer progression.

This chapter is reprinted with permission from:

A. E. Erickson, S. K. Lan Levengood, J. Sun, F. C. Chang, M. Zhang. “Fabrication and Characterization of Chitosan–Hyaluronic Acid Scaffolds with Varying Stiffness for Glio-blastoma Cell Culture.” *Adv Healthcare Mater* 1800295., doi: 10.1002/adhm.201800295 (2018).

Chapter 8: CHITOSAN-BASED COMPOSITE BILAYER SCAFFOLD FOR OSTEOCHONDRAL DEFECT REGENERATION

8.1. ABSTRACT

Prolonged osteochondral tissue damage can result in osteoarthritis and decreased quality of life. Multiphasic scaffolds, where different layers model different microenvironments, are a promising treatment approach, yet stable joining between layers during fabrication remains challenging. We fabricated a bilayer scaffold for osteochondral tissue regeneration using thermally induced phase separation (TIPS). The articular cartilage region was optimized for hyaluronic acid content and stiffness, while the subchondral bone region was defined by higher stiffness and osteoconductive hydroxyapatite content. Two distinct polymer solutions were layered before TIPS, and the resulting porous, bilayer scaffold was characterized by seamless interfacial integration and a mechanical stiffness gradient reflecting the native osteochondral microenvironment. Following co-culture with chondrocyte-like (SW-1353 or mesenchymal stem cells) and osteoblast-like cells (MG63), cell proliferation and migration to the interface, along with increased gene expression associated with relevant markers of osteogenesis and chondrogenesis, indicates the potential of this bilayer scaffold for osteochondral tissue regeneration.

8.2. INTRODUCTION

Osteochondral tissue is composed of an articular cartilage region and a subchondral bone region with a calcified cartilage interface linking the two distinct microenvironments. Osteochondral defects arise when damage or disease affect both regions [325] and treatment options vary from bone marrow stimulation to chondrocyte and/or graft transplantation [326, 327]. However, these treatments are associated with inherent complications [325, 328-330]. For example, therapies only targeting the cartilage zone without consideration of the interface or subchondral bone result in increased defect size, a weak tissue interface, and structural degradation of the underlying bone [331, 332]. Regeneration of osteochondral defects is nontrivial and requires synchronized vascularization and calcification in the bone region concurrently with avascular collagen deposition in the cartilage region [325].

Tissue engineering (TE) scaffolds provide a three-dimensional (3D), biodegradable template for cell attachment/differentiation. TE scaffolds can be used for treatment of osteochondral defects by providing synchronized, yet segregated support of two distinct cell populations with differing biochemical and biomechanical requirements. Monophasic scaffolds are inadequate mimics of the native microenvironment and therefore unable to simultaneously support chondrogenesis and osteogenesis. Thus, various bilayer and multilayer (3+ layers) 3D, porous scaffolds have been fabricated to address the unique characteristics of the osteochondral microenvironment. Porous scaffolds that mimic osteochondral extracellular matrix (ECM) are fabricated with a wide range of physical properties including tailored pore size [333-335], pore shape [336], mineral content [337, 338], or biochemical gradients [339, 340]. These studies demonstrate the efficacy of multilayer or multiphasic scaffolds *in vitro* [339, 341] and *in vivo* [342, 343]. Although promising, limitations of multiphasic scaffolds include time-consuming, iterative fabrication or joining procedures [339], as well as inadequate or unstable interfacial regions between layers. These significant limitations indicate a need for further innovation in the design and optimization of such scaffolds for osteochondral tissue engineering.

Synthetic polymers are often used in bone tissue engineering due to their superior mechanical integrity relative to natural polymers. However, synthetic polymers have slow degradation rates, harmful degradation products, and lack cell attachment and differentiation cues [344]. Natural polymers are more biocompatible, but their mechanical properties are suboptimal for many tissue engineering applications. Polyelectrolyte complexes (PECs), such as chitosan-alginate [46, 64] and chitosan–hyaluronic acid [182], formed via ionic interactions between natural cationic and anionic polymers, possess enhanced integrity and stiffness. Further, the addition of bioactive cues to PEC scaffolds promotes cell attachment, proliferation, and differentiation. The incorporation of bioactive cues specific to the distinct microenvironments present in native osteochondral tissue can promote tissue regeneration [341, 345-347].

In this study, we present a bilayer scaffold with a stable, calcified transition zone fabricated via a thermally induced phase separation (TIPS) fabrication process. The scaffold has two regions. The first region, a chitosan–hyaluronic acid cartilage layer, is defined by relatively lower stiffness and the presence of hyaluronic acid (HA), a glycosaminoglycan key to chondrocyte attachment and differentiation [345, 346]. The second region, a chitosan–alginate bone layer, was optimized for higher stiffness and osteoconductive hydroxyapatite nanorod (6% CA + HAp) content. Chitosan was selected as a major component of the bilayer scaffold as it supports attachment and proliferation of both osteoblasts [25, 62] and chondrocytes [64]. This report describes how each layer of the scaffold, or each base scaffold, was optimized to reflect structural, physical, and biological properties unique to the osteochondral microenvironment. The scaffold design process required a multi-step optimization involving material characterization and *in vitro* cell-based evaluation. By combining two distinct scaffolds optimized for cartilage and bone, respectively, using TIPS fabrication processes, a region between the two layers was established, resulting in a gradient transition zone resembling that of native osteochondral tissue. The biological performance of the optimized scaffold was characterized to investigate scaffold potential for osteochondral tissue engineering applications.

8.3. MATERIAL AND METHODS

8.3.1. Materials

Unless otherwise stated, all chemicals were purchased from Sigma Aldrich and used as received. Scaffolds were synthesized using chitosan (from shrimp shells, practical grade, MW = 190–375 kDa, $\geq$ 75% deacetylated), hyaluronic acid sodium salt (from S*treptococcus equi*, MW = $1.5–1.8 \times 10^6$ Da) and alginic acid sodium salt (from brown algae, medium viscosity). All tissue culture reagents (antibiotic–antimycotic (AA), Dulbecco’s phosphate buffered saline (D-PBS), Dulbecco’s modified Eagle medium (DMEM), TripLE, trypsin, and fetal bovine serum (FBS) were purchased from Life Technologies. Human chondrocyte-like (SW-1353) and human osteoblast-like (MG63) cells were used as received (American Type Culture Collection, Manassas, VA). Rat bone marrow derived mesenchymal stem cells (MSC) were isolated from Sprague-Dawley rat bone marrow aspirate as previously described [348] and cultured in fully supplemented DMEM. Cells were maintained according to manufacturer’s instructions in fully supplemented DMEM with 10% FBS and 1% AA at 37°C and 5% CO_2 in a fully humidified incubator.

8.3.2. Scaffold fabrication

8.3.2.1. Base Scaffold

Six different scaffolds (**Table 8.1**) were fabricated for optimization of the base scaffolds for the cartilage or bone regions. Pure chitosan (C) [60], chitosan–alginate (CA) [284, 305], and chitosan–hyaluronic acid (CHA) [182, 306] were prepared as previously reported. During scaffold fabrication, all homogenization steps were performed three times at 2000 RPM for 3 min using a Thinky mixer (ARM-300, Thinky USA, Laguna Hills, CA).

We fabricated 4 wt% pure chitosan scaffolds (4% C) by first adding 4 grams of chitosan to a 1 wt% acetic acid solution. For 6 wt% pure chitosan scaffolds (6% C), 6 grams of chitosan were added to a 2 wt% acetic acid solution. The higher acetic acid concentration was used to ensure dissolution of chitosan at the higher polymer concentration. Both solutions were homogenized, aged overnight at room temperature to ensure complete dissolution, and cast into a 24-well plate at 3 mL per well.

To fabricate 4 wt% chitosan–alginate scaffolds (4% CA), 4 grams of alginate were dissolved in 199 mL of DI water and stirred using a Thinky mixer. Upon alginate dissolution, chitosan (4 grams) and acetic acid (1 gram) were added and the solution was homogenized until dissolved. For 6% CA scaffolds, 6 grams of alginate was dissolved in 198 mL of DI water followed by the addition of 6 grams of chitosan and 2 grams of acetic acid. Upon chitosan dissolution, the polymer solutions were mixed in a blender for 5 min, cooled in a cold-water bath to prevent polymer solution overheating, and mixed in a blender again for 5 min. The scaffold solution was cast into a 24 well-plate at 3 mL per well.

We fabricated 4 wt% chitosan – hyaluronic acid (4% CHA) scaffolds by first preparing the chitosan and HA polymer solutions separately. Chitosan (4 wt%) and HA (1 wt%) were separately dissolved in 1 wt% acetic acid. For 6% CHA scaffolds, chitosan (6 wt%) was dissolved in 2 wt% acetic acid, to ensure dissolution of chitosan at the higher polymer concentration. The HA solution was created by dissolving 1 wt% HA in a 1 wt% acetic acid solution. Chitosan and HA polymer solutions were individually homogenized and aged overnight at room temperature. After dissolution, chitosan and HA polymer solutions were combined, homogenized, and mixed in a blender for 1 min. The resultant polymer solution was cast into a 24-well plate at 3 mL per well.

All 24-well plates containing the polymer solutions were centrifuged for 1–5 min at 2000 RPM to remove air bubbles, refrigerated for > 12 hours, frozen at −20°C for > 24 hours, and lyophilized using a Labconco Freezone 6 freeze dryer.

Table 8.1 summarizes the scaffold naming conventions. Naming conventions are based on a ratio of polymer mass to total solution volume. Specifically, for pure chitosan (C) scaffolds, the total polymer content (wt%) was equivalent to the amount of solubilized chitosan. A 6% pure chitosan scaffold contains 6 wt% chitosan. For CA scaffolds, the total polymer content was equivalent to the amount of solubilized chitosan plus the amount of solubilized alginate. A 6% CA scaffold contained 3 wt% chitosan and 3 wt% alginate for a 6 wt% total polymer content.

HA has poor solubility and high viscosity at moderate concentrations. Therefore, 1 wt% HA was the highest concentration used. The association between the naming convention of CHA scaffolds and the total polymer content is different from the C and CA scaffolds. Importantly, the naming convention, which is based on the chitosan concentration prior to blending, remains consistent with scaffolds presented in literature [182]. A 6% CHA scaffold contains a 6 wt% chitosan solution blended with a 1 wt% HA solution for a total of 3.5 wt% polymer.

Table 8.1 Scaffold naming nomenclature and composition.

Scaffold Type	Solution Fabrication (wt%)		Total Polymer (wt%)
	Step 1	Step 2	
4% C	4% C in 1% AA	---	4% C
6% C	6% C in 2% AA	---	6% C
4% CA	2% A in DI water	2% C in 0.5% AA	2% A + 2% C = 4% CA
6% CA	3% A in DI water	3% C in 1% AA	3% A + 3% C = 6% CA
4% CHA	4% C in 1% AA	1% HA in 1% AA	2% C + 0.5% HA = 2.5% CHA
6% CHA	6% C in 2% AA	1% HA in 1% AA	3% C + 0.5% HA = 3.5% CHA

C = chitosan, A = alginate, HA = hyaluronic acid, AA = acetic acid, CA = chitosan+alginate, CHA = chitosan+hyaluronic acid.

8.3.2.2. Composite chitosan–alginate + hydroxyapatite scaffolds

Hydroxyapatite nanorods (HAp) were synthesized based on a previously reported procedure [349] with slight modifications to obtain processing conditions encompassing ambient pressure and body temperature. Briefly, 0.75 M sodium citrate was added by drops to 0.1 M calcium nitrate. Sodium hydroxide was used to adjust pH to 9 and the solution was aged for 30 min at room temperature. A 0.06 M sodium phosphate monobasic solution was prepared, adjusted to pH 9, and then aged for 30 min. Under constant stirring, the solutions were mixed to achieve a precipitate with a Ca/P ratio of 1.67. The mixture was heated to 37°C under constant stirring for 2 days while maintaining a pH of 9. The nanorod precipitate (HAp) was filtered, washed with DI water, and dried at 70°C overnight. HAp was added to a 6% CA polymer solution (synthesis outlined above) to obtain concentrations of 0.1 wt%, 0.25 wt%, 0.5 wt%, 1 wt%, 2 wt%, and 3 wt% HAp. The composite polymer solution was blended, homogenized, and cast in a 24-well plate at 3 mL per well. The plate was centrifuged at 1000 RPM for 5 min, refrigerated for > 12 hours, placed in a −20°C freezer for > 24 hours, and lyophilized using a Labconco freeze dryer.

8.3.2.3. Bilayer scaffolds

The complete bilayer scaffold fabrication process is summarized in **Figure 8.1a**. During scaffold fabrication, all homogenization steps were conducted using a Thinky mixer three times at 2000 RPM for 3 min. Solutions for each layer of the bilayer scaffold were prepared separately. For the cartilage layer, a 4% CHA solution was produced by dissolving chitosan (4 wt%) and HA (1 wt%) separately in 1 wt% acetic acid. Chitosan and HA solutions were individually homogenized and aged overnight at room temperature. The polymer solutions were then homogenized and mixed in a blender for 1 min. Wells of a 24-well plate were filled with 1.5 mL of the 4% CHA polymer solution per well. The plate was then centrifuged and refrigerated for 1 hour to yield a firmer and more viscous solution. For the bone layer, a 6% CA + 0.5% HAp material solution was prepared by dissolving 6 grams of alginate in 198 mL of DI water and homogenizing. Upon dissolution, chitosan (6 grams) and acetic acid (2 grams) were added and the solution was homogenized, mixed in a blender for 5 min, and cooled in a cold-water bath. Hydroxyapatite nanorods (0.5 wt%) were then dispersed in the CA polymer solution. The 6% CA + HAp polymer solution was blended for 5 min and then mixed at 2000 RPM for 3 min with a Thinky mixer to eliminate bubbles. Then, 1.5 mL of the polymer solution was gently cast in each well on top of the refrigerated 4% CHA solution in a 24-well plate. The layered polymer solutions were centrifuged at 2000 RPM for 5 min to integrate the interface, refrigerated for > 12 hours, frozen at −20°C for > 24 hours, and lyophilized using a Labconco freeze dryer.

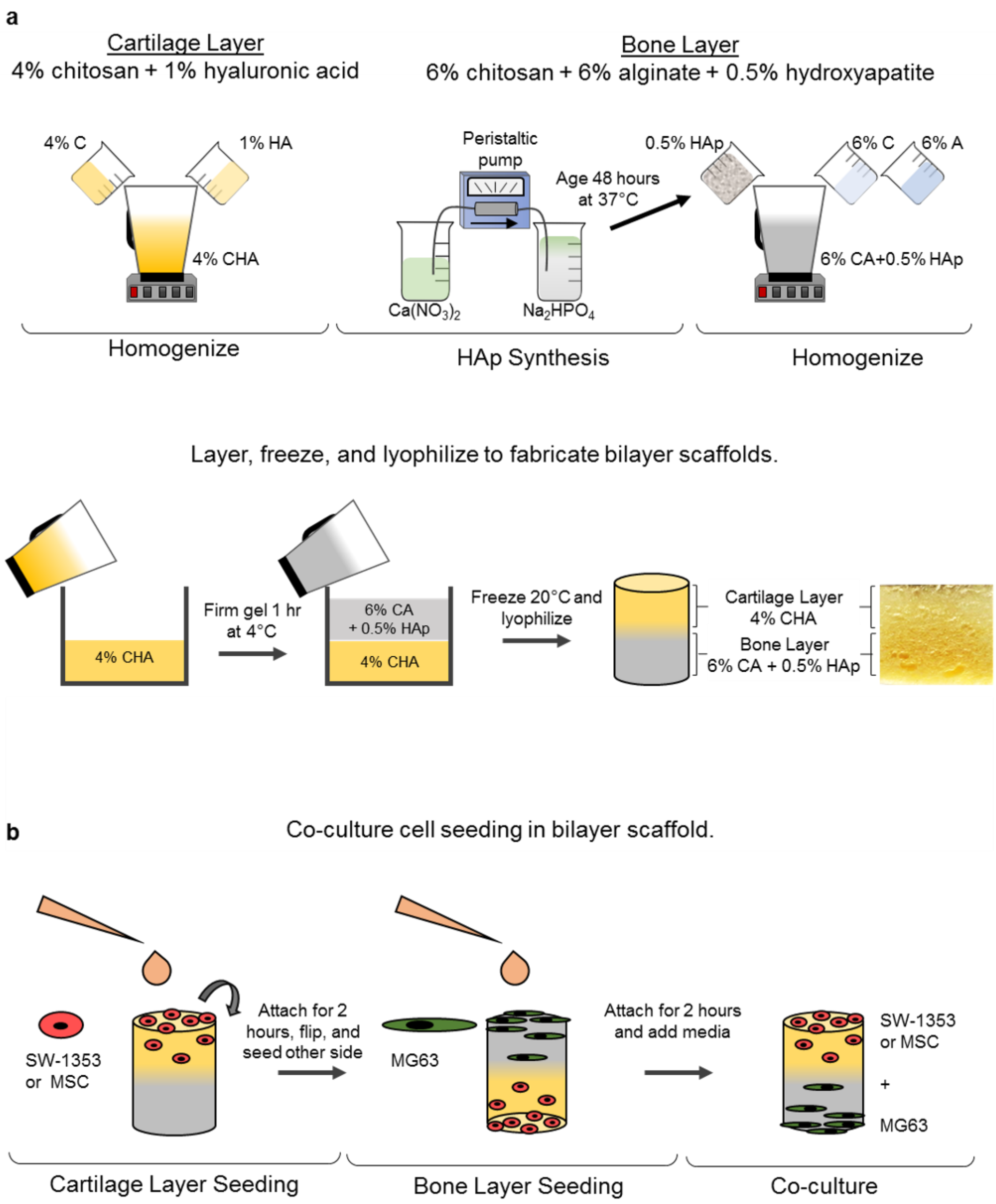

Figure 8.1. Bilayer scaffold synthesis and co-culture cell seeding. (**a**) The three-step fabrication process includes: (1) synthesis of HAp nanorods using a chemical precipitation method, (2) individual preparation of the 4% CHA and 6% CA + HAp solutions, and (3) layering the two solutions, freezing, and lyophilizing to achieve a gradient scaffold with an integrated interface region. (**b**) Co-culture seeding scheme in the bilayer scaffold where SW-1353 or MSC cells are first seeded in the cartilage layer (4% CHA), the scaffold is then flipped, and MG63 cells are seeded in the bone layer (6% CA + HAp).

8.3.2.4. Scaffold neutralization and sterilization.

All base and HAp-integrated scaffolds were cut into 2 mm-thick disks, quartered, and neutralized and/or crosslinked as summarized in **Table S8.1**. The bilayer scaffolds were cut into 6 mm-thick cylinders, quartered, and simultaneously neutralized and crosslinked. Neutralization, crosslinking, and sterilization steps were conducted under vacuum. All crosslinked/neutralized scaffolds were rinsed 3 times with DI water, and soaked in D-PBS or DI water on a shaker at 60 RPM overnight. After ethanol sterilization, all scaffolds were rinsed three times and soaked overnight in sterile D-PBS to remove residual ethanol. Before cell seeding, the scaffolds were transferred to fully supplemented cell culture media for at least 2 hours.

8.3.3. Microscopy

Scaffold pore morphology was visualized with a scanning electron microscope (SEM, JEOL JSM-7000F). Specifically, dry scaffolds were mounted on stubs using carbon tape and coated with Au/Pd for 60 seconds before imaging. HAp nanorod samples were prepared using a copper grid and imaged with a Transmission Electron Microscope (TEM, Philips EM430 TEM).

8.3.4. Pore Size Measurement

Individual pore areas were measured from SEM micrographs using ImageJ software. At least 14 pores were measured per base scaffold condition to determine mean pore area. For the bilayer scaffold, > 35 pores were measured in each layer. Pores were outlined using the freehand selection function in ImageJ and the area measured. Pore diameter was estimated using the mean pore area and assuming pores were a perfect circle.

8.3.5. Mechanical Testing

Compression testing was conducted with a Shimadzu Universal tester (AGS-X) using a 100 N load cell at a strain rate of 0.4 mm/min. Scaffolds were cut into 2-mm thick disks and tested in dry and hydrated states. Hydrated samples were crosslinked and/or neutralized and soaked in D-PBS for > 1 hr prior to testing. Testing of bilayer scaffolds was conducted using full thickness (6-mm height) hydrated scaffolds. At least four samples were tested per condition.

8.3.6. Porosity and density measurements

Bulk density of each scaffold was determined by measuring the scaffold mass to the ten-thousandth of a gram and the scaffold diameter using micrometers (n = 12). Porosity of bilayer scaffolds was measured using a modified liquid displacement method [350, 351]. Specifically, the weight (W_i) and volume (V_i) of a dry scaffold was recorded. The scaffold was fully submerged in isopropanol for 20 min under vacuum. The isopropanol-impregnated scaffold was weighed (W_f). Scaffold porosity (n = 5) was calculated as a ratio of the volume of the solvent in the scaffold pores to the volume of the dry scaffold as shown in **Equation 8.1**, where ρ is the density of isopropanol.

$$\mathrm{Porosity} = \frac{(W_f - W_i)/\rho}{V_i} \times 100 \qquad \textbf{(8.1)}$$

8.3.7. Cell seeding and cell proliferation in base scaffolds

Base scaffolds were seeded with 20,000 SW-1353, MSC, or MG63 cells suspended in 50 μL of fully supplemented DMEM. Scaffolds were incubated for 2 hours to allow for cell infiltration and attachment before adding fully supplemented media. Media were changed every 2–3 days for the 14-day culture period. Cell proliferation was evaluated at 2, 7, and 10 days using 10% alamarBlue® reagent in fully supplemented media (n = 4 per condition). Scaffolds were incubated for 4 hours in the alamarBlue® solution before an aliquot of the solution was transferred to a black-bottom 96-well plate. Fluorescence intensity was measured using a SpectraMax M5 microplate reader (Molecular Devices, Union City, CA) at an excitation wavelength of 560 nm and emission wavelength of 590 nm. Fluorescence intensity was converted to cell number based on standard curves created for each scaffold type/cell line. Excess alamarBlue® was aspirated and scaffolds were washed with D-PBS before fresh media was added after each time point.

8.3.8. Cell seeding, cell proliferation, and live cell imaging in bilayer scaffolds

One cell type was seeded into each layer of the bilayer scaffolds to evaluate metabolic activity of co-cultures (SW-1353 + MG63 or MSC + MG63) (**Figure 8.1b**). This culture condition is referenced throughout the text as a “co-culture.” In the cartilage region, 200,000 cells (SW-1353 or MSC) suspended in 100 µL of fully supplemented DMEM were seeded into the 4% CHA layer and incubated for 2 hours to allow cell infiltration and attachment. Scaffolds were then flipped and 200,000 MG63 cells in 100 µL of fully supplemented DMEM were seeded in the 6% CA + HAp layer. The scaffold was again incubated for 2 hours before the addition of fully supplemented media. Media were changed every 2–3 days over the 14-day culture period. Proliferative capacity (n = 3) was determined at 2, 4, 7, 10, and 14 days using the alamarBlue® assay as described above.

To view cell distribution and infiltration into the bilayer scaffold, live cell images were acquired using a Nikon inverted fluorescent microscope with appropriate filters on a Nikon Ri1 Color Cooled Camera system (Nikon instruments, Melville, NY). To differentiate cells seeded in each layer of the bilayer scaffolds, the SW-1353 or MSC cells were stained with red Vybrant® DiI cell-labeling (Molecular Probes, Thermo Fisher) rendering the cells red-orange when excited at 549 nm (565 nm emission). Cells (SW-1353 or MSC) were incubated for 30 min in red Vybrant® DiI at 1 µg/mL in D-PBS prior to seeding in the cartilage layer. MG63 cells were seeded in the bone layer with no prior staining. Before imaging after 1 and 14 days of culture, the entire bilayer scaffold was incubated for 30 min in 5 µM calcein AM (Thermo Fisher) in D-PBS. Calcein AM is a cell-permeant dye that is converted from colorless to a green-fluorescent calcein after hydrolysis when excited at 495 nm (emission 515 nm), and therefore can be used for determination of live cells. Cells in the cartilage layer, SW-1353 or MSC, were double stained and emitted both red and green fluorescence, depending on the excitation wavelength, and in the bone layer, MG63 were identified as green with no red signal. Merging images using ImageJ and Adobe Photoshop, revealed differences in excitation wavelength between DiI (red) and calcein AM (green) stained cells and allowed cells in the cartilage layer (SW-1353 or MSC) to be visualized as red-orange and bone layer cells (MG63) to be visualized as green.

8.3.9. PCR

After two weeks of culture, we detached cells from the bilayer scaffolds using TripLE Express and extracted ribonucleic acid (RNA) by following the manufacturer's protocol using the Qiagen RNeasy kit (Qiagen, Valencia, CA). Following the manufacturer's instructions, iScript cDNA synthesis kit (Bio-Rad, Hercules, CA) was used for reverse transcription (RT) to prepare cDNA. DNA transcripts were probed using SoAdvanced Universal SYBR Green Supermix (Bio-Rad) with the primers listed in **Table S8.2**. Thermocycling was performed on 10 µL of solution containing 5 µL SYBR Supermix, 300 nM primers (Integrated DNA Technologies, Coralville, IA), and cDNA concentrated at 4 ng/µL. The thermocycling was performed using the BioRad CFX96 System at 95°C for 3 min, 40 cycles at 95°C for 15 s, and 60°C for 1 min. All qRT-PCR data was analyzed with the CFX Manager software (Bio-Rad) where expression levels were normalized to a reference gene, GAPDH. Gene expression between conditions was normalized to MG63 expression on 2D tissue culture polystyrene (TCPS) (set to 1-fold) for comparison.

8.3.10. Statistical analysis

All data was analyzed to express mean ± standard deviation unless stated otherwise. The data were analyzed using one-sided or two-sided analysis of variance (ANOVA) with post-hoc

Tukey multiple comparisons testing for statistical significance ($p \leq 0.05$) in GraphPad Prism 7 (Prism version 7.04, Graph Pad Software, San Diego, CA).

8.4. RESULTS AND DISCUSSION

8.4.1. Base scaffold microstructure and other material properties

Repair of osteochondral defects requires simultaneous support of two cell populations, chondrogenic and osteogenic cells, that reside within distinct microenvironments – articular cartilage and subchondral bone. Differing biochemical and biomechanical cues in each region makes scaffold design challenging, necessitating a multiphasic scaffold approach. Biochemical and biomechanical optimization of the cartilage and bone regions of a bilayer scaffold was necessary to accurately mimic the layered osteochondral ECM. Pure chitosan (C), chitosan-alginate (CA), and chitosan–hyaluronic acid (CHA) base scaffolds were each fabricated with two polymer concentrations (4 wt% and 6 wt%) per scaffold composition and screened as candidate scaffolds for the cartilage or bone layers of the target osteochondral bilayer scaffold. The polymer concentrations were selected based on previous studies showing 4 wt% CA scaffolds support osteogenic and chondrogenic cell culture [62, 64]. Scaffold pore structure and morphology, observed with SEM (**Figure 8.2a**), displayed a defined, yet interconnected, open pore network for all scaffolds. Despite a similar overall polymer content, the 6% CA scaffolds had a significantly smaller mean pore cross-sectional area (1.10×10^4 µm^2) than the 6% C scaffolds (2.93×10^4 µm^2), likely due to the increased viscosity of the CA PEC ($p \leq 0.05$) (**Figure S8.1a**). Scaffold density (**Figure 8.2b)**, which increased with polymer content, differed among all scaffold compositions, ranging from 0.04 g/cm^3 to 0.08 g/cm^3, and similar to values cited for other highly porous polymeric foams [352].

Polymer content and density correlated with the compressive modulus or stiffness of the bulk, porous scaffold. The compressive modulus of dry and hydrated scaffolds increased as scaffold density increased (**Figure 8.2c, d**). Overall, the CA scaffolds were the stiffest followed by the C scaffolds, and CHA scaffolds. The low compressive modulus of both dry and hydrated CHA scaffolds was due to low total polymer content relative to the other scaffold types.

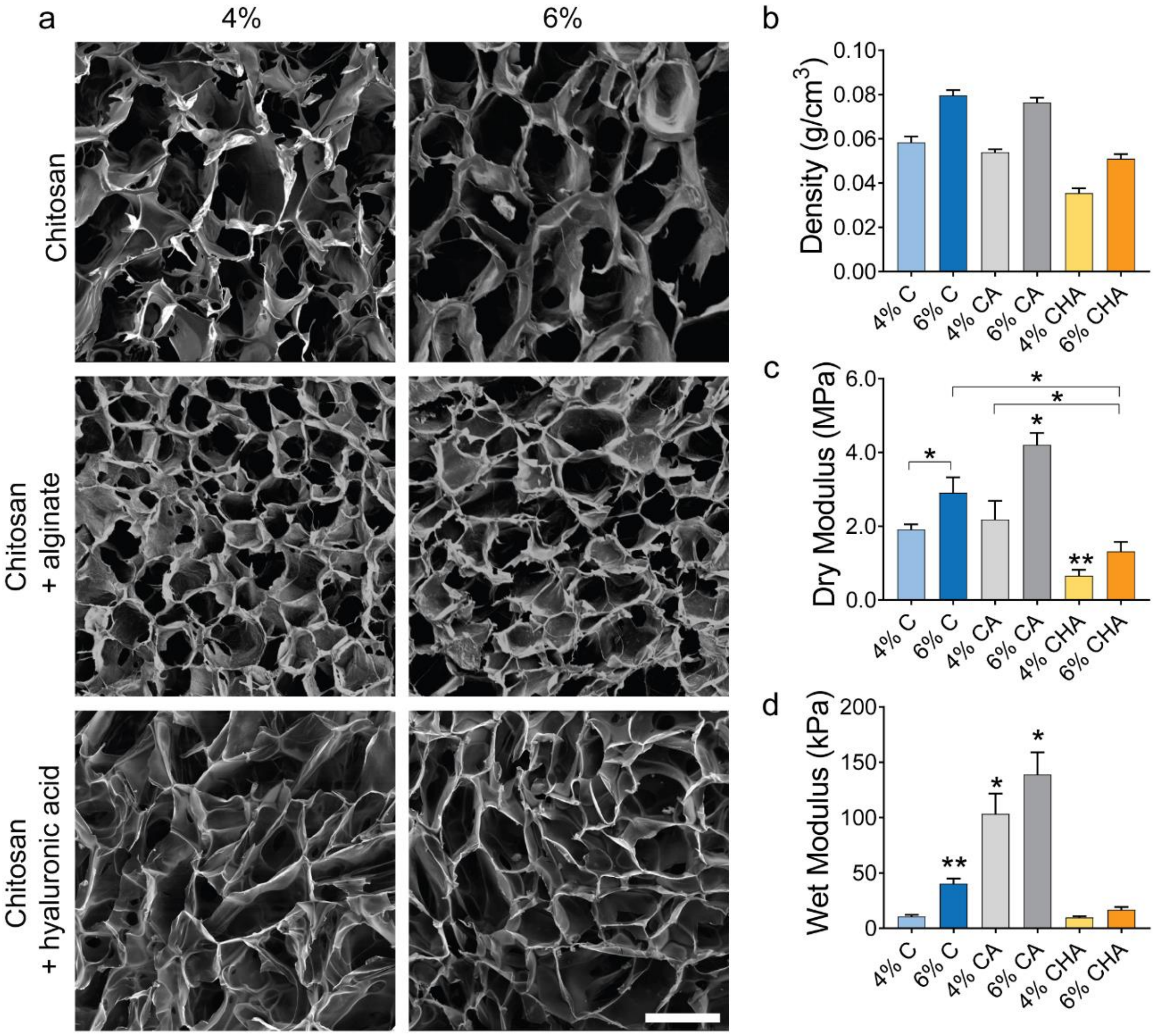

Figure 8.2. Base scaffold microstructure and physical property characterization. (**a**) SEM images showing pore morphology. Scale bar is 200 µm. (**b**) Dry bulk density of

all scaffolds significantly different ($p \leq 0.05$, $n = 12$). Compressive modulus of (**c**) dry scaffolds in MPa ($n = 4$) and (**d**) hydrated scaffolds in kPa ($n = 4$). *Statistically significant from all or specified conditions. **Statistically significant from all conditions, except 6% CHA. ($p \leq 0.05$)

8.4.2. Cell attachment and proliferation on base scaffolds

In addition to characterizing and optimizing the physical properties of the scaffold to reflect the *in vivo* microenvironment, the response of relevant cells to the scaffold in terms of attachment and proliferation is also critical. Growth profiles for chondrocyte-like cells (SW-1353), rat bone marrow mesenchymal stem cells (MSC), and osteoblast-like cells (MG63) were established for each base scaffold by using the metabolic assay alamarBlue® (**Figure 8.3**). The 4% CHA and 6% CHA scaffolds were seeded with chondrocyte-like SW-1353 or MSCs to evaluate their support of chondrogenic cells. Human SW-1353 have been used previously to evaluate cartilage regeneration [353, 354], and MSCs possess chondrogenic potential. The 4% and 6% C and CA scaffolds were seeded with osteoblast-like MG63, a cell line frequently used to evaluate osteogenic cell behavior on scaffolds [355, 356].

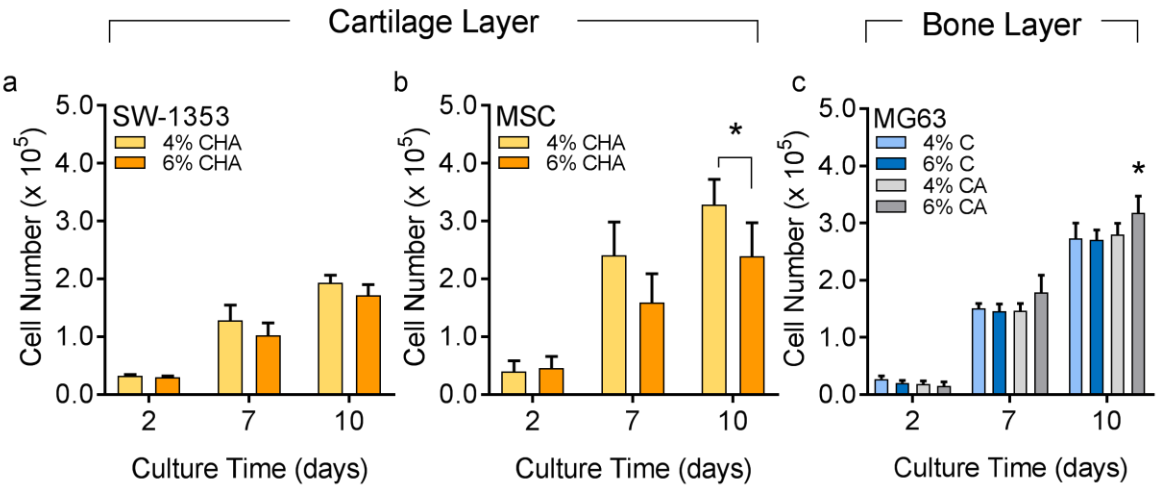

Figure 8.3. Cell proliferation on base scaffolds. (**a**) SW-1353 and (**b**) MSC cultured on 4% and 6% CHA, and (**c**) MG63 cultured on 4% C, 6% C, 4% CA, and 6% CA for 10 days (n = 4). *Statistical significance within specified time point. ($p \leq 0.05$).

8.4.2.1. Cartilage layer scaffold.

CHA scaffolds were evaluated as a potential chondral layer with the goal of mimicking native cartilage ECM comprised heavily of glycosaminoglycans. Chitosan has a proxy glycosaminoglycan structure [357] and HA, a component of native articular cartilage, is important in tissue homeostasis and chondrogenesis [345, 346, 358]. Combining chitosan and HA results in a stable PEC, blending the beneficial properties of both natural polymers. Lower polymer concentration scaffolds relative to bone layer scaffolds, as summarized in **Table 8.1,** were investigated for the cartilage layer because chondrocytes prefer lower stiffness substrates relative to osteogenic cells. Additionally, lower stiffness substrates may influence mesenchymal stem cell fate toward a chondrogenic phenotype [359].

In native articular cartilage, chondrocytes populate and deposit ECM to maintain healthy tissue. Cartilage layer bioactivity was evaluated using chondrocyte-like SW-1353 and MSCs with chondrogenic potential. An increase in metabolic activity from day 2 to day 10 was observed for SW-1353 and MSC cells in both 4% and 6% CHA scaffolds (**Figure 8.3a, b)**. The number of MSC cells on 4% CHA scaffolds was significantly higher than the number of MSCs on 6% CHA scaffolds at day 10. Based on proliferation and metabolic activity of the SW-1353 and MSC cells, we selected 4% CHA scaffolds for the cartilage layer of the osteochondral scaffold.

8.4.2.2. Bone layer scaffold.

Subchondral bone, composed of type I collagen and calcium phosphate, is a stiffer tissue than cartilage. Presentation of appropriate stiffness cues is crucial to regeneration of healthy tissue because mechanosensing by stem cells is a key factor in lineage mediation. Determining the optimal bone layer base scaffold required a two-phase evaluation: (1) characterization of cell proliferation on higher stiffness scaffolds to identify the base scaffold material, and (2) addition of hydroxyapatite nanorods (HAp) and optimization of HAp content in the base scaffold to enhance scaffold osteoconductivity. Osteoblast-like MG63 cells were cultured on the four stiffest scaffolds (4% C, 6% C, 4% CA, and 6% CA summarized in **Table 8.1**) (**Figure 8.2c, d**), resulting in increased metabolic activity for all scaffolds over the 10 day culture period (**Figure 8.3c**). At day 10, the number of MG63 cells on 6% CA scaffolds was significantly higher than on the C scaffolds or 4% CA scaffolds. The 6% CA scaffold was selected as the base material for the bone layer because of increased scaffold stiffness and superior support of osteogenic cell proliferation.

The addition of HAp, similar in composition to the inorganic component of bone [360, 361], promotes osteogenesis when integrated into chitosan scaffolds [362], and has shown promising results in bone TE *in vitro* and *in vivo*. Therefore, to further enhance the bioactivity of the bone layer, hydroxyapatite nanorods were added to the 6% CA base scaffold (**Figure 8.4a, b**). HAp nanorods were added in concentrations ranging from 0.1 wt% to 3 wt%. Pore morphologies in the HAp-integrated scaffolds was visualized with SEM (**Figure 8.4c)**. All HAp-incorporated scaffolds possessed an open, porous structure indicating that HAp addition does not hinder pore formation during TIPS. As the HAp concentration within the CA scaffold increased up to 3%, the dry bulk density of the scaffolds also increased (**Figure 8.4d**). Homogeneous HAp dispersal throughout the CA matrix was observed for all conditions, despite dispersal challenges cited in previous works [363]. In the CA scaffold, the strong ionic interaction between alginate and Ca^{+2} in HAp acted as a dispersant [364].

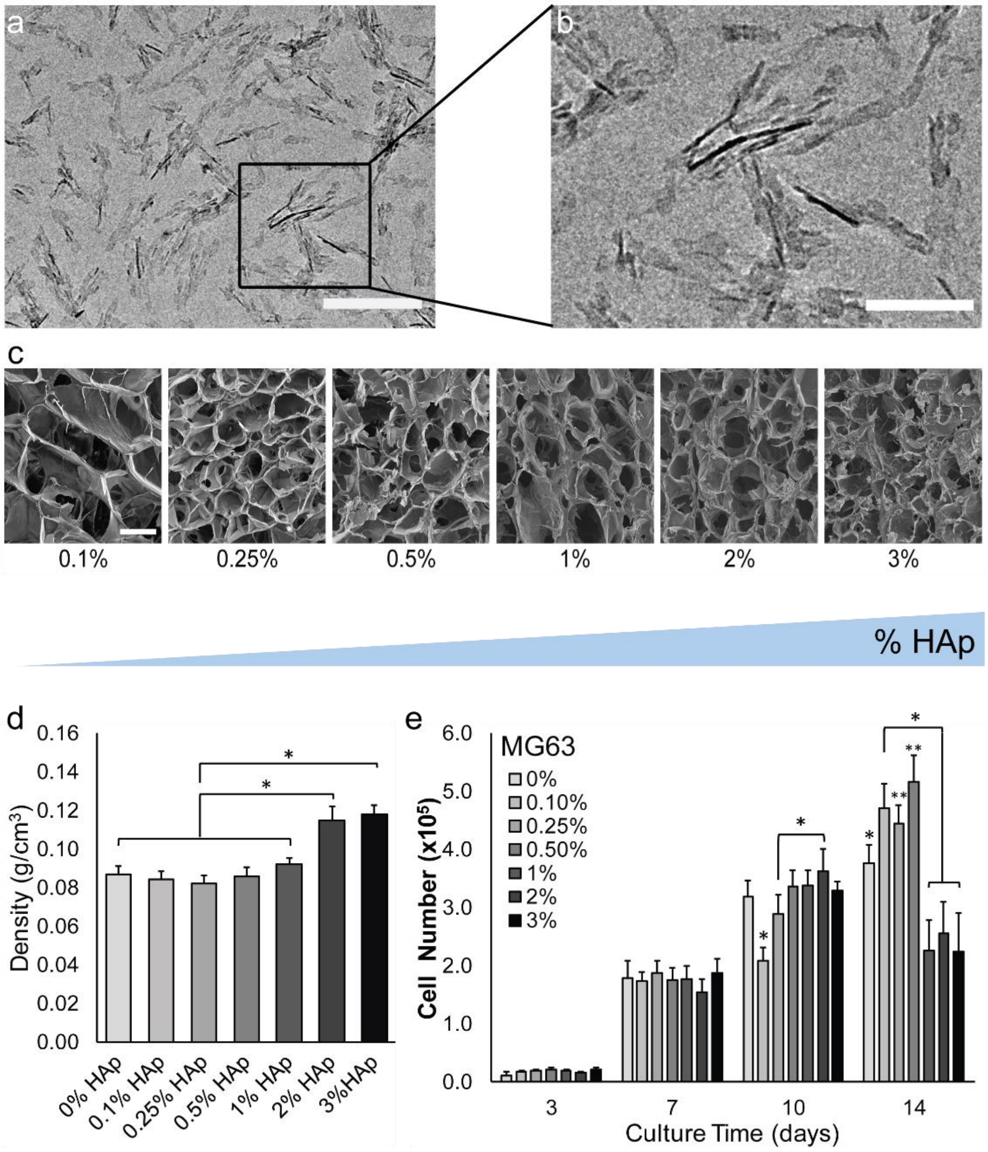

Figure 8.4. Effect of HAp concentration on 6% CA scaffold properties. (**a, b**) Visualization of HAp nanorods with TEM. Scale bars represent 200 nm, and 100 nm, respectively, in (a) and (b). (**c**) SEM images of scaffold pore morphology with varying HAp (HAp concentration increases from left to right). Scale bar represents 200 µm. (**d**) Density of CA + HAp composite scaffolds (n = 8) ($p \leq 0.05$). (**e**) MG63 proliferation on CA + HAp composite scaffolds over a 2-week culture period. *Statistically significant from all or specified conditions ($p \leq 0.05$). **Statistically significant from all conditions except 0.1% HAp ($p \leq 0.05$).

The proliferative capacity of MG63 cells in HAp-integrated scaffolds was determined by evaluating metabolic activity (**Figure 8.4e)**. At day 7, no significant difference in metabolic activity was observed for cells cultured on CA scaffolds with or without HAp. By day 14, scaffolds with ≥ 1 wt% HAp began to degrade and release cells into suspension, resulting in decreased cell number. After two-weeks of culture, the 6% CA + 0.5% HAp scaffolds demonstrated aqueous stability while supporting proliferation of osteogenic cells. Therefore, this scaffold was selected for the osteochondral scaffold bone layer.

8.4.3. Bilayer scaffold architecture and mechanical properties

TE scaffolds must be biochemically suited for attachment and proliferation of the desired cell type. Nevertheless, appropriate scaffold structural cues are also essential to generate functional tissue. After evaluating six different scaffolds for supporting attachment and proliferation of the appropriate cell type, we found that SW-1353 and MSC cells prefer a higher HA content scaffold with lower elastic modulus. The MG63 cells favor scaffolds with a higher elastic modulus and the highest HAp content while maintaining scaffold aqueous stability. We achieved a gradient interface by layering two polymer solutions with differing compositions and polymer contents (4% CHA and 6% CA + 0.5% HAp) before a single TIPS-lyophilization process.

The resultant bilayer scaffold pore structure, including the interface region, was visualized via SEM (**Figure 8.5a-d)**. The interface between the two distinct layers of the scaffold was amalgamated and seamless (**Figure 8.5c**) and the cartilage region (4% CHA) was less dense than the bone region (6% CA + HAp) (**Figure 8.5e**). Scaffold porosity followed a similar trend, where the 4% CHA layer porosity was higher than the 6% CA + HAp layer porosity. Importantly, both regions were highly porous with > 87% porosity. High porosity encourages recruitment and infiltration of native cells where the bioactive cues in each scaffold layer (i.e., HA and HAp) can help direct layer-specific ECM and tissue development. Pore size is a critical factor in cell attachment and infiltration, and can play a deterministic role in cell behavior [335]. Due to the higher polymer content of the bone layer, 6% CA + HAp scaffold, the mean pore area was significantly smaller (1.16×10^4 µm^2) than the cartilage layer 4% CHA scaffold (2.36×10^4 µm^2) (**Figure S8.1b)**. Based on mean pore area and the assumption of circular pores to estimate mean pore diameter, the pore diameters would be approximately 145 µm (cartilage) and 110 µm (bone), respectively. These diameters fall in the range of relevant pore sizes for cell growth and tissue regeneration [365].

Pore size, shape, and interconnectivity in TIPS-fabricated scaffolds is dependent on the solution properties and processing temperatures. Development of a homogenous, isotropic pore structure requires uniform thermal energy transfer during freezing and lyophilizing. Layering different polymer solutions can result in non-uniform pore structures as the overlying solution has no direct contact with the freezing surface. Uniform conduction between the two polymer solutions is particularly important to ensure a consistent and integrated interface to mimic the calcified cartilage region, which should help prevent bone ingrowth in the cartilage region [366]. Despite differing polymer solution densities and compositions, the freezing procedure reported here enabled ice crystal formation throughout the scaffold, as demonstrated by the consistent pore formation throughout the entirety of the bilayer scaffold. Further, pores bridge both scaffold layers, thereby creating a stable interface. A stable and interconnected interface is critical to prevent delamination, anchor the cartilage to the bone, and prevent zonal segregation from inhibiting integrated regeneration at the calcified cartilage interface [367, 368].

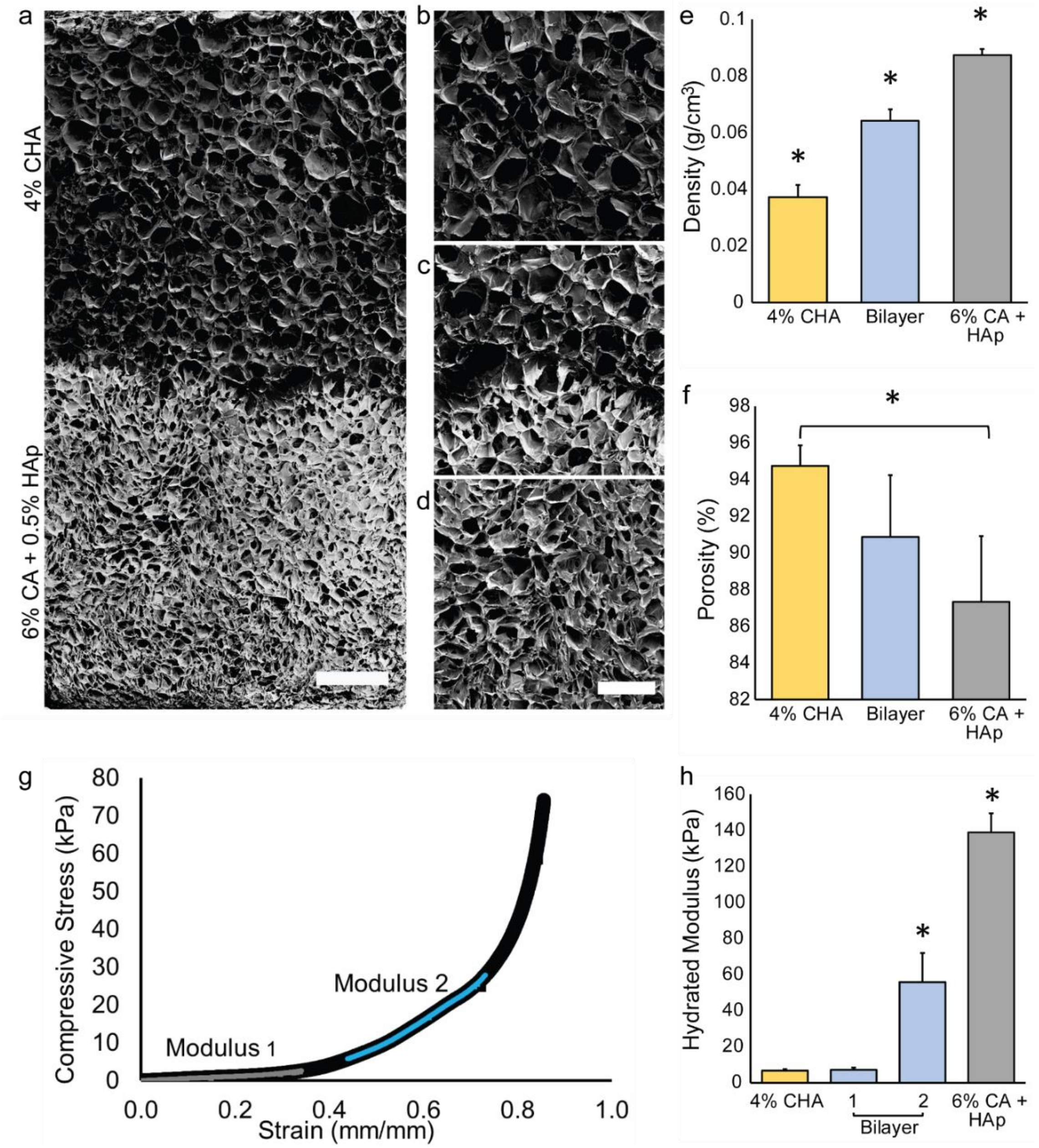

Figure 8.5. Bilayer scaffold characterization. (**a**) SEM of bilayer scaffold with increased magnification of the (**b**) 4% CHA, (**c**) interface, and (**d**) 6% CA + 0.5% HAp layers. Scale bar represents 1 mm in (a) and 500 µm in (b-d). (**e**) Scaffold dry bulk density (n = 4). (**f**) Scaffold porosity (n = 4). (**g**) Representative compressive stress–strain curve for hydrated bilayer scaffold with modulus 1 corresponding to CHA region and modulus 2 corresponding to the CA + HAp region. (**h**) Compressive modulus of hydrated bilayer scaffold compared to pure components (n = 4). *Statistically significant from all or specified conditions ($p \leq 0.05$). Scale bar represents (**a**) 1 mm and (**b-d**) 500 µm.

The stiffness gradient between the cartilage and bone layers of a multiphasic, osteochondral TE scaffold is hypothesized to help mediate lineage in undifferentiated cells [78, 277]. This bilayer scaffold displayed stress-strain behavior typical for porous polymers [308] (**Figure 8.5g)**. Two distinct linear-elastic regions corresponding to each scaffold layer (**Figure 8.5h**) suggest compression of the low stiffness region (4% CHA) prior to the stiffer region (6% CA + HAp). Modulus 1 is defined by a compressive modulus of 6.90 ± 1.29 kPa, whereby Modulus 2 represents a stiffer region with a compressive modulus of 55.84 ± 16.0 kPa (**Figure 8.5h**). Modulus 1 corresponds with the modulus of a 4% CHA scaffold (6.81 ± 0.70 kPa). The compressive modulus of a 6% CA + HAp scaffold was 139.0 ± 10.4 kPa, which is a 150% greater than modulus 2, suggesting that modulus 2 in the bilayer scaffold had some contribution from both the cartilage (4% CHA) and bone (6% CA + HAp) layers, indicating a stiffness gradient. In the native osteochondral microenvironment, the mechanical properties of the osteochondral region vary with patient age, activity, and location in the body, yet the compressive modulus has been cited at 98–270 MPa for subchondral bone [369] and 2–20 MPa for cartilage [370]. Despite advancements in materials and synthesis techniques, native osteochondral tissue has not been fully recapitulated using porous scaffolds. Polymeric scaffold stiffness is significantly less than native bone tissue, yet for non-load bearing bone or unique gradient microenvironments like the osteochondral tissue, a polymeric scaffold may be advantageous to promote healing at the interface. The stiffness of this bilayer scaffold is comparable to other natural polymer-based multiphasic scaffolds that have shown promise *in vivo* [339, 343].

8.4.4. In vitro assessment of bilayer scaffold

Cell attachment, proliferation, and invasion in the bilayer scaffold was determined using two growth factor-free co-culture conditions over a two-week culture period. Scaffold co-cultures included: (1) SW-1353 + MG63 and (2) MSC + MG63. SW-1353 or MSC cells were seeded in the cartilage layer (4% CHA) and MG63 was seeded in the bone layer (6% CA + 0.5% HAp) to mimic native tissue (seeding illustrated in **Figure 8.1b**). A significant increase in metabolic activity over a two-week culture period indicated the bilayer scaffold was amenable to simultaneous proliferation of these two co-cultures conditions (**Figure 8.6)**. Direct quantification of the specific contributions of each cell type to the increased metabolic activity or specific cell numbers associated with each cell line could not be determined using this assay model.

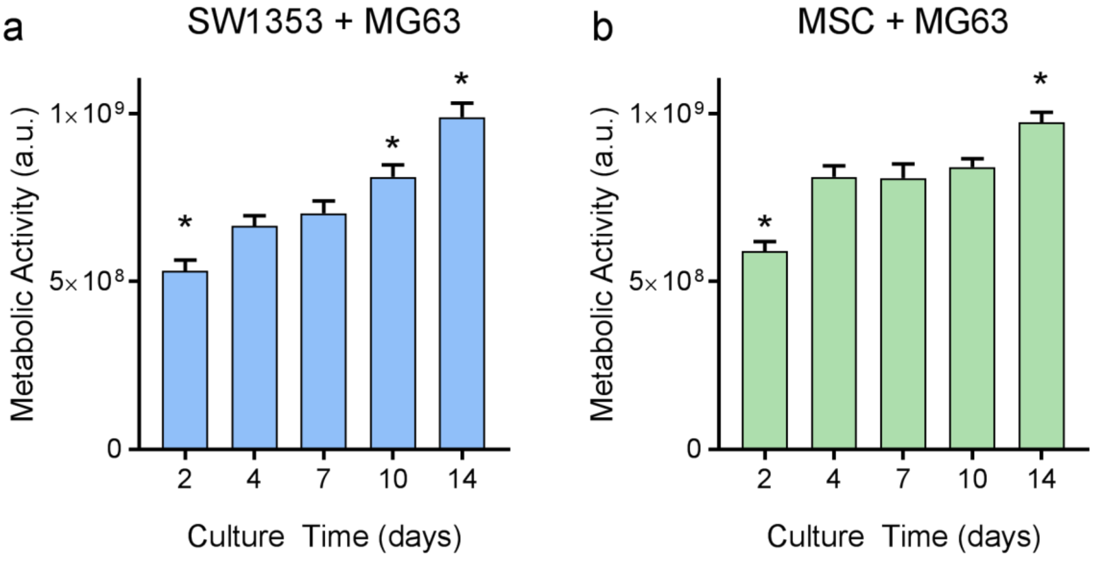

Figure 8.6. Proliferation of chondrogenic and osteogenic cells in bilayer scaffold evaluated by measuring metabolic activity. Evaluation of (**a**) SW-1353 + MG63 and (**b**) MSC + MG63 metabolic activity measured with alamarBlue® (n = 4) *Statistical significance relative to all other time points. ($p \leq 0.05$)

Cell migration and proliferation in each scaffold layer was visualized using fluorescence microscopy (**Figure 8.7)**. In the SW-1353 + MG63 co-culture condition (**Figure 8.7a, b**), an increase in the number of SW-1353 (top, red) and MG63 (bottom, green) cells was observed near the seeding surfaces of the scaffold relative to the scaffold interior at day 1. By day 14, cell density increased in all scaffold layers, and cells appeared to invade the scaffold interior relative to day 1. SW-1353 cells were mostly present as single cells and small cell clusters whereas the MG63 cells formed larger cell clusters. Although sparse, both green and red cells were observed at the interface at day 1. By day 14, the interface displayed a higher density of both cell types, suggesting that both cell types penetrated the scaffold to the interface. At the interface, small cell clusters of SW-1353 and larger cell clusters of MG63 were observed.

In the MSC + MG63 bilayer scaffold (**Figure 8.7c and d**), an increase in cell number at day 14 in the cartilage and bone regions was observed relative to the SW-1353 + MG63 bilayer scaffold**,** although the cell morphologies were similar. Again, the bone layer MG63 cells (bottom, green) form larger clusters than the MSCs in the cartilage layer (top, red). Both red and green cells were present at the interface again suggesting that both cell types penetrated the scaffold pore network.

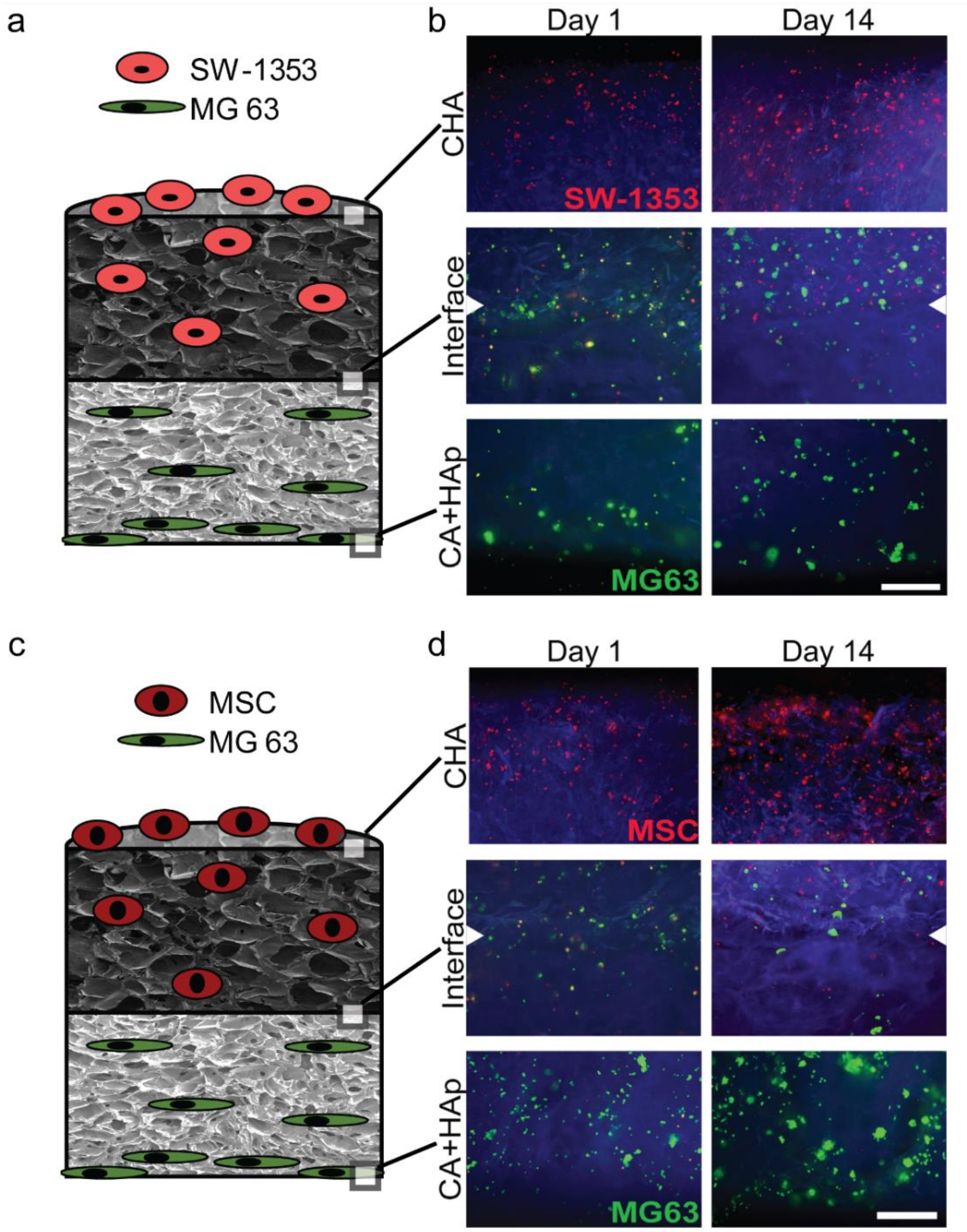

Figure 8.7. Proliferation and migration of chondrogenic and osteogenic cells in bilayer scaffold cross-sections. Evaluation of SW-1353 + MG63 with (**a**) illustration of seeding condition and (**b**) fluorescence imaging of SW-1353 (red) and MG63 (green) in cartilage layer (top), interface (middle, marked by white triangles), and bone layer (bottom) of bilayer scaffold (blue auto fluorescence). Evaluation of MSC + MG63 with (**c**) illustration of seeding condition and (**d**) fluorescence imaging of MSC (red) and MG63 (green) in cartilage layer (top), interface (middle, marked by white triangles), and bone layer (bottom) of bilayer scaffold (blue auto fluorescence). Scale bar is 500 μm in (b) and (d).

To try to correlate increased proliferation with increased functionality, we evaluated early chondrogenic (collagen type II) and osteogenic (osteocalcin) markers using qRT-PCR. Type II collagen plays a critical role in stem cell and chondrocyte maturation and is vital to the development and formation of the GAG-rich articular cartilage [371]. For bone remodeling, osteocalcin is a known osteogenic marker [372] where increased expression signifies osteoblast maturation (**Figure 8.8**). Each cell type was cultured separately on TCPS for comparison of gene expression in co-cultures on the bilayer scaffold relative to 2D TCPS. Gene expression for each condition was normalized to expression of the reference gene GAPDH. For comparison among 2D and co-culture conditions, gene expression was normalized to the 2D TCPS culture of MG63 (set to 1-fold) because both co-cultures contained MG63 cells. Increased expression of chondrogenic and osteogenic markers was observed for both co-cultures on the bilayer scaffolds relative to all 2D cultures, indicating that at early time points, chitosan-based bilayer scaffolds effectively support relevant cells.

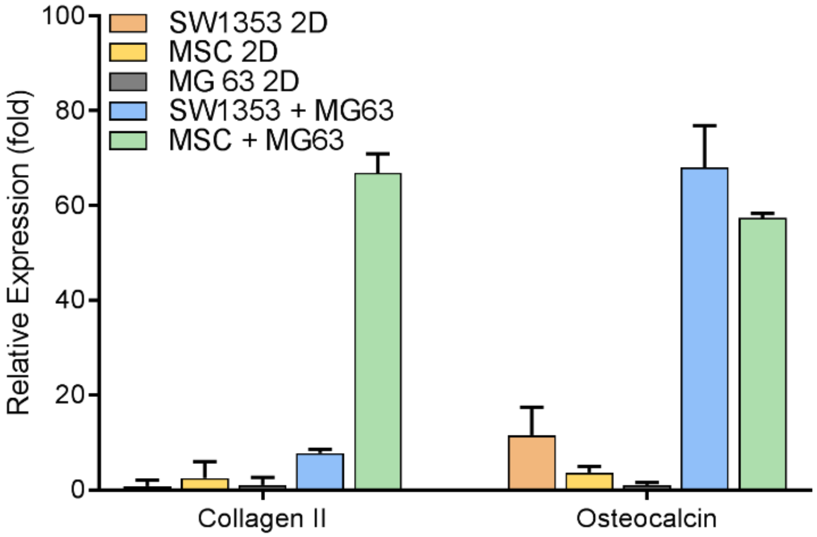

Figure 8.8. Relative expression of RNA content in cells cultured on 2D TCPS (SW1353, MSC, and MG63) versus co-cultures in bilayer scaffolds (SW-1353 + MG63 and MSC + MG63). Gene expression was normalized to a reference gene, GAPDH, and then normalized to expression of MG63 on 2D TCPS (set as 1-fold). (n = 3)

Multiphasic scaffolds have shown promise in regeneration of layered tissues, yet current multiphasic scaffold design is hindered by time-consuming, iterative fabrication techniques and insufficient amalgamation between layers. Here, we designed a biomimetic, bilayer scaffold using a straightforward, fast, and pH-neutral, single-stage fabrication approach. Our layered TIPS approach overcomes the onerous, iterative fabrication requirements of previous technologies while maintaining tunability of each layer. Tailoring bioactive factors and mechanical gradients in multiphasic scaffold layers is vital to support synchronized regeneration. In osteochondral TE, specialized integration and segregation of bioactive factors specific to the bone region or the cartilage region is crucial to enhance zonal organization of the regenerated osteochondral tissue. By exploiting TIPS and the enhanced aqueous stability of PECs, a highly porous, bilayer scaffold was fabricated entirely using natural polymers. Natural polymers are advantageous over synthetic polymers because of their biocompatibility and biodegradability and chitosan, a major component of the bilayer scaffold, has previously been shown to support attachment and proliferation of both osteoblasts [25, 62] and chondrocytes [64]. Importantly, the TIPS approach to layered scaffold fabrication has potential in osteochondral TE as well as for other complex layered tissues. By using a non-toxic, pH-neutral synthesis, future studies involving tailored growth factors integration could allow for sustained delivery and potential chemotactic recruitment of native cells directly to the defect site.

8.5. CONCLUSION

We developed a bilayer, polysaccharide, and GAG-based scaffold for osteochondral tissue regeneration using a simple, fast, and pH-neutral synthesis process. Each region of the bilayer scaffold was optimized with biomechanical and bioactive cues to enhance the proliferation of intended cell types (chondrogenic or osteogenic cells). Fabrication of this layered scaffold is advantageous over previously reported techniques due to the tunability of the elastic moduli of each layer as well as the integration of bioactive factors segregated to each specific region (HA in the cartilage region and HAp in the bone region). Additionally, the seamless gradient zone at the interface ensures stability by inhibiting delamination. The potential of this bilayer scaffold for osteochondral tissue engineering applications was characterized during a two-week co-culture where cell proliferation and infiltration to the scaffold interface was demonstrated.

SUPPLEMENTARY INFORMATION

Table S8.1. Summary of neutralization, crosslinking, and sterilization procedure for all scaffolds.

Scaffold Type	Neutralization and/or Crosslinking	Sterilization
C	1 M sodium carbonate for 1 hr	70% ethanol for 1 hr
CA	0.2 M calcium chloride for 15 min	70% ethanol for 1 hr
CHA	25 vol% ammonium hydroxide for 1 hr	70% ethanol for 1 hr
CA + HAp	0.2 M calcium chloride for 15 min	70% ethanol for 1 hr
CHA + CA + HAP (Bilayer)	0.1 M calcium chloride + 12.5% ammonium hydroxide for 1 hr	70% ethanol for 1 hr

Table S8.2. Chondrogenic (Col2A1) and osteogenic (osteocalcin) markers used for qRT-PCR expressed as forward and reverse primers. Expression levels were normalized to the reference gene, GAPDH.

Target	Forward (5' - 3')	Reverse (5’ - 3’)
GAPDH	5’-ACGGATTTGGTCGTATTGGG-3’	5’-TGATTTTGGAGGGATCTCGC-3’
Col2A1	5’-GAGGGCAATAGCAGGTTCACG-3’	5’-TGGGTGCAATGTCAAATGATG-3’
Osteocalcin	5’-CGCCTGGGTCTCTTCACTAC-3’	5’-CTCACACTCCTCGCCCTATT-3’

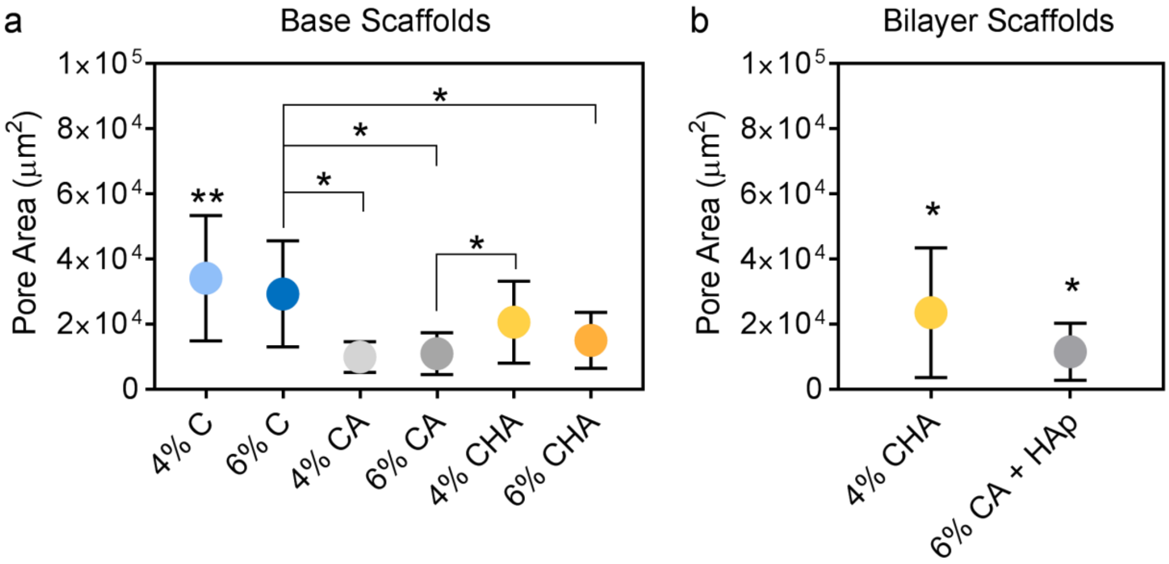

Figure S8.1. Scaffold pore area presented as mean ± standard deviation for (**a**) base material scaffolds (n = 14) and (**b**) each layer of the bilayer scaffold. (n > 35) *Statistical significance from all or specified conditions. **Statistically significant from all conditions except 6% C. ($p \leq 0.05$).

Chapter 9: SUMMARY OF MAJOR FINDINGS

Biomaterial scaffolds have a versatile role in biomedical research with uses ranging from support of tissue repair to development of more biologically relevant cancer tumor models and drug screening platforms. We outlined two scaffold fabrication techniques (electrospinning and thermally induced phase separation) and evaluated the resultant scaffolds for biological relevance. The goal of this dissertation was to present the rational design and fabrication of 2D chitosan-based electrospun nanofibers and 3D porous scaffolds for a diverse set of applications encompassing glioblastoma tumor modeling and osteochondral defect tissue engineering.

Scaling up electrospinning is a highly desirable prospect as nanofibers have a wide array of applications. Further, obtaining up to 102 identical electrospun mats ensures true replicate samples, a difficult feat for electrospun fibers. Using a centrifugal force feed, enhanced alignment and dimensional control was obtained using our novel high throughput centrifugal electrospinning system (HTP-CES). Tight control of both alignment and diameter is crucial in cell-based studies, where either variable can influence cell behavior.

Using highly aligned nanofibers fabricated with the HTP-CES system, we investigated the migratory behavior of glioblastoma multiform. The effect of the nanotopography versus hyaluronic acid coating was investigated for the development of a more biologically relevant GBM migration model. Literature has shown conflicting evidence of the influence of hyaluronic acid on GBM cell behavior. Here, the nanotopography of nanofibers alone was sufficient for cells to exhibit an elongated morphology suggesting a mesenchymal-like phenotype. Cells on the nanofiber substrates also exhibited higher resistance to chemotherapeutic induced cell death. The hyaluronic acid coating appeared to be optimized at 0.5% HA, where with the highest average and maximum cell speeds. Based on these findings, hyaluronic acid-coated nanofibers represent a rational platform for studying GBM cell motility and invasion.

Moving to 3D GBM tumor models for drug screening applications, chitosan–hyaluronic acid polyelectrolyte complex (PEC) scaffolds were fabricated with varying chitosan content. Each scaffold had a significantly different total density, porosity, and compressive modulus. All scaffolds architectures were amenable to cell culture exhibiting > 90% total porosity and pores on the order of 100–200 µm in diameter. The compressive moduli of the scaffolds were in a range that encompasses native brain tissue to tumor tissue. When scaffolds were used for culture of U-87 MG RFP cells, tumor spheroids formed in scaffolds with higher stiffness (4% and 8% CHA). The highest stiffness scaffold (8% CHA) exhibited increased drug resistance, and elevated expression of drug resistance, hypoxia, and invasion-related genes. These differences in cell morphology, drug resistance, and gene expression among the CHA scaffold conditions examined suggest an effect of matrix stiffness on GBM cells *in vitro*. CHA scaffolds represent a useful tool for *in vitro* modeling of the relationship between GBM cells and the surrounding tumor microenvironment. Tunability of the scaffold stiffness allows for extended investigation of cancer cell behavior during tumorigenesis, providing a tool to target and study therapy effectiveness at different stages of cancer progression.

Finally, we investigated a tissue engineering application of the 3D porous scaffolds. We used a pH-neutral synthesis process to fabricate a chitosan-based bilayer composite scaffold. Our layered TIPS approach to bilayer scaffold fabrication is advantageous over previously reported techniques due to the tunability of the elastic moduli of each layer as well as the integration of bioactive factors segregated to each specific region (HA in the cartilage region and HAp in the bone region). Here, we optimized each region of the bilayer scaffold with biomechanical and bioactive cues to enhance proliferation of either chondrogenic or osteogenic cells. After two-weeks of co-culture in the bilayer scaffold, cell proliferation and infiltration of the scaffold interface was demonstrated in media devoid of soluble or differentiation growth factors. Additionally, collagen type II and osteocalcin expression were upregulated in bilayer scaffold co-cultures relative to 2D TCPS culture of MG63. The promising initial results of this bilayer scaffold show potential for its application in osteochondral defect repair and extrapolation into other layered tissues.

Chapter 10: REFERENCES

1. Prevention, C.f.D.C.a., *The State of Aging and Health in America 2013*, U.D.o.H.a.H. Services, Editor. 2013: Atlanta, GA.
2. Kanavos, P., *The rising burden of cancer in the developing world.* Annals of Oncology, 2006. **17 Suppl 8**: p. viii15-viii23.
3. Woolf, A.D. and B. Pfleger, *Burden of major musculoskeletal conditions.* Bull World Health Organ, 2003. **81**(9): p. 646-56.
4. Porter, C.J., et al., *Acute and chronic kidney disease in elderly patients with hip fracture: prevalence, risk factors and outcome with development and validation of a risk prediction model for acute kidney injury.* BMC Nephrol, 2017. **18**(1): p. 20.
5. Loeser, R.F., et al., *Osteoarthritis: a disease of the joint as an organ.* Arthritis and Rheumatism, 2012. **64**(6): p. 1697-707.
6. Saidi, R.F. and S.K. Hejazii Kenari, *Challenges of organ shortage for transplantation: solutions and opportunities.* Int J Organ Transplant Med, 2014. **5**(3): p. 87-96.
7. Mao, A.S. and D.J. Mooney, *Regenerative medicine: Current therapies and future directions.* Proc Natl Acad Sci U S A, 2015. **112**(47): p. 14452-9.
8. Langer, R. and J.P. Vacanti, *Tissue engineering.* Science, 1993. **260**(5110): p. 920-6.
9. Parveen, S., K. Krishnakumar, and S. Sahoo, *New era in health care: tissue engineering.* J Stem Cells Regen Med, 2006. **1**(1): p. 8-24.
10. O'Brien, F.J., *Biomaterials & scaffolds for tissue engineering.* Materials Today, 2011. **14**(3): p. 88-95.
11. Horch, R.E., et al., *Cancer research by means of tissue engineering--is there a rationale?* J Cell Mol Med, 2013. **17**(10): p. 1197-206.
12. Network, O.P.a.T., *Organ by Waiting Time: Current U.S. Waiting Time,* U.S.D.o.H.a.H. Services, Editor. 2018.
13. Siclari, A., et al., *A Cell-free Scaffold-based Cartilage Repair Provides Improved Function Hyaline-like Repair at One year.* Clinical Orthopaedics and Related Research®, 2012. **470**(3): p. 910-919.
14. Levingstone, T.J., et al., *Cell-free multi-layered collagen-based scaffolds demonstrate layer specific regeneration of functional osteochondral tissue in caprine joints.* Biomaterials, 2016. **87**: p. 69-81.
15. Calabrese, G., et al., *Bone augmentation after ectopic implantation of a cell-free collagen-hydroxyapatite scaffold in the mouse.* Scientific Reports, 2016. **6**: p. 36399.
16. Levengood, S.L., et al., *Chitosan–poly(caprolactone) nanofibers for skin repair.* Journal of Materials Chemistry B, 2017. **5**(9): p. 1822-1833.
17. Kumbhar, J.V., et al., *In vitro and in vivo studies of a novel bacterial cellulose-based acellular bilayer nanocomposite scaffold for the repair of osteochondral defects.* International Journal of Nanomedicine, 2017. **12**: p. 6437-6459.
18. Mohiti-Asli, M., et al., *Ibuprofen loaded PLA nanofibrous scaffolds increase proliferation of human skin cells in vitro and promote healing of full thickness incision wounds in vivo.* Journal of Biomedical Materials Research Part B: Applied Biomaterials, 2017. **105**(2): p. 327-339.
19. Thompson, E.M., et al., *An Endochondral Ossification-Based Approach to Bone Repair: Chondrogenically Primed Mesenchymal Stem Cell-Laden Scaffolds Support Greater*

Repair of Critical-Sized Cranial Defects Than Osteogenically Stimulated Constructs In Vivo. Tissue Engineering Part A, 2016. **22**(5-6): p. 556-567.

20. Moradi, L., et al., *Regeneration of meniscus tissue using adipose mesenchymal stem cells-chondrocytes co-culture on a hybrid scaffold: In vivo study.* Biomaterials, 2017. **126**: p. 18-30.
21. Koo, Y., et al., *3D printed cell-laden collagen and hybrid scaffolds for in vivo articular cartilage tissue regeneration.* Journal of Industrial and Engineering Chemistry, 2018.
22. Scott, J.E., *Extracellular matrix, supramolecular organisation and shape.* J Anat, 1995. **187 (Pt 2)**: p. 259-69.
23. Agmon, G. and K.L. Christman, *Controlling stem cell behavior with decellularized extracellular matrix scaffolds.* Curr Opin Solid State Mater Sci, 2016. **20**(4): p. 193-201.
24. Keane, T.J. and S.F. Badylak, *Biomaterials for tissue engineering applications.* Semin Pediatr Surg, 2014. **23**(3): p. 112-8.
25. Levengood, S.L. and M. Zhang, *Chitosan-based scaffolds for bone tissue engineering.* Journal of Materials Chemistry B, 2014. **2**(21): p. 3161-3184.
26. Chan, B.P. and K.W. Leong, *Scaffolding in tissue engineering: general approaches and tissue-specific considerations.* European Spine Journal, 2008. **17**(Suppl 4): p. 467-479.
27. Mallick, K.K. and S.C. Cox, *Biomaterial scaffolds for tissue engineering.* Front Biosci (Elite Ed), 2013. **5**: p. 341-60.
28. Morais, J.M., F. Papadimitrakopoulos, and D.J. Burgess, *Biomaterials/tissue interactions: possible solutions to overcome foreign body response.* AAPS J, 2010. **12**(2): p. 188-96.
29. Stout, R.D., S.K. Watkins, and J. Suttles, *Functional plasticity of macrophages: in situ reprogramming of tumor-associated macrophages.* J Leukoc Biol, 2009. **86**(5): p. 1105-9.
30. Tidball, J.G. and S.A. Villalta, *Regulatory interactions between muscle and the immune system during muscle regeneration.* Am J Physiol Regul Integr Comp Physiol, 2010. **298**(5): p. R1173-87.
31. Collie, A.M., et al., *Differential monocyte/macrophage interleukin-1beta production due to biomaterial topography requires the beta2 integrin signaling pathway.* J Biomed Mater Res A, 2011. **96**(1): p. 162-9.
32. Bota, P.C., et al., *Biomaterial topography alters healing in vivo and monocyte/macrophage activation in vitro.* J Biomed Mater Res A, 2010. **95**(2): p. 649-57.
33. Franz, S., et al., *Artificial extracellular matrices composed of collagen I and high-sulfated hyaluronan promote phenotypic and functional modulation of human pro-inflammatory M1 macrophages.* Acta Biomaterialia, 2013. **9**(3): p. 5621-9.
34. Hersel, U., C. Dahmen, and H. Kessler, *RGD modified polymers: biomaterials for stimulated cell adhesion and beyond.* Biomaterials, 2003. **24**(24): p. 4385-415.
35. Ruoslahti, E., *The RGD story: a personal account.* Matrix Biol, 2003. **22**(6): p. 459-65.
36. Rodríguez-Vázquez, M., et al., *Chitosan and Its Potential Use as a Scaffold for Tissue Engineering in Regenerative Medicine.* Biomed Research International, 2015. **2015**: p. 821279.
37. Anitha, A., et al., *Chitin and chitosan in selected biomedical applications.* Progress in Polymer Science, 2014. **39**(9): p. 1644-1667.
38. Rinaudo, M., *Chitin and chitosan: Properties and applications.* Progress in Polymer Science, 2006. **31**(7): p. 603-632.
39. Younes, I. and M. Rinaudo, *Chitin and Chitosan Preparation from Marine Sources. Structure, Properties and Applications.* Marine Drugs, 2015. **13**(3): p. 1133-1174.

40. Khor, E. and L.Y. Lim, *Implantable applications of chitin and chitosan.* Biomaterials, 2003. **24**(13): p. 2339-49.
41. Roberts, G.A.F., *Structure of Chitin and Chitosan*, in *Chitin Chemistry*. 1992, Macmillan Education UK: London. p. 1-53.
42. Cho, Y.-W., et al., *Preparation and Solubility in Acid and Water of Partially Deacetylated Chitins.* Biomacromolecules, 2000. **1**(4): p. 609-614.
43. Tsai, W.B., et al., *RGD-conjugated UV-crosslinked chitosan scaffolds inoculated with mesenchymal stem cells for bone tissue engineering.* Carbohydr Polym, 2012. **89**(2): p. 379-87.
44. Im, S.Y., et al., *Growth factor releasing porous poly (ε-caprolactone)-chitosan matrices for enhanced bone regenerative rherapy.* Archives of Pharmacal Research, 2003. **26**(1): p. 76-82.
45. Croisier, F. and C. Jérôme, *Chitosan-based biomaterials for tissue engineering.* European Polymer Journal, 2013. **49**(4): p. 780-792.
46. Florczyk, S.J., et al., *Influence of processing parameters on pore structure of 3D porous chitosan-alginate polyelectrolyte complex scaffolds.* Journal of Biomedical Materials Research Part A, 2011. **98**(4): p. 614-20.
47. Tsao, C.T., et al., *Chitosan-PEG hydrogel with sol-gel transition triggerable by multiple external stimuli.* Macromol Rapid Commun, 2015. **36**(3): p. 332-8.
48. Tsao, C.T., et al., *Thermoreversible poly(ethylene glycol)-g-chitosan hydrogel as a therapeutic T lymphocyte depot for localized glioblastoma immunotherapy.* Biomacromolecules, 2014. **15**(7): p. 2656-62.
49. Tsao, C.T., et al., *Chitosan-based thermoreversible hydrogel as an in vitro tumor microenvironment for testing breast cancer therapies.* Mol Pharm, 2014. **11**(7): p. 2134-42.
50. Sun, J., et al., *Enzyme-immobilized clay nanotube–chitosan membranes with sustainable biocatalytic activities.* Physical Chemistry Chemical Physics, 2017. **19**(1): p. 562-567.
51. Erickson, A.E., et al., *High-throughput and high-yield fabrication of uniaxially-aligned chitosan-based nanofibers by centrifugal electrospinning.* Carbohydrate Polymers, 2015. **134**(Supplement C): p. 467-474.
52. Kievit, F.M., et al., *Aligned Chitosan-Polycaprolactone Polyblend Nanofibers Promote the Migration of Glioblastoma Cells.* Advanced Healthcare Materials, 2013. **2**(12): p. 1651-1659.
53. Naseeruteen, F., et al., *Adsorption of malachite green from aqueous solution by using novel chitosan ionic liquid beads.* International Journal of Biological Macromolecules, 2018. **107**: p. 1270-1277.
54. Bée, A., et al., *Magnetic chitosan/clay beads: A magsorbent for the removal of cationic dye from water.* Journal of Magnetism and Magnetic Materials, 2017. **421**: p. 59-64.
55. Ko, J.A., et al., *Preparation and characterization of chitosan microparticles intended for controlled drug delivery.* International Journal of Pharmaceutics, 2002. **249**(1): p. 165-174.
56. van der Lubben, I.M., et al., *Chitosan microparticles for oral vaccination:: preparation, characterization and preliminary in vivo uptake studies in murine Peyer's patches.* Biomaterials, 2001. **22**(7): p. 687-694.
57. Zhang, J., et al., *Enhanced cytotoxic and apoptotic potential in hepatic carcinoma cells of chitosan nanoparticles loaded with ginsenoside compound K.* Carbohydrate Polymers, 2018. **198**: p. 537-545.

58. Wang, T., et al., *Hyaluronic acid-coated chitosan nanoparticles induce ROS-mediated tumor cell apoptosis and enhance antitumor efficiency by targeted drug delivery via CD44.* Journal of Nanobiotechnology, 2017. **15**(1): p. 7.
59. Duse, L., et al., *Preparation and Characterization of Curcumin Loaded Chitosan Nanoparticles for Photodynamic Therapy.* physica status solidi (a), 2017. **0**(0): p. 1700709.
60. Jana, S., et al., *High-strength pristine porous chitosan scaffolds for tissue engineering.* Journal of materials chemistry, 2012. **22**(13): p. 6291-6299.
61. Erickson, A.E., et al., *Fabrication and Characterization of Chitosan–Hyaluronic Acid Scaffolds with Varying Stiffness for Glioblastoma Cell Culture.* Advanced Healthcare Materials, 2018. **0**(0): p. 1800295.
62. Li, Z.S., et al., *Chitosan-alginate hybrid scaffolds for bone tissue engineering.* Biomaterials, 2005. **26**(18): p. 3919-3928.
63. Balagangadharan, K., S. Dhivya, and N. Selvamurugan, *Chitosan based nanofibers in bone tissue engineering.* International Journal of Biological Macromolecules, 2017. **104**: p. 1372-1382.
64. Li, Z.S. and M.Q. Zhang, *Chitosan-alginate as scaffolding material for cartilage tissue engineering.* Journal of Biomedical Materials Research Part A, 2005. **75A**(2): p. 485-493.
65. Chicatun, F., et al., *8 - Collagen/chitosan composite scaffolds for bone and cartilage tissue engineering*, in *Biomedical Composites (Second Edition)*, L. Ambrosio, Editor. 2017, Woodhead Publishing. p. 163-198.
66. Gomes, S., et al., *Evaluation of nanofibrous scaffolds obtained from blends of chitosan, gelatin and polycaprolactone for skin tissue engineering.* International Journal of Biological Macromolecules, 2017. **102**: p. 1174-1185.
67. Yi, Z., et al., *Preparation, characterization, and evaluation of genipin crosslinked chitosan/gelatin three-dimensional scaffolds for liver tissue engineering applications.* Journal of Biomedical Materials Research Part A, 2016. **104**(8): p. 1863-1870.
68. Baniasadi, H., A. Ramazani S.A, and S. Mashayekhan, *Fabrication and characterization of conductive chitosan/gelatin-based scaffolds for nerve tissue engineering.* International Journal of Biological Macromolecules, 2015. **74**: p. 360-366.
69. Gu, Y., et al., *Chitosan/silk fibroin-based, Schwann cell-derived extracellular matrix-modified scaffolds for bridging rat sciatic nerve gaps.* Biomaterials, 2014. **35**(7): p. 2253-2263.
70. Meyer, C., et al., *Chitosan-film enhanced chitosan nerve guides for long-distance regeneration of peripheral nerves.* Biomaterials, 2016. **76**: p. 33-51.
71. Yannas, I.V., et al., *Synthesis and characterization of a model extracellular matrix that induces partial regeneration of adult mammalian skin.* Proc Natl Acad Sci U S A, 1989. **86**(3): p. 933-7.
72. O'Brien, F.J., et al., *The effect of pore size on cell adhesion in collagen-GAG scaffolds.* Biomaterials, 2005. **26**(4): p. 433-41.
73. Murphy, C.M., M.G. Haugh, and F.J. O'Brien, *The effect of mean pore size on cell attachment, proliferation and migration in collagen-glycosaminoglycan scaffolds for bone tissue engineering.* Biomaterials, 2010. **31**(3): p. 461-6.
74. Murphy, C.M. and F.J. O'Brien, *Understanding the effect of mean pore size on cell activity in collagen-glycosaminoglycan scaffolds.* Cell Adh Migr, 2010. **4**(3): p. 377-81.
75. Phelps, E.A. and A.J. Garcia, *Update on therapeutic vascularization strategies.* Regen Med, 2009. **4**(1): p. 65-80.

76. Ko, H.C., B.K. Milthorpe, and C.D. McFarland, *Engineering thick tissues--the vascularisation problem.* Eur Cell Mater, 2007. **14**: p. 1-18; discussion 18-9.
77. Buckley, C.T. and K.U. O'Kelly, *Maintaining cell depth viability: on the efficacy of a trimodal scaffold pore architecture and dynamic rotational culturing.* J Mater Sci Mater Med, 2010. **21**(5): p. 1731-8.
78. Engler, A.J., et al., *Matrix elasticity directs stem cell lineage specification.* Cell, 2006. **126**(4): p. 677-689.
79. Hutmacher, D.W., *Scaffolds in tissue engineering bone and cartilage.* Biomaterials, 2000. **21**(24): p. 2529-43.
80. Beningo, K.A. and Y.L. Wang, *Fc-receptor-mediated phagocytosis is regulated by mechanical properties of the target.* J Cell Sci, 2002. **115**(Pt 4): p. 849-56.
81. Romano, N.H., et al., *Protein-engineered biomaterials: nanoscale mimics of the extracellular matrix.* Biochim Biophys Acta, 2011. **1810**(3): p. 339-49.
82. Lyons, F.G., et al., *The healing of bony defects by cell-free collagen-based scaffolds compared to stem cell-seeded tissue engineered constructs.* Biomaterials, 2010. **31**(35): p. 9232-43.
83. Midha, R., et al., *Growth factor enhancement of peripheral nerve regeneration through a novel synthetic hydrogel tube.* Journal of Neurosurgery, 2003. **99**(3): p. 555-65.
84. Wang, L., et al., *Osteogenesis and angiogenesis of tissue-engineered bone constructed by prevascularized β-tricalcium phosphate scaffold and mesenchymal stem cells.* Biomaterials, 2010. **31**(36): p. 9452-9461.
85. Akmal, M., et al., *The effects of hyaluronic acid on articular chondrocytes.* Journal of Bone and Joint Surgery-British Volume, 2005. **87**(8): p. 1143-9.
86. Hench, L.L., *Bioactive materials: the potential for tissue regeneration.* Journal of Biomedical Materials Research, 1998. **41**(4): p. 511-8.
87. Wang, M., *Developing bioactive composite materials for tissue replacement.* Biomaterials, 2003. **24**(13): p. 2133-51.
88. Lysaght, M.J., A. Jaklenec, and E. Deweerd, *Great expectations: private sector activity in tissue engineering, regenerative medicine, and stem cell therapeutics.* Tissue Eng Part A, 2008. **14**(2): p. 305-15.
89. Place, E.S., N.D. Evans, and M.M. Stevens, *Complexity in biomaterials for tissue engineering.* Nature Materials, 2009. **8**(6): p. 457-70.
90. Antoni, D., et al., *Three-Dimensional Cell Culture: A Breakthrough in Vivo.* International Journal of Molecular Sciences, 2015. **16**(3): p. 5517-5527.
91. Edmondson, R., et al., *Three-Dimensional Cell Culture Systems and Their Applications in Drug Discovery and Cell-Based Biosensors.* Assay and Drug Development Technologies, 2014. **12**(4): p. 207-218.
92. McBeath, R., et al., *Cell shape, cytoskeletal tension, and RhoA regulate stem cell lineage commitment.* Dev Cell, 2004. **6**(4): p. 483-95.
93. Chen, C.S., et al., *Geometric control of cell life and death.* Science, 1997. **276**(5317): p. 1425-8.
94. Ramakrishna, S., et al., *Electrospun nanofibers: solving global issues.* Materials Today, 2006. **9**(3): p. 40-50.
95. Teo, W.E. and S. Ramakrishna, *A review on electrospinning design and nanofibre assemblies.* Nanotechnology, 2006. **17**(14): p. R89-R106.

96. Cooper, A., N. Bhattarai, and M.Q. Zhang, *Fabrication and cellular compatibility of aligned chitosan-PCL fibers for nerve tissue regeneration.* Carbohydrate Polymers, 2011. **85**(1): p. 149-156.
97. Cooper, A., et al., *Aligned chitosan-based nanofibers for enhanced myogenesis.* Journal of materials chemistry, 2010. **20**(40): p. 8904-8911.
98. Teo, W.E., W. He, and S. Ramakrishna, *Electrospun scaffold tailored for tissue-specific extracellular matrix.* Biotechnol J, 2006. **1**(9): p. 918-29.
99. Loh, Q.L. and C. Choong, *Three-Dimensional Scaffolds for Tissue Engineering Applications: Role of Porosity and Pore Size.* Tissue Engineering. Part B, Reviews, 2013. **19**(6): p. 485-502.
100. Aubert, J.H. and R.L. Clough, *Low-density, microcellular polystyrene foams.* Polymer, 1985. **26**(13): p. 2047-2054.
101. Pavia, F.C., et al., *Polymeric scaffolds prepared via thermally induced phase separation: tuning of structure and morphology.* J Biomed Mater Res A, 2008. **86**(2): p. 459-66.
102. Han, M.-J., *Biodegradable membranes for the controlled release of progesterone. 1. Characterization of membrane morphologies coagulated from PLGA/progesterone/DMF solutions.* Journal of Applied Polymer Science, 2000. **75**(1): p. 60-67.
103. Nam, Y.S. and T.G. Park, *Biodegradable polymeric microcellular foams by modified thermally induced phase separation method.* Biomaterials, 1999. **20**(19): p. 1783-90.
104. Sperling, L.H., *Introduction to Physical Polymer Science*. Second Edition ed. 1992, New York: John Wiley and Sons.
105. Ho, M.H., et al., *Preparation of porous scaffolds by using freeze-extraction and freeze-gelation methods.* Biomaterials, 2004. **25**(1): p. 129-38.
106. Siegel, R.L., K.D. Miller, and A. Jemal, *Cancer statistics, 2018.* CA Cancer J Clin, 2018. **68**(1): p. 7-30.
107. Jiang, W.G., et al., *Tissue invasion and metastasis: Molecular, biological and clinical perspectives.* Seminars in Cancer Biology, 2015. **35**: p. S244-S275.
108. Sarkar, S., et al., *Cancer development, progression, and therapy: an epigenetic overview.* Int J Mol Sci, 2013. **14**(10): p. 21087-113.
109. Helleday, T., et al., *DNA repair pathways as targets for cancer therapy.* Nat Rev Cancer, 2008. **8**(3): p. 193-204.
110. Norden, A.D., J. Drappatz, and P.Y. Wen, *Antiangiogenic therapies for high-grade glioma.* Nat Rev Neurol, 2009. **5**(11): p. 610-20.
111. Holle, A.W., J.L. Young, and J.P. Spatz, *In vitro cancer cell-ECM interactions inform in vivo cancer treatment.* Adv Drug Deliv Rev, 2016. **97**: p. 270-9.
112. Bissell, M.J. and W.C. Hines, *Why don't we get more cancer? A proposed role of the microenvironment in restraining cancer progression.* Nat Med, 2011. **17**(3): p. 320-9.
113. Krouskop, T.A., et al., *Elastic moduli of breast and prostate tissues under compression.* Ultrason Imaging, 1998. **20**(4): p. 260-74.
114. Paszek, M.J. and V.M. Weaver, *The tension mounts: mechanics meets morphogenesis and malignancy.* J Mammary Gland Biol Neoplasia, 2004. **9**(4): p. 325-42.
115. Levental, K.R., et al., *Matrix crosslinking forces tumor progression by enhancing integrin signaling.* Cell, 2009. **139**(5): p. 891-906.
116. Pelham, R.J., Jr. and Y.L. Wang, *Cell locomotion and focal adhesions are regulated by the mechanical properties of the substrate.* Biol Bull, 1998. **194**(3): p. 348-9; discussion 349-50.

117. Tse, J.R. and A.J. Engler, *Preparation of Hydrogel Substrates with Tunable Mechanical Properties.* Current Protocols in Cell Biology, 2010. **47**(1): p. 10.16.1-10.16.16.
118. Ghosh, K., et al., *Cell adaptation to a physiologically relevant ECM mimic with different viscoelastic properties.* Biomaterials, 2007. **28**(4): p. 671-679.
119. Zhang, D.Y. and S.L. Friedman, *Fibrosis-dependent mechanisms of hepatocarcinogenesis.* Hepatology, 2012. **56**(2): p. 769-75.
120. Paszek, M.J., et al., *Tensional homeostasis and the malignant phenotype.* Cancer Cell, 2005. **8**(3): p. 241-54.
121. Milosevic, M., et al., *The human tumor microenvironment: invasive (needle) measurement of oxygen and interstitial fluid pressure.* Semin Radiat Oncol, 2004. **14**(3): p. 249-58.
122. Ulrich, T.A., et al., *Probing cellular mechanobiology in three-dimensional culture with collagen-agarose matrices.* Biomaterials, 2010. **31**(7): p. 1875-84.
123. Wolf, K., et al., *Physical limits of cell migration: control by ECM space and nuclear deformation and tuning by proteolysis and traction force.* J Cell Biol, 2013. **201**(7): p. 1069-84.
124. Ulrich, T.A., E.M. de Juan Pardo, and S. Kumar, *The Mechanical Rigidity of the Extracellular Matrix Regulates the Structure, Motility, and Proliferation of Glioma Cells.* Cancer Research, 2009. **69**(10): p. 4167.
125. Zhang, W., et al., *Studying cancer stem cell dynamics on PDMS surfaces for microfluidics device design.* Sci Rep, 2013. **3**: p. 2332.
126. Harisi, R. and A. Jeney, *Extracellular matrix as target for antitumor therapy.* Onco Targets Ther, 2015. **8**: p. 1387-98.
127. Blehm, B.H., et al., *Deconstructing the role of the ECM microenvironment on drug efficacy targeting MAPK signaling in a pre-clinical platform for cutaneous melanoma.* Biomaterials, 2015. **56**: p. 129-39.
128. Sherman-Baust, C.A., et al., *Remodeling of the extracellular matrix through overexpression of collagen VI contributes to cisplatin resistance in ovarian cancer cells.* Cancer Cell, 2003. **3**(4): p. 377-86.
129. Shahal, T., et al., *Regulation of integrin adhesions by varying the density of substrate-bound epidermal growth factor.* Biointerphases, 2012. **7**(1-4): p. 23.
130. Benton, G., E. Crooke, and J. George, *Laminin-1 induces E-cadherin expression in 3-dimensional cultured breast cancer cells by inhibiting DNA methyltransferase 1 and reversing promoter methylation status.* FASEB J, 2009. **23**(11): p. 3884-95.
131. Muiznieks, L.D. and F.W. Keeley, *Molecular assembly and mechanical properties of the extracellular matrix: A fibrous protein perspective.* Biochimica et Biophysica Acta (BBA) - Molecular Basis of Disease, 2013. **1832**(7): p. 866-875.
132. Sabeh, F., R. Shimizu-Hirota, and S.J. Weiss, *Protease-dependent versus -independent cancer cell invasion programs: three-dimensional amoeboid movement revisited.* J Cell Biol, 2009. **185**(1): p. 11-9.
133. Benton, G., et al., *Multiple uses of basement membrane-like matrix (BME/Matrigel) in vitro and in vivo with cancer cells.* International Journal of Cancer, 2011. **128**(8): p. 1751-7.
134. Albini, A., et al., *A rapid in vitro assay for quantitating the invasive potential of tumor cells.* Cancer Research, 1987. **47**(12): p. 3239-45.
135. Stupp, R., et al., *Effects of radiotherapy with concomitant and adjuvant temozolomide versus radiotherapy alone on survival in glioblastoma in a randomised phase III study: 5-year analysis of the EORTC-NCIC trial.* Lancet Oncol, 2009. **10**(5): p. 459-66.

136. Stupp, R., et al., *Radiotherapy plus concomitant and adjuvant temozolomide for glioblastoma.* N Engl J Med, 2005. **352**(10): p. 987-96.
137. McDonald, M.W., et al., *Pattern of failure after limited margin radiotherapy and temozolomide for glioblastoma.* Int J Radiat Oncol Biol Phys, 2011. **79**(1): p. 130-6.
138. Oh, J., et al., *Glioblastoma: patterns of recurrence and efficacy of salvage treatments.* Can J Neurol Sci, 2011. **38**(4): p. 621-5.
139. Abbott, N.J., L. Rönnbäck, and E. Hansson, *Astrocyte–endothelial interactions at the blood–brain barrier.* Nature Reviews Neuroscience, 2006. **7**: p. 41.
140. Fang, C., et al., *Temozolomide nanoparticles for targeted glioblastoma therapy.* ACS Appl Mater Interfaces, 2015. **7**(12): p. 6674-82.
141. Liu, X.Q. and R.Z. Tang, *Biological responses to nanomaterials: understanding nano-bio effects on cell behaviors.* Drug Deliv, 2017. **24**(sup1): p. 1-15.
142. Rehfeldt, F., et al., *Cell responses to the mechanochemical microenvironment--implications for regenerative medicine and drug delivery.* Adv Drug Deliv Rev, 2007. **59**(13): p. 1329-39.
143. Hu, X., et al., *Electrospinning of polymeric nanofibers for drug delivery applications.* J Control Release, 2014. **185**: p. 12-21.
144. Suzuki, A., K. Hosoi, and K. Miyagi, *Broad poly(ethylene terephthalate) nanofiber sheet prepared by CO2 laser supersonic continuous multi-drawing.* Polymer, 2015. **60**: p. 252-259.
145. Estabridis, H.M., et al., *Cell Migration in 1D and 2D Nanofiber Microenvironments.* Ann Biomed Eng, 2018. **46**(3): p. 392-403.
146. Nain, A.S., et al., *Control of Cell Behavior by Aligned Micro/Nanofibrous Biomaterial Scaffolds Fabricated by Spinneret-Based Tunable Engineered Parameters (STEP) Technique.* Small, 2008. **4**(8): p. 1153-1159.
147. Puja, S., et al., *Aligned and suspended fiber force probes for drug testing at single cell resolution.* Biofabrication, 2014. **6**(4): p. 045006.
148. Zhang, H., et al., *Silk fibroin/sodium alginate composite nano-fibrous scaffold prepared through thermally induced phase-separation (TIPS) method for biomedical applications.* Materials Science and Engineering C, 2015. **55**: p. 8-13.
149. D'Arcy, J.M., et al., *Vapor-Phase Polymerization of Nanofibrillar Poly(3,4-ethylenedioxythiophene) for Supercapacitors.* Acs Nano, 2014. **8**(2): p. 1500-1510.
150. Wan, Y.Z., et al., *Directional fluid induced self-assembly of oriented bacterial cellulose nanofibers for potential biomimetic tissue engineering scaffolds.* Materials Chemistry and Physics, 2015. **149**: p. 7-11.
151. Wan, Y.Z., et al., *Bacterial cellulose-templated synthesis of free-standing silica nanotubes with a three-dimensional network structure.* Rsc Advances, 2015. **5**(60): p. 48875-48880.
152. Guo, Q., et al., *Supercapacitors based on hybrid carbon nanofibers containing multiwalled carbon nanotubes.* Journal of materials chemistry, 2009. **19**(18): p. 2810-2816.
153. Hiralal, P., et al., *Nanomaterial-Enhanced All-Solid Flexible Zinc-Carbon Batteries.* ACS nano, 2010. **4**(5): p. 2730-2734.
154. Balamurugan, R., S. Sundarrajan, and S. Ramakrishna, *Recent Trends in Nanofibrous Membranes and Their Suitability for Air and Water Filtrations.* Membranes, 2011. **1**: p. 232-248.
155. Cui, W., Y. Zhou, and J. Chang, *Electrospun nanofibrous materials for tissue engineering and drug delivery.* Sci. Technol. Adv. Mater., 2010. **11**: p. 014108.

156. Ignatious, F., et al., *Electrospun Nanofibers in Oral Drug Delivery.* Pharmaceutical Research, 2010. **27**(4): p. 576-588.
157. Zahedia, P., et al., *A review on wound dressings with an emphasis on electrospun nanofibrous polymeric bandages.* Polym. Adv. Technol., 2012. **21**: p. 77-95.
158. Yarin, A.L., *Branching in electrospinning of nanofibers.* Journal of Applied Physics, 2005. **98**(6): p. 064501.
159. Louis, D.N., *MOLECULAR PATHOLOGY OF MALIGNANT GLIOMAS.* Annual Review of Pathology: Mechanisms of Disease, 2006. **1**(1): p. 97-117.
160. Lefranc, F., J. Brotchi, and R. Kiss, *Possible Future Issues in the Treatment of Glioblastomas: Special Emphasis on Cell Migration and the Resistance of Migrating Glioblastoma Cells to Apoptosis.* Journal of Clinical Oncology, 2005. **23**(10): p. 2411-2422.
161. Beadle, C., et al., *The Role of Myosin II in Glioma Invasion of the Brain.* Molecular Biology of the Cell, 2008. **19**(8): p. 3357-3368.
162. Cukierman, E., et al., *Taking Cell-Matrix Adhesions to the Third Dimension.* Science, 2001. **294**(5547): p. 1708-1712.
163. Suzuki, S.O. and T. Iwaki, *Dynamic analysis of glioma cells: looking into "movement phenotypes".* Neuropathology, 2005. **25**(3): p. 254-62.
164. Liu, Z. and G. Vunjak-Novakovic, *Modeling tumor microenvironments using custom-designed biomaterial scaffolds.* Curr Opin Chem Eng, 2016. **11**: p. 94-105.
165. Johnson, J., et al., *Quantitative Analysis of Complex Glioma Cell Migration on Electrospun Polycaprolactone Using Time-Lapse Microscopy.* Tissue Engineering Part C-Methods, 2009. **15**(4): p. 531-540.
166. Kievit, F.M., et al., *Aligned chitosan-polycaprolactone polyblend nanofibers promote the migration of glioblastoma cells.* Advanced Healthcare Materials, 2013. **2**(12): p. 1651-9.
167. Rape, A., B. Ananthanarayanan, and S. Kumar, *Engineering strategies to mimic the glioblastoma microenvironment.* Adv Drug Deliv Rev, 2014. **79-80**: p. 172-83.
168. Kakita, A. and J.E. Goldman, *Patterns and Dynamics of SVZ Cell Migration in the Postnatal Forebrain.* Neuron, 1999. **23**(3): p. 461-472.
169. Schaar, B.T. and S.K. McConnell, *Cytoskeletal coordination during neuronal migration.* Proceedings of the National Academy of Sciences of the United States of America, 2005. **102**(38): p. 13652-13657.
170. Suzuki, S.O. and J.E. Goldman, *Multiple Cell Populations in the Early Postnatal Subventricular Zone Take Distinct Migratory Pathways: A Dynamic Study of Glial and Neuronal Progenitor Migration.* The Journal of Neuroscience, 2003. **23**(10): p. 4240-4250.
171. Agudelo-Garcia, P.A., et al., *Glioma Cell Migration on Three-dimensional Nanofiber Scaffolds Is Regulated by Substrate Topography and Abolished by Inhibition of STAT3 Signaling.* Neoplasia, 2011. **13**(9): p. 831-U96.
172. Giese, A. and M. Westphal, *Glioma invasion in the central nervous system.* Neurosurgery, 1996. **39**(2): p. 235-50; discussion 250-2.
173. Shih, A.H. and E.C. Holland, *Developmental neurobiology and the origin of brain tumors.* J Neurooncol, 2004. **70**(2): p. 125-36.
174. Gilbertson, R.J. and J.N. Rich, *Making a tumour's bed: glioblastoma stem cells and the vascular niche.* Nat Rev Cancer, 2007. **7**(10): p. 733-6.
175. Beliveau, A., et al., *Aligned Nanotopography Promotes a Migratory State in Glioblastoma Multiforme Tumor Cells.* Sci Rep, 2016. **6**: p. 26143.

176. Koons, B., et al., *Cancer Protrusions on a Tightrope: Nanofiber Curvature Contrast Quantitates Single Protrusion Dynamics.* Acs Nano, 2017. **11**(12): p. 12037-12048.
177. Liewald, D., et al., *Distribution of axon diameters in cortical white matter: an electron-microscopic study on three human brains and a macaque.* Biological Cybernetics, 2014. **108**(5): p. 541-557.
178. Rao, S.S., et al., *Mimicking white matter tract topography using core-shell electrospun nanofibers to examine migration of malignant brain tumors.* Biomaterials, 2013. **34**(21): p. 5181-5190.
179. Cox, B.D., et al., *New concepts regarding focal adhesion kinase promotion of cell migration and proliferation.* J Cell Biochem, 2006. **99**(1): p. 35-52.
180. Koochekpour, S., G.J. Pilkington, and A. Merzak, *Hyaluronic acid/CD44H interaction induces cell detachment and stimulates migration and invasion of human glioma cells in vitro.* International Journal of Cancer, 1995. **63**(3): p. 450-4.
181. Radotra, B. and D. McCormick, *Glioma invasion in vitro is mediated by CD44-hyaluronan interactions.* J Pathol, 1997. **181**(4): p. 434-8.
182. Florczyk, S.J., et al., *Porous chitosan-hyaluronic acid scaffolds as a mimic of glioblastoma microenvironment ECM.* Biomaterials, 2013. **34**(38): p. 10143-50.
183. Sun, C., et al., *Noninvasive nanoparticle strategies for brain tumor targeting.* Nanomedicine, 2017. **13**(8): p. 2605-2621.
184. Irani, M., G.M.M. Sadeghi, and I. Haririan, *The sustained delivery of temozolomide from electrospun PCL-Diol-b-PU/gold nanocompsite nanofibers to treat glioblastoma tumors.* Mater Sci Eng C Mater Biol Appl, 2017. **75**: p. 165-174.
185. Wei, X., et al., *Brain tumor-targeted drug delivery strategies.* Acta Pharm Sin B, 2014. **4**(3): p. 193-201.
186. Tseng, Y.Y., et al., *Concurrent delivery of carmustine, irinotecan, and cisplatin to the cerebral cavity using biodegradable nanofibers: In vitro and in vivo studies.* Colloids Surf B Biointerfaces, 2015. **134**: p. 254-61.
187. Tseng, Y.Y., et al., *Sustainable release of carmustine from biodegradable poly[((D,L))-lactide-co-glycolide] nanofibrous membranes in the cerebral cavity: in vitro and in vivo studies.* Expert Opin Drug Deliv, 2013. **10**(7): p. 879-88.
188. Ranganath, S.H. and C.H. Wang, *Biodegradable microfiber implants delivering paclitaxel for post-surgical chemotherapy against malignant glioma.* Biomaterials, 2008. **29**(20): p. 2996-3003.
189. Kuramitsu, S., et al., *Double-edged Sword in the Placement of Carmustine (BCNU) Wafers along the Eloquent Area: A Case Report.* NMC Case Rep J, 2015. **2**(1): p. 40-45.
190. Ranganath, S.H., et al., *The use of submicron/nanoscale PLGA implants to deliver paclitaxel with enhanced pharmacokinetics and therapeutic efficacy in intracranial glioblastoma in mice.* Biomaterials, 2010. **31**(19): p. 5199-207.
191. Mangraviti, A., et al., *Nanobiotechnology-based delivery strategies: New frontiers in brain tumor targeted therapies.* J Control Release, 2016. **240**: p. 443-453.
192. Irani, M., G. Mir Mohamad Sadeghi, and I. Haririan, *Gold coated poly (epsilon-caprolactonediol) based polyurethane nanofibers for controlled release of temozolomide.* Biomed Pharmacother, 2017. **88**: p. 667-676.
193. Thakkar, S. and M. Misra, *Electrospun polymeric nanofibers: New horizons in drug delivery.* Eur J Pharm Sci, 2017. **107**: p. 148-167.

194. Liu, W., S. Thomopoulos, and Y. Xia, *Electrospun nanofibers for regenerative medicine.* Advanced Healthcare Materials, 2012. **1**(1): p. 10-25.
195. Wang, X., B. Ding, and B. Li, *Biomimetic electrospun nanofibrous structures for tissue engineering.* Mater Today (Kidlington), 2013. **16**(6): p. 229-241.
196. Eckardstein, K.L.v., et al., *Local chemotherapy of F98 rat glioblastoma with paclitaxel and carboplatin embedded in liquid crystalline cubic phases.* Journal of Neuro-Oncology, 2005. **72**(3): p. 209-215.
197. Brem, H., et al., *Placebo-controlled trial of safety and efficacy of intraoperative controlled delivery by biodegradable polymers of chemotherapy for recurrent gliomas. The Polymer-brain Tumor Treatment Group.* Lancet, 1995. **345**(8956): p. 1008-12.
198. Horwitz, S.B., *Taxol (paclitaxel): mechanisms of action.* Annals of Oncology, 1994. **5 Suppl 6**: p. S3-6.
199. Hurwitz, C.A., et al., *Paclitaxel for the Treatment of Progressive or Recurrent Childhood Brain Tumors: A Pediatric Oncology Phase II Study.* Journal of Pediatric Hematology/Oncology, 2001. **23**(5): p. 277-281.
200. Milas, L., et al., *Enhancement of Tumor Radioresponse of a Murine Mammary Carcinoma by Paclitaxel.* Cancer Research, 1994. **54**(13): p. 3506-3510.
201. Niero, A., et al., *Paclitaxel and radiotherapy: sequence-dependent efficacy--a preclinical model.* Clinical Cancer Research, 1999. **5**(8): p. 2213-22.
202. Cahan, M.A., et al., *Cytotoxicity of taxol in vitro against human and rat malignant brain tumors.* Cancer Chemother Pharmacol, 1994. **33**(5): p. 441-4.
203. Tishler, R.B., et al., *Taxol sensitizes human astrocytoma cells to radiation.* Cancer Research, 1992. **52**(12): p. 3495-7.
204. Chang, S.M., et al., *A Phase II study of paclitaxel in patients with recurrent malignant glioma using different doses depending upon the concomitant use of anticonvulsants: a North American Brain Tumor Consortium report.* Cancer, 2001. **91**(2): p. 417-22.
205. Irani, M., G.M.M. Sadeghi, and I. Haririan, *The sustained delivery of temozolomide from electrospun PCL-Diol-b-PU/gold nanocompsite nanofibers to treat glioblastoma tumors.* Materials Science and Engineering: C, 2017. **75**: p. 165-174.
206. Tsang, L.L., et al., *Characterisation of urinary metabolites of temozolomide in humans and mice and evaluation of their cytotoxicity.* Cancer Chemother Pharmacol, 1990. **26**(6): p. 429-36.
207. Brem, S., et al., *Local delivery of temozolomide by biodegradable polymers is superior to oral administration in a rodent glioma model.* Cancer Chemother Pharmacol, 2007. **60**(5): p. 643-50.
208. Mehta, A.I., et al., *Current status of intratumoral therapy for glioblastoma.* J Neurooncol, 2015. **125**(1): p. 1-7.
209. Fan, C.H., et al., *Antiangiogenic-targeting drug-loaded microbubbles combined with focused ultrasound for glioma treatment.* Biomaterials, 2013. **34**(8): p. 2142-55.
210. Xu, X., et al., *BCNU-loaded PEG–PLLA ultrafine fibers and their in vitro antitumor activity against Glioma C6 cells.* Journal of Controlled Release, 2006. **114**(3): p. 307-316.
211. Tatter, S.B., *Recurrent malignant glioma in adults.* Curr Treat Options Oncol, 2002. **3**(6): p. 509-24.
212. Ramachandran, R., et al., *Theranostic 3-Dimensional nano brain-implant for prolonged and localized treatment of recurrent glioma.* Sci Rep, 2017. **7**: p. 43271.

213. Bregy, A., et al., *The role of Gliadel wafers in the treatment of high-grade gliomas.* Expert Rev Anticancer Ther, 2013. **13**(12): p. 1453-61.
214. Gallego, J.M., J.A. Barcia, and C. Barcia-Marino, *Fatal outcome related to carmustine implants in glioblastoma multiforme.* Acta Neurochir (Wien), 2007. **149**(3): p. 261-5; discussion 265.
215. Mu, F., et al., *Tumor resection with carmustine wafer placement as salvage therapy after local failure of radiosurgery for brain metastasis.* J Clin Neurosci, 2015. **22**(3): p. 561-5.
216. Han, D., et al., *In-vitro evaluation of MPA-loaded electrospun coaxial fiber membranes for local treatment of glioblastoma tumor cells.* Journal of Drug Delivery Science and Technology, 2017. **40**: p. 45-50.
217. Lei, C., et al., *Development of a gene/drug dual delivery system for brain tumor therapy: potent inhibition via RNA interference and synergistic effects.* Biomaterials, 2013. **34**(30): p. 7483-94.
218. Tseng, Y.Y., et al., *Advanced interstitial chemotherapy combined with targeted treatment of malignant glioma in rats by using drug-loaded nanofibrous membranes.* Oncotarget, 2016. **7**(37): p. 59902-59916.
219. Bago, J.R., et al., *Fibrin matrices enhance the transplant and efficacy of cytotoxic stem cell therapy for post-surgical cancer.* Biomaterials, 2016. **84**: p. 42-53.
220. Chang, J., et al., *Piezoelectric nanofibers for energy scavenging applications.* Nano Energy, 2012. **1**: p. 356-371.
221. Edmondson, D., et al., *Centrifugal electrospinning of highly aligned polymer nanofibers over a large area.* J. Mater. Chem, 2012. **22**: p. 18646-18652.
222. Thoppey, N.M., et al., *Edge electrospinning for high throughput production of quality nanofibers.* Nanotechnology, 2011. **22**(34).
223. Varesano, A., et al., *Multi-jet nozzle electrospinning on textile substrates: observations on process and nanofibremat deposition.* Polym Int, 2010. **59**: p. 1606-1615.
224. Varabhas, J.S., G.G. Chase, and D.H. Reneker, *Electrospun nanofibers from a porous hollow tube.* Polymer, 2008. **49**(19): p. 4226-4229.
225. Kumar, A., et al., *Controlling Fiber Repulsion in Multijet Electrospinning for Higher Throughput.* Macromol. Mater. Eng., 2010. **295**: p. 701-708.
226. Lukas, D., A. Sarkar, and P. Pokorny, *Self-organization of jets in electrospinning from free liquid surface: A generalized approach.* Journal of Applied Physics, 2008. **103**: p. 084309.
227. Jirsak, O., et al., *Polyamic Acid Nanofibers Produced by Needleless Electrospinning.* Journal of Nanomaterials, 2010. **2010**: p. 842831.
228. Patel, S., et al., *Bioactive Nanofibers: Synergistic Effects of Nanotopography and Chemical Signaling on Cell Guidance.* Nano Letters, 2007. **7**(7): p. 2122-2128.
229. Ghasemi-Mobarakeh, L., et al., *Electrospun poly(3-caprolactone)/gelatin nanofibrous scaffolds for nerve tissue engineering.* Biomaterials, 2008. **29**: p. 4532-4639.
230. Yin, Z., et al., *The regulation of tendon stem cell differentiation by the alignment of nanofibers.* Biomaterials, 2010. **31**(8): p. 2163-2175.
231. Matthews, J.A., et al., *Electrospinning of collagen nanofibers.* Biomacromolecules, 2002. **3**(2): p. 232-238.
232. Theron, A., E. Zussman, and A.L. Yarin, *Electrostatic field-assisted alignment of electrospun nanofibres.* Nanotechnology, 2001. **12**(3): p. 384-390.

233. Baji, A., et al., *Electrospinning of polymer nanofibers: Effects on oriented morphology, structures and tensile properties.* Composites Science and Technology, 2010. **70**(5): p. 703-718.
234. Li, D., Y.L. Wang, and Y.N. Xia, *Electrospinning nanofibers as uniaxially aligned arrays and layer-by-layer stacked films.* Advanced Materials, 2004. **16**(4): p. 361-366.
235. Bhattarai, N., et al., *Natural-Synthetic Polyblend Nanofibers for Biomedical Applications.* Advanced Materials, 2009. **21**(27): p. 2792-2797.
236. Sionkowska, A., *Current research on the blends of natural and synthetic polymers as new biomaterials: Review.* Progress in Polymer Science, 2011. **36**(9): p. 1254-1276.
237. O'Connell, B. *Oval Profile Plot*. Available from: http://rsbweb.nih.gov/ij/plugins/ovalprofile.html.
238. Hasegawa, M., et al., *Dissolving States of Cellulose and Chitosan in Trifluoroacetic-Acid.* Journal of Applied Polymer Science, 1992. **45**(10): p. 1857-1863.
239. Shalumon, K.T., et al., *Single step electrospinning of chitosan/poly(caprolactone) nanofibers using formic acid/acetone solvent mixture.* Carbohydrate Polymers, 2010. **80**(2): p. 413-419.
240. Sahoo, S., et al., *Synthesis of chitosan-polycaprolactone blend for control delivery of ofloxacin drug.* Carbohydrate Polymers, 2010. **79**(1): p. 106-113.
241. Cardoso, G.B.C., et al., *Novel hybrid membrane of chitosan/poly (ε-caprolactone) for tissue engineering.* Biomatter, 2014. **4**(1): p. e29508.
242. Ko, J., et al., *Using mathematical modeling to control topographical properties of poly (epsilon-caprolactone) melt electrospun scaffolds.* Journal of Micromechanics and Microengineering, 2014. **24**(6).
243. Zhao, S.L., et al., *Electrospinning of ethyl-cyanoethyl cellulose/tetrahydrofuran solutions.* Journal of Applied Polymer Science, 2004. **91**(1): p. 242-246.
244. Heikkila, P. and A. Harlin, *Parameter study of electrospinning of polyamide-6.* European Polymer Journal, 2008. **44**(10): p. 3067-3079.
245. Cui, W.G., et al., *Investigation on process parameters of electrospinning system through orthogonal experimental design.* Journal of Applied Polymer Science, 2007. **103**(5): p. 3105-3112.
246. Wang, C., et al., *Effect of concentration, voltage, take-over distance and diameter of pinhead on precursory poly (phenylene vinylene) electrospinning.* Pigment & Resin Technology, 2006. **35**(5): p. 278-283.
247. Macossay, J., et al., *Effect of needle diameter on nanofiber diameter and thermal properties of electrospun poly(methyl methacrylate).* Polymers for Advanced Technologies, 2007. **18**(3): p. 180-183.
248. Zhou, H.J., T.B. Green, and Y.L. Joo, *The thermal effects on electrospinning of polylactic acid melts.* Polymer, 2006. **47**(21): p. 7497-7505.
249. Theron, S.A., E. Zussman, and A.L. Yarin, *Experimental investigation of the governing parameters in the electrospinning of polymer solutions.* Polymer, 2004. **45**(6): p. 2017-2030.
250. Kim, C.W., et al., *Structural studies of electrospun cellulose nanofibers.* Polymer, 2006. **47**(14): p. 5097-5107.
251. Hao, W.T., et al., *Polyurethane Electrospun Mats Strengthened and Toughened by Physically Blended Polyhedral Oligomeric Silsesquioxane.* Journal of Applied Polymer Science, 2014. **131**(20).

252. Zhang, Y.Z., et al., *Coaxial electrospinning of (fluorescein isothiocyanate-conjugated bovine serum albumin)-encapsulated poly(epsilon-caprolactone) nanofibers for sustained release.* Biomacromolecules, 2006. **7**(4): p. 1049-1057.
253. Yim, E.K.F., et al., *Nanotopography-induced changes in focal adhesions, cytoskeletal organization, and mechanical properties of human mesenchymal stem cells.* Biomaterials, 2010. **31**(6): p. 1299-1306.
254. Eyler, C.E. and J.N. Rich, *Survival of the fittest: Cancer stem cells in therapeutic resistance and angiogenesis.* Journal of Clinical Oncology, 2008. **26**(17): p. 2839-2845.
255. Bellail, A.C., et al., *Microregional extracellular matrix heterogeneity in brain modulates glioma cell invasion.* International Journal of Biochemistry & Cell Biology, 2004. **36**(6): p. 1046-1069.
256. Ananthanarayanan, B., Y. Kim, and S. Kumar, *Elucidating the mechanobiology of malignant brain tumors using a brain matrix-mimetic hyaluronic acid hydrogel platform.* Biomaterials, 2011. **32**(31): p. 7913-7923.
257. Fortin Ensign, S., et al., *Implications of Rho GTPase Signaling in Glioma Cell Invasion and Tumor Progression.* Frontiers in Oncology, 2013. **3**(241).
258. Ohnishi, T., et al., *A Novel Model of Glioma Cell Invasion Using Organotypic Brain Slice Culture.* Cancer Research, 1998. **58**(14): p. 2935-2940.
259. Jain, A., et al., *Guiding intracortical brain tumour cells to an extracortical cytotoxic hydrogel using aligned polymeric nanofibres.* Nature Materials, 2014. **13**(3): p. 309-U118.
260. Bhattarai, N., et al., *Natural-Synthetic Polyblend Nanofibers for Biomedical Applications.* Advanced Materials, 2009. **21**(27): p. 2792-2797.
261. Maeda, N., et al., *Composite polysaccharide fibers prepared by electrospinning and coating.* Carbohydrate Polymers, 2014. **102**: p. 950-955.
262. Ahire, J.J., et al., *Hyaluronic acid-coated poly(d,l-lactide) (PDLLA) nanofibers prepared by electrospinning and coating.* Rsc Advances, 2016. **6**(41): p. 34791-34796.
263. Tinevez, J.Y., et al., *TrackMate: An open and extensible platform for single-particle tracking.* Methods, 2017. **115**: p. 80-90.
264. Fisher, B.J., et al., *Ki-67: A prognostic factor for low-grade glioma?* International Journal of Radiation Oncology Biology Physics, 2002. **52**(4): p. 996-1001.
265. Farin, A., et al., *Transplanted glioma cells migrate and proliferate on host brain vasculature: A dynamic analysis.* Glia, 2006. **53**(8): p. 799-808.
266. Giese, A., et al., *Dichotomy of astrocytoma migration and proliferation.* International Journal of Cancer, 1996. **67**(2): p. 275-282.
267. Dhruv, H.D., et al., *Reciprocal Activation of Transcription Factors Underlies the Dichotomy between Proliferation and Invasion of Glioma Cells.* Plos One, 2013. **8**(8).
268. Giese, A., et al., *Cost of migration: Invasion of malignant gliomas and implications for treatment.* Journal of Clinical Oncology, 2003. **21**(8): p. 1624-1636.
269. Winkler, F., et al., *Imaging Glioma Cell Invasion In Vivo Reveals Mechanisms of Dissemination and Peritumoral Angiogenesis.* Glia, 2009. **57**(12): p. 1306-1315.
270. Holland, E.C., *Glioblastoma multiforme: the terminator.* Proc Natl Acad Sci U S A, 2000. **97**(12): p. 6242-4.
271. Ortensi, B., et al., *Rai is a new regulator of neural progenitor migration and glioblastoma invasion.* Stem Cells, 2012. **30**(5): p. 817-32.
272. McNamara, M.G., S. Sahebjam, and W.P. Mason, *Emerging biomarkers in glioblastoma.* Cancers (Basel), 2013. **5**(3): p. 1103-19.

273. Umesh, V., et al., *Microenvironmental stiffness enhances glioma cell proliferation by stimulating epidermal growth factor receptor signaling.* Plos One, 2014. **9**(7): p. e101771.
274. Willis, A.L., et al., *Extracellular matrix determinants and the regulation of cancer cell invasion stratagems.* J Microsc, 2013. **251**(3): p. 250-60.
275. Petrecca, K., et al., *Failure pattern following complete resection plus radiotherapy and temozolomide is at the resection margin in patients with glioblastoma.* J Neurooncol, 2013. **111**(1): p. 19-23.
276. Mani, S.A., et al., *The epithelial-mesenchymal transition generates cells with properties of stem cells.* Cell, 2008. **133**(4): p. 704-15.
277. Discher, D.E., P. Janmey, and Y.L. Wang, *Tissue cells feel and respond to the stiffness of their substrate.* Science, 2005. **310**(5751): p. 1139-43.
278. Pogoda, K., et al., *Compression stiffening of brain and its effect on mechanosensing by glioma cells.* New Journal of Physics, 2014. **16**.
279. Wei, S.C., et al., *Matrix stiffness drives epithelial-mesenchymal transition and tumour metastasis through a TWIST1-G3BP2 mechanotransduction pathway.* Nat Cell Biol, 2015. **17**(5): p. 678-88.
280. Kievit, F.M., et al., *Proliferation and enrichment of CD133(+) glioblastoma cancer stem cells on 3D chitosan-alginate scaffolds.* Biomaterials, 2014. **35**(33): p. 9137-43.
281. Weiswald, L.B., D. Bellet, and V. Dangles-Marie, *Spherical cancer models in tumor biology.* Neoplasia, 2015. **17**(1): p. 1-15.
282. Calvet, C.Y., F.M. Andre, and L.M. Mir, *The culture of cancer cell lines as tumorspheres does not systematically result in cancer stem cell enrichment.* Plos One, 2014. **9**(2): p. e89644.
283. Hutmacher, D.W., *Biomaterials offer cancer research the third dimension.* Nat Mater, 2010. **9**(2): p. 90-3.
284. Kievit, F.M., et al., *Chitosan-alginate 3D scaffolds as a mimic of the glioma tumor microenvironment.* Biomaterials, 2010. **31**(22): p. 5903-10.
285. Xu, X., M.C. Farach-Carson, and X. Jia, *Three-dimensional in vitro tumor models for cancer research and drug evaluation.* Biotechnol Adv, 2014. **32**(7): p. 1256-68.
286. Rape, A.D., et al., *A synthetic hydrogel for the high-throughput study of cell-ECM interactions.* Nat Commun, 2015. **6**: p. 8129.
287. Martinez-Ramos, C. and M. Lebourg, *Three-dimensional constructs using hyaluronan cell carrier as a tool for the study of cancer stem cells.* Journal of Biomedical Materials Research, Part B, 2014. **103B**: p. 1249-1257.
288. Rao, S.S., et al., *Inherent interfacial mechanical gradients in 3D hydrogels influence tumor cell behaviors.* Plos One, 2012. **7**(4): p. e35852.
289. Hegedus, B., et al., *The interplay of cell-cell and cell-matrix interactions in the invasive properties of brain tumors.* Biophys J, 2006. **91**(7): p. 2708-16.
290. Kaufman, L.J., et al., *Glioma expansion in collagen I matrices: analyzing collagen concentration-dependent growth and motility patterns.* Biophys J, 2005. **89**(1): p. 635-50.
291. Yang, Y.L., S. Motte, and L.J. Kaufman, *Pore size variable type I collagen gels and their interaction with glioma cells.* Biomaterials, 2010. **31**(21): p. 5678-88.
292. Gordon, V.D., et al., *Measuring the mechanical stress induced by an expanding multicellular tumor system: a case study.* Exp Cell Res, 2003. **289**(1): p. 58-66.
293. Toole, B.P., *Hyaluronan: from extracellular glue to pericellular cue.* Nature Reviews Cancer, 2004. **4**(7): p. 528-39.

294. Rinaudo, M., *Main properties and current applications of some polysaccharides as biomaterials.* Polymer International, 2008. **57**(3): p. 397-430.
295. Gil, E.S., et al., *Mechanical improvements to reinforced porous silk scaffolds.* Journal of Biomedical Materials Research Part A, 2011. **99**(1): p. 16-28.
296. Kirdponpattara, S., et al., *Structural modification and characterization of bacterial cellulose-alginate composite scaffolds for tissue engineering.* Carbohydr Polym, 2015. **132**: p. 146-55.
297. Kleihues, P. and L.H. Sobin, *World Health Organization classification of tumors.* Cancer, 2000. **88**(12): p. 2887.
298. Sironen, R.K., et al., *Hyaluronan in human malignancies.* Exp Cell Res, 2011. **317**(4): p. 383-91.
299. Toole, B.P., *Hyaluronan-CD44 Interactions in Cancer: Paradoxes and Possibilities.* Clin Cancer Res, 2009. **15**(24): p. 7462-7468.
300. Veiseh, M. and E.A. Turley, *Hyaluronan metabolism in remodeling extracellular matrix: probes for imaging and therapy of breast cancer.* Integr Biol (Camb), 2011. **3**(4): p. 304-15.
301. Kim, Y. and S. Kumar, *CD44-mediated adhesion to hyaluronic acid contributes to mechanosensing and invasive motility.* Mol Cancer Res, 2014. **12**(10): p. 1416-29.
302. Wang, X., et al., *Hyaluronic acid-based scaffold for central neural tissue engineering.* Interface Focus, 2012. **2**(3): p. 278-291.
303. Shapiro, L. and S. Cohen, *Novel alginate sponges for cell culture and transplantation.* Biomaterials, 1997. **18**(8): p. 583-90.
304. Florczyk, S.J., et al., *Porous chitosan-hyaluronic acid scaffolds as a mimic of glioblastoma microenvironment ECM.* Biomaterials, 2013. **34**(38): p. 10143-10150.
305. Florczyk, S.J., et al., *3D porous chitosan-alginate scaffolds promote proliferation and enrichment of cancer stem-like cells.* Journal of Materials Chemistry B, 2016. **4**(38): p. 6326-6334.
306. Wang, K., et al., *Culture on 3D Chitosan-Hyaluronic Acid Scaffolds Enhances Stem Cell Marker Expression and Drug Resistance in Human Glioblastoma Cancer Stem Cells.* Advanced Healthcare Materials, 2016. **5**(24): p. 3173-3181.
307. Coimbra, P., et al., *Sodium hyaluronate/chitosan polyelectrolyte complex scaffolds for dental pulp regeneration: synthesis and characterization.* Int J Biol Macromol, 2011. **49**(4): p. 573-9.
308. Frydrych, M., et al., *Structure and mechanical properties of gelatin/sepiolite nanocomposite foams.* Journal of materials chemistry, 2011. **21**(25): p. 9103-9111.
309. Pettikiriarachchi, J.T.S., et al., *Biomaterials for Brain Tissue Engineering.* Australian Journal of Chemistry, 2010. **63**: p. 1143-1154.
310. Rao, S.S., et al., *Glioblastoma behaviors in three-dimensional collagen-hyaluronan composite hydrogels.* ACS Appl Mater Interfaces, 2013. **5**(19): p. 9276-84.
311. Netti, P.A., et al., *Role of extracellular matrix assembly in interstitial transport in solid tumors.* Cancer Research, 2000. **60**(9): p. 2497-503.
312. Hutmacher, D.W., et al., *Can tissue engineering concepts advance tumor biology research?* Trends in Biotechnology, 2010. **28**(3): p. 125-133.
313. Lee, S.Y., *Temozolomide resistance in glioblastoma multiforme.* Genes & Diseases, 2016. **3**(3): p. 198-210.

314. Bleau, A.-M., J.T. Huse, and E.C. Holland, *The ABCG2 resistance network of glioblastoma.* Cell Cycle, 2009. **8**(18): p. 2937-2945.
315. Emery, I.F., et al., *Expression and function of ABCG2 and XIAP in glioblastomas.* Journal of Neuro-Oncology, 2017. **133**(1): p. 47-57.
316. Bertout, J.A., S.A. Patel, and M.C. Simon, *The impact of O2 availability on human cancer.* Nature Reviews Cancer, 2008. **8**(12): p. 967-75.
317. Wigerup, C., S. Pahlman, and D. Bexell, *Therapeutic targeting of hypoxia and hypoxia-inducible factors in cancer.* Pharmacology & Therapeutics, 2016. **164**: p. 152-169.
318. Radotra, B., D. McCormick, and A. Crockard, *CD44 plays a role in adhesive interactions between glioma cells and extracellular matrix components.* Neuropathol Appl Neurobiol, 1994. **20**(4): p. 399-405.
319. Pietras, A., et al., *Osteopontin-CD44 Signaling in the Glioma Perivascular Niche Enhances Cancer Stem Cell Phenotypes and Promotes Aggressive Tumor Growth.* Cell Stem Cell, 2014. **14**(3): p. 357-369.
320. Mooney, K.L., et al., *The role of CD44 in glioblastoma multiforme.* J Clin Neurosci, 2016. **34**: p. 1-5.
321. Ramachandran, R.K., et al., *Expression and prognostic impact of matrix metalloproteinase-2 (MMP-2) in astrocytomas.* Plos One, 2017. **12**(2): p. e0172234.
322. Mikheeva, S.A., et al., *TWIST1 promotes invasion through mesenchymal change in human glioblastoma.* Molecular Cancer, 2010. **9**(1): p. 194.
323. Iser, I.C., et al., *The Epithelial-to-Mesenchymal Transition-Like Process in Glioblastoma: An Updated Systematic Review and In Silico Investigation.* Medicinal Research Reviews, 2017. **37**(2): p. 271-313.
324. Medici, D., E.D. Hay, and B.R. Olsen, *Snail and Slug promote epithelial-mesenchymal transition through beta-catenin-T-cell factor-4-dependent expression of transforming growth factor-beta3.* Mol Biol Cell, 2008. **19**(11): p. 4875-87.
325. Hunziker, E.B., *Articular cartilage repair: basic science and clinical progress. A review of the current status and prospects.* Osteoarthritis and Cartilage, 2002. **10**(6): p. 432-463.
326. Bekkers, J.E., et al., *Cartilage Repair in Football (Soccer) Athletes: What Evidence Leads to Which Treatment? A Critical Review of the Literature.* Cartilage, 2012. **3**(1 Suppl): p. 43S-9S.
327. Cole, B.J., C. Pascual-Garrido, and R.C. Grumet, *Surgical management of articular cartilage defects in the knee.* Journal of Bone and Joint Surgery-American Volume, 2009. **91**(7): p. 1778-90.
328. Smith, G.D., G. Knutsen, and J.B. Richardson, *A clinical review of cartilage repair techniques.* Journal of Bone and Joint Surgery-British Volume, 2005. **87B**(4): p. 445-449.
329. Lopez-Ruiz, E., et al., *Polymers, scaffolds and bioactive molecules with therapeutic properties in osteochondral pathologies: what's new?* Expert Opinion on Therapeutic Patents, 2016. **26**(8): p. 877-890.
330. Bexkens, R., et al., *Donor-site morbidity after osteochondral autologous transplantation for osteochondritis dissecans of the capitellum: a systematic review and meta-analysis.* Knee Surg Sports Traumatol Arthrosc, 2017. **25**(7): p. 2237-2246.
331. Schinhan, M., et al., *Critical-size defect induces unicompartmental osteoarthritis in a stable ovine knee.* J Orthop Res, 2012. **30**(2): p. 214-20.
332. Madry, H., C.N. van Dijk, and M. Mueller-Gerbl, *The basic science of the subchondral bone.* Knee Surg Sports Traumatol Arthrosc, 2010. **18**(4): p. 419-33.

333. Nie, T., et al., *Fabrication of poly(L-lactic acid) tissue engineering scaffolds with precisely controlled gradient structure.* Materials Letters, 2016. **176**: p. 25-28.
334. Oh, S.H., et al., *In vitro and in vivo characteristics of PCL scaffolds with pore size gradient fabricated by a centrifugation method.* Biomaterials, 2007. **28**(9): p. 1664-71.
335. Di Luca, A., et al., *Gradients in pore size enhance the osteogenic differentiation of human mesenchymal stromal cells in three-dimensional scaffolds.* Sci Rep, 2016. **6**: p. 22898.
336. Aydin, H.M., *A Three-Layered Osteochondral Plug: Structural, Mechanical, and in vitro Biocompatibility Analysis.* Advanced Engineering Materials, 2011. **13**(12): p. B511-B517.
337. Yusong, P., et al., *Prediction of mechanical properties of multilayer gradient hydroxyapatite reinforced poly(vinyl alcohol) gel biomaterial.* Journal of Biomedical Materials Research Part B: Applied Biomaterials, 2013. **101B**(5): p. 729-735.
338. Kon, E., et al., *Orderly osteochondral regeneration in a sheep model using a novel nano-composite multilayered biomaterial.* J Orthop Res, 2010. **28**(1): p. 116-24.
339. Levingstone, T.J., et al., *Collagen-based multilayered scaffold shows potential for osteochondral defect repair.* Journal of Tissue Engineering and Regenerative Medicine, 2014. **8**: p. 82-83.
340. Oh, S.H., T.H. Kim, and J.H. Lee, *Creating growth factor gradients in three dimensional porous matrix by centrifugation and surface immobilization.* Biomaterials, 2011. **32**(32): p. 8254-8260.
341. Galperin, A., et al., *Integrated Bi-Layered Scaffold for Osteochondral Tissue Engineering.* Advanced Healthcare Materials, 2013. **2**(6): p. 872-883.
342. He, A., et al., *Repair of osteochondral defects with in vitro engineered cartilage based on autologous bone marrow stromal cells in a swine model.* Sci Rep, 2017. **7**: p. 40489.
343. Levingstone, T.J., et al., *Multi-layered collagen-based scaffolds for osteochondral defect repair in rabbits.* Acta Biomaterialia, 2016. **32**: p. 149-160.
344. Schaefer, D., et al., *Tissue-engineered composites for the repair of large osteochondral defects.* Arthritis and Rheumatism, 2002. **46**(9): p. 2524-2534.
345. Yoo, H.S., et al., *Hyaluronic acid modified biodegradable scaffolds for cartilage tissue engineering.* Biomaterials, 2005. **26**(14): p. 1925-33.
346. Kim, G., et al., *Preventive effect of hyaluronic acid on the suppression of attachment and migration abilities of bovine chondrocytes by IL-1 alpha in vitro.* Journal of Veterinary Medical Science, 2003. **65**(3): p. 427-430.
347. Shu, R., et al., *Hydroxyapatite accelerates differentiation and suppresses growth of MC3T3-E1 osteoblasts.* Journal of Biomedical Materials Research Part A, 2003. **67A**(4): p. 1196-1204.
348. Florczyk, S.J., et al., *Enhanced bone tissue formation by alginate gel-assisted cell seeding in porous ceramic scaffolds and sustained release of growth factor.* Journal of Biomedical Materials Research Part A, 2012. **100A**(12): p. 3408-3415.
349. Jin, X., et al., *Hydrothermal synthesis of hydroxyapatite nanorods in the presence of sodium citrate and its aqueous colloidal stability evaluation in neutral pH.* J Colloid Interface Sci, 2015. **443**: p. 125-30.
350. Zhang, R.Y. and P.X. Ma, *Poly(alpha-hydroxyl acids) hydroxyapatite porous composites for bone-tissue engineering. I. Preparation and morphology.* Journal of Biomedical Materials Research, 1999. **44**(4): p. 446-455.

351. Hsu, Y.Y., et al., *Effect of polymer foam morphology and density on kinetics of in vitro controlled release of isoniazid from compressed foam matrices.* Journal of Biomedical Materials Research, 1997. **35**(1): p. 107-116.
352. Dorati, R., et al., *Design of 3D scaffolds for tissue engineering testing a tough polylactide-based graft copolymer.* Materials Science & Engineering C-Materials for Biological Applications, 2014. **34**: p. 130-139.
353. Cecen, B., et al., *Biocompatibility and biomechanical characteristics of loofah based scaffolds combined with hydroxyapatite, cellulose, poly-l-lactic acid with chondrocyte-like cells.* Materials Science and Engineering: C, 2016. **69**: p. 437-446.
354. Lu, H.-T., et al., *Alterative effects of an oral alginate extract on experimental rabbit osteoarthritis.* Journal of Biomedical Science, 2015. **22**(1): p. 64.
355. Trombetta, R., et al., *3D Printing of Calcium Phosphate Ceramics for Bone Tissue Engineering and Drug Delivery.* Annals of Biomedical Engineering, 2017. **45**(1): p. 23-44.
356. Gupta, P., et al., *Biomimetic, Osteoconductive Non-mulberry Silk Fiber Reinforced Tricomposite Scaffolds for Bone Tissue Engineering.* Acs Applied Materials & Interfaces, 2016. **8**(45): p. 30797-30810.
357. Kim, I.Y., et al., *Chitosan and its derivatives for tissue engineering applications.* Biotechnol Adv, 2008. **26**(1): p. 1-21.
358. Knudson, C.B. and W. Knudson, *Hyaluronan and CD44: modulators of chondrocyte metabolism.* Clin Orthop Relat Res, 2004(427 Suppl): p. S152-62.
359. Olivares-Navarrete, R., et al., *Substrate Stiffness Controls Osteoblastic and Chondrocytic Differentiation of Mesenchymal Stem Cells without Exogenous Stimuli.* Plos One, 2017. **12**(1): p. e0170312.
360. Batchelar, D.L., et al., *Bone-composition imaging using coherent-scatter computed tomography: Assessing bone health beyond bone mineral density.* Medical Physics, 2006. **33**(4): p. 904-915.
361. Malmberg, P. and H. Nygren, *Methods for the analysis of the composition of bone tissue, with a focus on imaging mass spectrometry (TOF-SIMS).* Proteomics, 2008. **8**(18): p. 3755-3762.
362. Chesnutt, B.M., et al., *Design and characterization of a novel chitosan/nanocrystalline calcium phosphate composite scaffold for bone regeneration.* J Biomed Mater Res A, 2009. **88**(2): p. 491-502.
363. Venkatesan, J. and S.-K. Kim, *Chitosan Composites for Bone Tissue Engineering—An Overview.* Marine Drugs, 2010. **8**(8): p. 2252-2266.
364. Kim, H.L., et al., *Preparation and characterization of nano-sized hydroxyapatite/alginate/chitosan composite scaffolds for bone tissue engineering.* Mater Sci Eng C Mater Biol Appl, 2015. **54**: p. 20-5.
365. Yang, S., et al., *The design of scaffolds for use in tissue engineering. Part I. Traditional factors.* Tissue Eng, 2001. **7**(6): p. 679-89.
366. Hunziker, E.B. and I.M. Driesang, *Functional barrier principle for growth-factor-based articular cartilage repair.* Osteoarthritis Cartilage, 2003. **11**(5): p. 320-7.
367. Kreklau, B., et al., *Tissue engineering of biphasic joint cartilage transplants.* Biomaterials, 1999. **20**(18): p. 1743-9.
368. Niederauer, G.G., et al., *Evaluation of multiphase implants for repair of focal osteochondral defects in goats.* Biomaterials, 2000. **21**(24): p. 2561-74.

369. Schlichting, K., et al., *Influence of Scaffold Stiffness on Subchondral Bone and Subsequent Cartilage Regeneration in an Ovine Model of Osteochondral Defect Healing.* The American Journal of Sports Medicine, 2008. **36**(12): p. 2379-2391.
370. Shepherd, D.E. and B.B. Seedhom, *The 'instantaneous' compressive modulus of human articular cartilage in joints of the lower limb.* Rheumatology (Oxford), 1999. **38**(2): p. 124-32.
371. Bobick, B.E., et al., *Regulation of the Chondrogenic Phenotype in Culture.* Birth Defects Research Part C-Embryo Today-Reviews, 2009. **87**(4): p. 351-371.
372. Marom, R., et al., *Characterization of adhesion and differentiation markers of osteogenic marrow stromal cells.* Journal of Cellular Physiology, 2005. **202**(1): p. 41-48.

VITA

Ariane Erickson was born to David and Elizabeth Erickson and grew up in Butte, Montana with her two siblings, Danielle and Zachary. She attended college at Montana Tech. During her time at Montana Tech, Ariane received the Copper Club scholarship and completed two NSF-funded undergraduate research projects under the direction of Dr. C. Hank Rawlins. She received a Bachelor of Science in Metallurgical and Materials Engineering in 2012 and was awarded Outstanding Student of the Year for the department. She began her graduate studies under Professor Miqin Zhang at the University of Washington in 2012. During her time in the Zhang lab, she was awarded the Stoebe Fellowship, an NIH T-32 training grant, and the NSF Graduate Research Fellowship. In August 2018, she graduated from the University of Washington.